To the Graduate Council:

I am submitting herewith a dissertation written by Md. Ruhul Amin entitled "An Analytical And Experimental Investigation Of The Effect Of Large Wall Roughness Elements On The Natural Convection Heat Transfer In Rectangular Enclosures." I have examined the final copy of this dissertation for form and content and recommend that it be accepted in partial fulfillment of the requirements for the degree of Doctor of Philosophy, with a major in Mechanical Engineering.

Robert J. Krane

Robert J. Krane, Major Professor

We have read this dissertation and recommend its acceptance:

J Roger Parsons

J. W. Hodgson

Joseph J. Perona

Accepted for the Council:

C W Minkel

Vice Provost and
Dean of The Graduate School

AN ANALYTICAL AND EXPERIMENTAL INVESTIGATION OF THE EFFECT OF LARGE WALL ROUGHNESS ELEMENTS ON THE NATURAL CONVECTION HEAT TRANSFER IN RECTANGULAR ENCLOSURES

A Dissertation
Presented for the
Doctor of Philosophy
Degree
The University of Tennessee, Knoxville

Md. Ruhul Amin

August 1989

ACKNOWLEDGMENT

The author appreciates the patience and constant guidance of his research advisor, Professor R. J. Krane, whose valuable suggestions and encouragement made completion of this dissertation possible. The author is also grateful to the other members of the doctoral committee, J. R. Parsons, J. W. Hodgson and J. J. Perona for their careful review of this dissertation.

The author would like to express his thanks to his colleagues, the graduate students at UTK, for their help, encouragement and pleasant company. The author is most appreciative of his parents and wife for their continued patience, encouragement and support throughout this study.

The author is grateful to the Department of Mechanical and Aerospace Engineering at UTK for the financial support during his graduate study.

The author wishes to dedicate this dissertation to his parents, wife and daughter.

ABSTRACT

The purpose of this research was to determine the effects of placing large roughness elements on the hot vertical wall of a two-dimensional, rectangular enclosure on the rate of natural convection heat transfer across that enclosure. The enclosure of interest is assumed to be vertically-oriented with isothermal vertical walls maintained at two different temperatures, to have adiabatic horizontal walls, and to be completely filled with a Newtonian fluid. Both sinusoidal and rectangular roughness elements were investigated; however, the main focus of this investigation was on the use of rectangular elements. The roughness elements were assumed to be designed such that the total amount of fluid in the enclosure was equal to the amount of fluid in the corresponding smooth-walled enclosure. The consequences of not complying with this assumption were explored and shown to be significant.

Both numerical and experimental investigations of the problem were performed. The numerical solutions of the natural convection flows of interest in smooth-walled enclosures and enclosures containing either sinusoidal or rectangular roughness elements were obtained using the NACHOS finite element code. The experimental work was performed solely for the purpose of validating the NACHOS code for laminar, natural convection flows in two-dimensional enclosures containing large wall roughness elements. The code was shown to predict the temperature distributions in the fluid measured with a Mach-Zehnder interferometer and local wall heat flux (local Nusselt number) distribution measured with a Wollaston prism interferometer within the experimental uncertainty. Thus, the NACHOS code was successfully verified for the purposes of the present work.

An extensive parametric study was performed using NACHOS. The effects of adding wall roughness elements on the rate of natural convection heat transfer across an enclosure are reported in terms of the ratio of the overall Nusselt number in an enclosure containing roughness elements to the overall Nusselt number in the smooth-walled enclosure $[(\overline{Nu})_R/(\overline{Nu})_S]$ with the same aspect ratio, W/H. The highest value of $(\overline{Nu})_R/(\overline{Nu})_S$ (the greatest enhancement of the heat transfer) found in this work was 1.355; which was obtained at a Grashof number, Gr_H, of 4.07×10^6 in an enclosure containing four sinusoidal elements. The sinusoidal elements were shown to not only increase the rate of heat transfer near the bottom of the hot vertical wall, but to significantly increase the local rates of heat transfer on those segments of the cold vertical wall that are directly opposite to the elements. This effect was not observed in any of the flows investigated when rectangular elements were employed.

The ratio of Nusselt numbers, $(\overline{Nu})_R/(\overline{Nu})_S$, for enclosures containing rectangular roughness elements was shown to be a function of the Grashof number, Gr_H, the Prandtl number, Pr, the aspect ratio of the enclosure, W/H, and the amplitude, A, the period, δ, and the phase shift, δ_0, of the roughness element array. The values of all of these parameters, except that of the phase shift, δ_0, are shown to significantly affect the ratio of overall Nusselt numbers, $(\overline{Nu})_R/(\overline{Nu})_S$.

TABLE OF CONTENTS

CHAPTER	PAGE

CHAPTER **PAGE**

CHAPTER		PAGE

LIST OF TABLES

TABLE PAGE

LIST OF FIGURES

FIGURE **PAGE**

FIGURE PAGE

FIGURE		PAGE

FIGURE		PAGE

FIGURE		PAGE

NOMENCLATURE

A^*	amplitude of roughness element, see Figure 1
A	dimensionless amplitude of roughness element, A^*/H
c_p	constant pressure specific heat of fluid
g	magnitude of accelaration due to gravity
Gr_H	Grashof number, $g\beta\,(T_H{}^* - T_C{}^*)\,H^3/\nu^2$
k	thermal conductivity of fluid
H	height of the enclosure
$(\overline{Nu})_R$	average Nusselt number of an enclosure containing roughness elements
$(\overline{Nu})_S$	average Nusselt number of a smooth-walled enclosure
$Nu(y)$	local Nusselt number
P^*	motion pressure
P	dimensionless motion pressure, $P^*H^2/\rho\nu^2$
Pr	Prandtl number, $\mu c_p/k$
$\dot{q}_w$	local heat flux
$\dot{Q}$	overall rate of heat transfer
s^*	distance measured along the left-hand vertical wall of the enclosure containing roughness elements
s	dimensionless distance measured along the left-hand vertical wall of the enclosure containing roughness elements, s^*/H
T^*	temperature
T	dimensionless fluid temperature, $(T^* - T_C{}^*)/(T_H{}^* - T_C{}^*)$
$T_H{}^*$	hot wall temperature
$T_C{}^*$	cold wall temperature
u^*	x^*- component of velocity

u	dimensionless x-component of velocity, u^*H/ν
v^*	y^*-component of velocity
v	dimensionless y-component of velocity, v^*H/ν
$\vec{V}^*$	velocity vector
W	width of enclosure
x^*,y^*	spatial coordinates, see Figure 1
x,y	dimensionless spatial coordinates, x^*/H, y^*/H
$\bar{x}^*,\bar{y}^*$	local coordinates for rectangular roughness elements, see Figure 2
$\bar{x},\bar{y}$	dimensionless local coordinates for rectangular roughness elements, $\bar{x}^*/H$, $\bar{y}^*/H$
x_L^*	x^*-coordinate of the left-hand vertical wall
x_L	x-coordinate of the left-hand vertical wall, x_L^*/H
β	coefficient of thermal expansion of fluid
ψ^*	stream fuction defined by equation (2.30a) and (2.30b)
ψ	dimensionless stream fuction, ψ^*/ν
δ^*	period of roughness elements
δ	dimensionless period of roughness elements, δ^*/H
δ_0^*	phase shift of rectangular roughness elements
δ_0	dimensionless phase shift of rectangular roughness elements, δ_0^*/H
$\mathcal{H}^*$	heat function defined by equations (2.37a) and (2.37b)
$\mathcal{H}$	dimensionless heat function, $\mathcal{H}^*/k(T_H^* - T_C^*)$
ϕ	phase angle of sinusoidal roughness elements
μ	dynamic viscosity of fluid
ν	kinematic viscosity of fluid
ρ	density of fluid
$\vec{\omega}^*$	vorticity vector

CHAPTER 1
INTRODUCTION

1.1 Motivation for the Present Research

Natural convection is one of the more active areas of heat transfer research. A large volume of literature has been generated on this mode of heat transfer for various geometries and boundary conditions, and for a variety of fluids.

Many engineering applications involve heat transfer by natural convection. In recent years the cooling of electronic equipment has become one of the more important of these applications. Because it is inherently reliable, natural convection heat transfer is commonly used to cool electronic equipment. Electronic circuit cards often form vertical channels, or complete enclosures, depending on their mounting configurations and end conditions. The roughness elements on the surfaces of such circuit cards can affect the heat transfer rates from the cards. Thus, a fundamental understanding of the detailed mechanisms of the natural convection heat transfer in arrays of circuit cards with rough surfaces could lead to the more efficient design of cooling systems for electronic equipment.

Natural convection heat transfer is also an important factor in the design of building energy systems, since the heat transfer inside a room may be controlled by natural convection. The walls of a room can be rough due to the presence of windows, doors, and shelves. These roughness elements may significantly influence the heat transfer rates to or from the walls. Therefore, the ability to predict the influence of wall roughness elements on natural convection heat transfer may result in more efficient building energy systems.

The literature survey in Section 1.3 shows that the details of the mechanisms by which large surface roughness elements affect natural convection heat transfer are presently not well understood. Thus, it may be concluded that a better understanding of the effects of large roughness elements on natural convection flows is required. Hence, the objective of this research is to perform a combined numerical and experimental investigation of the effect of large wall roughness elements on the natural convection heat transfer in one specific geometry, namely, the rectangular enclosure.

1.2 Problem Description

Consider the natural convection heat transfer across the vertically-oriented, two-dimensional rectangular enclosures shown in Figure 1. Each enclosure is assumed to be completely filled with the same Newtonian fluid. The vertical walls of the enclosures are isothermal surfaces with the left-hand vertical wall of each enclosure maintained at a higher temperature, T^*_H, than the temperature of the right-hand vertical wall, T^*_C. The horizontal walls of each enclosure are adiabatic surfaces. As a result of the temperature difference (T^*_H-T^*_C) between the vertical walls, a natural convection flow occurs in each enclosure.

The enclosure shown in Figure (1a) has smooth vertical walls. The natural convection flows in this enclosure have been the subject of many numerical and experimental studies. Thus, reliable correlations are available for predicting the rate of heat transfer across this enclosure. The objective of the present research is to determine the effect of placing large roughness elements on the hot vertical wall of such an enclosure on the rate of heat transfer across the enclosure. As shown in Figures (1b) and (1c), both sinusoidal and rectangular roughness elements are of interest. It should be noted that each enclosure with roughness elements is designed

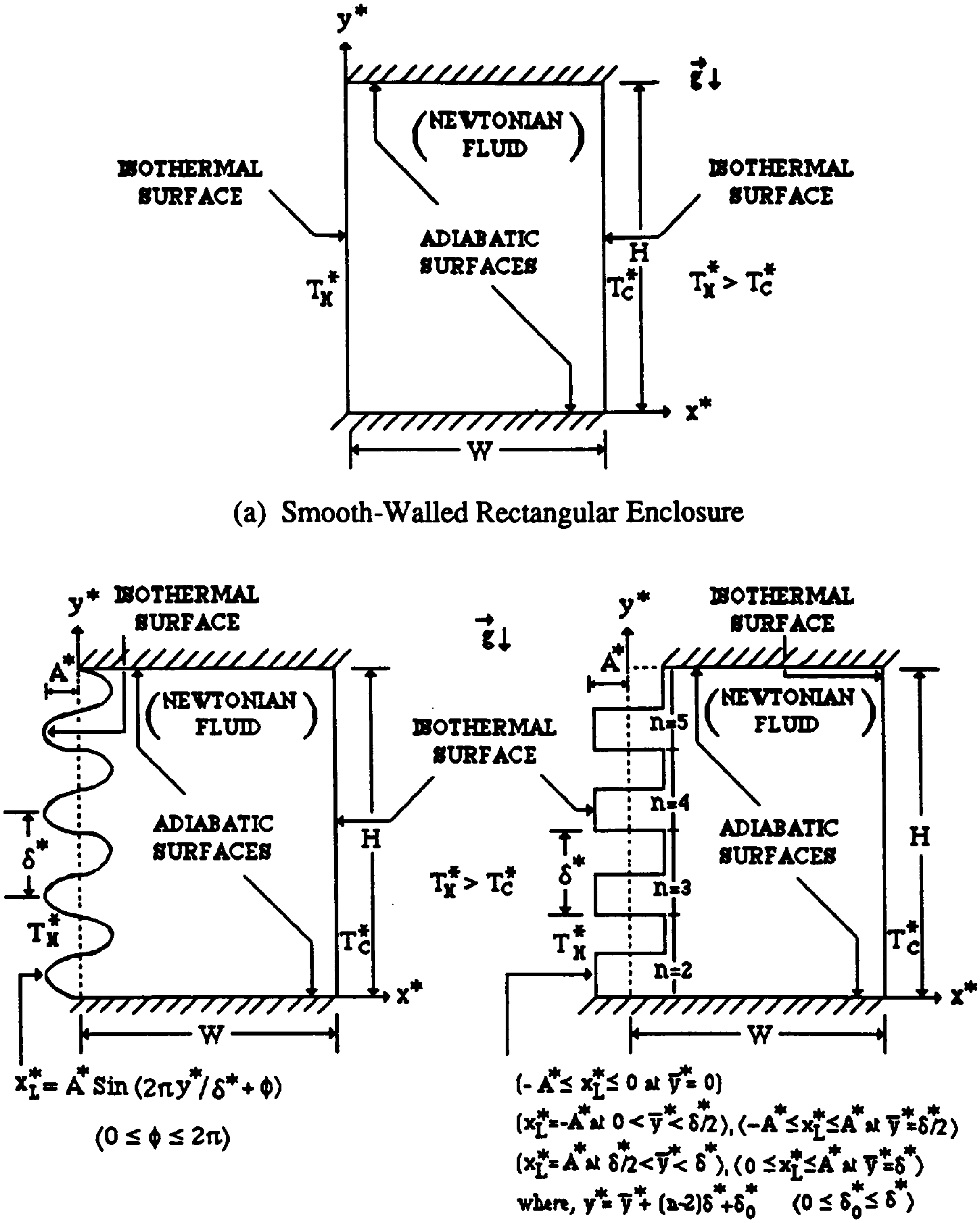

(a) Smooth-Walled Rectangular Enclosure

(b) Rectangular Enclosure with a Periodic Array of Large Sinusoidal Roughness Elements on the Hot Wall

(c) Rectangular Enclosure with a Periodic Array of Large Rectangular Roughness Elements on the Hot Wall

Figure 1. Enclosure Geometries to be Investigated

such that the volume of fluid in this enclosure is the same as the volume of fluid in the corresponding enclosure with smooth vertical walls and the same aspect ratio. This is necessary for the purpose of this investigation since attaching large roughness elements to a vertical wall can appreciably reduce the volume of fluid in the enclosure from that contained in the intially smooth-walled enclosure and thereby tend to reduce the overall thermal resistance of the fluid to natural convection heat transfer across the enclosure. This effect would preclude an equitable comparison between the corresponding enclosures with smooth walls and rough walls.

1.3 Literature Survey

1.3.1 General References on Natural Convection Heat Transfer

The textbooks by Jaluria (1980) and Gebhart, et al. (1988) are excellent sources of information on all aspects of natural convection heat transfer. The textbook by Bejan (1984) provides a vital and interesting view of natural convection from a new perspective.

1.3.2 External Natural Convection Flows on Rough Surfaces

Yao (1983) performed an analytical and numerical study of the natural convection heat transfer on a wavy vertical surface. He employed a coordinate transformation which transformed the irregular wavy surface into a flat surface for which natural convection equations were solved numerically by a finite-difference method. To illustrate the method, Yao examined the specific case of a vertical wall with a sinusoidal surface. His numerical results show that near the leading edge the value of the local Nusselt number depends on the slope of the wavy surface. He also showed that as the natural convection boundary layer grows thicker in the downstream direction, the amplitude of the oscillating local Nusselt number gradually decreases. Ramakrishna, et al. (1978) analytically studied the heat transfer rate from an isothermal vertical rough surface by introducing a friction factor in the shear stress term of the governing equations. They used a correlation to express the friction factor in terms of the absolute roughness height of the surface. Their analysis shows that due to the surface roughness, the heat transfer rate increases by about 50 percent from that of a corresponding smooth surface. Al-Arabi and El-Refae (1978) experimentally investigated the natural convection heat transfer in air from isothermal, upward-facing plates with triangular corrugations. They found that the heat transfer to the surrounding air decreases with increases of both the corrugation period and the corrugation angle. Jofre and Barron (1967) in their experimental investigation concluded that heat transfer from an isothermal vertical rough plate in air for Rayleigh numbers in the range of 10^4 to $2x10^9$ increases by a factor of two from that of a smooth plate. The surface roughness elements used in their experiments were horizontal ribs of triangular cross section, which were 0.76 mm high. They used the experimental data of Eckert and Jackson (1951) for smooth plate heat transfer to determine the heat transfer augmentation due to the surface roughness.

Several investigators studied the effects of wall roughness on heat transfer from cylinders. Prasolov (1961) performed an experiment on the natural convection heat transfer from a horizontal cylinder with distributed roughness elements on the surface. He found that for Rayleigh numbers less than or equal to 10^5 and greater than or equal to $3x10^6$ there is no increase in heat transfer. For Rayleigh numbers in the range from $3x10^5$ to 10^6, however, he found that the heat transfer increased by a factor of 1.5-1.9 due to surface roughness. He also concluded that with the increase of Rayleigh number the heat transfer enhancement increases up to some maximum value and then decreases. Prasolov's experiments have been repeated by Heya, et al. (1982) for Rayleigh numbers from 4.8×10^4 to 7.0×10^7 in air and 2.4×10^6 to 1.9×10^8 in water. They concluded that surface roughness has little or no influence on heat transfer coefficients under those conditions.

Fujii, et al. (1973) performed an experimental study of natural convection in water and spindle oil along a vertical cylinder with several different types of surface roughness elements. They found that in the turbulent regime, the local heat transfer coefficient increases slightly in water and decreases slightly in oil. The maximum variation of the local heat transfer coefficient is of the order of 10 percent in comparison with that for a smooth surface.

Sastri, et al. (1976) investigated natural convection from a vertical cylinder that was roughened by wrapping it with copper wire. They performed their investigation in air for Rayleigh numbers in the range of 7×10^8 to 3.5×10^9 and concluded that the overall heat transfer increases by up to 50 percent in comparison with that from a smooth cylinder. They did not explain the differences between their results and the results obtained by Fujii, et al. (1973).

The investigations discussed above are limited to the effects of roughness elements on external natural convection flows, not on natural convection flows in enclosures.

1.3.3 The Effects of Surface Roughness on Natural Convection Flows in Channels

Vajravelu and Sastri (1978) investigated the problem of natural convection in an incompressible viscous fluid bounded by a long, vertical wavy wall and a flat wall. In their investigation, attention was focused on the effects of wall waviness the flow and the heat transfer in the channel, especially when the fluid motion is generated due to the difference in the wall temperatures. The authors assumed that the flow may be decomposed into a mean part and a perturbed part. Following this assumption and using numerical methods, they evaluated the zeroth-order, first order, and total solution of the problem for different values of the Grashof number, Prandtl number, heat source or sink, wall temperature ratio, and wall-waviness. They showed that the waviness of the wall contributed the perturbed part of the solution. The mean part of the solution is given by the flow in a flat-walled channel. Vajravelu and Sastri (1980) also studied the natural convection in a channel when both of the walls of the channel were wavy surfaces. Prasada Rao, et al. (1983) investigated the free convection flows in a vertical channel bounded by a flat wall and an opposite wavy wall with a uniform magnetic field applied to the fluid in the presence of heat source or sink in the fluid. They also assumed that the flow is composed of a mean part and a perturbed part. They solved the governing equations numerically and tabulated the values of the Nusselt numbers for different values of the various parameters in the problem, including a "wall-waviness" parameter and the Grashof number.

Rao (1982) investigated the effects of wall waviness on the steady, two-dimensional, laminar free convection between two vertical walls of different temperatures with variable internal heat sources in the fluid and accounted for the effects of viscous dissipation. He split the governing equations into two parts using a linearization technique. One part governs the fully developed mean flow in a flat-walled channel and the other part governs the perturbations to the mean flow resulting from the waviness of the channel walls. He obtained approximate solutions for the flow and heat transfer using the Galerkin technique. He examined four different kinds of geometric configurations (left wall wavy and right wall smooth, right wall wavy and left wall smooth, both walls wavy with same "wall-waviness" parameter, and both walls wavy having different "wall-waviness" parameters) and three different expressions for the heat source distribution (constant heat sources, temperature-dependent heat sources, and heat sources which vary linearly with the temperature). The author found that for all the cases the amplitudes of the heat transfer coefficients at the walls of the channel increase with increasing value of the heat source parameter.

Elsherbiny, et al. (1978) made experimental measurements of the free convective heat transfer across inclined air layers that are heated from below and bounded by one V-corrugated plate and one flat plate. They showed that the natural convection heat transfer between the two plates is same whether the V-corrugated plate is above or below. They also showed that in the range of Rayleigh numbers from 10 to $4x10^6$ and for the same average plate spacing, the convective heat transfer across the air layer between a V-corrugated wall and a flat plate is up to 50 percent greater than that for two parallel flat plates.

Chinnappa (1970) experimentally investigated the heat transfer by natural convection from a heated, 60^0 angle, V-corrugated plate to a cooled flat plate above it, and obtained correlations for the Nusselt number.

1.3.4 The Effects of Surface Roughness Elements on Natural Convection Flows in Enclosures

Review papers by Ostrach (1972), Catton (1978), Ostrach(1982), and Hoogendorn (1986) summarize much of the work done on natural convection flows in enclosures. None of these reviews, however discuss the effects of wall roughness elements on natural convection flows in enclosures.

Probert and Ward (1974) performed an experimental investigation of techniques to improve the thermal resistance of vertical, air-filled, rectangular enclosures with one vertical hot wall opposed by a vertical cold wall. They investigated three different methods for increasing the thermal resistance of such an enclosure: (1) locating the hot and cold vertical walls an optimum distance apart, (2) the use of internal baffles attached to the enclosure walls, and (3) altering the enclosure shape. Since baffles constitute "large roughness elements", only the second technique is of interest here. The experiments of Probert and Ward show that the thermal resistance of an enclosure can be increased by (a) installing two vertical baffles, one on the bottom horizontal wall near the hot vertical wall and one on the top horizontal wall near the cold vertical wall and, (b) attaching several horizontal baffles to the cold vertical wall.

Kaviany (1984) studied the effects on natural convection of a semi-cylindrical protuberance, which was located on the adiabatic bottom wall of an otherwise square cavity with isothermal vertical walls maintained at different temperatures and adiabatic horizontal walls. His numerical study employed a finite difference technique and assumed a fluid with a Prandtl number of 0.71 and a range of Rayleigh numbers up to 10^4. He concludes that the protuberance causes a decrease in the local heat transfer rate on the lower portion of the cold vertical wall. This decrease in heat transfer rate is more pronounced with increasing Rayleigh number until a critical value of Rayleigh number is reached. Then the rate of decrease becomes less pronounced with further increases of Rayleigh number. For a fixed enclosure size, the critical value of the Rayleigh number depends on the radius of the protuberance. The author reports that for an enclosure with a nondimensional proturberance radius of 0.2, the value of the critical Rayleigh number is $5x10^3$. Bilski, et al. (1986) performed experimental investigation on the laminar natural convection flows in square and partially partitioned enclosures with two vertical isothermal walls and two horizontal insulated walls for a range of Rayleigh numbers from 10^5 to 10^6 and compared their results with those of numerical studies. In this study the vertical partitions were attached to the top and bottom adiabatic walls. These partitions were partial; that is, they did not extend over the full height of the enclosure.

None of the above authors studied the effects of large wall roughness elements attached to the vertical walls of an enclosure on the natural convection flows in an enclosure. Only three such studies could be found in the open literature. These studies are discussed below.

Anderson and Bohn (1986) performed an experimental investigation of the effects of large surface roughness elements on the natural convection heat transfer in a cubical enclosure filled with water. The top and bottom horizontal walls of the enclosure were heavily insulated. One vertical wall was a smooth, isothermal, cold wall. The opposing vertical wall was roughened by adding distributed roughness elements, which consisted of a series of intersecting groves rotated 45^0 from the horizontal. The ratio of the height of each roughness element to the enclosure height was 0.0034. Anderson and Bohn used both isothermal and constant flux boundary conditions for the rough vertical wall and covered the range of Rayleigh numbers and modified Rayleigh numbers from 7.7×10^9 to 7.3×10^{10} and 6.8×10^{11} to 9.2×10^{12}, respectively. Their experiment showed that, due to the surface roughness elements on the isothermal heated wall, the overall Nusselt number of the enclosure was increased by 15 percent from that of a corresponding smooth-walled enclosure at Rayleigh number 3.3×10^{10}. The local Nusselt number of the rough-walled enclosure increased by about 40 percent from that of a corresponding smooth-walled enclosure at a Rayleigh number of 4.1×10^{10}, measured at a location slightly above the midpoint of the isothermal heated wall. In this study the investigatiors did not consider the effects of not keeping the volume of the enclosure constant when making a comparison between smooth and rough-walled enclosures. They also did not explore the effects of changing the aspect ratio of the enclosure and the size of the roughness elements.

Shakerin and Loehrke (1987) performed a numerical study of the effects of roughness elements on natural convection in a vertical enclosure bounded by two isothermal vertical walls and two adiabatic horizontal walls. Either one or two roughness elements were mounted on the hot vertical wall. The height of the roughness element was of the order of boundary layer thickness. They performed their study with an enclosure aspect ratio of unity, a range of Rayleigh numbers from 0.72×10^5 to 10^8, and a Prandtl number of 0.7. They also computed a case with a Rayleigh number of 10^6 and a Prandtl number of 7.0. They extended the study for a case with an aspect ratio of 3.0, a Prandtl number of 0.7, and a Rayleigh number of 10^6. They found that regions of low heat transfer occur just below and above the roughness elements due to the decelerated flows in these regions. The authors concluded that for an enclosure with an aspect ratio of 1.0, filled with a fluid with a Prandtl number of 0.7, and at a Rayleigh number of 10^6, the presence of roughness elements increased the overall Nusselt number of the enclosure by 12 percent from that of a corresponding smooth-walled enclosure. In this study, the authors did not keep the volume of fluid in the enclosure constant in order to make a fair comparison with a corresponding smooth walled enclosure. They also did not study the effects of distributing the roughness elements over the entire height of the hot vertical wall.

Shakerin, et al. (1988) performed both numerical and experimental studies of the effects of roughness elements on natural convection in a vertical enclosure.

This study is a continuation of the previous work by Shakerin and Loehrke (1987). The enclosure geometry, boundary conditions, parameters ranges, and the results of the numerical study of this paper are identical to those reported in the 1987 paper. The authors perform a qualitative comparison of their experimental results for the flow pattern and the isotherms with their numerical results. The isotherms in their experimental study were obtained by setting the Mach Zhender Interferometer used in the experiment to an infinite fringe setting. In their experimental investigation, the authors did not perform any quantitative measurements of the heat flux distributions along the solid boundaries of the enclosure.

The above review of previous studies of the effects of large roughness elements on vertical walls of enclosures on natural convection may be summarized by noting that: (1) Only three studies of this type have been performed; (2) None of these studies maintained the volume of fluid in the enclosure constant when roughness elements were added; thereby precluding a proper comparison of smooth-wall and rough-wall results; (3) The combined effects of distributing large roughness elements over the entire height of a vertical wall and changing the aspect ratio of the enclosure have not been explored; (4) The effects of large roughness elements other than those of rectangular shape have not been investigated; and (5) No numerical modeling of the problem of interest here, verified by quantitative experiments has been done.

Therefore, it may be concluded that there is a need for a continued numerical and experimental study that will examine the effects of large wall roughness elements on the natural convection flows in rectangular enclosures in a more definitive manner than has been done in previous studies.

The literature on numerical methods and experimental techniques is briefly reviewed below.

1.3.5 Literature on Numerical Methods

Historically, the finite difference method (FDM) has been the most popular numerical method for problems in heat transfer and fluid mechanics. Detailed presentations of the application of the finite difference technique to problems in the thermal sciences may be found in texts such as Roache (1976), Patankar (1980), Anderson, et al. (1984), Jaluria and Torrance (1986), and Oran and Boris (1987). The use of the FDM is most advantageous when each domain boundary lies along a constant value of a spatial coordinate (i.e. for geometries with "regularly-shaped" boundaries).

The central finite difference technique was used in the present research to solve the Poisson equations that govern the distributions of the stream function and the heat function (Kimura and Bejan, 1983) of the smooth-walled enclosure (Figure 1a) and the enclosure with large rectangular roughness elements (Figure 1c). These calculations constituted "post-processing" operations, since they were performed after the solution for the natural convection flow in the enclosure had been solved by the methods described below.

The other major technique used for the numerical solution of problems in thermal sciences is the finite element method (FEM). Many authors such as Huebner (1975), Zienkiewicz (1977), Baker (1983), and Minkowycz, et al. (1988) present detailed discussions of the FEM. Significant advances have been made in finite element methodology in recent years. Using this method, it becomes relatively easy to formulate the discretized governing equations for nonuniform grids and for irregular geometries. Also, as reported by Denny and Clever (1974), the FEM has a greater computational efficiency than the FDM in calculating quantities like the wall heat flux.

The numerical solution of the equations governing the natural convection flow in the enclosure was done by using the general purpose finite element code called NACHOS, which was originally written by Dr. David K. Gartling of Sandia Laboratories and subsequently modified by Beach (1985a) to run on the IBM 3081 at The University of Tennessee, Knoxville. The code was also used in the "post-processing" operations to solve the Poisson equation that governs the stream function distribution of the enclosure with large sinusoidal roughness elements (Figure 1b).

Using the NACHOS code, Beach (1985b) obtained highly accurate numerical results for natural convection flows in smooth-walled enclosures as verified by comparison with the experimental results of Krane and Jessee (1983). The NACHOS code was easily applied to the enclosures of interest here, which have irregular boundaries.

1.3.6 Literature on Experimental Techniques

The temperature of the solid structural elements in the experimental apparatus was measured with copper-constantan thermocouples. Excellent discussions of temperature measurements with thermocouples are given by Baker, et al. (1975), and by Holman (1984).

The temperature distribution in the air in the test enclosure was measured with a Mach Zhender Interferometer, while a Wollaston Prism Interferometer was used to measure the heat flux distributions along the enclosure walls. Detailed discussions of the design, construction, and use of these interferometers are given by Eckert and Goldstein (1976), Sernas (1977), Heidari and Parsons (1980), Irby and Parsons (1981), and Jessee (1985).

CHAPTER 2
FORMULATION OF THE ANALYTICAL MODEL

2.1 Introduction

The governing equations and the boundary conditions for the natural convection flows in the enclosures shown in Figure 1 are presented below, as are the governing equations and boundary conditions for the stream function and the so-called "heat function" (Kimura and Bejan, 1983). The stream function and heat function are of interest since they are used along with isotherms to graphically portray the numerical results obtained in this investigation.

After recasting all of the governing equations and boundary conditions in terms of nondimensional variables, the resulting nondimensional parameters are identified and their physical meanings are discussed.

2.2 Modeling Assumptions

For the present work it is assumed that the flows of interest are steady-state, two-dimensional, laminar natural convection flows of a Newtonian fluid, which completely fills the enclosure being considered. It is also assumed that the Boussinesq approximation is valid, that the fluid is a radiatively nonparticipating medium, and that viscous dissipation and compressive work are negligibly small.

The objective of this research is to determine the effect of placing large roughness elements on the hot vertical wall of a vertically-oriented, rectangular enclosure on the rate of heat transfer across such an enclosure. To meet this objective, it is necessary to compare the overall rate of heat transfer across a smooth-walled enclosure to that across the corresponding enclosure to which roughness elements have been added. In order to insure that any difference in the rates of heat transfer across the two enclosures is solely due to the addition of the roughness elements, two conditions must be met. First, it is obvious that both enclosures must contain the same Newtonian fluid. The second condition is a bit more subtle. It requires that the total amount of fluid in each of the two enclosures being compared must be kept the same. The satisfaction of this condition is necessary since mounting large wall roughness elements in a smooth-walled enclosure without otherwise altering the enclosure geometry reduces the amount of fluid in the enclosure. In general, this would cause a change in the overall resistance offered by the fluid to heat transfer across the enclosure. In this case it would be impossible to determine whether it was an alteration of the flow in the enclosure, or the decrease in the amount of fluid in the enclosure due to the addition of the roughness elements, or both of these effects, that caused any change in the rate of heat transfer across the enclosure. This condition has been ignored by other investigators even though (as will be shown below) it can be quite important.

Both sinusoidal and rectangular roughness elements were employed in this investigation. The requirement for keeping the amount of fluid in the enclosure identical to that in the corresponding smooth-walled enclosure is quite simple to satisfy for the sinusoidal roughness elements. As shown in Figure (1b), it merely requires that the origin of the sine wave that forms the left-hand vertical wall lie on the plane $x^* = 0$, which coincides with the location of the left-hand vertical wall in the corresponding smooth-walled enclosure. The analogous requirements for the rectangular elements may be determined by inspection of Figure 2, which shows the detailed geometry of one period of a rectangular roughness element array. Figure 2 shows that, if the amount of fluid in the enclosure is to be kept equal to the

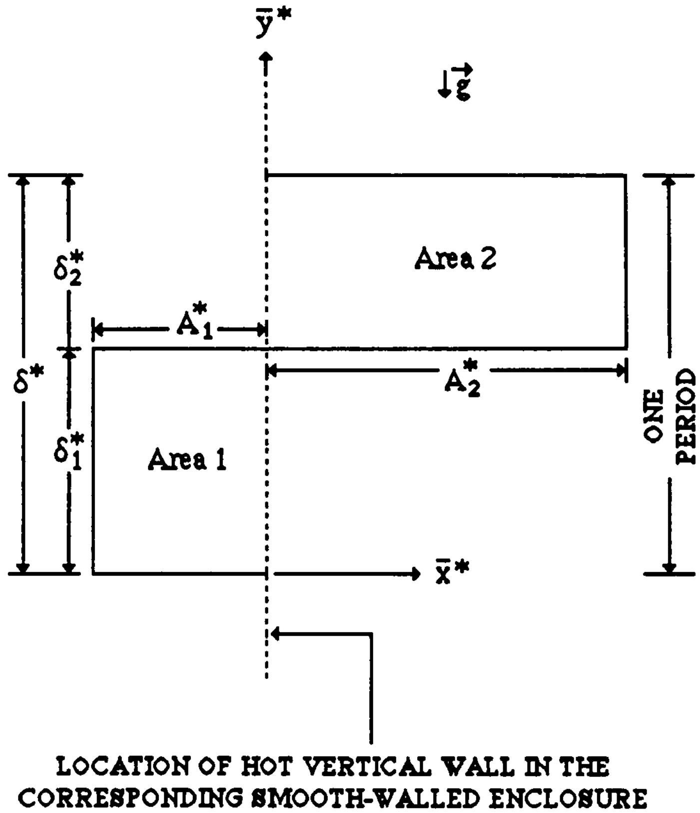

Figure 2. Basic Geometry of the Rectangular Elements - Shown in Local Coordinates

amount of fluid in the corresponding smooth-walled enclosure, that (area 1) must be equal to (area 2), or

$$A_1^* \delta_1^* = A_2^* \delta_2^* \ . \tag{2.1}$$

Figure 2 also shows that, in general, the spacing between the elements, δ_1^*, is not equal to the width of the elements, δ_2^*. For all of the cases considered in this investigation, however, it was assumed that the amplitudes A_1^* and A_2^* are equal, or

$$A_1^* = A_2^* \equiv A^* \tag{2.2}$$

such that the spacing between the elements and the width of the elements are identical; that is,

$$\delta_1^* = \delta_2^* = \delta^*/2 \tag{2.3}$$

where δ^* is the period of the roughness element array. It was also assumed that (H/δ^*) is always an integer. This integer is denoted by N_{PER}. These two assumptions serve to reduce the total number of cases considered in the computational and experimental studies to a reasonable size.

2.3 Governing Equations and Boundary Conditions for the Natural Convection Flows in the Enclosures

2.3.1 The Governing Equations In Physical Variables

Based on the modeling assumptions stated above, the governing equations for the natural convection flows in the enclosures are given in terms of physical variables by

Conservation of Mass

$$\frac{\partial u^*}{\partial x^*} + \frac{\partial v^*}{\partial y^*} = 0 \qquad (2.4a)$$

Newton's Second Law (x^*- Direction)

$$\rho \left[u^* \frac{\partial u^*}{\partial x^*} + v^* \frac{\partial u^*}{\partial y^*} \right] = - \frac{\partial P^*}{\partial x^*} + \mu \left[\frac{\partial^2 u^*}{\partial x^{*2}} + \frac{\partial^2 u^*}{\partial y^{*2}} \right] \qquad (2.4b)$$

Newton's Second Law (y^*- Direction)

$$\rho \left[u^* \frac{\partial v^*}{\partial x^*} + v^* \frac{\partial v^*}{\partial y^*} \right] = - \frac{\partial P^*}{\partial y^*} + \mu \left[\frac{\partial^2 v^*}{\partial x^{*2}} + \frac{\partial^2 v^*}{\partial y^{*2}} \right] + \rho g \beta (T^* - T^*_C) \qquad (2.4c)$$

and,

Conservation of Energy

$$\rho c_p \left[u^* \frac{\partial T^*}{\partial x^*} + v^* \frac{\partial T^*}{\partial y^*} \right] = k \left[\frac{\partial^2 T^*}{\partial x^{*2}} + \frac{\partial^2 T^*}{\partial y^{*2}} \right] \qquad (2.4d)$$

where, u^* and v^* are the velocity components in the x^*- and y^*-directions, T^* is the temperature, P^* is the "motion pressure" (defined as the actual pressure in the fluid less the pressure when the fluid is at rest at the reference temperature), g is the magnitude of the acceleration due to gravity, and ρ, μ, β, c_P, and k are the density, dynamic viscosity, coefficient of volumetric thermal expansion, constant pressure specific heat, and thermal conductivity of the fluid, respectively. The temperature of the cold vertical wall of the enclosure, T^*_C, serves as the reference temperature in the buoyancy force term in the Newton's second law (equation 2.4c).

Equations (2.4) govern the flows in both the smooth-walled and rough-walled enclosures shown in Figure 1.

2.3.2 The Boundary Conditions In Physical Variables

The boundary conditions for the top and the bottom horizontal walls, the right-hand vertical wall (the "cold wall"), and the left-hand vertical wall (the "hot wall") are the same for each of the three enclosures shown in Figure 1. For the top horizontal wall the boundary conditions are given by:

$$u^*(x^*, H) = 0 \tag{2.5a}$$

$$v^*(x^*, H) = 0 \tag{2.5b}$$

and,

$$\frac{\partial T^*(x^*, H)}{\partial y^*} = 0 \tag{2.5c}$$

for $(-A^* \leq x^* \leq W)$.

Similarly, the boundary conditions on the bottom horizontal wall are given by:

$$u^*(x^*, 0) = 0 \tag{2.6a}$$

$$v^*(x^*, 0) = 0 \tag{2.6b}$$

and,

$$\frac{\partial T^*(x^*, 0)}{\partial y^*} = 0 \tag{2.6c}$$

for $(-A^* \leq x^* \leq W)$.

The boundary conditions on the right-hand vertical wall (the "cold wall") of each enclosure are given by:

$$u^*(W, y^*) = 0 \tag{2.7a}$$

$$v^*(W, y^*) = 0 \tag{2.7b}$$

and,

$$T^*(W, y^*) = T^*_C \tag{2.7c}$$

for $(0 \leq y^* \leq H)$.

The boundary conditions on the left-hand vertical wall (the "hot wall") are given by:

$$u^*(x^*_L, y^*) = 0 \tag{2.8a}$$

$$v^*(x^*_L, y^*) = 0 \tag{2.8b}$$

$$T^*(x^*_L, y^*) = T^*_H \tag{2.8c}$$

where, x^*_L is the x^*-coordinate of the left-hand vertical wall and $(0 \leq y^* \leq H)$. For the smooth-walled enclosure shown in Figure (1a)

$$x^*_L = 0 \tag{2.9}$$

For the enclosure with sinusoidal roughness elements (Figure 1b)

$$x^*_L = A^* \operatorname{Sin} (2\pi \frac{y^*}{\delta^*} + \phi) \tag{2.10}$$

where ϕ is a phase angle defined such that $(0 \leq \phi \leq 2\pi)$. Finally, for the enclosure with rectangular roughness elements (Figure 1c) x^*_L is given for <u>each period</u> of the roughness element array by the following set of equations:

$$(- A^*_1 \leq x^*_L \leq 0) \quad \text{for } \overline{y}^* = 0 \quad (\text{for all n, except n} = 2 \text{ when } \delta^*_0 = 0) \tag{2.11a}$$

$$x^*_L = - A^*_1 \quad \text{for } \overline{y}^* = 0 \quad (\text{when n} = 2 \text{ and } \delta^*_0 = 0) \tag{2.11b}$$

$$x^*_L = - A^*_1 \quad \text{for } (0 < \overline{y}^* < \delta^*_1) \tag{2.11c}$$

$$(- A^*_1 \leq x^*_L \leq A^*_2) \quad \text{for } \overline{y}^* = \delta^*_1 \, (\text{for all n, except n} = N_{PER} + 1 \text{ when } \delta^*_0 = \delta^*/2) \tag{2.11d}$$

$$x^*_L = - A^*_1 \quad \text{for } \overline{y}^* = \delta^*_1 \quad (\text{when n} = N_{PER} + 1 \text{ and } \delta^*_0 = \delta^*/2) \tag{2.11e}$$

$$x^*_L = A^*_2 \quad \text{for } (\delta^*_1 < \overline{y}^* < \delta^*) \tag{2.11f}$$

and,

$$(0 \le x^*_L \le A^*_2) \quad \text{for } \overline{y}^* = \delta^* \tag{2.11g}$$

where, $\overline{y}^*$ is a <u>local</u> coordinate used to define a <u>single period</u> of the wall roughness element array as shown in Figure 2.

As noted in section 2.2, in the present work the amplitudes A^*_1 and A^*_2 are assumed to be equal, or

$$A^*_1 = A^*_2 = A^* \tag{2.2}$$

such that the spacing between the elements and the width of the elements are identical, that is

$$\delta^*_1 = \delta^*_2 = \delta^*/2 \ . \tag{2.3}$$

Substituting equations (2.2) and (2.3) in equations (2.11) yields the following set of relations for x^*_L for an enclosure with rectangular roughness elements:

$$(-A^* \le x^*_L \le 0) \quad \text{for } \overline{y}^* = 0 \quad (\text{for all n, except n} = 2 \text{ when } \delta^*_0 = 0) \tag{2.12a}$$

$$x^*_L = -A^* \quad \text{for } \overline{y}^* = 0 \quad (\text{when n} = 2 \text{ and } \delta^*_0 = 0) \tag{2.12b}$$

$$x^*_L = -A^* \quad \text{for } (0 < \overline{y}^* < \delta^*/2) \tag{2.12c}$$

$$(-A^* \le x^*_L \le A^*) \quad \text{for } \overline{y}^* = \delta^*/2 \ (\text{for all n, except n} = N_{PER} + 1 \text{ when } \delta^*_0 = \delta^*/2) \tag{2.12d}$$

$$x^*_L = -A^* \quad \text{for } \bar{y}^* = \delta^*/2 \ (\text{when } n = N_{PER} + 1 \text{ and } \delta^*_0 = \delta^*/2) \qquad (2.12e)$$

$$x^*_L = A^* \quad \text{for } (\delta^*/2 < \bar{y}^* < \delta^*) \qquad (2.12f)$$

and,

$$(0 \le x^*_L \le A^*) \quad \text{for } \bar{y}^* = \delta^* \ . \qquad (2.12g)$$

The vertical coordinate indicating the distance of each point on the hot wall above the bottom of the enclosure is given by the relation

$$y^* = \bar{y}^* + (n-2)\,\delta^* + \delta^*_0 \qquad (2.13)$$

where, δ^* is the period of the wall roughness element array, δ^*_0 accounts for any phase shift of the array, and n is a positive integer that identifies a specific period in the array. (n) is defined such that it assumes a value of 1 for $y^* \le \delta^*_0$ and then increases in increments of 1 for each period traversed in moving up the wall roughness element array until it reaches a maximum possible value of $n_{max} = (H/\delta^* + 1) = (N_{PER} + 1)$.

The boundary conditions $u^* = v^* = 0$ reflect the well-known requirement that the velocity of a viscous fluid, relative to solid surface, must be zero at the surface. The thermal boundary conditions $T^*(x^*_L, y^*) = T^*_H$ and $T^*(W, y^*) = T^*_C$ correspond to the specified isothermal conditions on the vertical walls, the condition $\partial T^*/\partial y^* = 0$ on the top and bottom horizontal walls is required by the adiabatic nature of these surfaces.

2.3.3 The Overall Rate of Heat Transfer Across an Enclosure

The local heat flux distribution along either vertical surface of an enclosure is given by

$$\dot{q}_W = \dot{q}_W(y^*) = -k\frac{\partial T^*}{\partial n^*} \tag{2.14}$$

where the derivative of the temperature is taken in the direction locally normal to the surface.

The overall rate of heat transfer across an enclosure, $\dot{Q}$, is of primary importance in the present work. This quantity is easily computed after a solution of the governing equations has been completed. The computation merely involves the integration of the local heat flux distribution along either vertical wall of the enclosure. For convenience, the right vertical wall was chosen for this purpose since it is always a plane surface, even in an enclosure containing roughness elements. Thus, we have

$$\dot{Q} = \int_0^H \dot{q}_W dy^* = -k\int_0^H \frac{\partial T^*(W,y^*)}{\partial x^*} dy^* \,. \tag{2.15}$$

2.3.4 The Nondimensional Form of the Governing Equations

Substituting the nondimensional variables

$$u = \frac{u^*}{(\nu/H)} \tag{2.16a}$$

$$v = \frac{v^*}{(\nu/H)} \tag{2.16b}$$

$$P = \frac{P^*}{\rho(\nu/H)^2} \tag{2.16c}$$

$$T = \frac{T^* - T^*_C}{T^*_H - T^*_C} \tag{2.16d}$$

$$x = \frac{x^*}{H} \tag{2.16e}$$

and,

$$y = \frac{y^*}{H} \tag{2.16f}$$

into equations (2.4) yields the following nondimensional set of governing equations for the natural convection flows in the enclosures :

Conservation of Mass

$$\frac{\partial u}{\partial x} + \frac{\partial v}{\partial y} = 0 \tag{2.17a}$$

Newton's Second Law (x-Direction)

$$u\frac{\partial u}{\partial x} + v\frac{\partial u}{\partial y} = -\frac{\partial P}{\partial x} + \frac{\partial^2 u}{\partial x^2} + \frac{\partial^2 u}{\partial y^2} \tag{2.17b}$$

Newton's Second Law (y-Direction)

$$u\frac{\partial v}{\partial x} + v\frac{\partial v}{\partial y} = -\frac{\partial P}{\partial y} + \frac{\partial^2 v}{\partial x^2} + \frac{\partial^2 v}{\partial y^2} + [\, Gr_H \,]\, T \tag{2.17c}$$

and,

Conservation of Energy

$$u\frac{\partial T}{\partial x} + v\frac{\partial T}{\partial y} = (\mathrm{Pr})^{-1}\left[\frac{\partial^2 T}{\partial x^2} + \frac{\partial^2 T}{\partial y^2}\right] \qquad (2.17d)$$

where:

$$Gr_H = \frac{\beta g(T^*_H - T^*_C)H^3}{\nu^2} = \text{Grashof number} = \left[\frac{\text{buoyancy force}}{\text{viscous force}}\right] \qquad (2.18a)$$

$$\mathrm{Pr} = \frac{c_p \mu}{k} = \text{Prandtl number} = \left[\frac{\text{diffusivity of momentum}}{\text{diffusivity of thermal energy}}\right]. \qquad (2.18b)$$

2.3.5 The Nondimensional Forms of the Boundary Conditions

Rewriting equations (2.5) in terms of the nondimensional variables given in equations (2.16) gives the following boundary conditions for the top horizontal wall of an enclosure:

$$u(x, 1) = 0 \qquad (2.19a)$$

$$v(x, 1) = 0 \qquad (2.19b)$$

and,

$$\frac{\partial T(x, 1)}{\partial y} = 0 \qquad (2.19c)$$

for $(-A \leq x \leq W/H)$.

Similarly, the boundary conditions on the bottom horizontal wall given by equations (2.6) are transformed into the following nondimensional forms

$$u(x,0)=0 \tag{2.20a}$$

$$v(x,0)=0 \tag{2.20b}$$

and,

$$\frac{\partial T(x,0)}{\partial y}=0 \tag{2.20c}$$

for $(-A \leq x \leq W/H)$.

Rewriting equations (2.7) in terms of the nondimensional variables yields the following set of nondimensional boundary conditions for the right-hand vertical wall of each enclosure:

$$u(\frac{W}{H},y)=0 \tag{2.21a}$$

$$v(\frac{W}{H},y)=0 \tag{2.21b}$$

and,

$$T(\frac{W}{H},y)=0 \tag{2.21c}$$

for $(0 \leq y \leq 1)$.

The nondimensional form of the boundary conditions on the left-hand vertical wall are found by rewriting equations (2.8) in terms of the nondimensional variables to get

$$u(x_L,y)=0 \tag{2.22a}$$

$$v(x_L,y)=0 \tag{2.22b}$$

and,

$$T(x_L,y)=1 \tag{2.22c}$$

where $x_L = (x^*_L/H)$ is the x-coordinate of the left-hand vertical wall and $(0 \le y \le 1)$. For the smooth-walled enclosure shown in Figure (1a) equation (2.9) gives

$$x_L = 0 \ . \tag{2.23}$$

For the enclosure with sinusoidal roughness elements as shown in Figure (1b)

$$x_L = A \operatorname{Sin}\left(2\pi \frac{y}{\delta} + \phi\right) \tag{2.24}$$

where $A = A^*/H$ is the dimensionless amplitude of the elements, $\delta = \delta^*/H$ is the dimensionless period of the sinusoidal roughness element array, and, as before, ϕ is the phase angle of the array, which is defined such that $(0 \le \phi \le 2\pi)$. For the enclosure with rectangular roughness elements, as shown in Figure (1c), the nondimensional forms of the equations which give x_L for <u>each period</u> of the roughness element array are found by substituting the nondimensional variables into equation (2.12) to get

$$(-A \le x_L \le 0) \quad \text{for } \bar{y} = 0 \quad (\text{for all n, except n} = 2 \text{ when } \delta_0 = 0) \tag{2.25a}$$

$$x_L = -A \quad \text{for } \bar{y} = 0 \quad (\text{when n} = 2 \text{ and } \delta_0 = 0) \tag{2.25b}$$

$$x_L = -A \quad \text{for } (0 < \bar{y} < \delta/2) \tag{2.25c}$$

$$(-A \le x_L \le A) \quad \text{for } \bar{y} = \delta/2 \ (\text{for all n, except n} = N_{PER} + 1 \text{ when } \delta_0 = \delta/2) \tag{2.25d}$$

$$x_L = -A \quad \text{for } \bar{y} = \delta/2 \text{ (when } n = N_{PER} + 1 \text{ and } \delta_0 = \delta/2) \qquad (2.25e)$$

$$x_L = A \quad \text{for } (\delta/2 < \bar{y} < \delta) \qquad (2.25f)$$

and,

$$(0 \le x_L \le A) \quad \text{for } \bar{y} = \delta \qquad (2.25g)$$

where $A = A^*/H$ is the nondimensional amplitude of the rectangular roughness elements, $\delta = \delta^*/H$ is the nondimensional period of the roughness element array and $\bar{y} = \bar{y}^*/H$ is the dimensionless local vertical coordinate for a single period of the array. Finally, the dimensionless distance of a point on the hot vertical wall above the bottom of the enclosure is found by substituting the nondimensional variables into equation (2.13) to get

$$y = \bar{y} + (n - 2)\,\delta + \delta_0 \qquad (2.26)$$

where $\delta_0 = \delta^*_0/H$ is the dimensionless phase shift of the array. As before, n is a positive integer, the value of which identifies a specific element in the array. In nondimensional terms, n is defined such that it assumes a value of 1 for $y \le \delta_0$ and increases in increments of 1 for each period traversed in moving up the wall roughness element array until it reaches a maximum possible value, $n_{max} = (1/\delta + 1) = (N_{PER} + 1)$.

2.3.6 <u>The Dimensionless Form of the Overall Rate of Heat Transfer Across an Enclosure</u>

Rewriting equation (2.14) for the local heat flux distribution along a vertical wall of an enclosure in terms of dimensionless variables yields

$$Nu(y) = \left[\frac{\dot{q}_w H}{k(T^*_H - T^*_C)} \right] = - \frac{\partial T}{\partial n} \tag{2.27}$$

where Nu(y) is the local Nusselt number. Similarly, rewriting equation (2.15) in terms of dimensionless variables gives the following expression for the overall rate of heat transfer across an enclosure

$$\overline{Nu} = \left[\frac{\dot{Q}}{k(T^*_H - T^*_C)} \right] = - \int_0^1 \frac{\partial T(W/H, y)}{\partial x} dy \tag{2.28}$$

where $\overline{Nu}$ is the overall Nusselt number for an enclosure.

The nondimensional forms of the governing equations (Equations 2.17) and the boundary conditions (Equations 2.19-2.26) show the following functional dependencies of the overall Nusselt number for :

(1) <u>a smooth-walled enclosure</u>

$$(\overline{Nu})_S = \overline{Nu}_S[Gr_H, Pr, W/H] \ , \tag{2.29a}$$

(2) <u>an enclosure with sinusoidal roughness elements</u>

$$(\overline{Nu})_R = \overline{Nu}_R \ [Gr_H, Pr, W/H, A, \delta, \phi] \ , \tag{2.29b}$$

and,

(3) <u>an enclosure with rectangular roughness elements</u>

$$(\overline{Nu})_R = \overline{Nu}_R[Gr_H, Pr, W/H, A, \delta, \delta_0] \ . \tag{2.29c}$$

2.4 The Governing Equations and Boundary Conditions For the Stream Function and the Heat Function

2.4.1 Introduction

Most of the numerical results in this investigation are presented in graphical form using plots of the isotherms, streamlines and heat lines to portray the flows in the enclosures. An isotherm plot is obtained by submitting the discrete temperature distribution computed as part of the solution of the governing equations for the flow in the enclosure to a contouring program. The corresponding distributions of the stream function and the heat function, however, must be computed from their governing equations before they can be submitted to the contouring program to obtain the streamline and heat line plots. Thus, the governing equations and the boundary conditions for the stream function and the heat function are developed below.

2.4.2 The Governing Equation and Boundary Conditions For the Stream Function

The stream function, ψ^*, is defined by the following relations

$$u^* = \frac{\partial \psi^*}{\partial y^*} \tag{2.30a}$$

and,

$$v^* = -\frac{\partial \psi^*}{\partial x^*} \tag{2.30b}$$

which are designed such that ψ^* satisfies the equation (2.4a) for conservation of mass exactly. The governing equation for ψ^* is found from the definition of the vorticity vector, $\bar{\omega}^*$, which is given by

$$\vec{\omega}^* = \nabla \times \vec{V}^* \tag{2.31}$$

where $\vec{V}^*$ is the velocity vector. For the two-dimensional flows of interest here, equations (2.30) and (2.31) are easily shown to give

$$\frac{\partial^2 \psi^*}{\partial x^{*2}} + \frac{\partial^2 \psi^*}{\partial y^{*2}} = -\omega^*_Z = \left(\frac{\partial u^*}{\partial y^*} - \frac{\partial v^*}{\partial x^*}\right) \tag{2.32}$$

which is the governing equation for the stream function in physical variables. The right-hand side of this equation is evaluated using the velocity distribution obtained from the solution of the governing equations for the flow in the enclosure. The boundary conditions for equation (2.32) are given by

$$\psi^*(x^*_L, y^*) = 0 \tag{2.33a}$$

$$\psi^*(W, y^*) = 0 \tag{2.33b}$$

for $(0 \le y^* \le H)$, and

$$\psi^*(x^*, 0) = 0 \tag{2.33c}$$

$$\psi^*(x^*, H) = 0 \tag{2.33d}$$

for $(0 \le x^* \le W)$.

Recasting equations (2.32) and (2.33) in terms of the dimensionless variables gives the following nondimensional forms of the governing equation and the boundary conditions for the stream function as

$$\frac{\partial^2\psi}{\partial x^2} + \frac{\partial^2\psi}{\partial y^2} = \left(\frac{\partial u}{\partial y} - \frac{\partial v}{\partial x}\right) \tag{2.34}$$

and,

$$\psi(x_L , y) = 0 \tag{2.35a}$$

$$\psi(W/H , y) = 0 \tag{2.35b}$$

for $(0 \leq y \leq 1)$, and

$$\psi(x , 0) = 0 \tag{2.35c}$$

$$\psi(x , 1) = 0 \tag{2.35d}$$

for $(0 \leq x \leq W/H)$, where

the dimensionless stream function is given by:

$$\psi = \frac{\psi^*}{\nu} . \tag{2.36}$$

2.4.3 The Governing Equations and Boundary Conditions For the Heat Function

Kimura and Bejan (1983) defined the heat function, $\mathcal{H}^*$, by the relations

$$\frac{\partial \mathcal{H}^*}{\partial y^*} = \rho c_p u^*(T^* - T^*_C) - k\frac{\partial T^*}{\partial x^*} = \begin{bmatrix} \text{total transport of energy by convection} \\ \text{and conduction in the } x^*\text{- direction} \end{bmatrix} \tag{2.37a}$$

$$-\frac{\partial \mathcal{H}^*}{\partial x^*} = \rho c_p v^*(T^* - T^*_C) - k\frac{\partial T^*}{\partial y^*} = \begin{bmatrix} \text{total transport of energy by convection} \\ \text{and conduction in the } y^*\text{- direction} \end{bmatrix} \tag{2.37b}$$

such that $\mathcal{H}^*$ satisfies the equation (2.4d) for conservation of energy exactly. Differentiating equation (2.37a) with respect to y* and equation (2.37b) with respect to x^* and subtracting the results gives the following governing equation for $\mathcal{H}^*$ in physical variables:

$$\frac{\partial^2 \mathcal{H}^*}{\partial x^{*2}} + \frac{\partial^2 \mathcal{H}^*}{\partial y^{*2}} = \left\{ \rho c_P \right\} \left\{ \frac{\partial}{\partial y^*} \left[u^*(T^* - T^*_C) \right] - \frac{\partial}{\partial x^*} \left[v^*(T^* - T^*_C) \right] \right\} . \tag{2.38}$$

The right hand side of equation (2.38) is evaluated using the velocity and temperature distributions obtained from the solution of the governing equations for the flow in the enclosure. The boundary conditions for equation (2.38) are given below. Along the bottom horizontal wall

$$\mathcal{H}^*(x^*, 0) = 0 \tag{2.39a}$$

for ($x^*_L \leq x^* \leq W$). Along the left-hand vertical wall

$$\mathcal{H}^*(x^*_L, y^*) = \int_0^{s^*} \dot{q}_w \, ds^* = \int_0^{s^*} \left(-k \frac{\partial T^*}{\partial n^*} \right) ds^* \tag{2.39b}$$

for ($0 \leq y^* \leq H$), where s^* is the total distance measured along the surface of the left-hand vertical wall starting from the intersection of this wall with the bottom horizontal wall of the enclosure. s^* varies in the range

$$(0 \leq s^* \leq s^*_{Max})$$

where $s^*_{Max} = s^*$ at $y^* = H$ is the maximum possible length measured along the left-hand vertical wall. For a smooth-walled enclosure, $s^*_{Max} = H$; while for an enclosure containing roughness elements, $s^*_{Max} > H$. Thus, along the top horizontal wall

$$\mathcal{H}^*(x^*, H) = \int_0^{s^*_{Max}} \left(-k\frac{\partial T^*}{\partial n^*}\right) ds^* = (\text{Constant}) = \dot{Q} \tag{2.39c}$$

for $(x^*_L \leq x^* \leq W)$, where $\dot{Q}$ is the total rate of heat transfer across the enclosure given by equation (2.15). Finally, along the right-hand vertical wall

$$\mathcal{H}^*(W, y^*) = \dot{Q} + \int_H^{y^*} \left(-k\frac{\partial T^*(W, y^*)}{\partial x^*}\right) dy^* \tag{2.39d}$$

for $(0 \leq y^* \leq H)$.

Rewriting equations (2.38) and (2.39) in terms of the dimensionless variables gives the following nondimensional forms of the governing equation and boundary conditions for the heat function

$$\frac{\partial^2 \mathcal{H}}{\partial x^2} + \frac{\partial^2 \mathcal{H}}{\partial y^2} = \Pr\left[\frac{\partial(uT)}{\partial y} - \frac{\partial(vT)}{\partial x}\right] \tag{2.40}$$

$$\mathcal{H}(x, 0) = 0 \quad \text{for } (x_L\big|_{y=0} \leq x \leq W/H) \tag{2.41a}$$

$$\mathcal{H}(x_L, y) = \int_0^s \mathrm{Nu}(y)\, ds = \int_0^s \left(-\frac{\partial T}{\partial n} \right) ds \quad \text{for } (0 \le y \le 1) \tag{2.41b}$$

$$\mathcal{H}(x, 1) = \int_0^{s_{Max}} \left(-\frac{\partial T}{\partial n} \right) ds = (\text{Constant}) = \overline{\mathrm{Nu}} \quad \text{for } (x_L \Big|_{y=1} \le x \le W/H) \tag{2.41c}$$

$$\mathcal{H}(1, y) = \overline{\mathrm{Nu}} + \int_1^y \left(-\frac{\partial T(W/H, y)}{\partial x} \right) dy \quad \text{for } (0 \le y \le 1) \tag{2.41d}$$

where, $\mathcal{H} = \dfrac{\mathcal{H}^*}{k\,(T^*_H - T^*_C)}$ is the nondimensional heat function and Nu(y) and $\overline{\mathrm{Nu}}$ are the local and overall Nusselt numbers given by equations (2.27) and (2.28), respectively.

2.4.4 The Physical Interpretation of the Heat Function

The physical meaning of the heat function, $\mathcal{H}$, is easily understood through a comparison with the stream function, ψ. As is well-known: (1) the stream function is defined such that it satisfies the equation for conservation of mass exactly, (2) lines of constant ψ, called "streamlines", are everywhere tangent to the velocity vector so that there is no mass flowrate across a streamline, and (3) the mass flowrate between two neighboring streamlines is a constant. Thus, a contour plot of the stream function shows the streamlines, which provide a "picture" of the flowfield. By analogy: (1) the heat function, $\mathcal{H}$, is defined such that it satisfies the equation for conservation of energy exactly, (2) lines of constant $\mathcal{H}$, called "heat lines", are everywhere tangent to the total energy flux vector, which accounts for the total transport of thermal energy by the combined action of conduction and convection, and (3) the total rate of thermal energy transport between any two neighboring heat lines is a constant. Thus, for the heat function a contour plot shows the heat lines, which provide a "picture" of the energy transport paths by the combined effects of convection and conduction through a flowfield.

The use of isotherm, streamline and heat line plots to graphically portray the numerical results of this study facilitates the physical explanation of these results. Equations (2.41) show that the horizontal walls of an enclosure are heat lines with heat function, $\mathcal{H}$, equal to zero on the bottom horizontal wall and to the overall Nusselt number on the top horizontal wall. The heat function increases from zero at the bottom of the left-hand vertical wall to the overall Nusselt number at the top of that wall as heat is transfered from this (hot) wall to the fluid. Thus, a series of heat lines will appear to emanate from the left-vertical wall. These particular heat lines, which are locally normal to the left-hand vertical wall, will extend across the width of the enclosure until they intersect the right-hand vertical wall where they are also locally normal to the surface. Thus, the heat function decreases in value from that of the overall Nusselt number at the top of the right-hand vertical wall to zero at the bottom of this wall as heat is transfered from the fluid to this (cold) wall.

CHAPTER 3

THE NUMERICAL INVESTIGATION

3.1 Introduction

This chapter and its associated appendices describe the numerical techniques used to solve the governing equations for: (1) the natural convection flow in an enclosure, and (2) the stream function and heat function for such a flow. The overall scope of the numerical investigation is outlined in the form of the computational matrix. Finally, a brief discussion of the computational grid is included.

3.2 The Numerical Solution of the Governing Equations for the Natural Convection Flows in the Enclosures

Numerical solutions of equations (2.17), which govern the natural convection flows in the enclosures, were obtained for smooth-walled rectangular enclosures and for rectangular enclosures containing sinusoidal and rectangular wall roughness elements using the finite element code NACHOS. The boundary conditions on the horizontal walls and on the right-hand (cold) vertical wall are given by equations (2.19), (2.20) and (2.21) for all three types of enclosures. The boundary conditions on the left-hand (hot) vertical wall are given by equations (2.22) and (2.23) for a smooth-walled enclosure, by equations (2.22) and (2.24) for an enclosure with sinusoidal roughness elements, and by equations (2.22), (2.25) and (2.26) for an enclosure with rectangular roughness elements.

The NACHOS code was developed by Dr. David K. Gartling of Sandia Laboratories (Gartling, 1977a,b). The code was later modified by Mr. Tim Beach at the University of Tennessee, Knoxville to run on the IBM/3081 (Beach,1985).

NACHOS is based on the Galerkin form of the finite element method and is designed for the solution of both transient and steady-state, two-dimensional, laminar flows that are governed by the Navier-Strokes Equations. The detailed derivations of the finite element equations on which NACHOS is based and an extensive discussion of this program are given by Gartling (1977a,b). Following Said (1986), abbreviated discussions of the formulation of the finite element equations, the element construction, and the solution algorithm for the NACHOS code are given in Appendix A.

3.3 The Numerical Solution of the Governing Equations for the Stream Function and the Heat Function

Equation (2.34) is the governing equation for the stream function. The boundary conditions for this equation are given by equations (2.35). Similarly, equation (2.40) is the governing equation for the heat function and its boundary conditions are given by equations (2.41). Equations (2.34) and (2.40) are Poisson equations that cannot be solved until the equations governing the natural convection flow in the enclosure have been solved because the right-hand members of these equations are functions of the fluid velocity components, u and v, and the fluid temperature, T. The solutions of equations (2.34) and (2.40) were obtained numerically using the finite difference techniques that are presented in Appendix B. These computations were performed only for the flows in the smooth-walled enclosures and the enclosures containing rectangular roughness elements. The streamlines, isotherms and heat lines were plotted for all these flows using the contouring program SURFACE II.

The streamlines and isotherms for the flows in enclosures with sinusoidal wall roughness elements were computed and plotted using the post-processing capabilities of the NACHOS code. The heat function was not computed, nor the heat lines plotted, for these flows.

3.4 The Computational Matrix

The functional dependencies of the overall Nusselt number for the enclosures investigated in this research are given by equations (2.29). These relationships were used to develop the computational matrix that is presented below in the following tables.

For the smooth-walled enclosures, it was shown that the Nusselt number is given by

$$(\overline{Nu})_S = \overline{Nu_S}\,[Gr_H\,,\ Pr\,,\ W/H] \qquad (3.1)$$

where Gr_H is the Grashof number built on the enclosure height, Pr is the Prandtl number, and W/H is the aspect ratio of the enclosure. As shown in Table 1, a total of 14 cases were run for smooth-walled enclosures. The results of these cases enable the comparisons required to determine any changes in the rates of heat transfer for corresponding enclosures with roughness elements.

The Nusselt number relationship for an enclosure with sinusoidal roughness elements is given by

$$(\overline{Nu})_R = \overline{Nu_R}\,[Gr_H\,,\ Pr\,,\ W/H\,,\ A\,,\ \delta\,,\ \phi] \qquad (3.2)$$

where Gr_H, Pr, and W/H are as defined above, A is the dimensionless amplitude of a roughness element, δ is the dimensionless period of the roughness element array, and ϕ is the phase angle of the array. The values of these parameters for the 9 cases

Table 1. Cases Run for Smooth-Walled Enclosures

Case No.	Gr_H	Pr	W/H
1	1.55×10^3	0.72	1.0
2	1.49×10^4	0.72	1.0
3	1.43×10^5	0.72	1.0
4	3.41×10^5	4.52	1.0
5	1.69×10^6	0.72	0.4
6	1.90×10^6	0.72	0.4
7	4.07×10^3	4.52	0.4
8	4.07×10^4	4.52	0.4
9	4.07×10^5	4.52	0.4
10	4.07×10^6	4.52	0.4
11	6.64×10^3	4.52	0.34
12	6.64×10^4	4.52	0.34
13	6.64×10^5	4.52	0.34
14	6.64×10^6	4.52	0.34

(15-23) that were run for enclosures with sinusoidal roughness elements are presented in Table 2.

Finally, the Nusselt number relationship for enclosures with rectangular roughness elements is given by

$$(\overline{Nu})_R = \overline{Nu}_R[Gr_H\,,\ Pr\,,\ W/H\,,\ A\,,\ \delta\,,\ \delta_0] \tag{3.3}$$

where Gr_H, Pr, and W/H are as defined above, A is the dimensionless amplitude of a rectangular roughness element, δ is the dimensionless period of the roughness element array, and δ_0 is the dimensionless phase shift of the array. The values of these parameters for the 29 cases (24-52) run for enclosures with rectangular roughness elements are presented in Table 3.

As discussed in Chapter 2, the amount of fluid in the corresponding enclosures with and without roughness elements was kept the same in this work in order that the true effects of adding the roughness elements on the heat transfer could be determined. To explore the effects of adding rectangular roughness elements in such a manner that the total amount of fluid in the corresponding enclosures is <u>not</u> kept constant, the four cases (53-56) shown in Table 4 were run.

3.5 <u>The Computational Grid</u>

A typical finite element grid used by NACHOS to perform the computations in an enclosure with rectangular roughness elements is shown in Figure 3. This particular grid, which was used for enclosures with W/H = 0.4, $\delta = 0.25$, A = 0.12, and $\delta_0 = 0.125$, is <u>nonuniform</u> and contains 399 elements. The elements were arranged such that more of them are packed into regions in which there are large gradients in the velocity and/or temperature.

Table 2. Cases Run for Enclosures with Sinusoidal Roughness Elements

Case No.	Gr_H	Pr	W/H	A	δ	ϕ
15	1.55×10^3	0.72	1.0	0.12	0.25	0
16	1.49×10^4	0.72	1.0	0.12	0.25	0
17	1.43×10^5	0.72	1.0	0.12	0.25	0
18	3.41×10^5	4.52	1.0	0.12	0.25	0
19	4.07×10^3	4.52	0.4	0.12	0.25	0
20	4.07×10^4	4.52	0.4	0.12	0.25	0
21	4.07×10^5	4.52	0.4	0.12	0.25	0
22	4.07×10^6	4.52	0.4	0.12	0.25	0
23	4.07×10^6	4.52	0.4	0.12	0.50	0

Table 3. Cases Run for Enclosures with Rectangular Roughness Elements

Case No.	Gr_H	Pr	W/H	A	δ	δ_0
24	4.07×10^3	4.52	0.4	0.12	0.25	0.125
25	4.07×10^3	4.52	0.4	0.06	0.25	0.125
26	4.07×10^3	4.52	0.4	0.12	0.50	0.25
27	4.07×10^3	4.52	0.4	0.06	0.50	0.25
28	4.07×10^3	4.52	0.4	0.12	0.25	0
29	4.07×10^3	4.52	0.4	0.12	0.50	0
30	4.07×10^4	4.52	0.4	0.12	0.25	0.125
31	4.07×10^4	4.52	0.4	0.06	0.25	0.125
32	4.07×10^4	4.52	0.4	0.12	0.50	0.25
33	4.07×10^4	4.52	0.4	0.06	0.50	0.25
34	4.07×10^4	4.52	0.4	0.12	0.25	0
35	4.07×10^5	4.52	0.4	0.12	0.50	0

Table 3 (Cont'd). Cases Run for Enclosures with Rectangular Roughness Elements

Case No.	Gr_H	Pr	W/H	A	δ	δ_0
36	4.07×10^5	4.52	0.4	0.12	0.25	0.125
37	4.07×10^5	4.52	0.4	0.06	0.25	0.125
38	4.07×10^5	4.52	0.4	0.12	0.50	0.25
39	4.07×10^5	4.52	0.4	0.06	0.50	0.25
40	4.07×10^5	4.52	0.4	0.12	0.25	0
41	4.07×10^5	4.52	0.4	0.12	0.50	0
42	4.07×10^6	4.52	0.4	0.12	0.25	0.125
43	4.07×10^6	4.52	0.4	0.06	0.25	0.125
44	4.07×10^6	4.52	0.4	0.12	0.50	0.25
45	4.07×10^6	4.52	0.4	0.12	0.25	0
46	4.07×10^6	4.52	0.4	0.12	0.50	0

Table 3 (Cont'd). Cases Run for Enclosures with Rectangular Roughness Elements

Case No.	Gr_H	Pr	W/H	A	δ	δ_0
47	6.64×10^3	4.52	0.34	0.06	0.25	0.125
48	6.64×10^4	4.52	0.34	0.06	0.25	0.125
49	6.64×10^5	4.52	0.34	0.06	0.25	0.125
50	6.64×10^6	4.52	0.34	0.06	0.25	0.125
51	1.69×10^6	0.72	0.4	0.12	0.25	0
52	1.90×10^6	0.72	0.4	0.12	0.25	0

Table 4. Cases Run for Enclosures with Rectangular Roughness Elements that Do Not Contain the Same Amounts of Fluid As the Corresponding Smooth-Walled Enclosures

Case No.	Gr_H	Pr	W/H	A	δ	δ_0
53	4.07×10^3	4.52	0.4	0.06	0.25	0.125
54	4.07×10^4	4.52	0.4	0.06	0.25	0.125
55	4.07×10^5	4.52	0.4	0.06	0.25	0.125
56	4.07×10^6	4.52	0.4	0.06	0.25	0.125

$W/H = 0.4$
$A = 0.12$
$\delta = 0.25$
$\delta_0 = \delta/2 = 0.125$
No. of Elements = 399

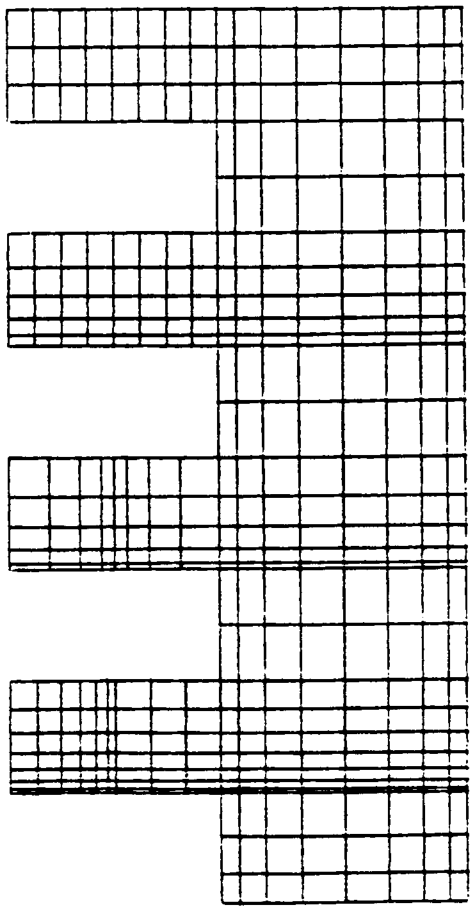

Figure 3. Typical Nonuniform Computational Grid

The number of elements in the nonuniform grids used to compute the flows in the smooth-walled enclosures, enclosures with sinusoidal roughness elements, and enclosures with rectangular roughness elements are shown in Tables 5, 6, and 7, respectively, as functions of the geometric parameters for each of these types of enclosures.

The finite difference calculations for the stream function and the heat function (Appendix B) were always performed with the same grid spacing used in NACHOS to compute the corresponding flow field.

Table 5. Number of Elements Used for Computations in Smooth-Walled Enclosures

W/H	No. of Elements
1.0	256
0.4	336
0.34	280

Table 6. Number of Elements Used for Computations in Enclosures with Sinusoidal Roughness Elements

W/H	δ	A	ϕ	No. of Elements
1.0	0.25	0.12	0	256
0.4	0.25	0.12	0	160

Table 7. Number of Elements Used for Computations in Enclosures with Rectangular Roughness Elements

W/H	δ	A	δ_0	No. of Elements
0.4	0.25	0.12	0.125	399
0.4	0.25	0.06	0.125	352
0.4	0.50	0.12	0.25	395
0.4	0.50	0.06	0.25	338
0.34	0.25	0.06	0.125	352
0.4	0.25	0.12	0	399
0.4	0.50	0.12	0	395

CHAPTER 4
THE EXPERIMENTAL INVESTIGATION

4.1 Introduction

This chapter discusses the major aspects of the experimental investigation including the apparatus, the instrumentation and data acquisition systems, the experimental and data reduction procedures, and the dimensionless parameters for the experiments.

4.2 Objective of the Experimental Investigation

The NACHOS finite element code was validated for natural convection flows in smooth-walled rectangular enclosures by Beach (1985b) who compared results computed with this code with the experimental results of Krane and Jessee (1983). No such validation of the NACHOS code has been made, however, for natural convection flows in enclosures containing large wall roughness elements. Thus, the objective of the present experimental investigation is to validate the NACHOS code for natural convection flows in rectangular enclosures that contain large wall roughness elements. The achievement of this objective should provide the necessary confidence in the numerical results of the present work.

4.3 Selection of the Test Fluid

The choice of a specific test fluid influences both the size of the experimental apparatus and many of the details of its design. Thus, the test fluid must be chosen before the detailed design of the apparatus can be accomplished. For reasons of simplicity in both the design and operation of the apparatus, air was selected as the test fluid. This choice of test fluid also permitted the use of an enclosure that is small enough for the entire flowfield to be viewed in each of the interferometers used in the experiments without moving either the enclosure or the interferometers.

4.4 The Overall Design of the Experiments

In order to perform the desired experimental validation of the NACHOS code, it was necessary to design and construct an apparatus that enabled the controlled reproduction of the natural convection flows of interest in the laboratory and to employ instrumentation systems that permitted accurate, repeatible measurements of these flows. An enclosure with large rectangular roughness elements of the type shown in Figure 1c was chosen for the experiments since most of the numerical calculations were performed for roughness elements of this type. It was also much easier to manufacture this enclosure than an enclosure with sinusoidal roughness elements.

It was decided to perform the experimental validation of NACHOS by comparing temperature distributions in the fluid and the heat flux distributions on the walls of the enclosure computed with this code with the corresponding temperature and heat flux distributions measured, respectively, with a Mach-Zehnder interferometer and a Wollaston Prism interferometer.

4.5 Design of the Experimental Apparatus

4.5.1 General description of the Apparatus

The apparatus consists of the following major parts: (1) an outer enclosure made from 1/4 inch and 1/2 inch thick aluminum plates, (2) a smooth, isothermal, vertical, enclosure wall made of copper, (3) an isothermal, vertical enclosure wall which is made of copper and has large rectangular roughness elements, (4) two heavily insulated horizontal walls, (5) two 1 inch thick plexiglas end pieces, (6) two glass end windows, and (7) numerous screws and gaskets for assembly, alignment, and sealing purposes. All of these parts are shown in the transverse and longitudinal cross-sectional views of the apparatus given in Figures 4 and 5.

As shown in Figures 4 and 5, the basic "two-dimensional" test enclosure contains air and is bounded by the two copper vertical walls (one smooth and the other having roughness elements), the two heavily insulated horizontal surfaces, and the glass end windows, which restrict the third dimension of the enclosure to a finite extent. The enclosure height, H, and width, W, (both of which are shown in Figure 1c) are 3.448 (in) and 1.379 (in), respectively. The length of the enclosure in the longitudinal direction is 9.7 (in). These enclosure dimensions were chosen so that: (1) a single interferogram could capture the entire flowfield in the enclosure on both of the interferometers used, (2) the flows in the enclosure are essentially two-dimensional over most of the length of the enclosure, and (3) the roughness elements on the hot vertical wall could be easily manufactured.

4.5.2 Design of the Isothermal Walls

The design details of the vertical walls of the enclosure are shown in Figures 6 and 7. These walls are constructed of copper because the high thermal conductivity of this material permits each wall to be maintained in an essentially isothermal condition.

The thermal conditioning of the vertical walls of the enclosure is accomplished by using a Haake Model NK22 constant temperature bath and circulator to pass a stream of hot (or cold) water through the heat exchanger passages milled in the back of each wall. The geometry of these heat exchanger

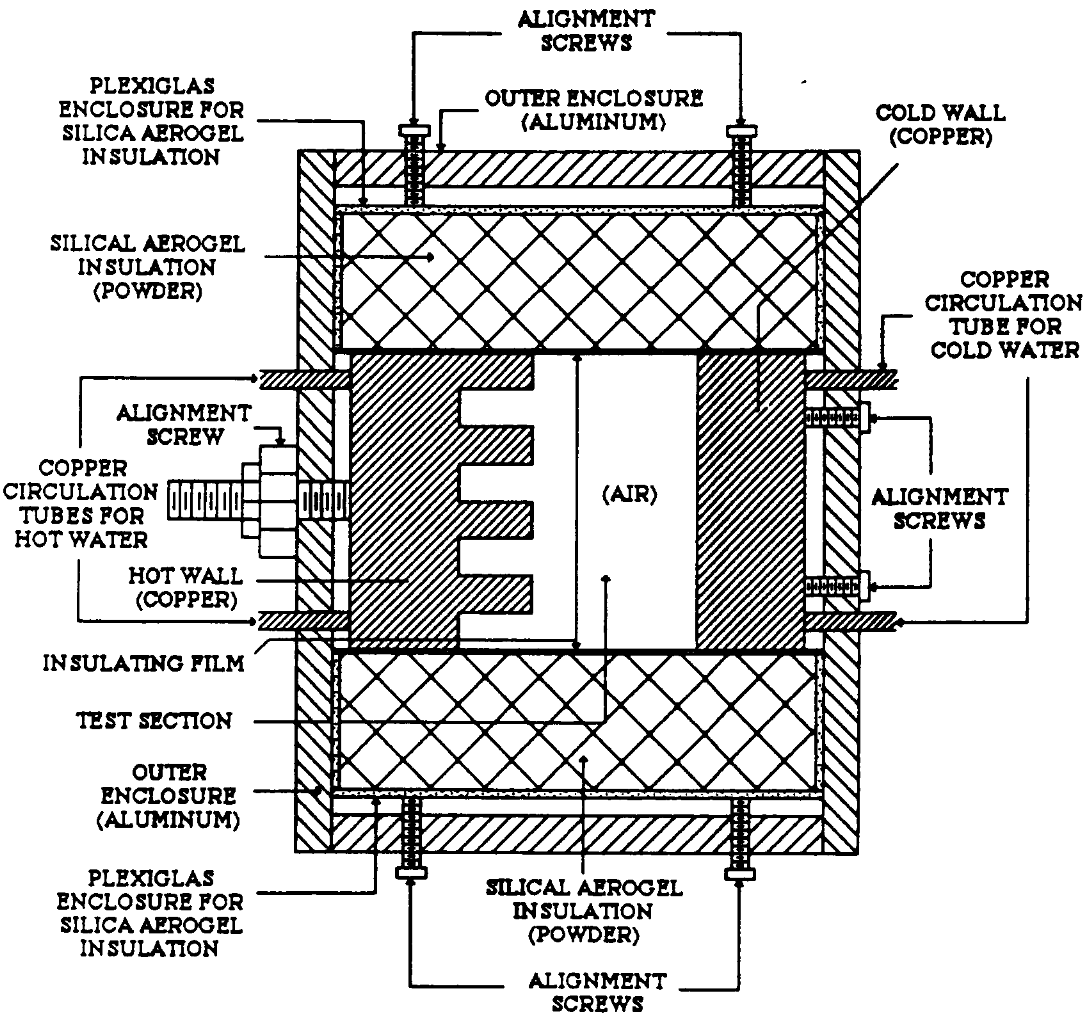

Figure 4. Transverse Cross-Sectional View of the Test Enclosure

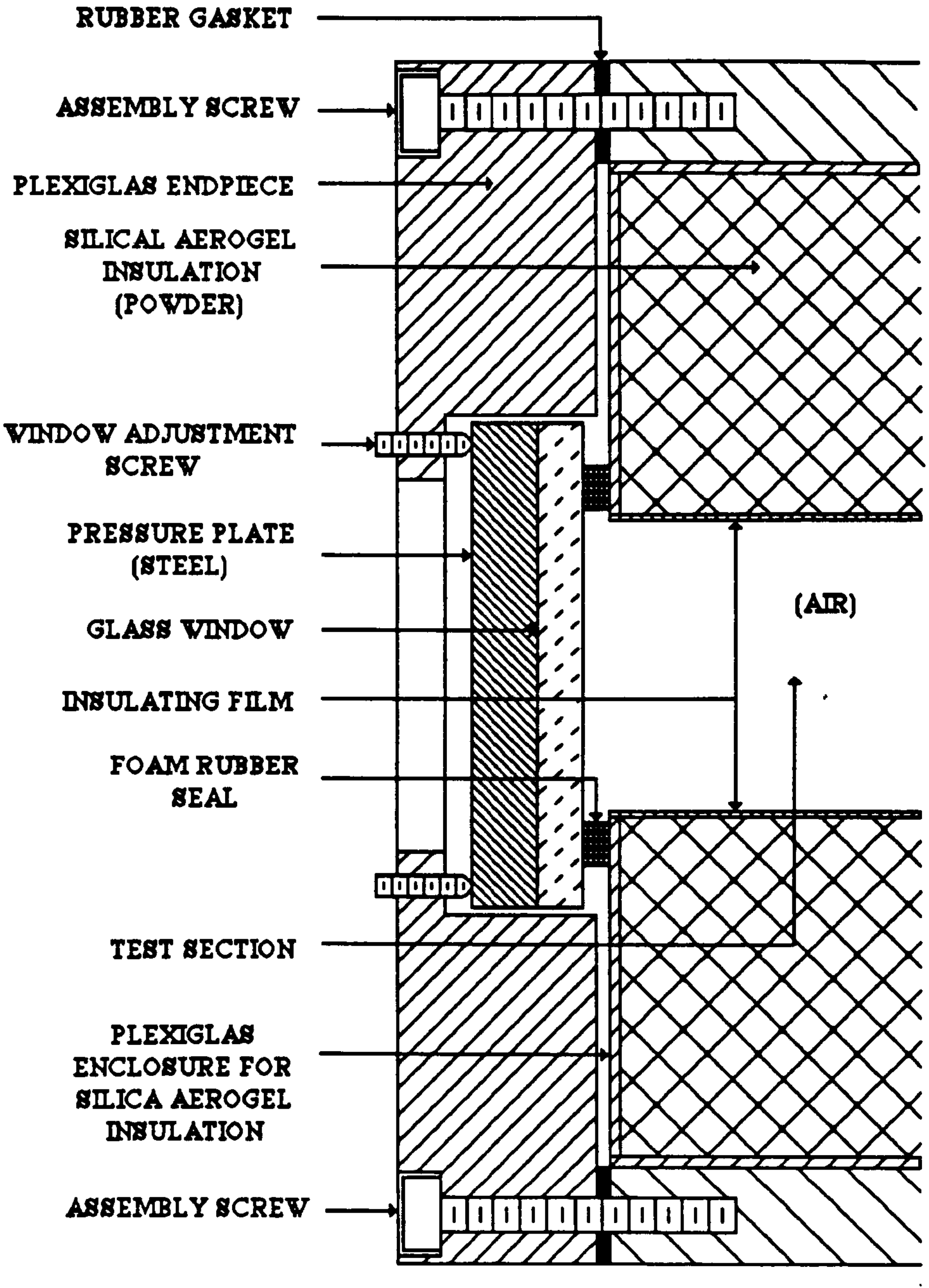

Figure 5. Partial Longitudinal Cross-Sectional View of the Test Enclosure

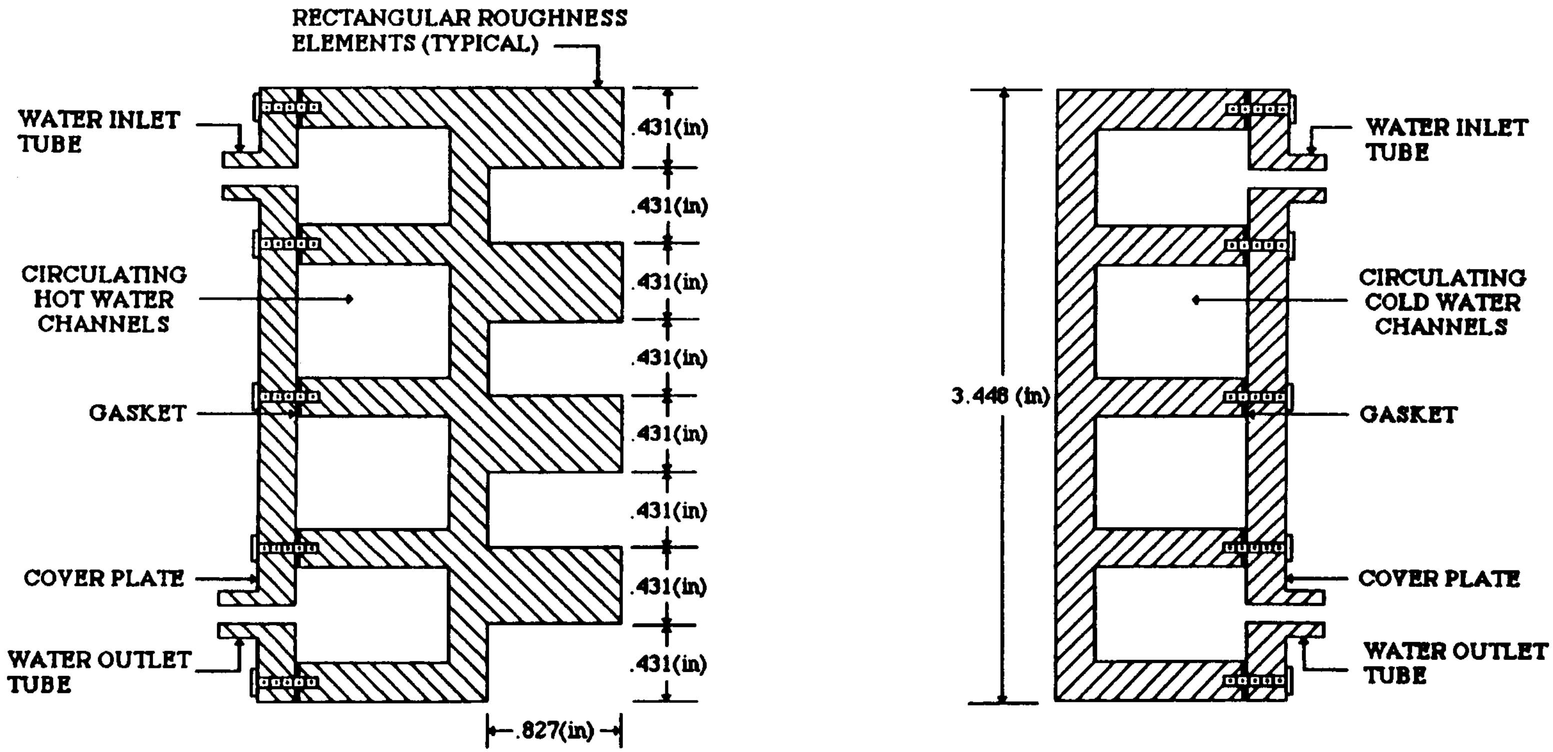

(a) Cross Sectional View of Hot Wall

(b) Cross Sectional View of Cold Wall

Figure 6. Cross-Sectional Views of the Isothermal Vertical Walls of the Test Enclosure

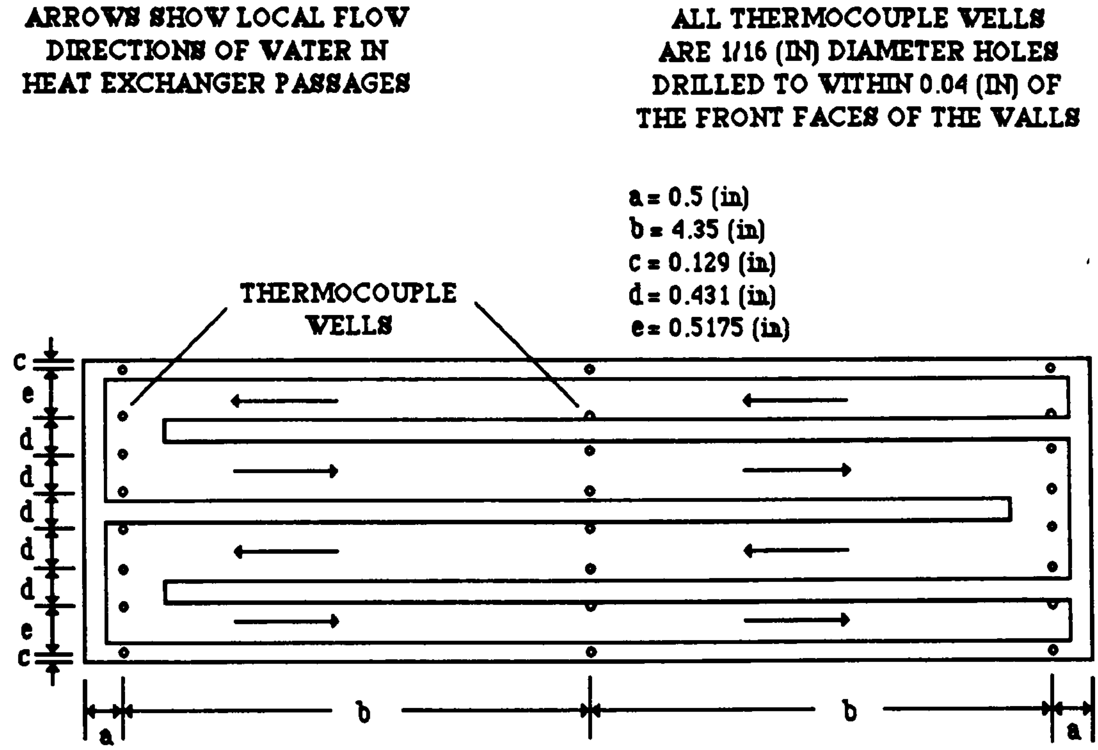

(a) Heat Exchanger Passages for Circulating Water Through the Hot Wall

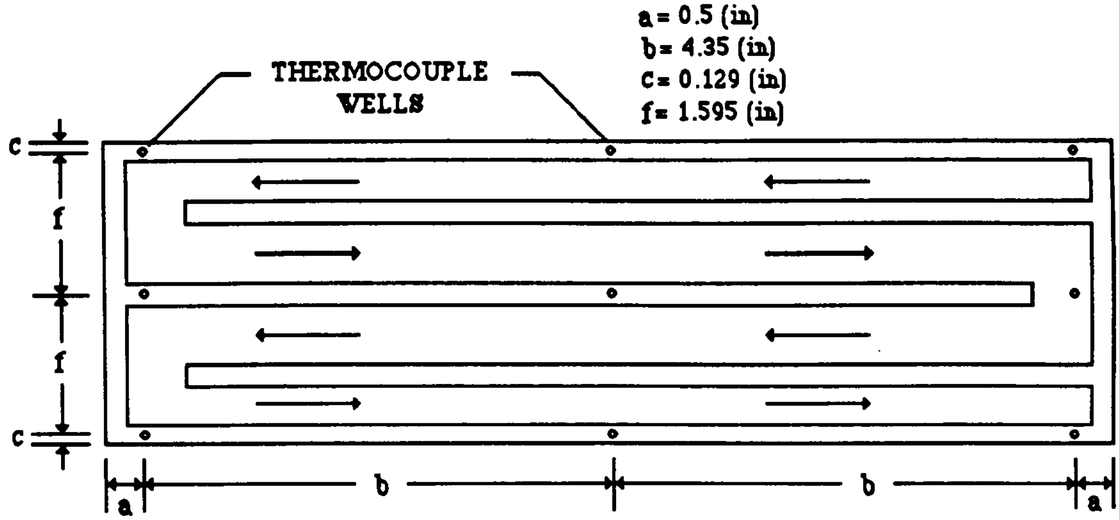

(b) Heat Exchanger Passages for Circulating Water Through the Cold Wall

Figure 7. Heat Exchanger Passages and Thermocouple Wells on the Outside Faces of the Vertical Walls of the Enclosure

passages is shown in Figure 7. The back surface of each vertical wall is formed by a 1/4 (in) thick copper cover plate, which is attached to the main body of the wall by screws and is sealed by a rubber gasket. Two 0.335 (in) I.D. copper tubes attached to each cover plate serve as the inlet and outlet for the flow of water used to heat, or cool, that wall.

The cold vertical wall has a smooth surface as shown in Figure 6b. The hot vertical wall, as shown in Figure 6a, has a periodic array of four roughness elements. The period of each element in the array, δ^*, is 0.862 (in). The distance between two elements, δ_1^*, and the thickness of each element, δ_2^*, are both 0.431 (in). The distance between the crest and the trough of each roughness element is 0.827 (in). Since the period of the lowest element in the array begins at the bottom surface of the enclosure, the phase angle, δ_0^*, of the array is zero.

The vertical walls contain numerous thermocouple wells which will be described below.

4.5.3 <u>Design of the Insulated Walls</u>

The top and bottom horizontal walls of the test enclosure are heavily insulated surfaces of identical construction. Each wall is made from a 0.03 (in) thick film of clear plastic insulating material. This material, which has a low thermal conductivity and is normally used to insulate windows during the winter, is manufactured by the Home Products Division of the 3M Corporation, St. Paul, Minnesota. As shown in Figure 4, a film is stretched tightly across the one open side of each of two rectangular plexiglas boxes which are mounted above and below the vertical walls and are oriented such that the insulating films form the top and bottom horizontal surfaces of the test enclosure. The film is attached to each plexiglas box by double-sided transparent tape. A great deal of care was taken in mounting the film on the boxes since the interferometric techniques used to measure the temperature and heat flux distributions on the enclosure walls require that these surfaces be as smooth and flat as possible.

The thin-film horizontal walls of the enclosure are each backed by a 1.375 (in) thick layer of silica aerogel, an insulating material that comes in the form of a powder. Silica aerogel, which is manufactured by Monsanto Chemical Company of St. Louis, Missouri, has a thermal conductivity approximately 85% that of air. The 1.375 (in) thick layers of silica aerogel that back the thin-film horizontal walls were formed by filling each of the two plexiglas boxes with silica aerogel through a 1/2 (in) diameter hole drilled in a sidewall of the box for that purpose. During the filling process each box was shaken vigorously in all directions and a 3/8 (in) diameter wooden dowel was used to pack the powder inside the box through the 1/2 (in) hole. It was anticipated that these actions taken during the filling process might mar, or even rupture, the thin-film wall of the box. Thus, a 1/4 (in) thick plexiglas plate was put over this delicate surface and held in place by several C-clamps. This plate was then removed before the box was installed in the apparatus.

4.5.4 Design of the End Pieces and Windows

The design details of the transverse vertical end pieces are shown in Figure 5. Each end piece was cut from a 1 (in) thick block of plexiglas and is fastened to the outer aluminum frame of the apparatus by four assembly screws. A thin rubber gasket is installed between each end piece and the aluminum frame. A 4 9/16 (in) high by 2 1/2 (in) wide rectangular hole was cut in each end piece to accomodate the glass end window, which fits snugly into this hole. The glass end windows are made from 3/16 (in) thick float glass, which was handpicked to insure the highest possible optical quality. As may be seen in Figure 5, a highly compressible foam rubber gasket (0.185 in thick) is used to insulate the end windows from the enclosure walls and to seal the test enclosure.

A 3.25 (in) long by 1/4 (in) high by 1/8 (in) wide steel pressure plate is glued along each vertical edge of the outer surface of each window. Three adjustment screws are provide for each window. Two of the screws bear on one pressure plate and the third screw on the other pressure plate. When these screws are properly adjusted they: (1) seal the enclosure by compressing the foam rubber gasket, and (2) align each window such that the two windows are parallel to each other and perpendicular to the optical paths of the interferometers.

4.6 Descriptions of the Instrumentation and Data Acquisition Systems

4.6.1 Required Measurements

In order to achieve the objective of the experimental investigation it was necessary to measure: (1) the air temperature in the laboratory, (2) the temperatures of the vertical walls of the enclosure, (3) the temperature distribution in the air in the test enclosure, and (4) the local heat flux distributions on all four walls of the enclosure. The air temperature in the laboratory was measured using an accurate mercury-in-glass thermometer and the temperatures of the vertical walls of the enclosure with thermocouples.

In order to avoid the insertion of any physical probes that would disturb the relatively weak natural convection flows in the enclosure, purely optical techniques were employed to make all of the measurements inside the enclosure. A Mach-Zehnder interferometer was used to measure the temperature distribution in the air in the enclosure and a Wollaston Prism interferometer to measure the local heat flux distributions on the enclosure walls. All of the instrumentation systems and the data acquisition system for the thermocouples are discussed below.

4.6.2 The Thermocouple and Data Acquisition Systems

The temperatures of the vertical (copper) walls of the enclosure were measured using 36 gauge copper-constantan thermocouples manufactured by Omega Engineering Corporation. Twenty four such thermocouples were used to measure the temperature distribution in the hot (rough) wall, while nine were used to measure the temperature distribution in the cold wall. All of these thermocouples are inserted in 1/16 (in) diameter wells that are drilled to within 0.04 (in) of the front faces of the walls and are held in place by thermally-conductive glue. The exact locations of the thermocouple wells are shown in Figure 7. The thermocouple leads, which are approximately 7 feet long, pass through matching holes in the back cover plates of the vertical walls. As shown in Figure 6, the 24 thermocouples mounted in the hot wall are grouped into three vertical arrays with each array containing 8 thermocouples. Each of these thermocouples is located in the center of a crest, or trough, of the roughness element array except those which are located nearest to the top and bottom edges of the hot wall.

The thermocouple output voltages were read, converted to ^{0}C, and recorded, by a Hewlett-Packard 9826 micro-computer in conjunction with an HP 3497-A data acquisition system.

4.6.3 The Mach-Zehnder Interferometer (MZI)

An MZI was used to measure the temperature distribution in the air in the enclosure. The basic therory of this instrument is quite simple. A beam of light from a source is split into two seperate beams. One of these beams is passed directly through the test section and the other beam, called the "reference beam", is guided around the test section. The beams are then recombined and focused on a screen. The nonuniform temperature distribution in the test fluid causes a nonuniform distribution of the index of refraction in this fluid. Thus, the beam that passes through the test section is deflected and when it it is recombined with the reference beam an interference pattern is formed on the screen. If the instrument is operating in the "infinite fringe mode", the interference pattern shows the distribution of isotherms in the fluid. In the "wedge fringe mode", the local deflection of each fringe in the interference pattern from its reference position; that is, the position corresponding to a uniform temperature distribution in the test section, is proportional to the change in the temperature of the fluid at the point from the reference temperature. Thus, if the interference pattern is recorded on film (which is called an interferogram), the temperature distribution in the fluid can be determined by measuring the deflections of the wedge fringes from their reference positions. More detailed explanation of the theory of the design and operation of the MZI may be found in the works by Hauf and Grigull (1970), Merzkirch (1974), and Eckert and Goldstein (1976).

The Aerolab 6-inch MZI located in the Natural Convection Laboratory at the University of Tennessee, Knoxville was used in the present investigation. The optical arrangement of this instrument is shown in Figure 8. The MZI was adjusted to obtain the desired fringe mode and the He-Ne laser beam collimated using the procedures developed by Jessee (1985). When this instrument was operated in the wedge fringe mode, a photograph was first taken of the undisturbed fringes. Then, the test section was heated and cooled and a second photograph was taken of the deflected fringes. A Nikon Shopscope measuring microscope was then used

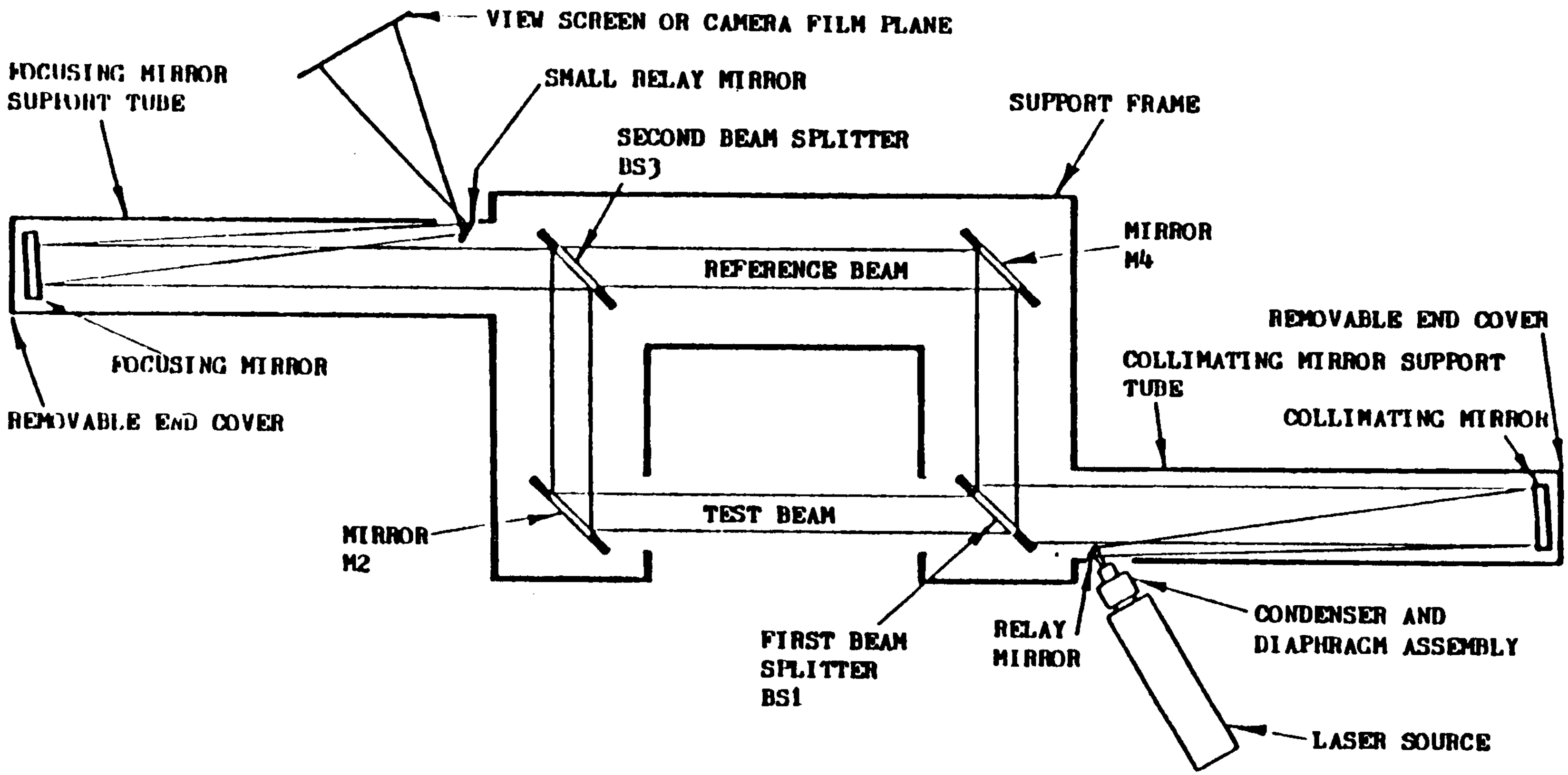

Figure 8. Optical Arrangement of the Mach-Zehnder Interferometer [Jessee (1985)]

to"read" these interferograms; that is, to measure the deflections of the fringes. The resulting data was reduced according to the procedures developed by Jessee (1985). These procedures are outlined in Appendix C.

The interferograms were taken with a polaroid camera using Polaroid Type 55 Positive-Negative film.

4.6.4 The Wollaston Prism Interferometer (WPI)

The local heat flux distributions on the enclosure walls were measured with a WPI. Like the MZI, the WPI depends on the presence of a nonuniform distribution of the index of refraction in the test fluid for its operation. With the WPI, however, the measured deflection of a fringe is proportional to the temperature gradient, which is related through the Fourier conduction law to the local heat flux. Detailed explanations of the theory of the design and operation of the WPI are given in Hauf and Grigull (1970), Sernas, et al (1972), Merzkirch (1974), and Eckert and Goldstein (1976).

The WPI used in the present experiments was custom-designed and built by Dr. J. R. Parsons and his students at the Natural Convection Laboratory of the University of Tennessee, Knoxville. The optical arrangement of this instrument is shown in Figure 9. The instrument was adjusted and the He-Ne laser beam collimated using the procedures reported by Irby and Parsons (1981). As with the MZI, two photographs were taken for each experiment: one with the test fluid at a uniform temperature and the other with a nonuniform temperature distribution in the test fluid. The Nikon measuring microscope was used to read these interferograms. The resulting data were reduced using the procedures of Sernas (1977), which are outlined in Appendix D.

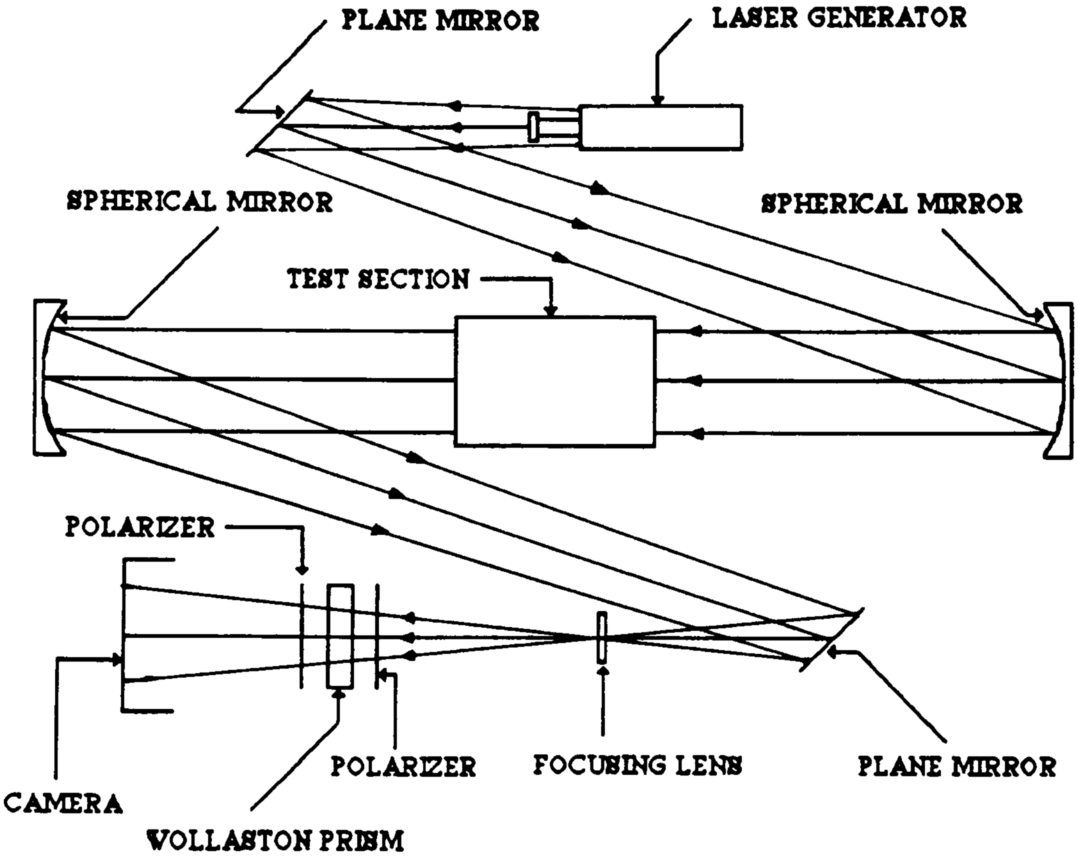

Figure 9. Optical Arrangement of the Wollaston Prism Interferometer

4.7 Description of the Experiments Performed

4.7.1 The Dimensionless Parameters for the Experiments

In order to achieve the experimental objective of validating the NACHOS code for natural convection flows in rectangular enclosures that contain rectangular wall roughness elements, two experiments were performed: one to measure the temperature distribution with the Mach-Zehnder interferometer and the other to measure the wall heat flux distributions with the Wollaston Prism interferometer. The values of the dimensionless parameters for these experiments are given in Table 8. Ideally, both interferograms should have been made for the same flow. In practice however, it was necessary to take one interferogram, move the experiment, and then take the other interferogram at a later time. Thus, as shown in Table 8, the values of the Grashof numbers for the two interferograms differ by approximately 12% due to the variations of the temperature difference between the vertical walls and the average fluid temperature $[(T_H^* - T_C^*)/2]$ in the two experiments. The enclosure geometries for the two experiments, as defined by the parameters W/H, A, δ and δ_0, were identical. The difference in the Grashof numbers at which the two interferograms were taken, however, required that the experimental results for the temperature and wall heat flux distributions be compared with the numerical results of two seperate runs made with NACHOS using the exact Grashof numbers in the experiments (1.69×10^6 for the MZI experiment and 1.90×10^6 for the WPI experiment).

Table 8. Dimensionless Parameters And the Type of Data Taken In Each Experiment

Expt. No.	Gr_H	Pr	W/H	A	δ	δ_0	Data Taken		
							MZI	WPI	Wall Temps.
1	1.69×10^6	0.72	0.4	0.12	0.25	0	√		√
2	1.90×10^6	0.72	0.4	0.12	0.25	0		√	√

4.7.2 Test Procedure

Before performing the experiments, the enclosure was assembled and aligned as described in detail in Appendix E. The distance between the hot and cold vertical walls of the enclosure was such that the aspect ratio (W/H) was 0.4.

The assembled enclosure was then placed in the optical path of the Wollaston Prism interferometer. The end windows were adjusted and the test section was aligned in the He-Ne laser beam as described in Appendix E. An interferogram of the undisturbed fringes in the test section was then recorded photographically. Next, the constant-temperature baths and circulators were started and allowed to run for six hours until the test section reached a steady-state condition for which the Grashof number, Gr_H, was 1.9×10^6. After the enclosure reached steady-state, the following operations were performed: (1) an interferogram of the disturbed fringes in the flow field was recorded photographically, (2) the readings of the thermocouples embedded in the vertical walls of the enclosure were recorded, and (3) the room temperature was recorded. Finally, the interferograms were read to determine the fringe shifts, which were employed to determine the local heat flux distributions on the vertical walls as described in Appendix D.

After reducing the WPI data, the test enclosure was moved into the optical path of the Mach-Zehnder interferometer and the end windows along with the test section were aligned again according to the procedure described in Appendix E. Using the technique described by Jessee (1985), the MZI was then adjusted to the wedge fringe setting and an interferogram of the undisturbed wedge fringes was recorded photographically. The constant-temperature baths and circulators were then started and allowed to run for six hours until the test enclosure reached a steady-state condition for which the Grashof number, Gr_H, was 1.69 x 10^6. After the steady-state condition was achieved, the following operations were performed : (1) an interferogram of the disturbed fringes was recorded photographically, (2) the readings of the thermocouples embedded in the vertical walls of the enclosure were recorded, and (3) the room temperature was recorded. Following the procedure specified by Jessee (1985), the MZI was then adjusted to the infinite fringe setting to produce a fringe pattern that portrays the isotherms in the flow field and an interferogram was recorded photographically. The wedge fringe interferograms from the MZI were then read and the resulting data used to determine the temperature distribution in the flow field as described in Appendix C.

All of the data taken in the experiments, including the interferograms, are presented in Appendices F and G, and discussed in Chapter 5.

CHAPTER 5

PRESENTATION AND INTERPRETATION OF RESULTS

5.1 Introduction

Extensive discussions of both the experimental and numerical results of this work are given below. The initial discussion, which is concerned with the experimental validation of the NACHOS code, is followed by discussions of the numerical results for the natural convection flows in : (1) smooth-walled enclosures, (2) enclosures containing large sinusoidal roughness elements, and (3) enclosures containing large rectangular roughness elements.

5.2 Fidelity of the Experimental Conditions to the Assumptions of the Theoretical Model

As stated in Chapter 4, the objective of the experimental investigation is to validate the NACHOS code for natural convection flows in rectangular enclosures that contain large wall roughness elements. Two experiments were carried out in the same enclosure that contain rectangular wall roughness elements using air as the test fluid. In one experiment, for which the Grashof number was 1.69×10^6, the temperature field in the enclosure was measured with the Mach-Zehnder interferometer. In the other experiment, which was conducted at a Grashof number of 1.90×10^6, the Wollaston prism interferometer was used to measure the local heat flux distribution on the walls of the enclosure. All of the remaining dimensionless parameters were identical for both experiments, that is, the Prandtl number (Pr) was 0.72, the aspect ratio of the enclosure (W/H) was 0.4, the dimensionless roughness element amplitude (A) was 0.12, the dimensionless period of the roughness element array (δ) was 0.25, and the dimensionless phase shift of the array (δ_0) was 0 for both experiments.

Before comparing the results of these experiments with the numerical results, it should be shown that the experimental conditions adequately represented the assumptions in the theoretical model. Specially, the theoretical model assumes that the flows of interest are two-dimensional, steady-state, laminar natural convection flows that occur in rectangular enclosures with large roughness elements on one vertical wall. The vertical walls of the enclosure are assumed to be isothermal surfaces maintained at two different temperatures and the horizontal walls are assumed to be adiabatic surfaces. The fidelity of the experimental conditions to these assumptions will now be addressed.

First, it is obvious that the geometry of the experimental enclosure is identical to the geometry specified in the theoretical model, except that it has a <u>finite</u> length in the direction parallel to the isothermal vertical walls. Arnold (1978), however, demonstrated that when the ratio of the length of the enclosure to the distance between the vertical walls is greater than approximately 6.5, that three-dimensional effects are negligibly small and the rate of heat transfer across the enclosure may be accurately computed using a two-dimensional model. Since this ratio is slightly greater than 7 for the present experimental enclosure, it may be concluded that the flows in these experiments were essentially two-dimensional.

In order to achieve steady-state conditions in the experiments, the constant-temperature baths and circulators were turned on and the apparatus was left undisturbed for a period of six hours before any data was taken. At the end of the six hour period, thermocouple readings indicated that the enclosure wall temperatures were not changing with time and visual inspection of the interference fringes on a screen did not detect any fluctuations in the flow field. Thus, the experimental flows were both steady-state and laminar.

The measured temperature distributions in the hot and cold vertical walls of the enclosure for the Wollaston prism interferometer experiments are shown in Figure 10. As may be seen in this Figure, the average temperature of the hot wall was 29.31 (^{0}C) [84.76 (^{0}F)]. The maximun deviation of any temperature from this average temperature was 0.22 (^{0}C) [0.40 (^{0}F)] and the difference between the maximum and minimum temperatures measured was 0.42 (^{0}C) [0.76 (^{0}F)]. Similarly, the average temperature of the cold wall was 10.08 (^{0}C) [50.14 (^{0}F)]. The maximum deviation of any temperature from this average temperature was 0.17 (^{0}C) [0.31 (^{0}F)] and the difference between the maximum and minimum temperatures measured was 0.30 (^{0}C) [0.54 (^{0}F)]. Thus, it may be concluded that the vertical walls of the enclosure in the Wollaston prism interferometer experiment were essentially isothermal surfaces. The corresponding temperature distributions given in Figure 11 yield virtually identical statistics and lead to the same conclusion for the experiment performed with the Mach-Zehnder interferometer.

El Sherbiny, Hollands and Raithby (1982) claim that to obtain an adiabatic boundary condition in a natural convection flow in an enclosure when the test fluid is air at near atmospheric conditions, that the enclosure boundary must be made from a material with a thermal conductivity at least an order of magnitude smaller than that of air. Since such materials do not exist, they state that "... the adiabatic boundary condition is not attainable in air." This consideration led to the design of the horizontal walls used in the present experiments, which is described in section 4.5.3. These walls are made from 0.03 inch thick films of clear plastic window insulation backed by 1.375 inch thick layers of silica aerogel. This material has

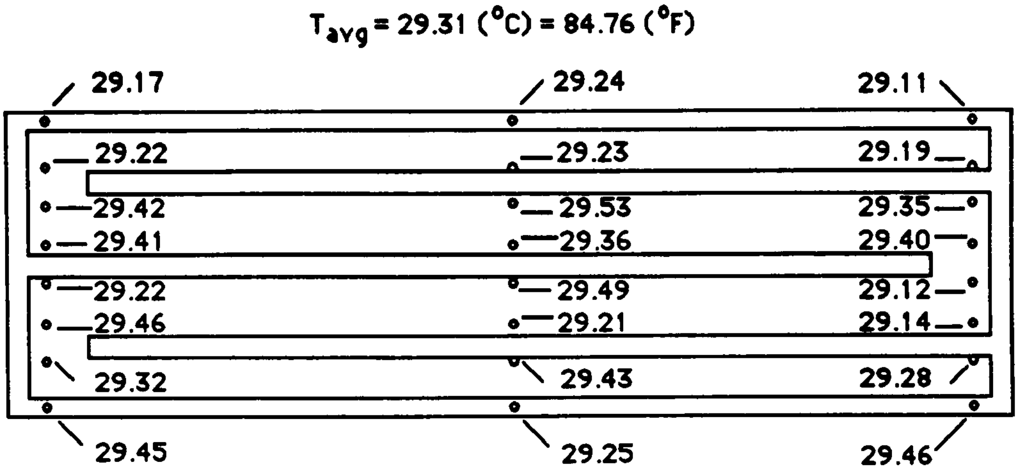

(a) Hot Wall Temperatures

Note: All Temperatures are Shown in ^{0}C.
The Uncertainty of the Measured Temperatures is $\pm$ 0.1 ^{0}C.
Room Temperature = 19.8 ^{0}C (67.64 ^{0}F).

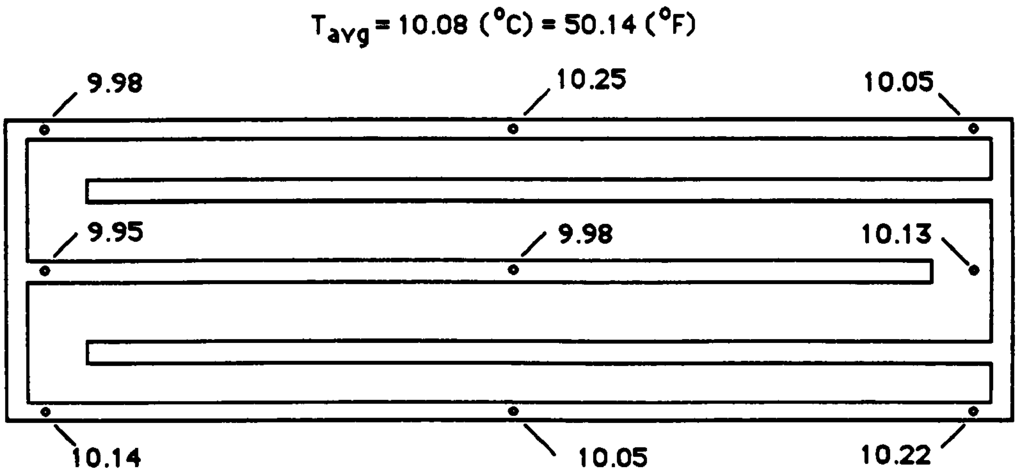

(b) Cold Wall Temperatures

Figure 10. Measured Temperature Distributions in the Vertical Walls of the Enclosure for the Wollaston Prism Interferometer Experiment

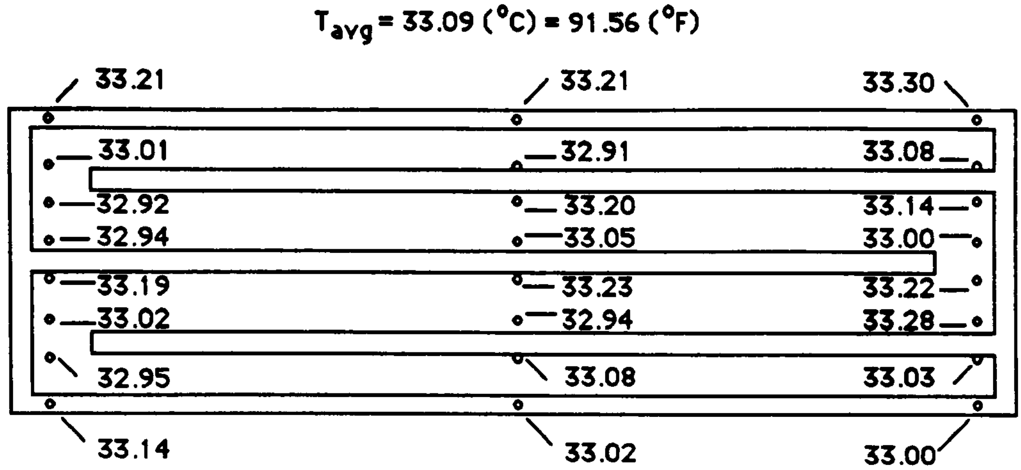

(a) Hot Wall Temperatures

Note: All Temperatures are Shown in ^{0}C.
The Uncertainty of the Measured Temperatures is $\pm 0.1\ ^0$C.
Room Temperature = 24 ^{0}C (75.20 ^{0}F).

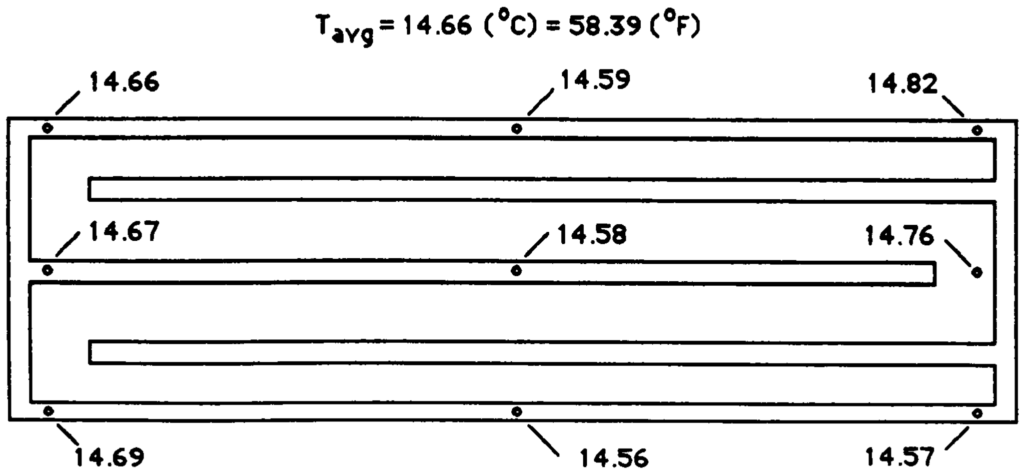

(b) Cold Wall Temperatures

Figure 11. Measured Temperature Distributions in the Vertical Walls of the Enclosure for the Mach-Zehnder Interferometer Experiment

a thermal conductivity approximately 85% that of air, which is extremely low, but still does not meet the criterion of El Sherbiny, et al. This thermal conductivity is <u>much</u> lower, however, than that of any other materials used to build "adiabatic" surfaces in previous experiments. Thus, it was anticipated that the horizontal walls in the present experiment would more closely approximate the desired adiabatic boundary condition than did the insulated surfaces used in all previous experiments.

The heat fluxes on all of the internal surfaces of the enclosure were measured with the Wollaston prism interferometer. The resulting interferograms and the raw data taken from these interferograms are presented in Appendix G. <u>No fringe shifts could be detected on the horizontal walls of the enclosure. Thus, within the experimental uncertainty of the WPI (13.92%) the horizontal walls were essentially adiabatic surfaces.</u> A "rule-of-thumb" in Wollaston prism interferometry suggests that experimental conditions should be such that fringe shifts are not less than 1/2 the width of a fringe. Inspection of the interferogram in Figure G2 shows that this criterion was not completely satisfied in the present experiment. Thus, general conclusions about the viability of the new design used for the adiabatic walls cannot be drawn until more definitive experiments have been performed. For the present purposes, however, it seems safe to state that the heat fluxes on the horizontal walls in the experimental apparatus were negligibly small. Therefore, it may be conclude that : (1) within the limits of experimental uncertainty, the experimental conditions closely approximate the conditions assumed in the theoretical model, and (2) the experimental results may be used to validate the NACHOS code.

5.3 Experimental Validation of the NACHOS Code

As mentioned above, the Wollaston prism interferograms and the raw data taken from these interferograms are presented in Appendix G. Both the calculated and the experimentally-determined local Nusselt number distributions along the entire length of the hot (rough) vertical wall are presented in Figure 12. As may be seen in Figure 12, the agreement between these numerical and experimental results is reasonably good. Numerical integration of the local heat flux distribution on the hot wall yields an overall Nusselt number, $\overline{Nu}$, ($= \bar{h}H/k$), of 9.77, while integrating the corresponding experimental results gives an overall Nusselt number of 10.4. The 6.45% discrepancy between these two values is well within the experimental uncertainty (13.92%) of the WPI.

The numerically and the experimentally determined local Nusselt number distributions on the cold (smooth) vertical wall are presented in Figure 13. Reasonable quantitative agreement is obtained over the central portion of the cold wall and NACHOS correctly predicts the qualitative trends of the experimental data near the top and bottom of this wall. Nontrivial deviations between the numerically and experimentally determined local Nusselt number distributions do occur, however, near the top and bottom of the cold wall. The deviations near the bottom of the cold wall are easily explained, since the heat fluxes in this region are so low that they cannot be resolved with the WPI. Thus, the three experimental values of the local Nusselt number near the bottom of the cold wall are shown in Figure 13 as zero, while the corresponding numerical values vary in the range from approximately 1 to 3. No comparable explanation for the deviations near the top of the cold wall is readily available.

The overall Nusselt number, $\overline{Nu}$, is given by numerical integration along the cold wall as 10.05, while the corresponding experimentally determined value is

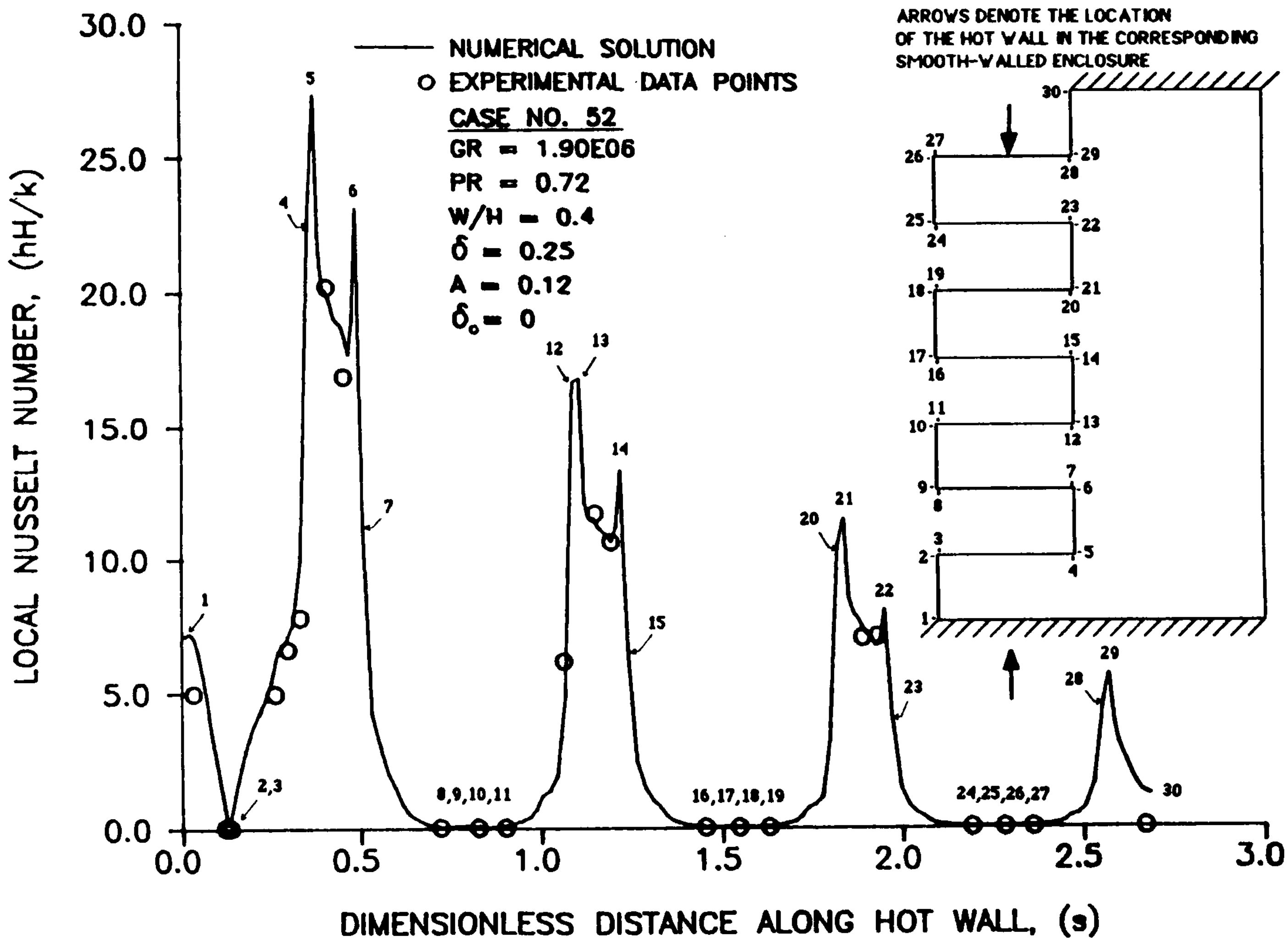

Figure 12. Comparison of Numerical and Experimental Results for the Local Nusselt Number Distribution Along the Hot Vertical Wall of the Enclosure

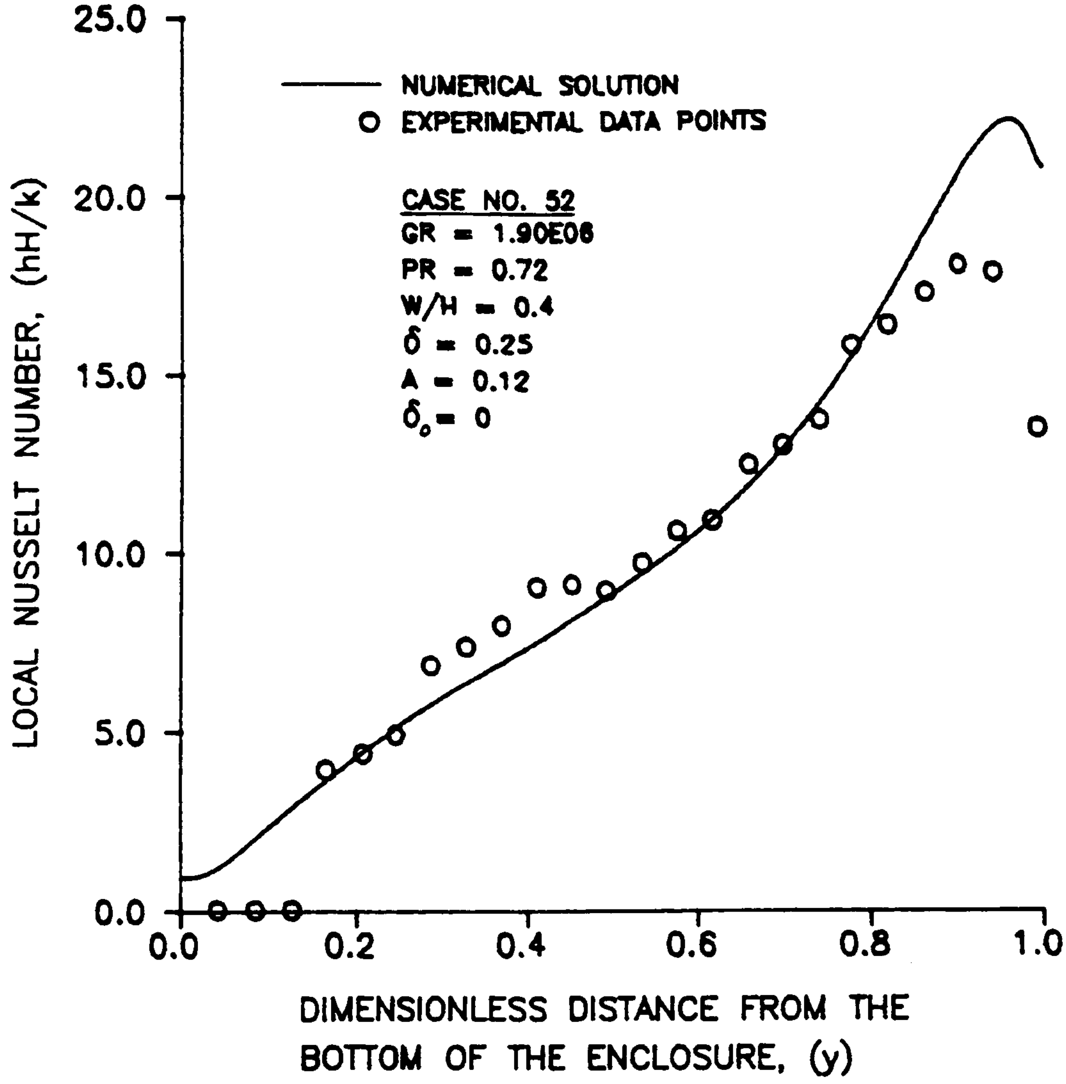

Figure 13. Comparison of Numerical and Experimental Results for the Local Nusselt Number Distribution Along the Cold Wall

9.33. The 7.16% discrepancy between these two values is well within the experimental uncertainty of the WPI (13.92%) as is the 11.4% discrepancy between the experimentally determined values of the overall Nusselt numbers on the hot and cold walls (10.4 and 9.33, respectively). The 2.7% discrepancy between the numerically determined values of the overall Nusselt number on the hot wall (9.77) and that for the cold wall (10.05) is more difficult to explain, but is probably due to the relatively crude trapezoidal rule that was used to perform the numerical integrations of the local Nusselt number distributions.

As discussed above, since no fringe shifts could be detected on the horizontal walls of the enclosure, these walls are assumed to have behaved (within the experimental uncertainty of the WPI) as adiabatic surfaces in the experiment. The computed heat fluxes on these surfaces are, of course, identically zero.

The temperature distributions in the enclosure were measured with the Mach-Zehnder interferometer. The interferograms from the MZI and the raw data taken from these inteferograms are presented in Appendix F. An uncertainty analysis of the MZI data is given in Appendix H. It shows that the uncertainty in the measured temperatures is $\pm$ 1.28 ^{0}R. This corresponds to a maximum uncertainty of 0.06 in the demensionless temperature, T.

A comparison of the numerically and experimentally determined dimensionless temperature distributions along the horizontal plane across the enclosure at $y^*/H = 0.56$ is presented in Figure 14 and shows good agreement between these results. Similar comparisons of the temperature distributions along the bottom and top horizontal walls of the enclosure are presented in Figures 15 and 16, respectively. The quantitative agreement between the numerical and experimental results is not as good along the bottom and top horizontal surfaces as it is along the horizontal plane at $y^*/H = 0.56$, although NACHOS correctly

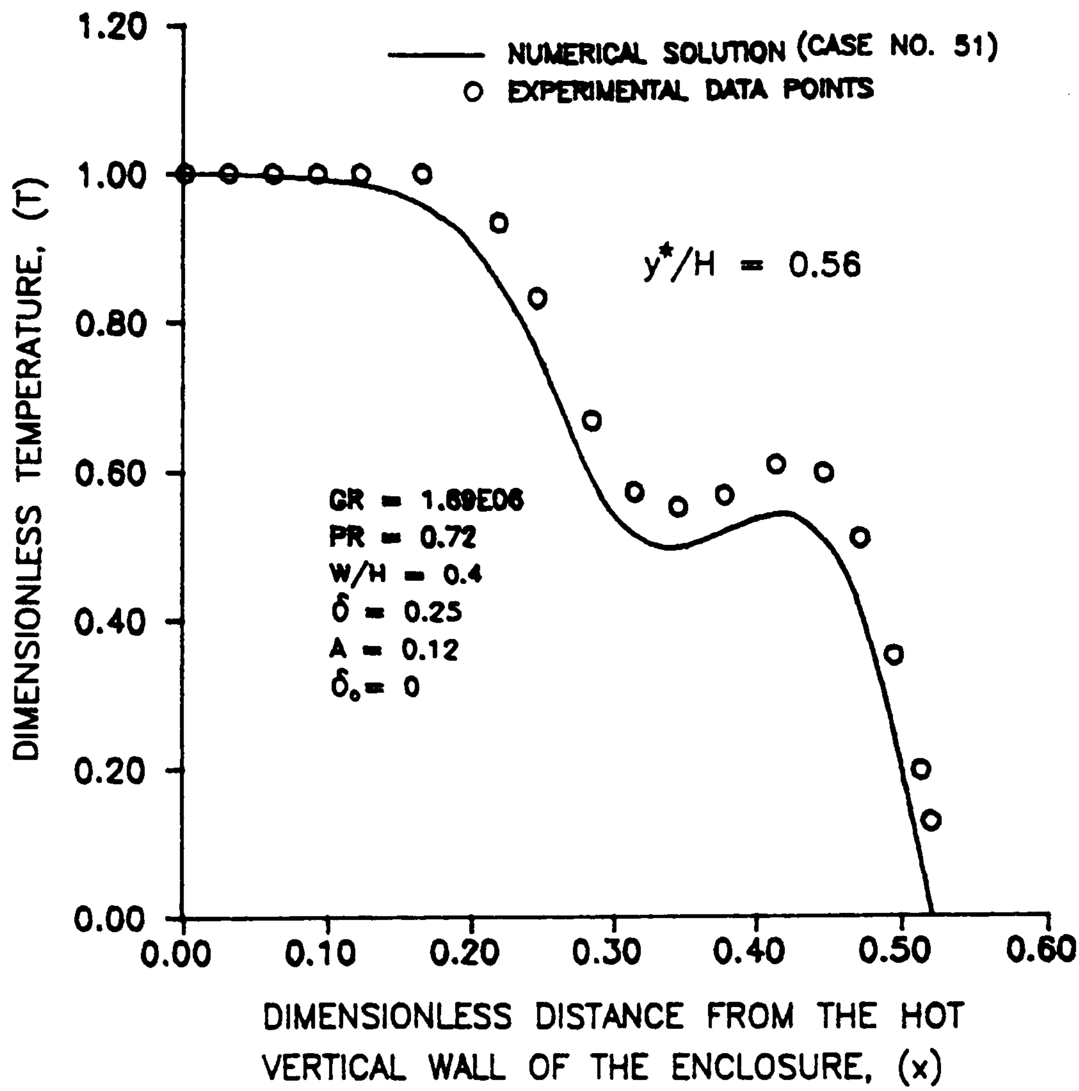

Figure 14. Comparison of Numerical and Experimental Results for the Temperature Distribution Along the Horizontal Plane at $y^*/H = 0.56$

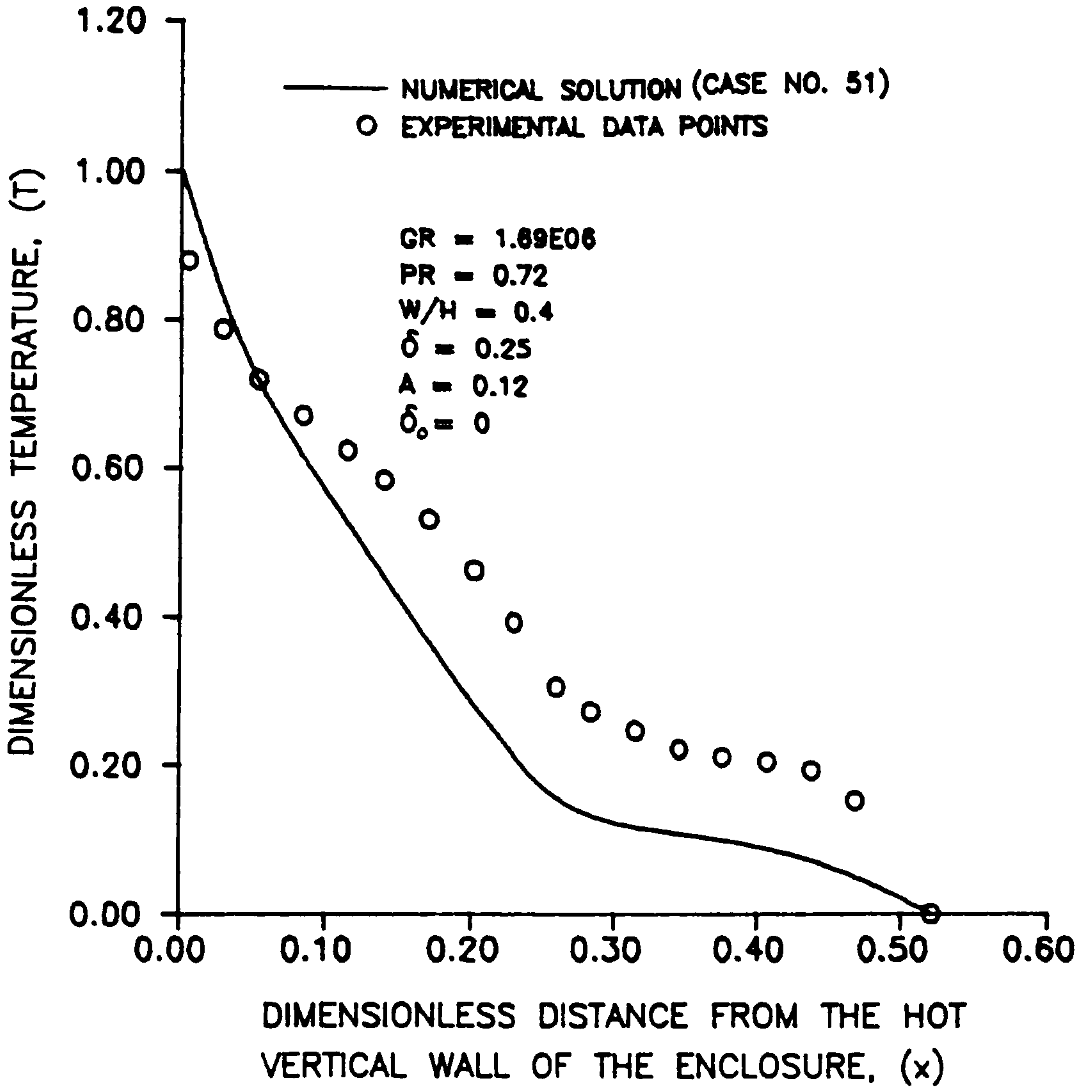

Figure 15. Comparison of Numerical and Experimental Results for the Temperature Distribution Along the Bottom Horizontal Wall of the Enclosure

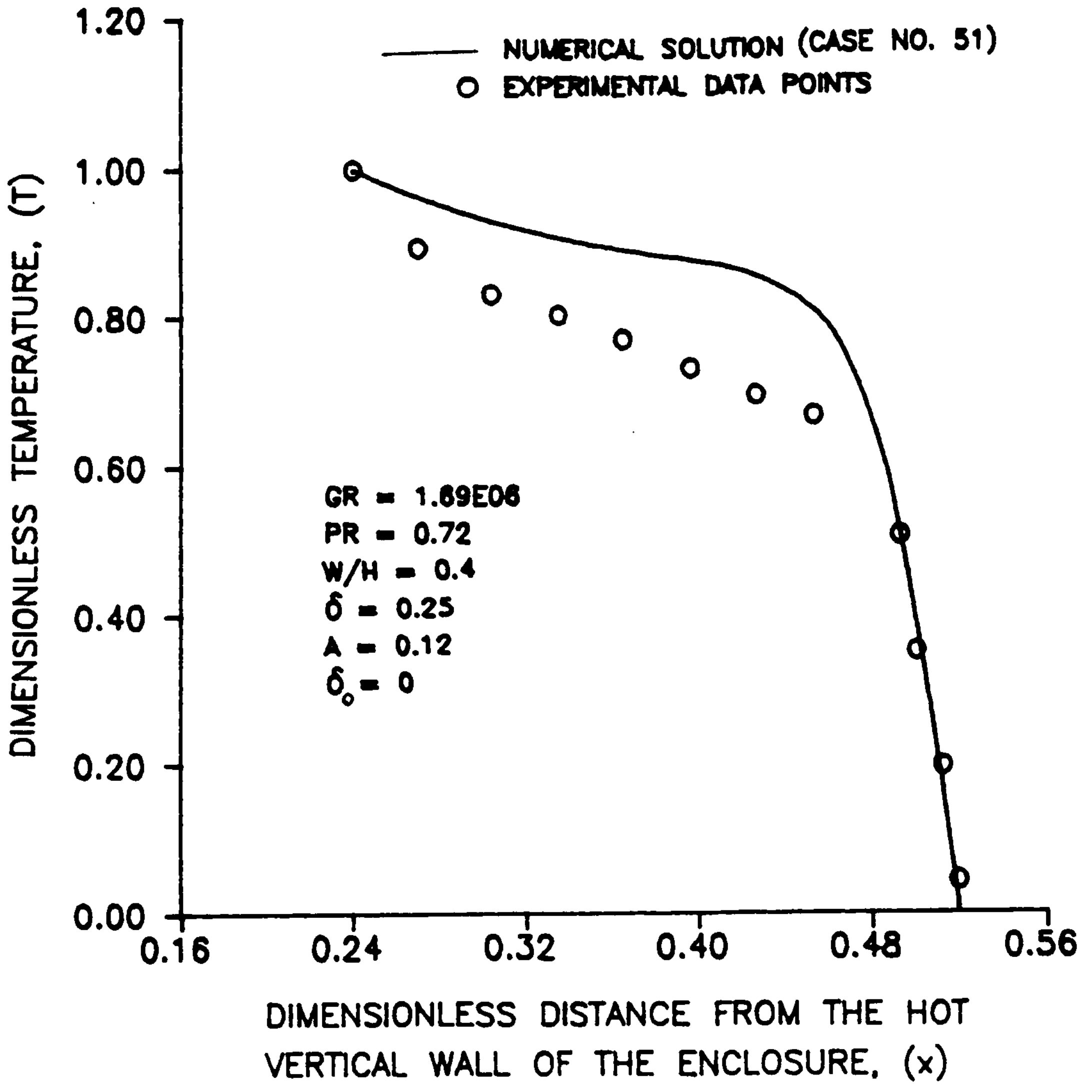

Figure 16. Comparison of Numerical and Experimental Results for the Temperature Distribution Along the Top Horizontal Wall of the Enclosure

predicts the qualitative trends of the temperature distributions on these surfaces. The lack of better quantitative agreement for the temperature distributions on the horizontal walls may be attributed to two probable sources of error. First, the Mach-Zehnder interferogram was more difficult to read on the horizontal walls due to slight imperfections (wrinkles and sagging) on these surfaces. The second source of error is associated with the fact that the horizontal walls were not <u>perfectly</u> adiabatic surfaces (even though this could not be resolved with the WPI). This is important since El Sherbiny, Hollands, and Raithby (1982) have shown that the temperature distribution on an insulated, but not perfectly adiabatic, surface will differ from that on a perfectly adiabatic surface due to what they call "convectively induced conduction and radiation heat transfers".

Finally, excellent qualitative agreement is obtained between the experimentally determined isotherms in the enclosure with those computed using NACHOS, as is shown in Figure 17. The interferogram in Figure 17(a) was obtained with the MZI in the infinite fringe setting.

Consideration of the above comparisons between numerical and experimental results leads to the conclusion that <u>the NACHOS code has been validated for natural convection flows in rectangular enclosures that contain large wall roughness elements</u>. Thus, all further discussions will be focused on the extensive numerical results computed for such enclosures using NACHOS.

5.4 Results of the Numerical Investigation

5.4.1 Preliminary Comments

The objective of the present research is to determine the effects of placing large roughness elements on the hot vertical wall of the smooth-walled rectangular

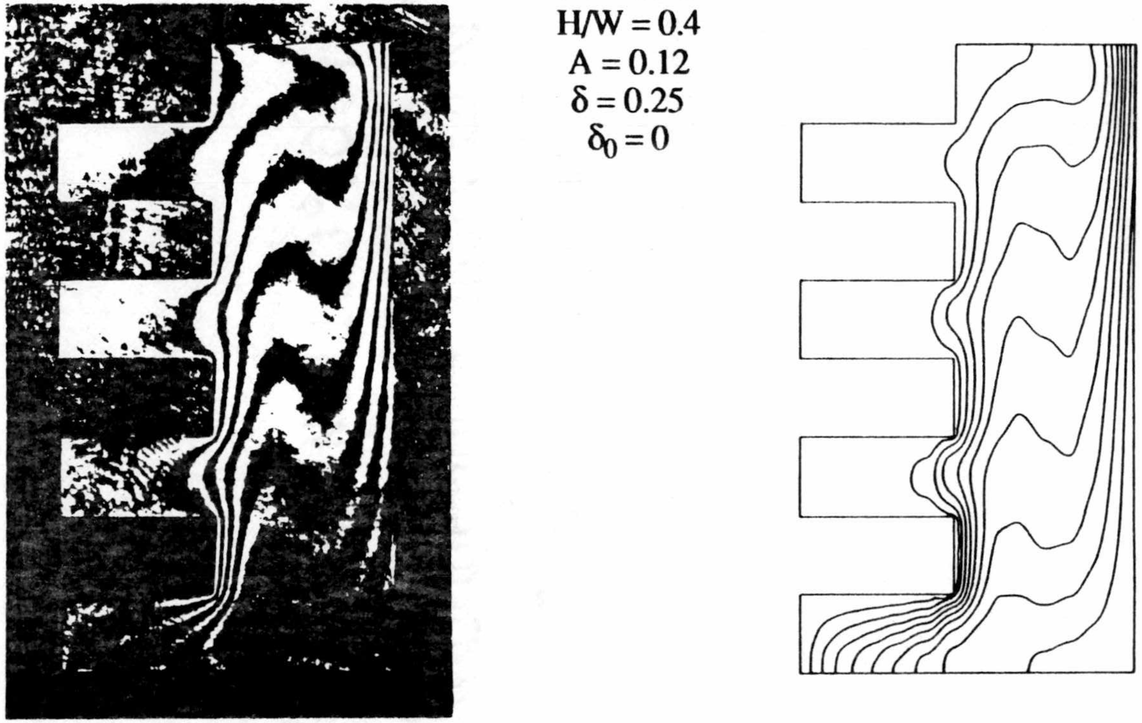

Case No. 51

$Gr = 1.69 \times 10^6$

$Pr = 0.72$

$H/W = 0.4$

$A = 0.12$

$\delta = 0.25$

$\delta_0 = 0$

(a) Mach-Zehnder Interferometer (Infinite Fringe Setting Showing the Isotherms)

(b) Isotherms Computed With NACHOS

Figure 17. Comparison of the Experimentally Determined Isotherms With Those Computed With the NACHOS Code

enclosure shown in Figure (1a) on the rate of natural convection heat transfer across such an enclosure. This objective was achieved by performing extensive numerical calculations with the experimentally verified NACHOS code. Computations were completed for the natural convection flows in smooth-walled enclosures [Figure (1a)] and for enclosures containing either sinusoidal roughness elements [Figure (1b)] or rectangular roughness elements [Figure (1c)]. The parametric study is composed of the 56 cases defined in Tables 1, 2, 3, and 4 in Chapter 3. <u>It would have been desireable to include many more cases in the parametric study, however, the cost of executing additional cases with the NACHOS code was prohibitive.</u>

5.4.2 <u>Results for Smooth-Walled Enclosures</u>

In order to assess the effects of adding roughness elements on the rate of natural convection heat transfer across an enclosure, it is necessary to first determine the overall Nusselt number, $\overline{Nu}$, for the original smooth-walled enclosure. As shown before, the overall Nusselt number for a smooth-walled enclosure is given by the functional relationship

$$(\overline{Nu})_S = \overline{Nu}_S\,[\,Gr_H, Pr, W/H\,] \tag{5.1}$$

where Gr_H is the Grashof number built on the enclosure height, Pr is the Prandtl number and W/H is the aspect ratio of the enclosure. Thus, 14 cases in which these three parameters were varied were computed for smooth-walled enclosures. The results of these computations, which are presentated in Table 9, served as the basis for comparison of the rates of heat transfer across smooth-walled and rough-walled enclosures.

Table 9. Results of the Numerical Study for Smooth-Walled Enclosures

Case No.	Gr_H	Pr	W/H	$(\overline{Nu})_S$
1	1.55×10^3	0.72	1.0	1.108
2	1.49×10^4	0.72	1.0	2.226
3	1.43×10^5	0.72	1.0	4.450
4	3.41×10^5	4.52	1.0	10.371
5	1.69×10^6	0.72	0.4	9.745
6	1.90×10^6	0.72	0.4	10.040
7	4.07×10^3	4.52	0.4	3.013
8	4.07×10^4	4.52	0.4	6.081
9	4.07×10^5	4.52	0.4	11.333
10	4.07×10^6	4.52	0.4	21.639
11	6.64×10^3	4.52	0.34	3.472
12	6.64×10^4	4.52	0.34	7.001
13	6.64×10^5	4.52	0.34	12.937
14	6.64×10^6	4.52	0.34	24.557

The physics of the natural convection flows in vertically-oriented, smooth-walled rectangular enclosures are well-understood [Bejan(1984), Gebhart, et al. (1988)] and, therefore, will be discussed here only in enough detail to show that NACHOS correctly computes the essential features of these flows. At low Grashof numbers, the horizontal temperature distribution across the enclosure is almost linear over most of the vertical extent of the enclosure, except in "end regions" near the horizontal walls, and the heat transfer across the enclosure is mainly by conduction. Thus, this is known as the "conduction regime". As would be anticipated, the overall Nusselt number, $\overline{Nu}$, approaches a value of 1.0 at the lower end of the conduction regime. At high Grashof numbers, the so-called "boundary-layer regime" occurs in which thin boundary regions are formed on the vertical walls and the heat transfer across the enclosure is dominated by convection. In this practically-important flow regime the temperature is constant across the width of the enclosure between the thin layers on the vertical walls and the vertical temperature distribution shows that the flow in the "core region" has a stable, linear thermal stratification. The conduction and boundary-layer flow regimes are separated by the "transition regime", which occurs over an intermediate range of Grashof numbers. In the transition regime the layers on the vertical walls are thicker than those in the boundary-layer regime and the temperature is <u>not</u> constant across the core region as it is in the boundary-layer regime.

The streamlines and isotherms for a flow in a square enclosure (W/H = 1.0) at a Grashof number of 3.41 x 10^5 and a Prandtl number of 4.52, which is characteristic of water, are shown in Figure 18. The presence of the thin layers on the vertical walls, a constant temperature on each horizontal plane across the core region and the stable thermal stratification in the core region all indicate that this flow is in the boundary-layer regime. This agrees with the findings of many other

Case No. 4

Gr = 3.41×10^5 Pr = 4.52 W/H = 1.0 $(\overline{Nu})_S = 10.371$

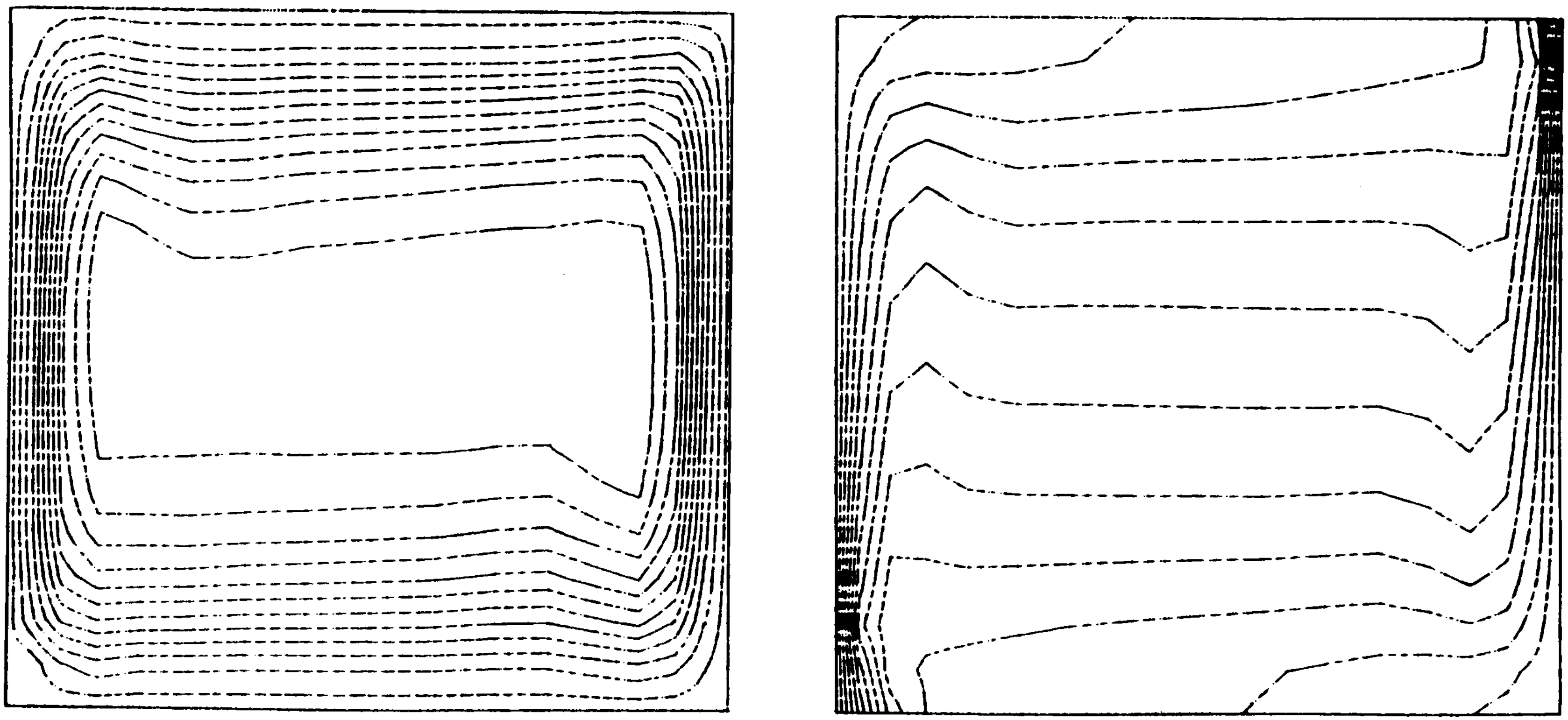

(a) Streamlines

(b) Isotherms

Figure 18. Computed Streamlines and Isotherms for a Flow in the Boundary-Layer Regime in a Square, Smooth-Walled Enclosure

investigators [Gebhart, et al. (1988)]. It should also be noted that Beach (1985) showed that the NACHOS code gives excellent predictions of the experimentally-determined temperature, velocity and heat flux distributions obtained by Krane and Jessee (1983) for a natural convection flow in air ($Pr = 0.71$) in a square enclsoure ($W/H = 1.0$) at a Grashof number of 2.66×10^5.

The streamlines, isotherms and heat lines for a series of flows that occur in water ($Pr = 4.52$) in an enclosure with an aspect ratio of $W/H = 0.4$ as the Grashof number is increased from 4.07×10^3 to 4.07×10^6 are presentated in Figures 19 through 22. These distributions, which for the flow at $Gr_H = 4.07 \times 10^3$ are portrayed in Figure 19, along with the computed value of 3.013 for the overall Nusselt number, show that this flow is in the conduction regime.

The results for the two flows at Grashof numbers of 4.07×10^4 and 4.07×10^5 are presented in Figures 20 and 21, respectively. These results clearly indicate that both of these flows are in the transition regime. Finally, the streamlines, isotherms, and heat lines for the flow that occurs at a Grashof number of 4.07×10^6, which are presented in Figure 22, show that this flow is in the boundary-layer regime.

Figure 23 illustrates the effect that the increasing Grashof number in this series of four flows has on the temperature distribution across the horizontal plane at $y^*/H = 0.55$. The temperature distribution for the flow at a Grashof number of 4.07×10^3, which is in the conduction regime, is essentially linear. The temperature distribution at the highest Grashof number of 4.07×10^6, however, shows the large temperature changes across the thin layers on the vertical walls and the uniform temperature across the core region between these layers that are characteristic of the boundary-layer regime. The temperature distributions for the flows at Grashof numbers of 4.07×10^4 and 4.07×10^5, which are in the transition

Case No. 7

$Gr = 4.07 \times 10^3$ $Pr = 4.52$ $W/H = 0.4$ $(\overline{Nu})_S = 3.013$

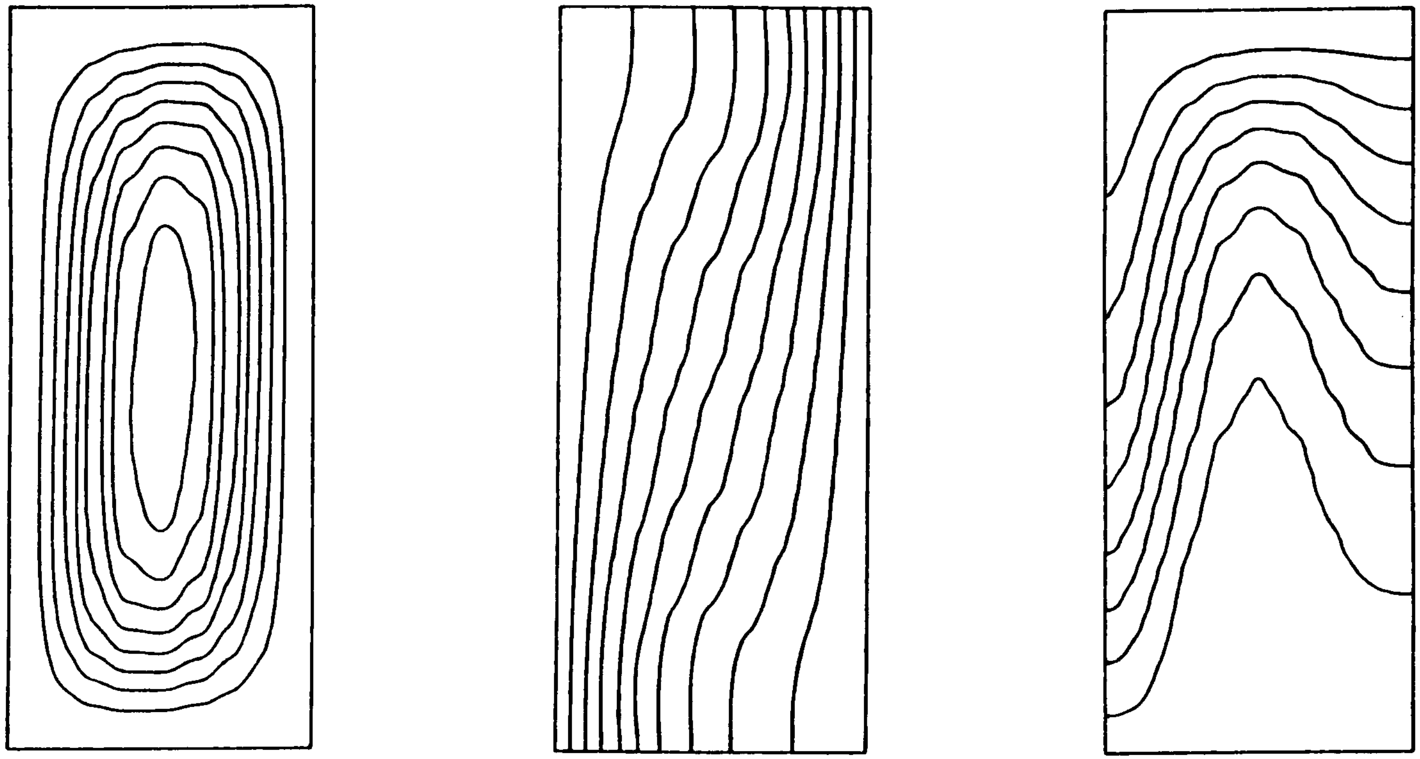

(a) Streamlines (b) Isotherms (c) Heat lines

Figure 19. Computed Streamlines, Isotherms, and Heat Lines for a Flow in the Conduction Regime in a Smooth-Walled Enclosure

Case No. 8

$Gr = 4.07 \times 10^4$ $Pr = 4.52$ $W/H = 0.4$ $(\overline{Nu})_S = 6.081$

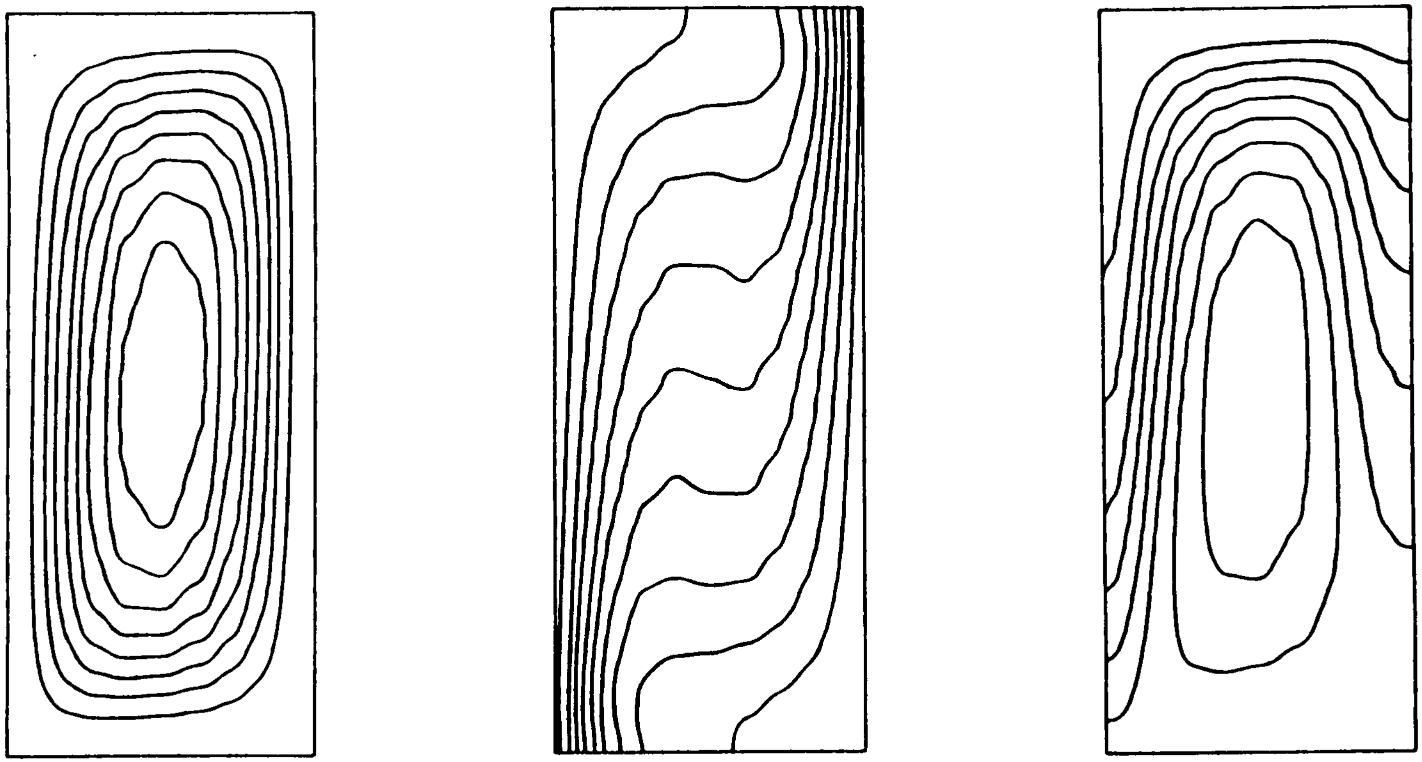

(a) Streamlines (b) Isotherms (c) Heat lines

Figure 20. Computed Streamlines, Isotherms, and Heat Lines for a Flow in the Transition Regime in a Smooth-Walled Enclosure

Case No. 9

$Gr = 4.07 \times 10^5$ $Pr = 4.52$ $W/H = 0.4$ $(\overline{Nu})_S = 11.333$

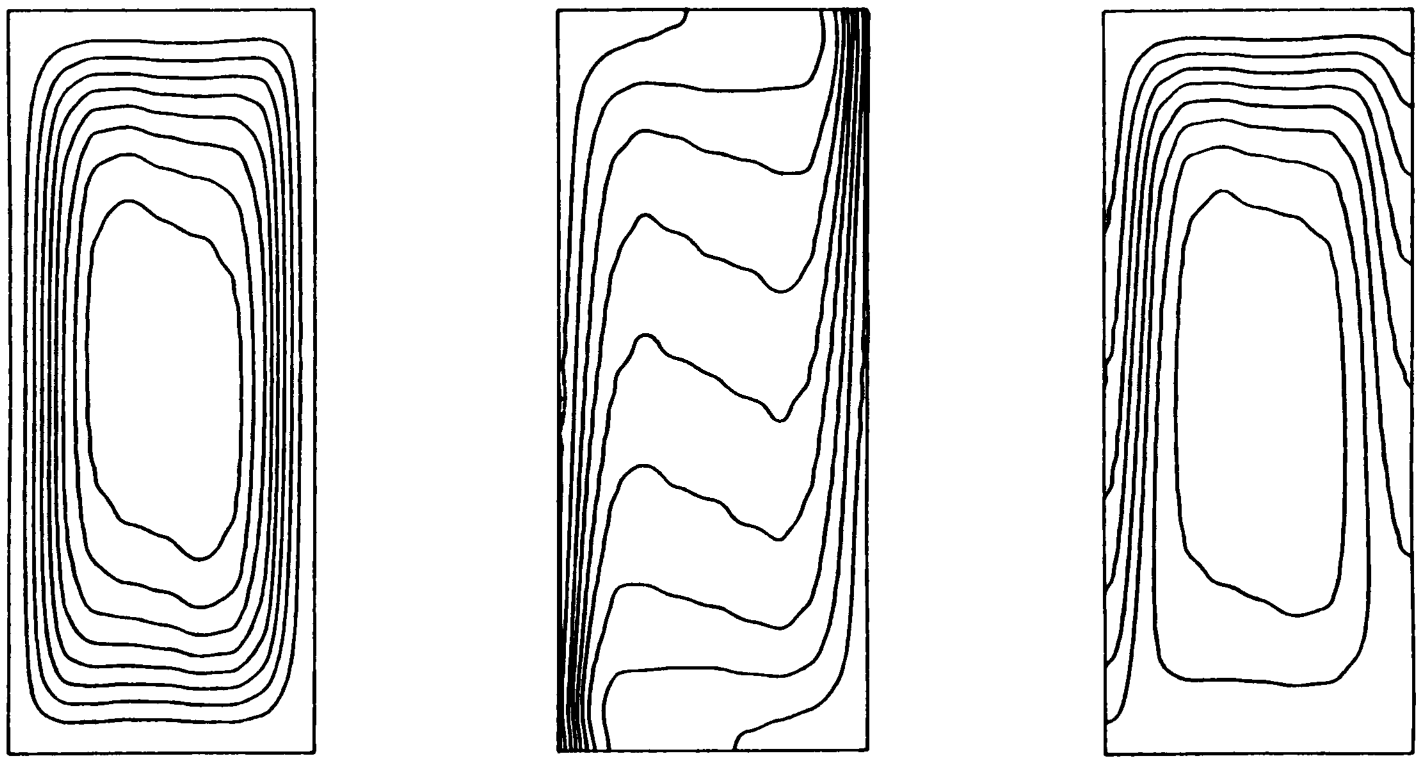

(a) Streamlines (b) Isotherms (c) Heat lines

Figure 21. Computed Streamlines, Isotherms, and Heat Lines for a Flow in the Transition Regime in a Smooth-Walled Enclosure

Case No. 10

Gr = 4.07×10^6 Pr = 4.52 W/H = 0.4 $(\overline{Nu})_S = 21.639$

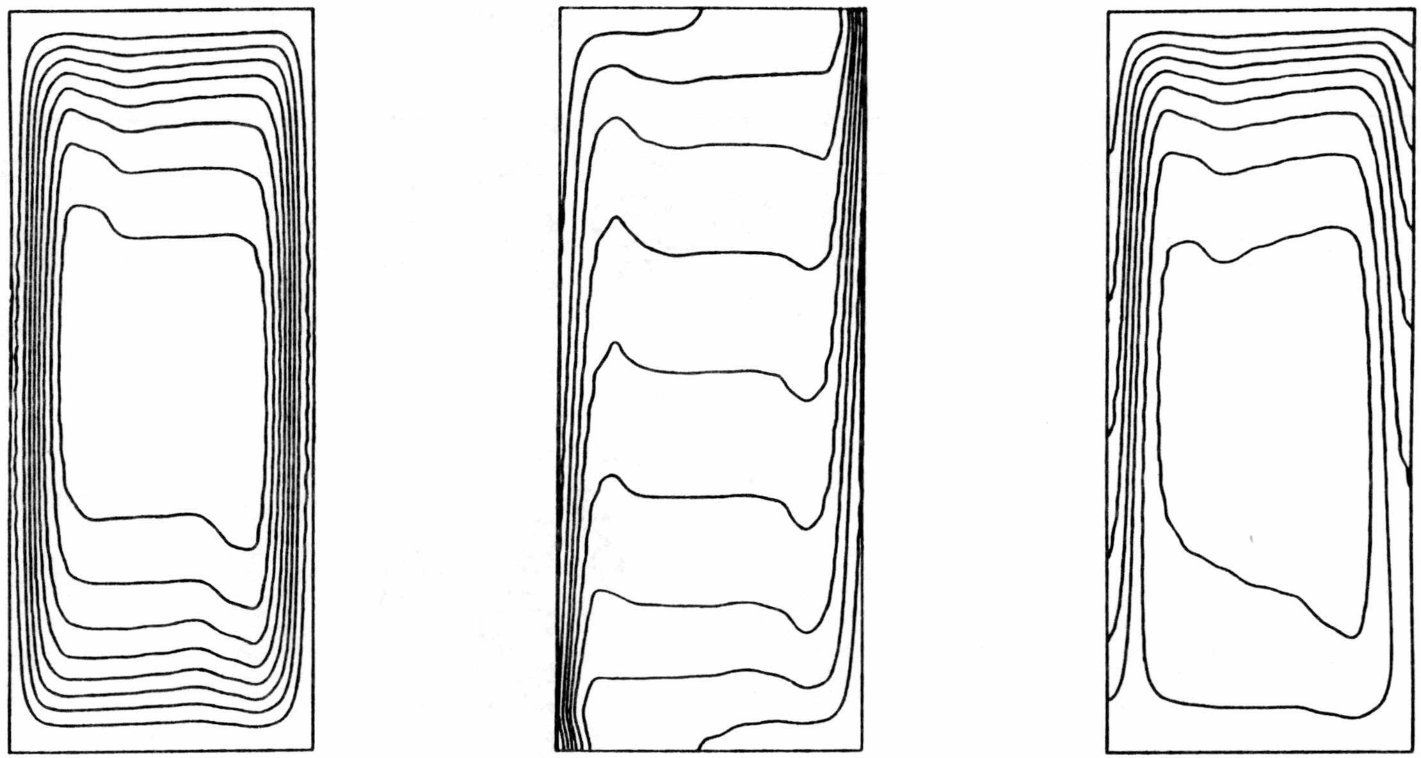

(a) Streamlines (b) Isotherms (c) Heat lines

Figure 22. Computed Streamlines, Isotherms, and Heat Lines for a Flow in the Boundary-Layer Regime in a Smooth-Walled Enclosure

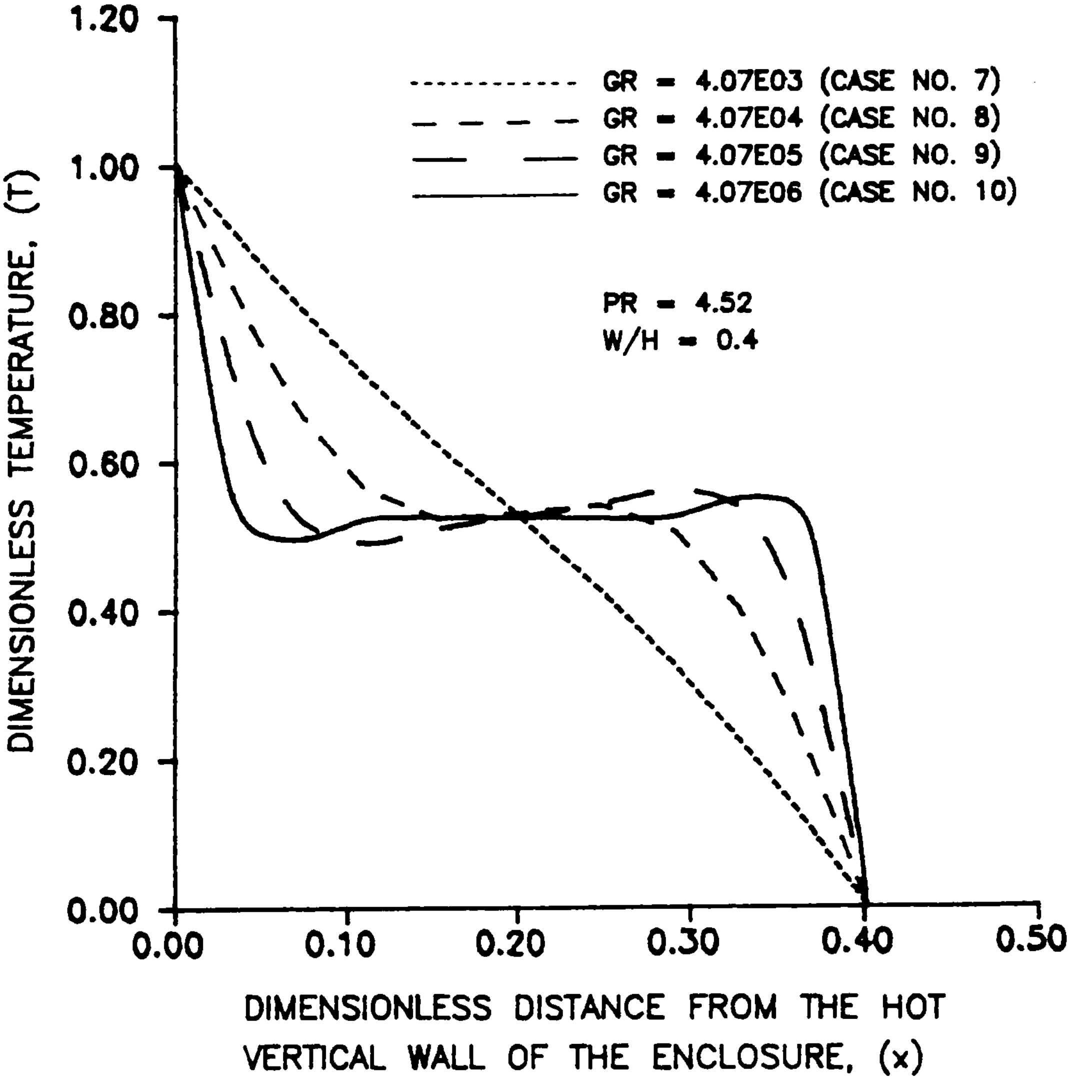

Figure 23. The Effect of Grashof Number on the Horizontal Temperature Distribution Across a Smooth-Walled Enclosure at $y^*/H = 0.55$

regime, show that the layers that are formed on the vertical walls in this regime are thicker than those in the boundary-layer regime and that the temperature is neither constant, nor linearly varying, across the core region in this regime.

The local Nusselt number distributions on the vertical walls for the flow in the boundary-layer regime ($Gr_H = 4.07 \times 10^6$) are presented in Figure 24. As expected, these results show that the highest rates of heat transfer occur near the bottom of the hot wall and the top of the cold wall.

The results presented above for smooth-walled enclosures will now be used to assess the effects of adding large sinusoidal or rectangular roughness elements on the rate of heat transfer across the enclosure.

5.4.3 Results for Enclosures Containing Sinusoidal Roughness Elements

The primary focus of the present work is on the effects of employing rectangular roughness elements; however, nine cases (cases 15-23) were executed to briefly examine the effects of using sinusoidal roughness elements. The results of these cases are reported in Table 10. The effects of adding roughness elements on the rate of natural convection heat transfer across the enclosure are presented in terms of the ratio of the average Nusselt number in the rough-walled enclosure to the average Nusselt number in the smooth-walled enclosure, or:

$$(\overline{Nu})_{\substack{\text{Rough-Walled}\\ \text{Enclosure}}} \Big/ (\overline{Nu})_{\substack{\text{Smooth-Walled}\\ \text{Enclosure}}} \equiv (\overline{Nu})_R/(\overline{Nu})_S \; . \qquad (5.2)$$

When this parameter has a value greater than, or less than, unity, the elements have enhanced or decreased, respectively, the rate of heat transfer across the enclosure.

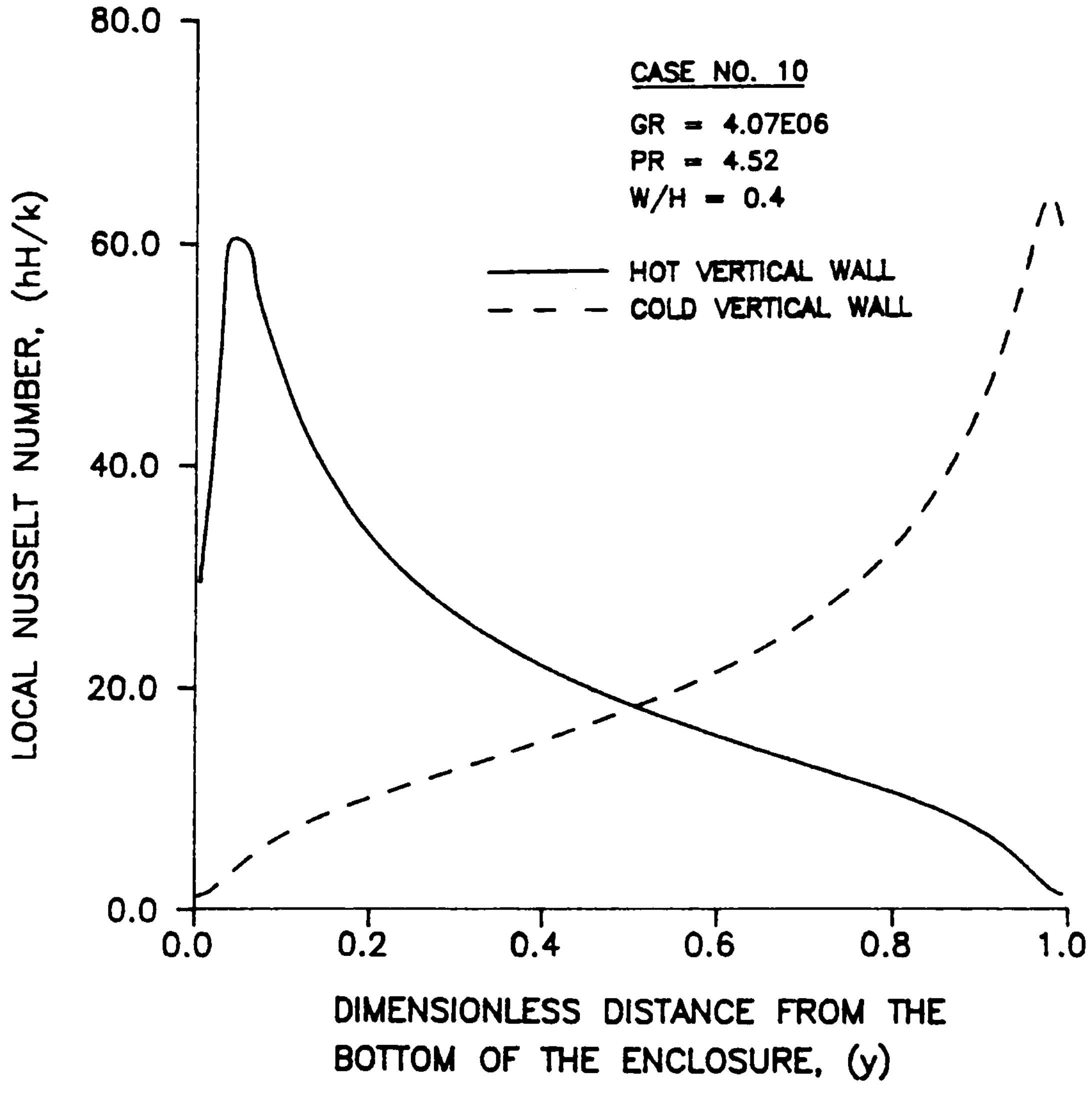

Figure 24. Local Nusselt Number Distributions Along the Hot and Cold Vertical Walls of a Smooth-Walled Enclosure for a Flow in the Boundary-Layer Regime

Table 10. Results of the Numerical Study for Enclosures with Sinusoidal Roughness Elements

Case No.	Gr_H	Pr	W/H	A	δ	φ	$(\overline{Nu})_R$	$\frac{(\overline{Nu})_R}{(\overline{Nu})_S}$
15	1.55×10^3	0.72	1.0	0.12	0.25	0	1.175	1.061
16	1.49×10^4	0.72	1.0	0.12	0.25	0	2.243	1.007
17	1.43×10^5	0.72	1.0	0.12	0.25	0	4.392	0.987
18	3.41×10^5	4.52	1.0	0.12	0.25	0	11.031	1.064
19	4.07×10^3	4.52	0.4	0.12	0.25	0	3.263	1.083
20	4.07×10^4	4.52	0.4	0.12	0.25	0	5.965	0.981
21	4.07×10^5	4.52	0.4	0.12	0.25	0	12.797	1.129
22	4.07×10^6	4.52	0.4	0.12	0.25	0	29.317	1.355
23	4.07×10^6	4.52	0.4	0.12	0.50	0	23.944	1.107

This parameter is also used below to report the effects of adding rectangular roughness elements. Beacuse of the limited extent of the parametric study for sinusoidal roughness elements, the results of this study will not be discussed in as great a depth as will the results of the study for the rectangular roughness elements.

As before, the overall Nusselt number for an enclosure with sinusoidal roughness elements is given by

$$(\overline{Nu})_R = \overline{Nu}_R \,[\, Gr_H, Pr, W/H, A, \delta, \phi \,] \tag{5.3}$$

where Gr_H, Pr and W/H are as defined above, A is the dimensionless amplitude of a roughness element, δ is the dimensionless period of the roughness element array and ϕ is the phase angle of the array. The effects of changing the amplitude, A, of the roughness elements and the phase angle, ϕ, were not investigated. Instead, the values of $A = 0.12$ and $\phi = 0$ were used for all of the cases presented here. Each of the other four parameters was varied in at least one case in the study. Recall that each enclosure with roughness elements is designed such that it contains the same volume of fluid as the corresponding enclosure with smooth vertical walls and the same aspect ratio.

Cases 15, 16, and 17 were all calculated for air (Pr = 0.72) in a square enclosure (W/H = 1.0) with a roughness element period, δ, of 0.25 that gives 4 elements on the hot vertical wall. The effects of increasing the Grashof number from 1.55×10^3 to 1.43×10^5 on the ratio of overall Nusselt numbers, $(\overline{Nu})_R/(\overline{Nu})_S$, for these three flows are shown in Figure 25. This figure shows that: (1) over the limited range of Grashof numbers investigated, the ratio of Nusselt numbers decreases monotonically with increasing Grashof number, (2) at the

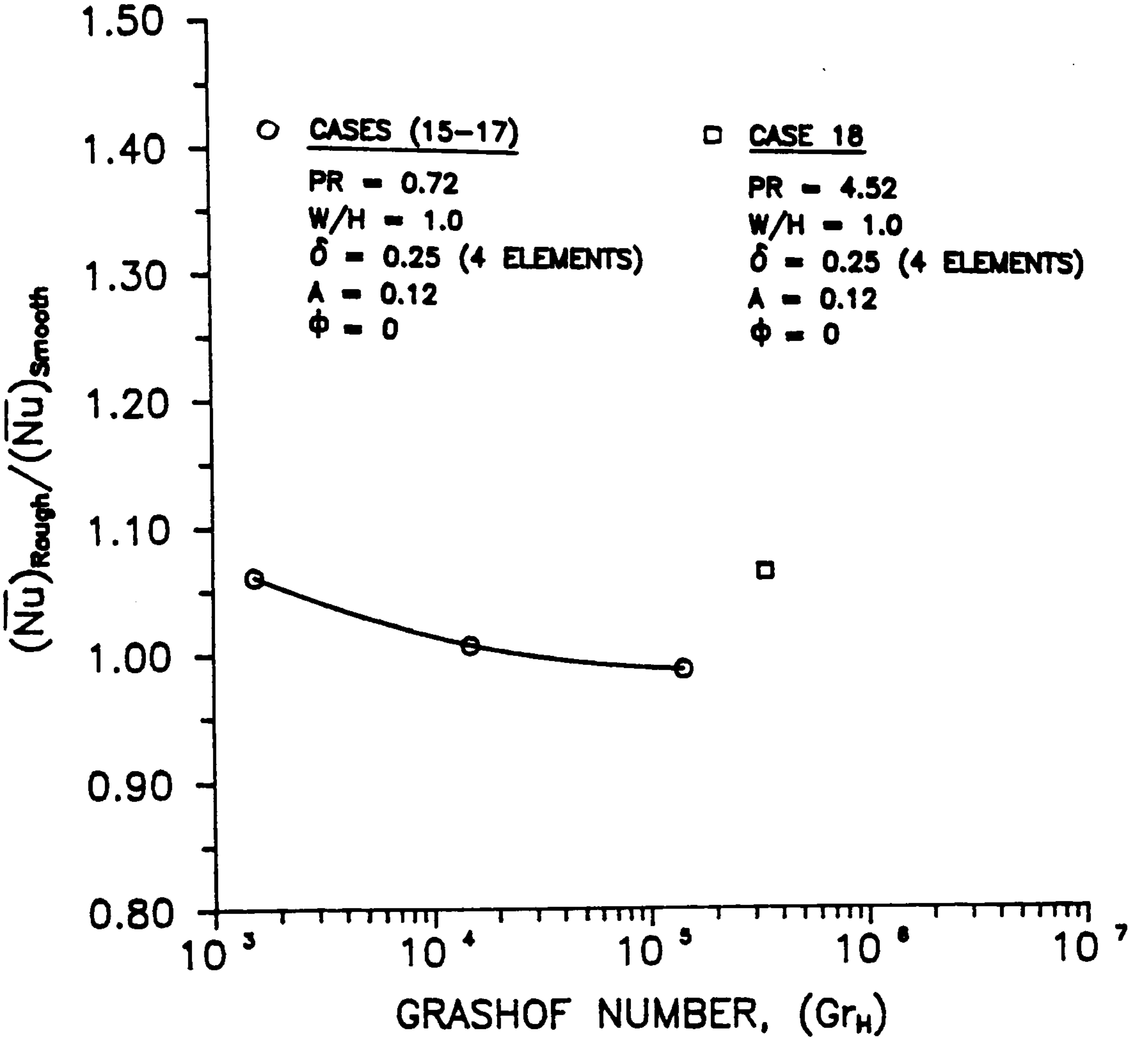

Figure 25. The Effect of Grashof Number on the Ratio of Nusselt Numbers in a Square Enclosure With Four Sinusoidal Roughness Elements

lowest Grashof number of 1.55×10^3 the ratio of Nusselt numbers is greater than unity (1.061), indicating that the elements enhance the heat transfer across the enclosure, (3) at the highest Grashof number, the ratio of Nusselt number is 0.987, which indicates that the elements have slightly decreased the rate of heat transfer, (4) heat transfer enhancement due to adding the elements is relatively small and occurs at the lower values of the Grashof numbers at which conduction is a dominant mode of heat transfer, and (5) decreases in the heat transfer due to the presence of the roughness elements are very small (less than 2%) and occur at Grashof numbers that are in the transition flow regime in the corresponding smooth-walled enclosures.

The flow computed in case 18 occurs in an enclosure with the same geometry as the flows in cases 15-17, but in water (Pr = 4.52) and at a higher Grashof number of 3.41×10^5. The ratio of Nusselt numbers for this flow, which has a value of 1.064 that indicates enhancement, is also plotted in Figure 25. Because this was the only flow calculated at a Prandtl number of 4.52 for this geometry, it is impossible to draw any general conclusions; however, it may be postulated that there is a strong Prandtl number effect on the ratio of Nusselt numbers. This will be discussed further below.

The streamline and isotherm distributions for case 18 are shown in Figure 26. They indicate that: (1) this flow is in the equivalent of the boundary-layer regime for a rough-walled enclosure, (2) the flow along the hot wall penetrates the spaces between adjacent roughness elements less and less as it proceeds up the wall, (3) the largest rates of heat transfer on the hot wall occur near the tips of the roughness elements, and (4) the rate of heat transfer from each successive element decreases rapidly as the flow proceeds up the wall, which suggests that only the

Case No. 18

$Gr = 3.41 \times 10^5$ $Pr = 4.52$ $WH = 1.0$ $\delta = 0.25$ $A = 0.12$ $\phi = 0$ $(\overline{Nu})_R = 11.031$ $(\overline{Nu})_{Rough}/(\overline{Nu})_{Smooth} = 1.064$

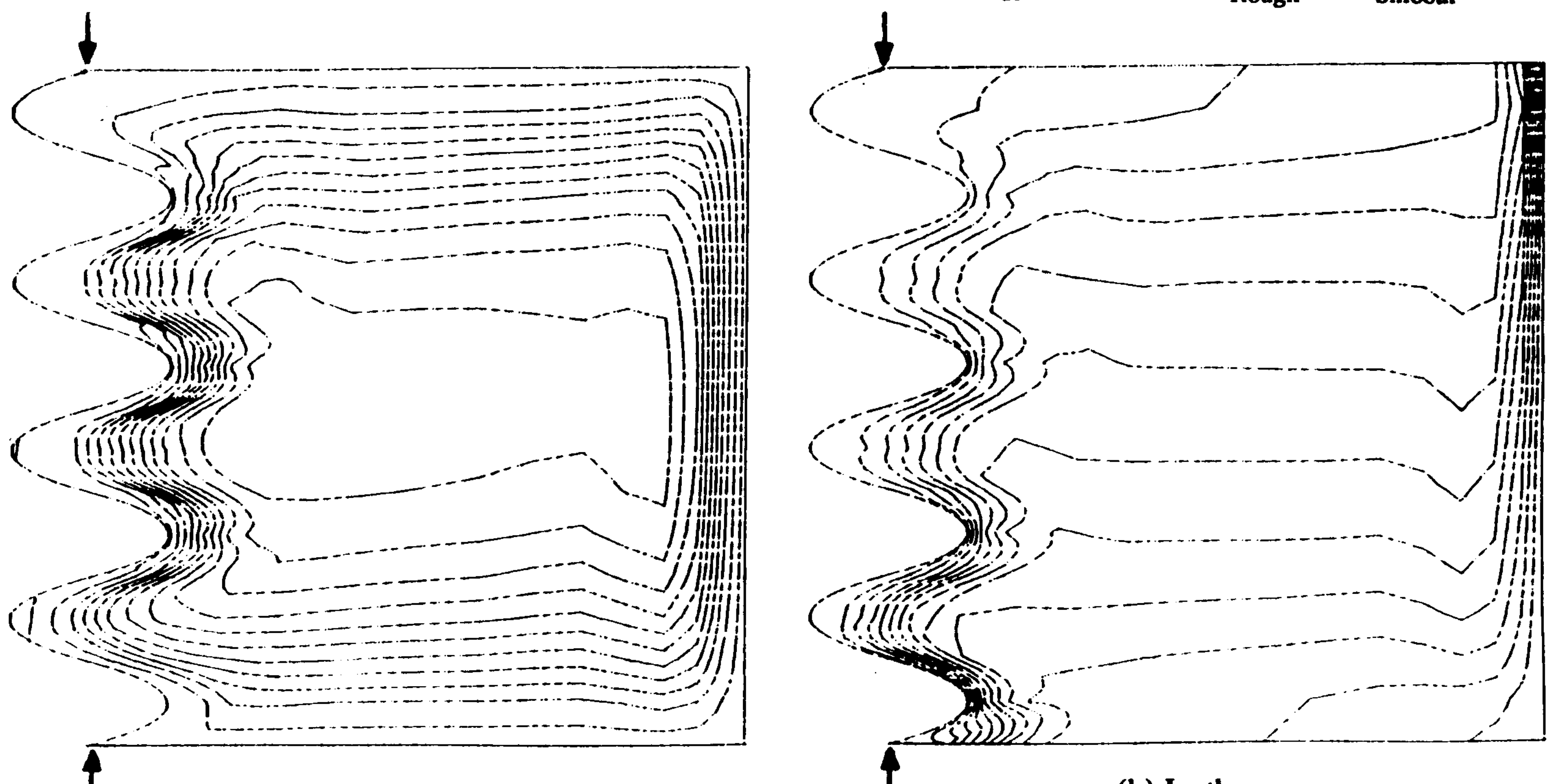

(a) Streamlines (b) Isotherms

[Arrows Denote the Location of the Hot Wall in the Corresponding Smooth-Walled Enclosure]

Figure 26. Computed Streamlines and Isotherms in a Square Enclosure With Sinusoidal Wall Roughness Elements

lower elements may play an important role in altering the rate of heat transfer across the enclosure.

Cases 19, 20, 21 and 22 were all calculated for flows in water ($Pr = 4.52$) in an enclosure with an aspect ratio, W/H, of 0.4 and a roughness element period, δ, that gives four elements on the hot wall. The effect of increasing the Grashof number from 4.07×10^3 to 4.07×10^6 on the ratio of overall Nusselt numbers, $(\overline{Nu})_R/(\overline{Nu})_S$, for these flows is presented in Figure 27. This Figure shows that: (1) over the range of Grashof numbers investigated, the ratio of Nusselt numbers, $(\overline{Nu})_R/(\overline{Nu})_S$, first decreases and then increases with increasing Grashof number, (2) for all Grashof numbers, except those in a narrow range centered about a value of approximately 2×10^4, the elements enhance the heat transfer across the enclosure, (3) only in this very narrow range of Grashof numbers do the elements decrease the rate of heat transfer, (4) at Grashof numbers below this narrow range in which the elements decrease the heat transfer, the enhancement is relatively modest, with the ratio $(\overline{Nu})_R/(\overline{Nu})_S$ achieving a maximum value of 1.083 at a Grashof number of 4.07×10^3, (5) for Grashof numbers above this range, substantial enhancements of the heat transfer are caused by the elements with the maximum value of the ratio $(\overline{Nu})_R/(\overline{Nu})_S$ of 1.355 being obtained at the (highest) Grashof number of 4.07×10^6 (case 22).

Figure 28 illustrates the effect that increasing the Grashof number in this series of four flows has on the temperature distribution across the horizontal plane at $y^*/H = 0.438$. The same general trend is observed here as was in Figure 23 for flows in smooth-walled enclosures; that is, at the lowest Grashof number of 4.07×10^3 (case 19), the temperature distribution is linear across most of the enclosure indicating that conduction is the dominant mode of heat transfer, while at the highest Grashof number of 4.07×10^6 (case 22) there is a boundary-layer regime

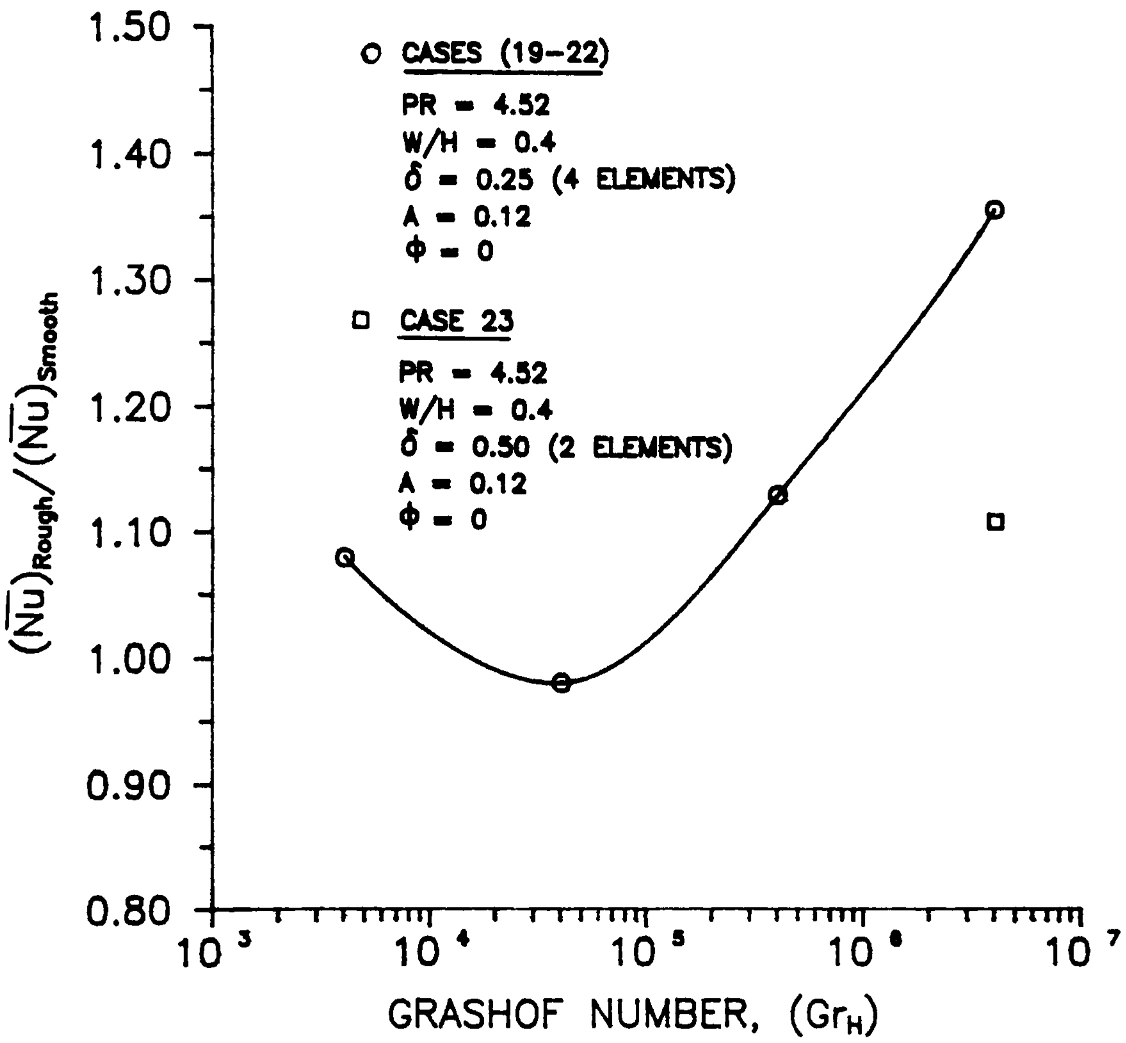

Figure 27. The Effect of Grashof Number on the Ratio of Nusselt Numbers for Flows in an Enclosure With Sinusoidal Roughness Elements and an Aspect Ratio of W/H = 0.4

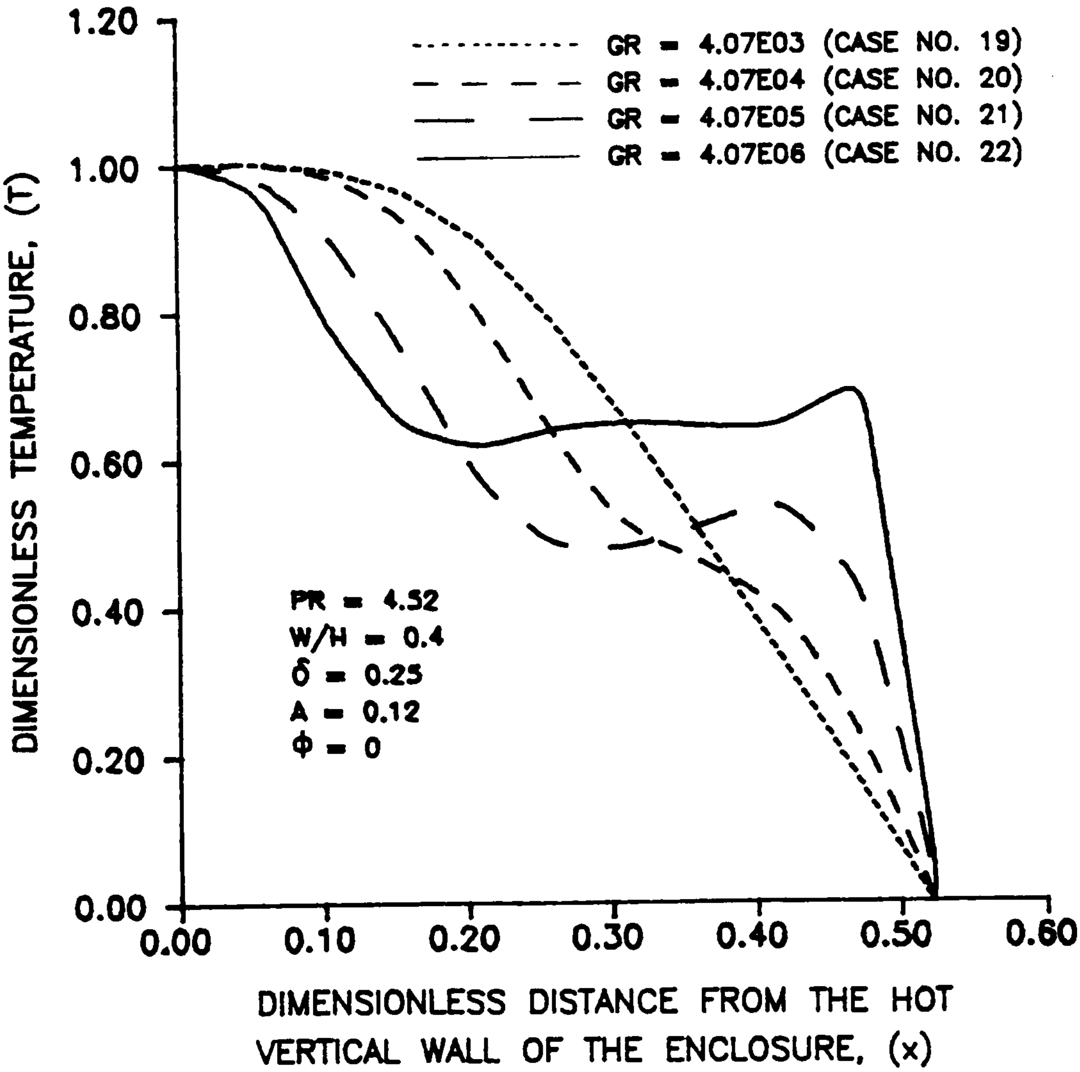

Figure 28. The Effect of Grashof Number on the Horizontal Tempertaure Distribution at $y^*/H = 0.438$ in an Enclosure With Sinusoidal Roughness Elements

in which there are relatively thin boundary regions formed on the vertical walls and the temperature between these regions is essentially constant. Convection is the dominant mode of heat transfer in this regime. At the intermediate Grashof numbers of 4.07 x 10^4 and 4.07 x 10^5, the temperature profiles show that these flows are in a transition regime.

The streamlines and isotherms for the flow in case 22, which are shown in Figure 29, indicate that this flow is in a boundary-layer flow regime. The calculations for air in a square enclosure that were presented in Figure 25 showed enhancement only in the conduction flow regime. Unlike these results, the results for water in an enclosure with an aspect ratio of 0.4 indicate that the sinusoidal elements will provide enhancement of the heat transfer across the enclosure in <u>both</u> the conduction and boundary layer regimes. (Note: Further calculations at higher Grashof numbers <u>might</u> reveal the same trend in the results for air in a square enclosure, however, these calculations were not performed.) Both Figures 25 and 27 indicate that in the transition flow regime sinusoidal roughness elements will either decrease the heat transfer or, at best, provide minimal enhancement. An interesting feature of the flow in case 22 may be observed in Figure 29(b). The local thickness of the thermal boundary layer on the cold vertical wall clearly decreases on those segments of this wall that are directly opposite the three uppermost elements on the hot wall. This, of course, indicates local increases in the rate of heat transfer on the cold wall opposite these three elements.

The flow computed in case 23 also occurs in water and in an enclosure that is identical to the enclosures in cases 19-22, except that the period of the roughness elements, δ, is 0.5 (instead of 0.25 as in cases 19-22) so that there are only 2 elements on the hot wall in this flow. The data point for this flow, which is also plotted in Figure 27, shows that at a Grashof number of 4.07 x 10^6 the ratio of

Case No. 22

$Gr = 4.07 \times 10^6$ $Pr = 4.52$ $WH = 0.4$ $\delta = 0.25$ $A = 0.12$ $\phi = 0$ $(\overline{Nu})_R = 29.317$ $(\overline{Nu})_{Rough} / (\overline{Nu})_{Smooth} = 1.355$

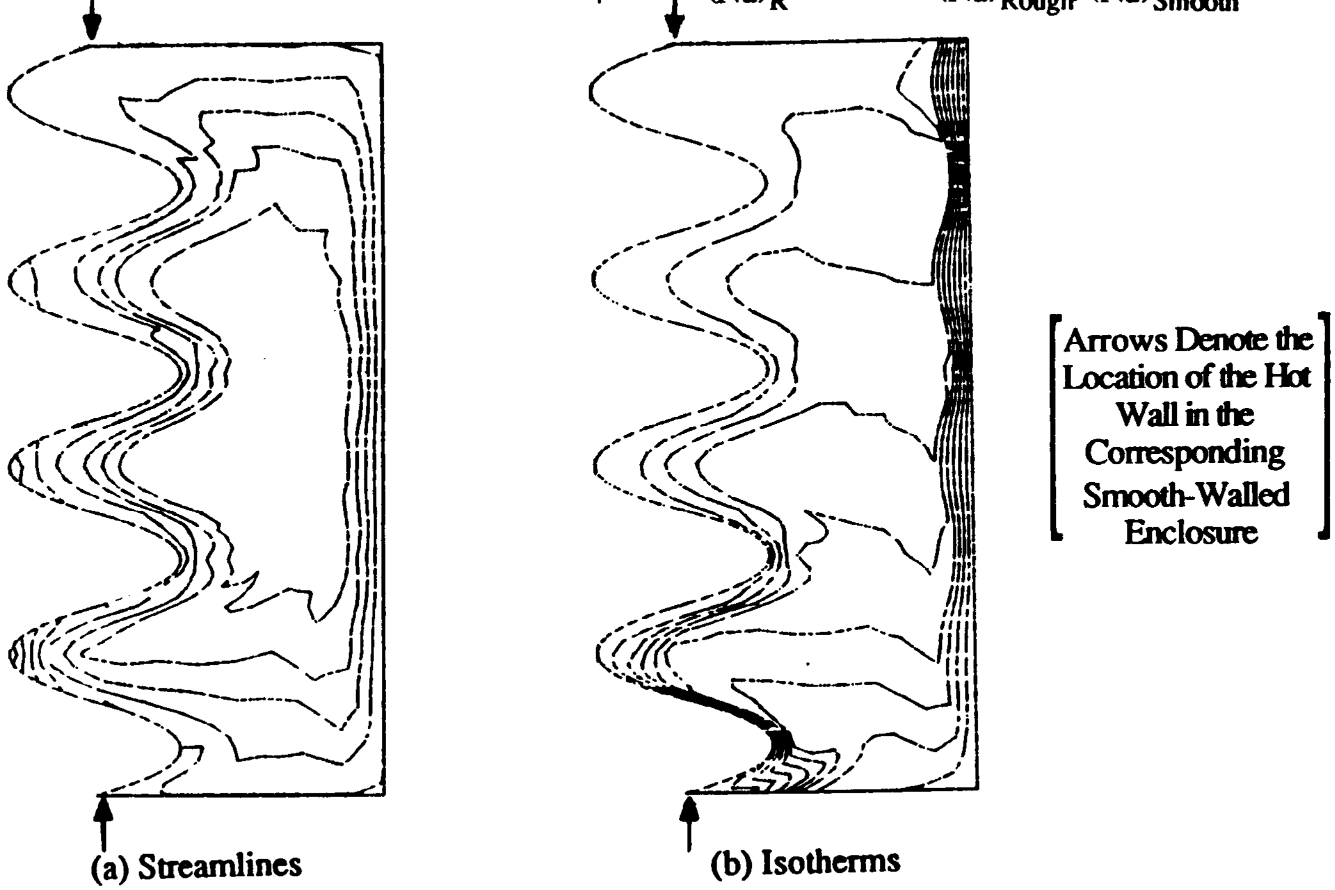

Figure 29. Computed Streamlines and Isotherms in an Enclosure With an Aspect Ratio of W/H = 0.4 that Contains Four Sinusoidal Wall Roughness Elements (Case No. 22)

Nusselt numbers, $(\overline{Nu})_R/(\overline{Nu})_S$, is only 1.107, as compared to the value of 1.355 obtained in case 22 with four roughness elements. Thus, reducing the number of elements from 4 to 2 results in a significant reduction in the heat transfer enhancement. The streamlines and isotherms for case 23, which are presented in Figure 30, show that this flow is in the boundary layer regime.

5.4.4 Results for Enclosures Containing Rectangular Roughness Elements

The primary focus of the present work is on the effects of employing rectangular roughness elements. Thus, thirty-three cases (cases 24-56) were excuted in the parametric study being reported here for such elements. The results of these cases are presented in Tables 11 and 12 in terms of the ratio of the overall Nusselt numbers, $(\overline{Nu})_R/(\overline{Nu})_S$, which was also used to report the results for sinusoidal roughness elements.

As shown in Chapter 3, the overall Nusselt number for an enclosure with rectangular roughness elements is given by

$$(\overline{Nu})_R = \overline{Nu}_R\,[\,Gr_H, Pr, W/H, A, \delta, \delta_0\,] \tag{5.4}$$

where Gr_H, Pr, and W/H are as defined above, A is the dimensionless amplitude of a rectangular roughness elements, δ is the dimensionless period of the rectangular roughness element array, and δ_0 is the dimensionless phase shift of the array ($\delta_0 = \delta_0^*/H$). All of these six quantities were varied in the parametric study. Each of the enclosures for cases 24-52 was designed such that it contains the same volume of fluid as the corresponding enclosure with smooth vertical walls and the same aspect ratio. The enclosures for four cases (cases 53-56); however, were pourposely designed such that the addition of the elements decreased the volumes

Case No. 23

$Gr = 4.07 \times 10^6$ $Pr = 4.52$ $WH = 0.4$ $\delta = 0.50$ $A = 0.12$ $\phi = 0$ $\overline{(Nu)}_R = 23.944$ $\overline{(Nu)}_{Rough} / \overline{(Nu)}_{Smooth} = 1.107$

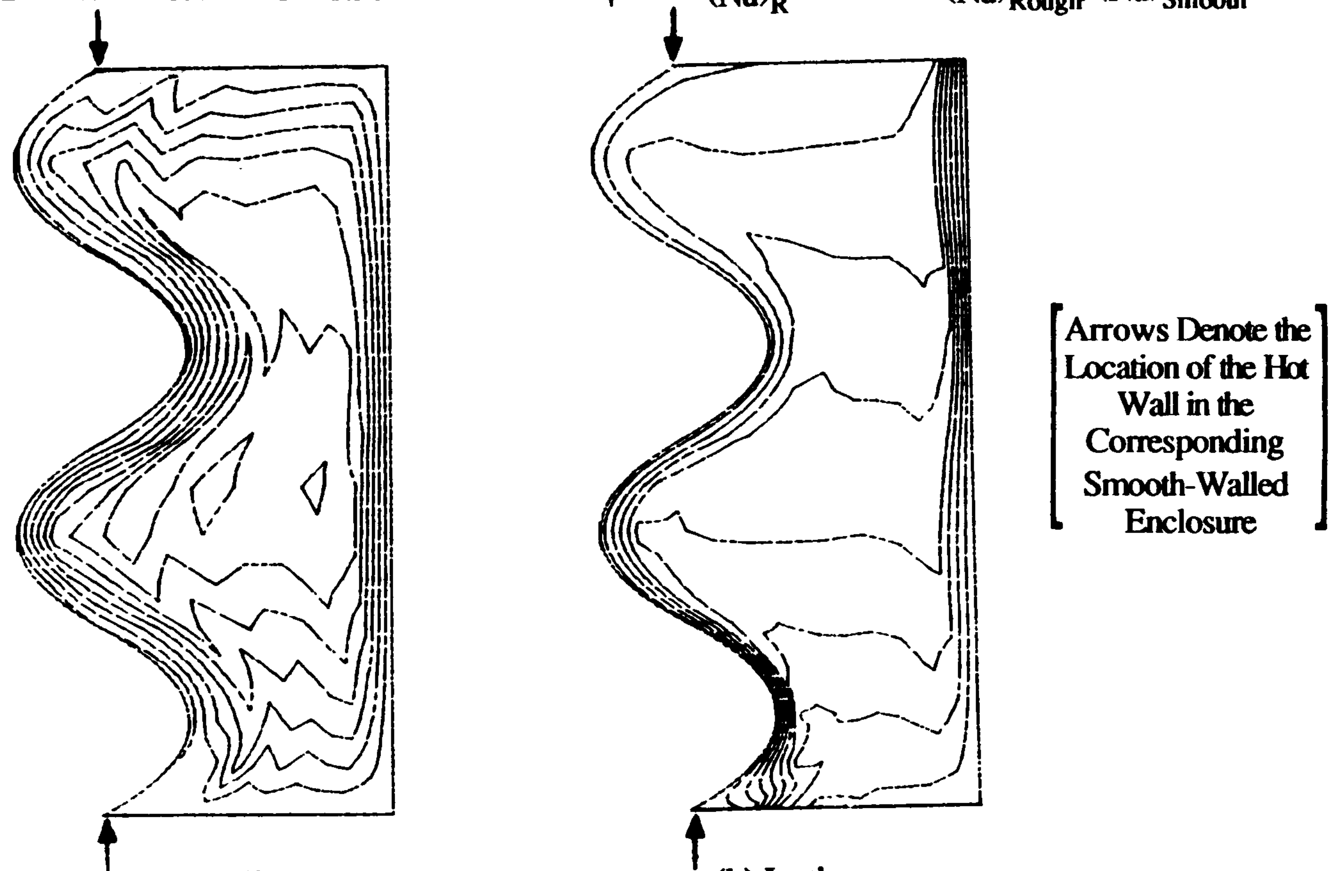

(a) Streamlines

(b) Isotherms

Figure 30. Computed Streamlines and Isotherms in an Enclosure With an Aspect Ratio of W/H = 0.4 that Contains Two Sinusoidal Wall Roughness Elements (Case No. 23)

Table 11. Results of the Numerical Study for Enclosures with Rectangular Roughness Elements

Case No.	Gr_H	Pr	W/H	A	δ	δ_0	$(\overline{Nu})_R$	$\frac{(\overline{Nu})_R}{(\overline{Nu})_S}$
24	4.07×10^3	4.52	0.4	0.12	0.25	0.125	3.451	1.145
25	4.07×10^3	4.52	0.4	0.06	0.25	0.125	3.056	1.014
26	4.07×10^3	4.52	0.4	0.12	0.50	0.25	3.284	1.090
27	4.07×10^3	4.52	0.4	0.06	0.50	0.25	2.982	0.999
28	4.07×10^3	4.52	0.4	0.12	0.25	0	3.458	1.148
29	4.07×10^3	4.52	0.4	0.12	0.50	0	3.285	1.090
30	4.07×10^4	4.52	0.4	0.12	0.25	0.125	5.786	0.952
31	4.07×10^4	4.52	0.4	0.06	0.25	0.125	5.910	0.972
32	4.07×10^4	4.52	0.4	0.12	0.50	0.25	5.799	0.954
33	4.07×10^4	4.52	0.4	0.06	0.50	0.25	5.913	0.972
34	4.07×10^4	4.52	0.4	0.12	0.25	0	5.748	0.945
35	4.07×10^5	4.52	0.4	0.12	0.50	0	5.752	0.946

Table 11 (Cont'd). Results of the Numerical Study for Enclosures with Rectangular Roughness Elements

Case No.	Gr_H	Pr	W/H	A	δ	δ_0	$(\overline{Nu})_R$	$\frac{(\overline{Nu})_R}{(\overline{Nu})_S}$
36	4.07×10^5	4.52	0.4	0.12	0.25	0.125	11.288	0.996
37	4.07×10^5	4.52	0.4	0.06	0.25	0.125	11.241	0.992
38	4.07×10^5	4.52	0.4	0.12	0.50	0.25	11.889	1.050
39	4.07×10^5	4.52	0.4	0.06	0.50	0.25	11.533	1.018
40	4.07×10^5	4.52	0.4	0.12	0.25	0	11.311	0.998
41	4.07×10^5	4.52	0.4	0.12	0.50	0	11.896	1.050
42	4.07×10^6	4.52	0.4	0.12	0.25	0.125	24.176	1.117
43	4.07×10^6	4.52	0.4	0.06	0.25	0.125	23.716	1.096
44	4.07×10^6	4.52	0.4	0.12	0.50	0.25	23.385	1.081
45	4.07×10^6	4.52	0.4	0.12	0.25	0	24.314	1.124
46	4.07×10^6	4.52	0.4	0.12	0.50	0	23.479	1.085

Table 11 (Cont'd). Results of the Numerical Study for Enclosures with Rectangular Roughness Elements

Case No.	Gr_H	Pr	W/H	A	δ	ϕ	$(\overline{Nu})_R$	$\frac{(\overline{Nu})_R}{(\overline{Nu})_S}$
47	6.64×10^3	4.52	0.34	0.06	0.25	0.125	3.593	1.035
48	6.64×10^4	4.52	0.34	0.06	0.25	0.125	6.734	0.962
49	6.64×10^5	4.52	0.34	0.06	0.25	0.125	12.942	1.0
50	6.64×10^6	4.52	0.34	0.06	0.25	0.125	27.153	1.106
51	1.69×10^6	0.72	0.4	0.12	0.25	0	9.743	1.0
52	1.90×10^6	0.72	0.4	0.12	0.25	0	10.047	1.001

Table 12. Results for the Cases Run for Enclosures with Rectangular Roughness Elements that Do Not Contain the Same Amounts of Fluid As the Corresponding Smooth-Walled Enclosures

Case No.	Gr_H	Pr	W/H	A	δ	δ_0	$(\overline{Nu})_R$	$\frac{(\overline{Nu})_R}{(\overline{Nu})_S}$	%Reduction in the Volume of Fluid
53	4.07×10^3	4.52	0.4	0.06	0.25	0.125	3.453	1.146	15.0
54	4.07×10^4	4.52	0.4	0.06	0.25	0.125	5.779	0.950	15.0
55	4.07×10^5	4.52	0.4	0.06	0.25	0.125	11.230	0.991	15.0
56	4.07×10^6	4.52	0.4	0.06	0.25	0.125	23.130	1.069	15.0

of fluid in these enclosures with respect to the corresponding smooth-walled enclosures.

Cases 28, 34, 40 and 45 were all calculated for flows in water (Pr = 4.52) in an enclosure with an aspect ratio, W/H, of 0.4, four rectangular roughness elements ($\delta = 0.25$) with an amplitude, A, of 0.12 and a roughness element array phase shift, δ_0, of 0. (This is the equivalent enclosure with rectangular roughness elements to the enclosure examined in cases 19, 20, 21 and 22 that contained sinusoidal roughness elements except that $\delta_0 = 0$ for the former enclosure and $\phi = 0$ for the later enclosure.) The effects of increasing the Grashof number from 4.07 x 10^3 to 4.07 x 10^6 on the ratio of overall Nusselt numbers, $(\overline{Nu})_R/(\overline{Nu})_S$, for these four flows is shown in Figure 31. This figure shows that: (1) over the range of Grashof numbers investigated, the ratio of Nusselt numbers, $(\overline{Nu})_R/(\overline{Nu})_S$, first decreases and then increases with increasing Grashof number, (2) for all Grashof numbers, except those in the range from approximately 2 x 10^4 to 4 x 10^5, the elements enhance the heat transfer across the enclosure, (3) only in this range of Grashof numbers do the elements decrease the rate of heat transfer, (4) at Grashof numbers below the range in which the elements decrease the heat transfer, the enhancement can be fairly substantial, with the ratio of Nusselt numbers, $(\overline{Nu})_R/(\overline{Nu})_S$, achieving a maximum value of 1.148 at the lowest Grashof number of 4.07 x 10^3, (5) for Grashof numbers above this range, the enhancement of the heat transfer by the elements is of the same magnitude as that for Grashof numbers below this range, with a maximum value of the ratio $(\overline{Nu})_R/(\overline{Nu})_S$ of 1.124 being obtained at the highest Grashof number of 4.07 x 10^6. This behavior is qualitatively identical to that portrayed in Figure 27 for the corresponding flows in an enclosure that is geometrically similar to the enclosure being considered here, except that it contains sinusoidal roughness elements with a phase angle,

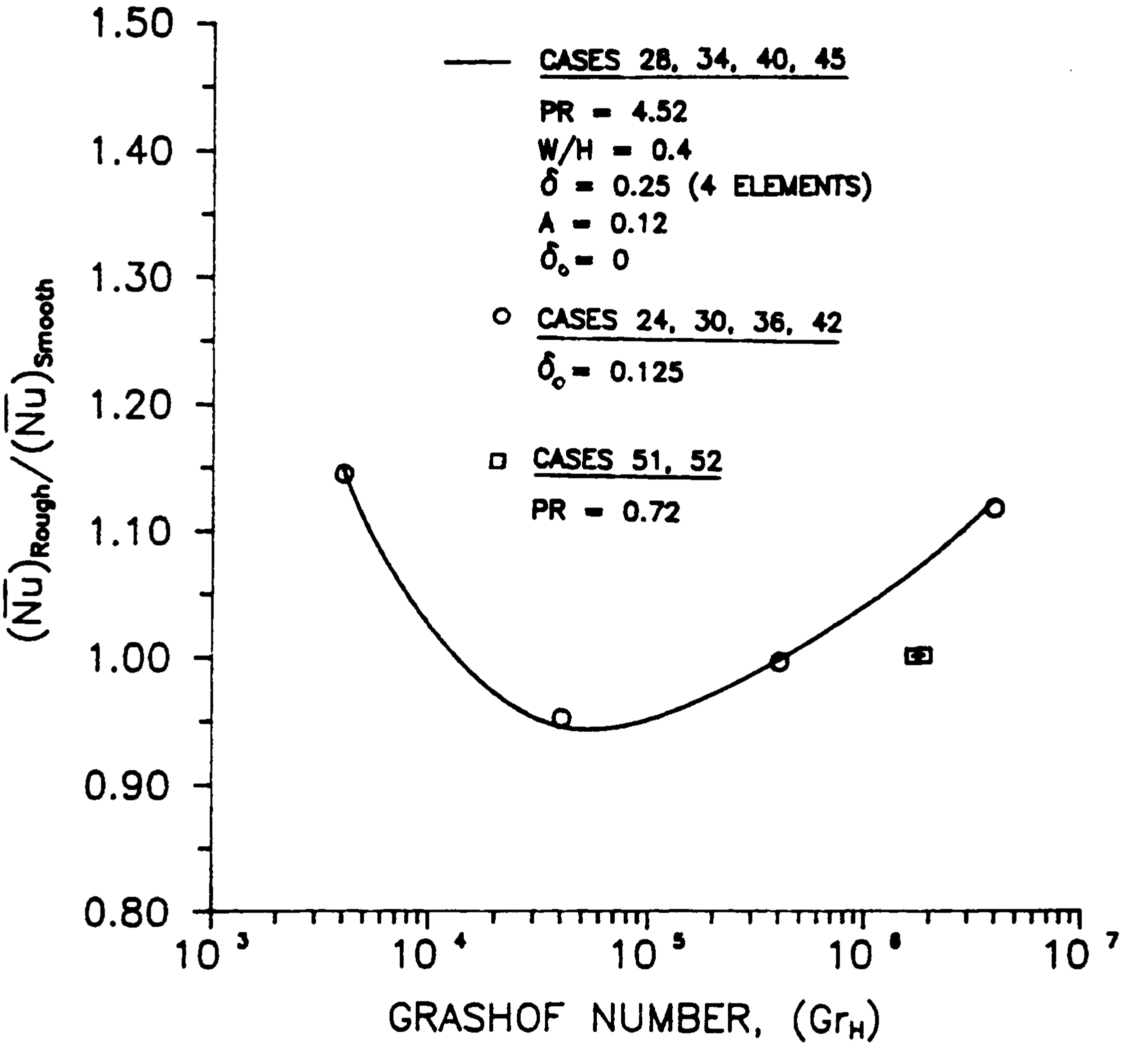

Figure 31. The Effects of Grashof Number, Phase Shift, and Prandtl Number on the Ratio of Nusselt Numbers for Flows in an Enclosure With an Aspect Ratio of W/H = 0.4 and Containing Rectangular Roughness Elements

$\phi = 0$. The enhancement was much higher (1.355, as opposed to 1.124); however, for the flow in the enclosure with sinusoidal roughness elements.

The streamlines, isotherms and heat lines for each of the flows in cases 28, 34, 40 and 45 are presented in Figures 32-35, respectively. These plots clearly show that: (1) the flows at Grashof numbers of 4.07×10^3 (case no. 28) and 4.07×10^4 (case no. 34) are in a conduction regime, (2) the flow at a Grashof number of 4.07×10^5 (case no.40) is in a transition regime, and (3) the flow at a Grashof number of 4.07×10^6 (case no. 45) is in a boundary-layer regime. This trend with increasing Grashof numbers for the flows to progress from a conduction regime, through a transition regime, to a boundary-layer regime is also indicated by the horizontal temperature distributions across the plane at $y^*/H = 0.55$ in the flows in cases 28, 34, 40 and 45, as shown in Figure 36.

Recall that the isotherm plot shown in Figure 29(b) for the corresponding flow at a Grashof number of 4.07×10^6 (case no. 22) in an enclosure with <u>sinusoidal</u> roughness elements showed local decreases in the thermal boundary layer thickness on the <u>cold</u> wall in the regions opposite the uppermost three elements on the hot wall. As is evident in Figure 35, no such decreases in the thickness of the thermal boundary layer on the cold wall occur in the corresponding flow of case no. 45 for rectangular roughness elements. This difference between these two flows in enclosures with sinusoidal and rectangular roughness elements may also be observed in Figure 37, which does not reveal any local increases in the Nusselt number in regions on the cold wall opposite the rectangular elements on the hot wall.

The local Nusselt number distribution along the hot vertical wall for the flow in case no. 45 ($Gr = 4.07 \times 10^6$) is presented in Figure 38. This figure shows that: (1) the largest rates of heat transfer from the hot wall occur near the tips of

Case No. 28

$Gr = 4.07 \times 10^3$ $Pr = 4.52$ $W/H = 0.4$ $\delta = 0.25$ $A = 0.12$ $\delta_0 = 0$ $(\overline{Nu})_R = 3.458$ $(\overline{Nu})_R/(\overline{Nu})_S = 1.148$

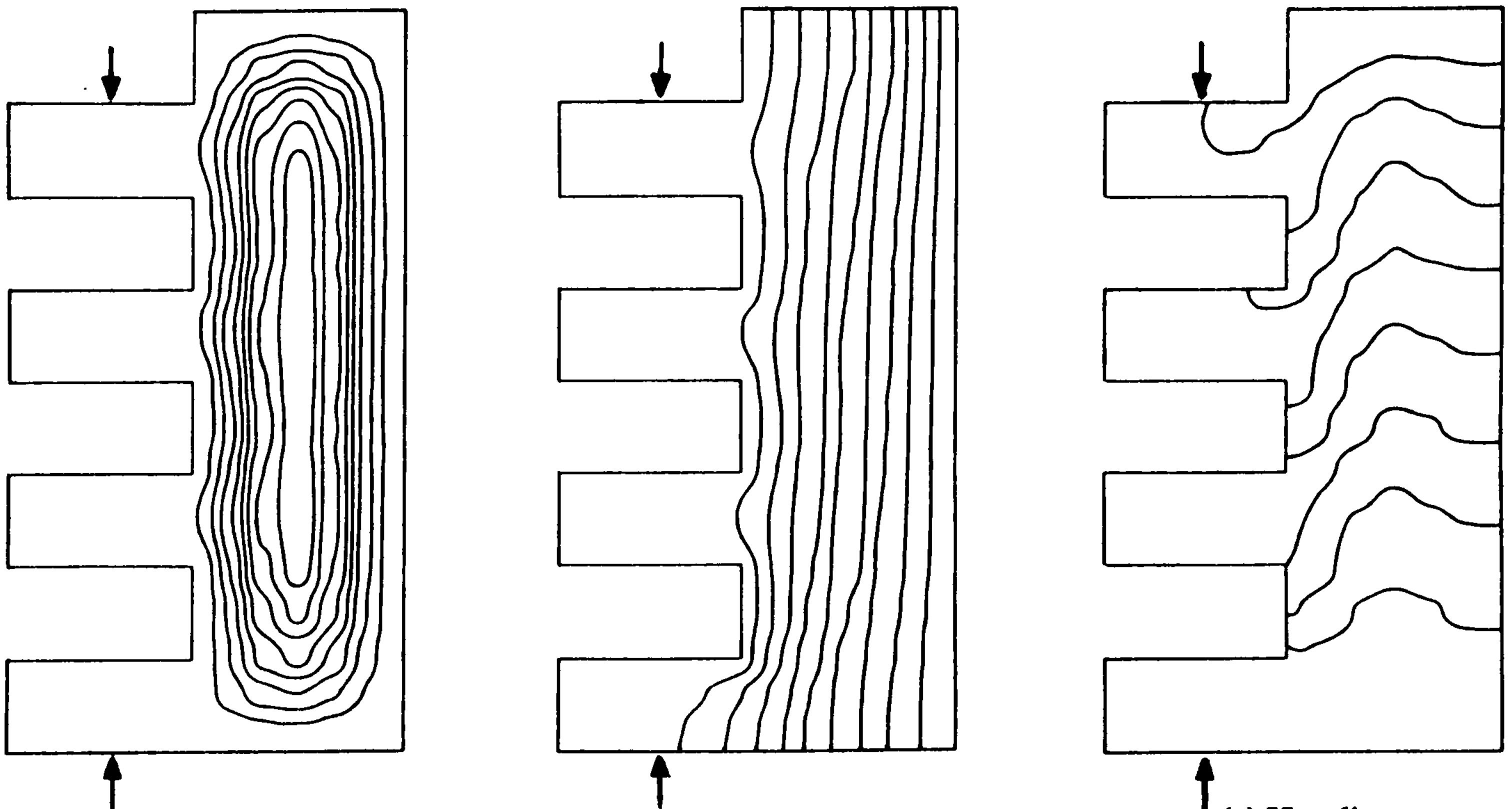

(a) Streamlines (b) Isotherms (c) Heat lines

[Arrows Denote the Location of the Hot Wall in the Corresponding Smooth-Walled Enclosure]

Figure 32. Computed Streamlines, Isotherms, and Heat Lines in an Enclosure With an Aspect Ratio of W/H = 0.4 that Contains Rectangular Wall Roughness Elements (Case No. 28)

Case No. 34

$Gr = 4.07 \times 10^4$ $Pr = 4.52$ $W/H = 0.4$ $\delta = 0.25$ $A = 0.12$ $\delta_0 = 0$ $\overline{(Nu)}_R = 5.748$ $\overline{(Nu)}_R/\overline{(Nu)}_S = 0.945$

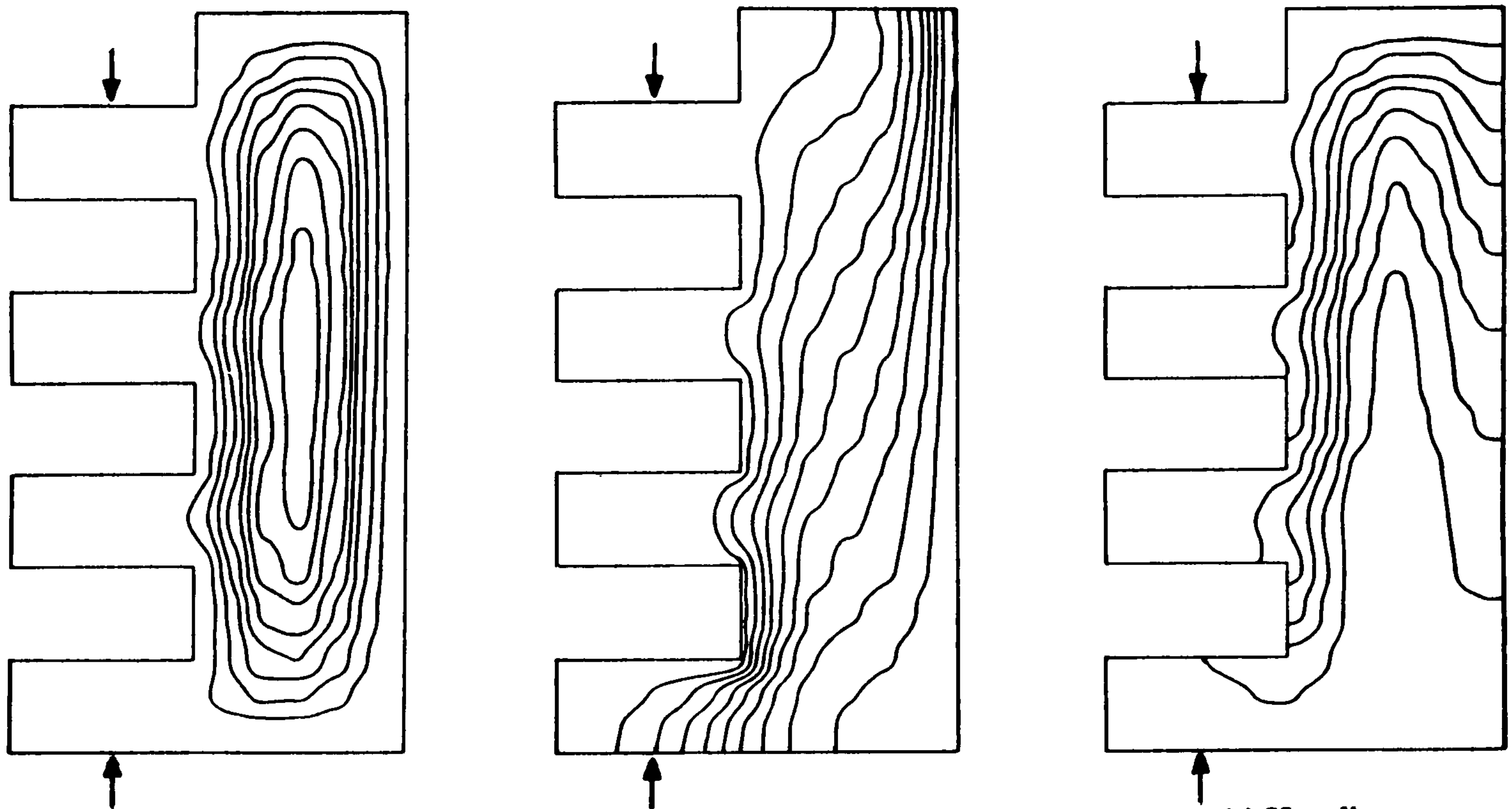

(a) Streamlines (b) Isotherms (c) Heat lines

[Arrows Denote the Location of the Hot Wall in the Corresponding Smooth-Walled Enclosure]

Figure 33. Computed Streamlines, Isotherms, and Heat Lines in an Enclosure With an Aspect Ratio of W/H = 0.4 that Contains Rectangular Wall Roughness Elements (Case No. 34)

Case No. 40

$Gr = 4.07 \times 10^5$ $Pr = 4.52$ $W/H = 0.4$ $\delta = 0.25$ $A = 0.12$ $\delta_0 = 0$ $\overline{(Nu)}_R = 11.311$ $\overline{(Nu)}_R/\overline{(Nu)}_S = 0.998$

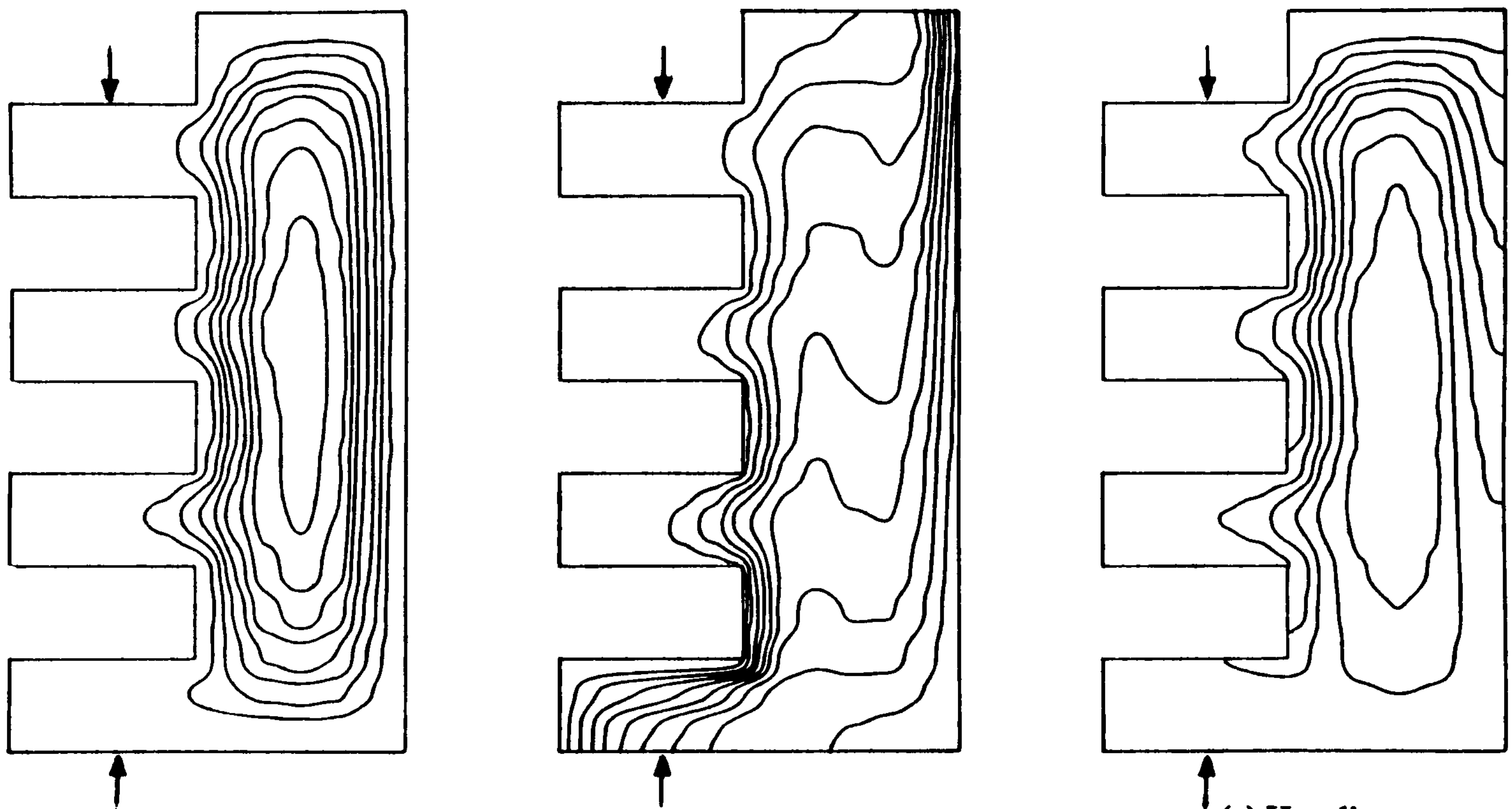

(a) Streamlines (b) Isotherms (c) Heat lines

[Arrows Denote the Location of the Hot Wall in the Corresponding Smooth-Walled Enclosure]

Figure 34. Computed Streamlines, Isotherms, and Heat Lines in an Enclosure With an Aspect Ratio of W/H = 0.4 that Contains Rectangular Wall Roughness Elements (Case No. 40)

<u>Case No. 45</u>

$Gr = 4.07 \times 10^6$ $Pr = 4.52$ $W/H = 0.4$ $\delta = 0.25$ $A = 0.12$ $\delta_0 = 0$ $\overline{(Nu)}_R = 24.314$ $\overline{(Nu)}_R/\overline{(Nu)}_S = 1.124$

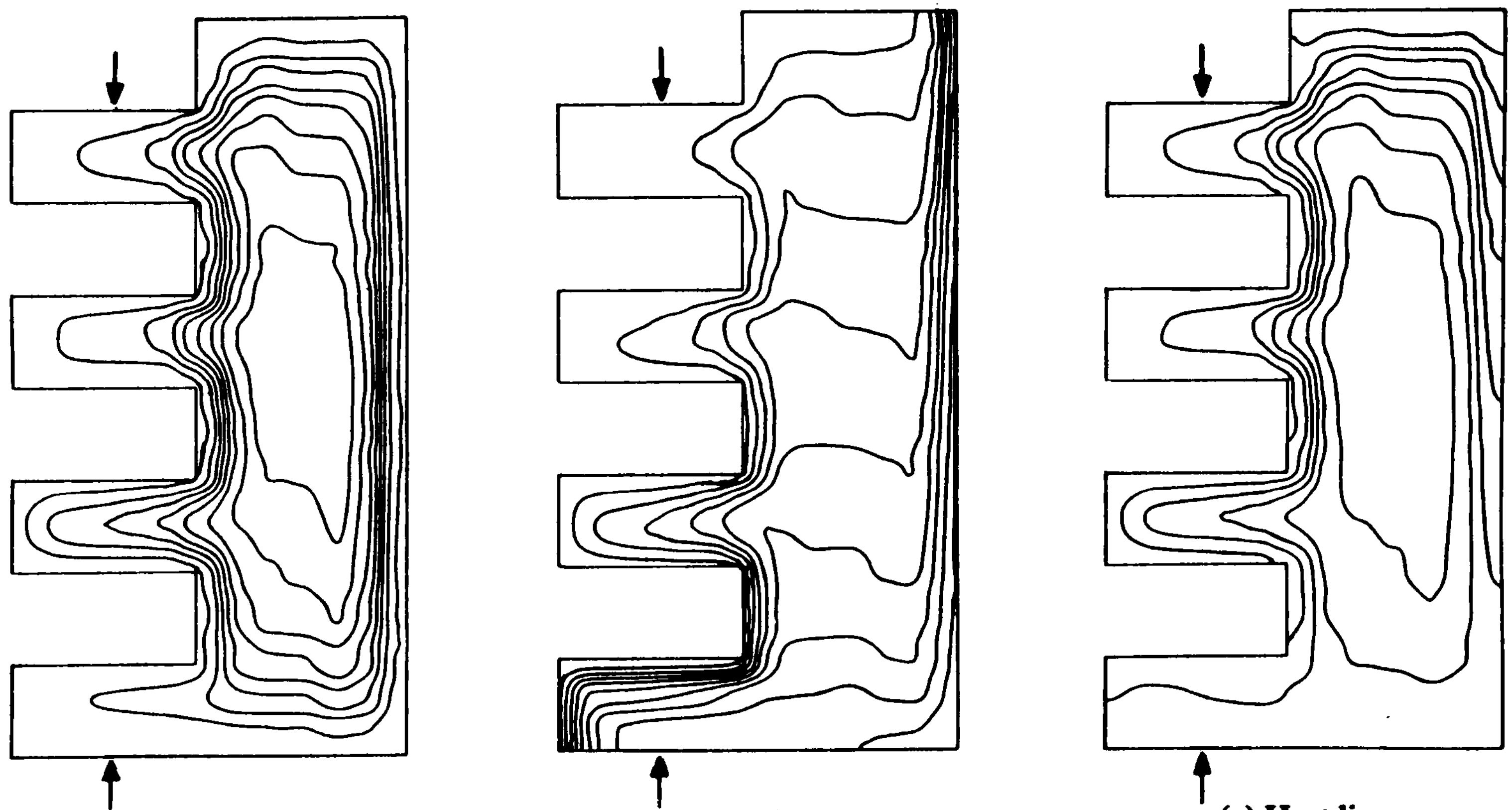

(a) Streamlines (b) Isotherms (c) Heat lines

[Arrows Denote the Location of the Hot Wall in the Corresponding Smooth-Walled Enclosure]

Figure 35. Computed Streamlines, Isotherms, and Heat Lines in an Enclosure With an Aspect Ratio of W/H = 0.4 that Contains Rectangular Wall Roughness Elements (Case No. 45)

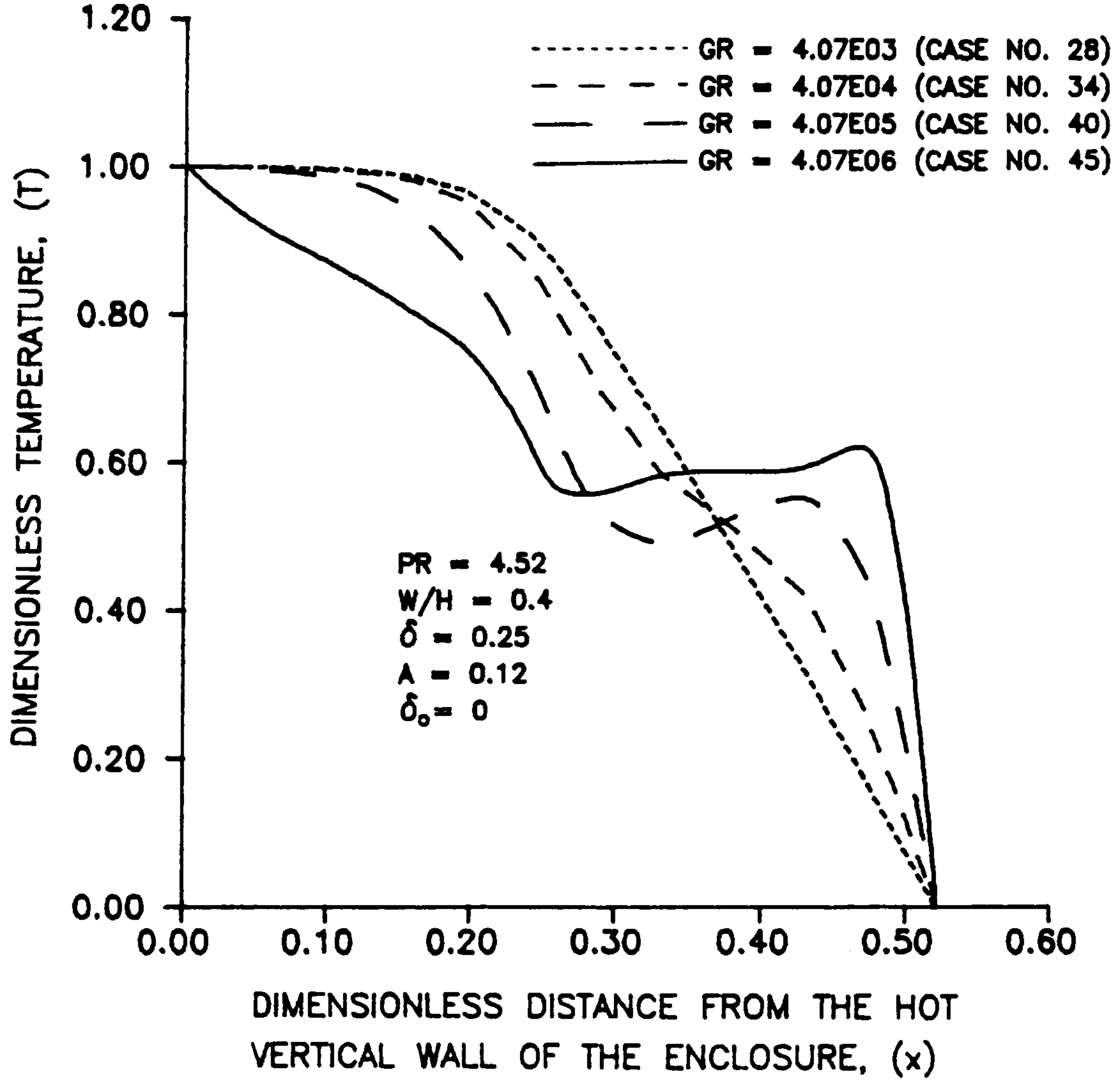

Figure 36. The Effect of Grashof Number on the Horizontal Temperature Distribution at $y^*/H = 0.55$ in an Enclosure With Rectangular Roughness Elements

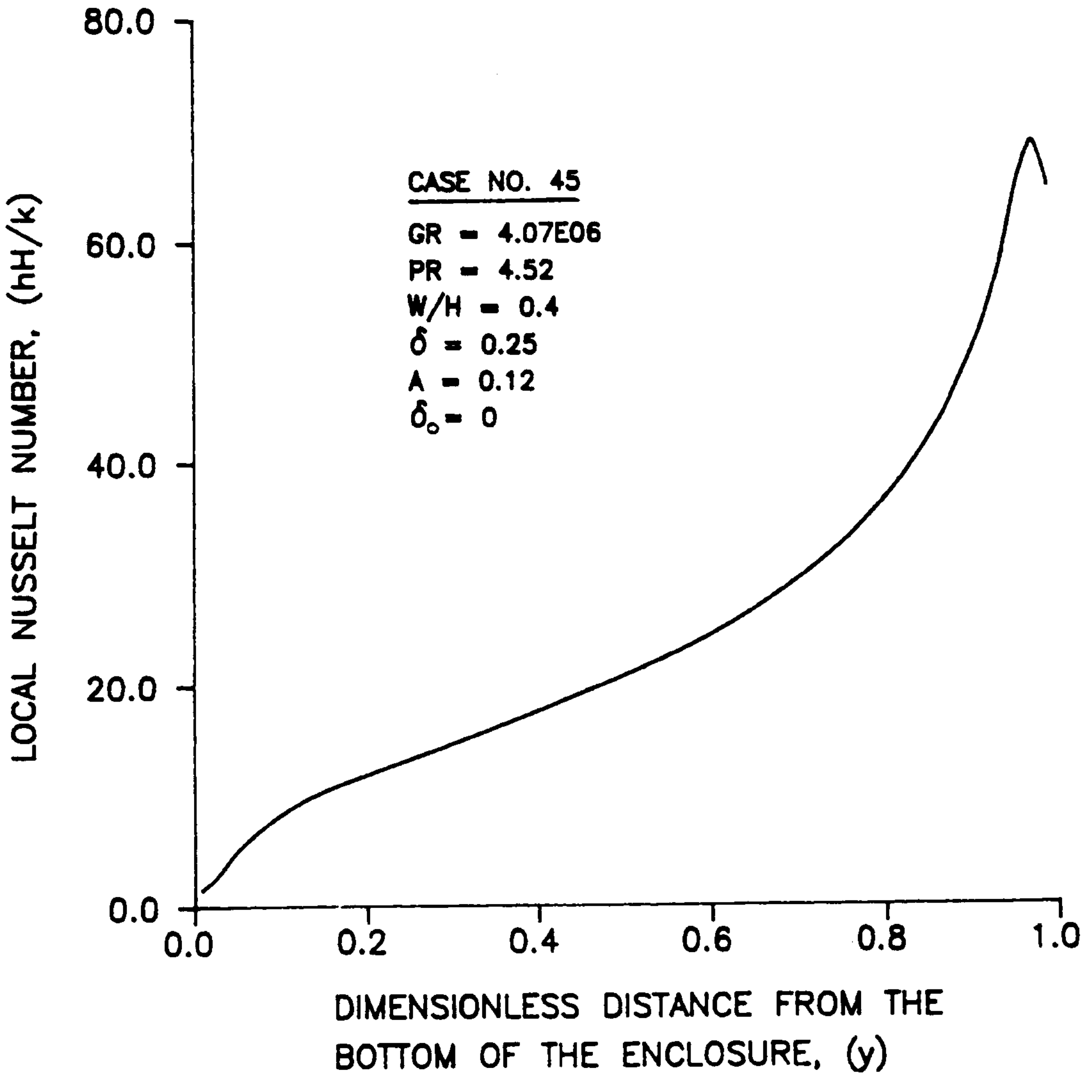

Figure 37. Local Nusselt Number Distribution Along the Cold Wall of an Enclosure With Rectangular Roughness Elements (Case No. 45)

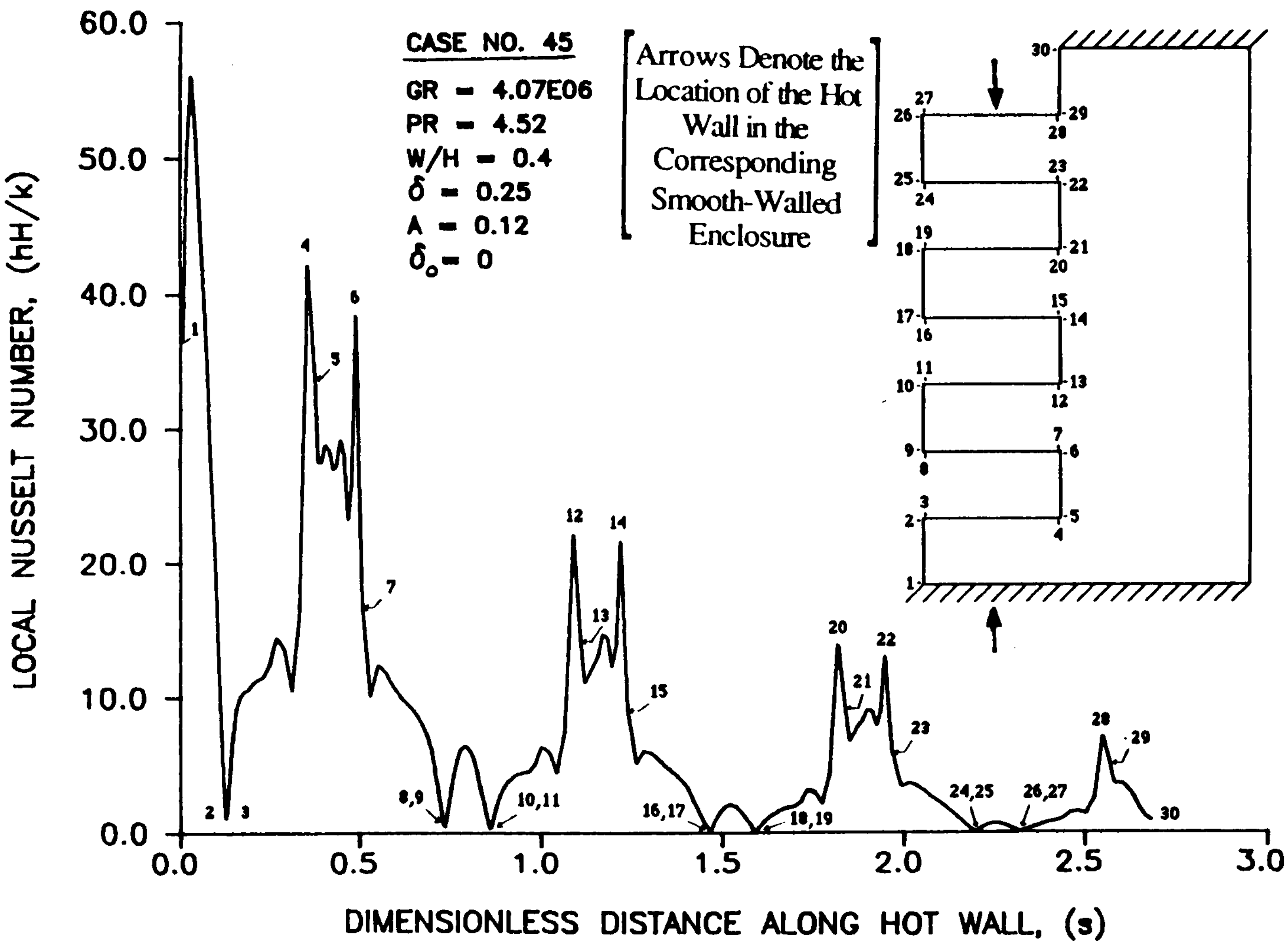

Figure 38. Local Nusselt Number Distribution Along the Hot Wall of an Enclosure With Rectangular Roughness Elements (Case No. 45)

the roughness elements, and (2) the rate of heat transfer from each roughness element decreases rapidly as the flow proceeds up the wall, which suggests that (as with the sinusoidal elements) only the lower elements may play an important role in altering the rate of heat transfer from the hot wall. Note, however, that the upper elements in the sinusoidal array were shown to change the rate of heat transfer on the cold vertical wall.

The flows in cases 51 and 52 were computed for the same enclosure as the enclosure used in cases 28, 34, 40 and 45; however, these flows were assumed to take place in air (Pr = 0.72), instead of water. The ratios of overall Nusselt numbers for cases 51 and 52 are also plotted in Figure 31, where they are denoted by the square plotting symbols. These results show that: (1) there are essentially no changes in the rates of heat transfer in these flows from those in the corresponding smooth-walled enclosures [$(\overline{Nu})_R/(\overline{Nu})_S \approx 1.0$], and (2) there is a significant Prandtl number effect on the heat transfer enhancement by the roughness elements, at least at these two Grashof numbers (1.69×10^6 and 1.90×10^6) in the boundary-layer flow regime. (The curve in Figure 31 shows that $(\overline{Nu})_R/(\overline{Nu})_S \approx$ 1.08 at these Grashof numbers for a Prandtl number of 4.52.)

The effect of changing the dimensionless phase shift of the roughness element array, δ_0, on the ratio $(\overline{Nu})_R/(\overline{Nu})_S$ is also shown in Figure 31. The enclosures in cases 24, 30, 36 and 42 are identical to those in cases 28, 34, 40 and 45, respectively, except that the ;latter four cases were calculated for $\delta_0 = 0$, while the former four cases were calculated for $\delta_0 = 0.125$. The Nusselt number ratios for cases 24, 30, 36 and 42, which are denoted in Figure 31 by the round plotting symbols, are virtually identical to those for cases 28, 34, 40 and 45, respectively. Thus, at least in the limited range of values considered here (0 - 0.125), there is a negligible effect of the phase shift of the roughness element array, δ_0, on the ratio of Nusselt numbers, $(\overline{Nu})_R/(\overline{Nu})_S$.

The effect of varing the dimensionless amplitude of the roughness elements, A (= A*/H), on the ratio of Nusselt numbers, $(\overline{Nu})_R/(\overline{Nu})_S$, is shown in Figure 39. The solid curve in this figure portrays the effect of changing the Grashof number on the ratio of Nusselt numbers for flows in water (Pr = 4.52) in an enclosure that has an aspect ratio, W/H, of 0.4, 4 roughness elements in the hot wall (δ = 0.25), a dimensionless element amplitude, A, of 0.12, and a dimensionless element array phase shift, δ_0, of 0.125. This curve was constructed using the results of cases 24, 30, 36 and 42. The analogous results for flows in water in an identical enclosure, except that A = 0.06 instead of 0.12 , are given by the dashed curve in Figure 39, which was constructed using the results of cases 25, 31, 37 and 43. Comparison of these two curves show that over the range of Grashof numbers considered, that decreasing the amplitude, A, of the elements from 0.12 to 0.06: (1) drastically reduces the enhancement of the heat transfer in the conduction regime, (2) broadens the range of Grashof numbers in the transition regime in which the elements reduce the heat transfer, and (3) reduces the heat transfer enhancement by the elements in the boundary-layer regime. Although only two amplitudes were considered, these results lead to the conclusion that increasing the amplitude of the elements (A) increases the enhancement of the heat transfer in both the conduction and the boundary-layer flow regimes and decreases the range of Grashof numbers in the transition regime in which the elements reduce the heat transfer.

The effects of varing the aspect ratio of the enclosure, W/H, on the ratio of Nusselt numbers, $(\overline{Nu})_R/(\overline{Nu})_S$, is also shown in Figure 39. The four data points represented by the circular plotting symbols are for cases 47-50, which are flows in water in an enclosure that is identical to that in cases 25, 31, 37 and 43, except

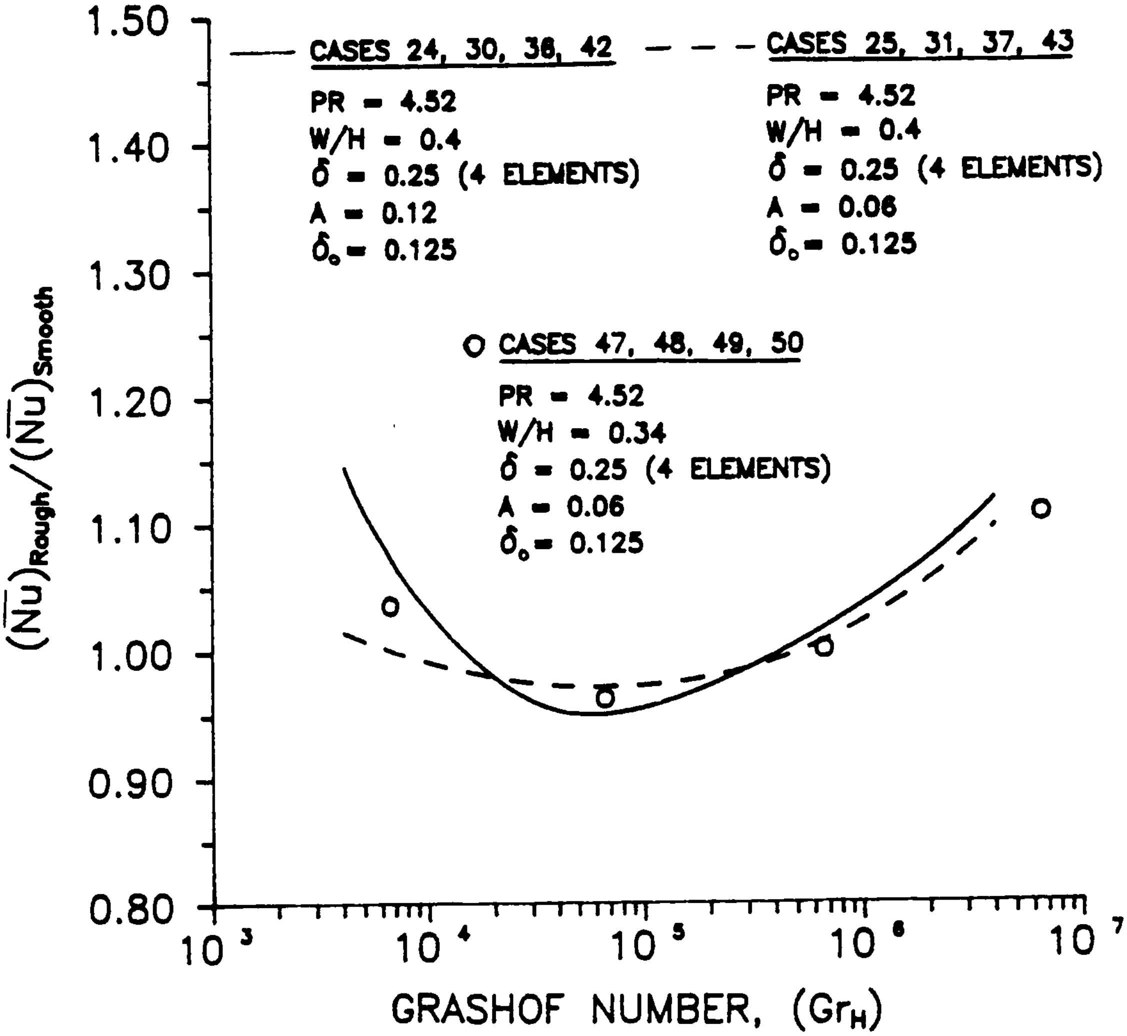

Figure 39. The Effects of Grashof Number, Roughness Element Amplitude, and Enclosure Aspect Ratio on the Ratio of Nusselt Numbers for an Enclosure With Four Rectangular Roughness Elements

that the aspect ratio has been reduced from 0.4 to 0.34. Thus, these four data points should be compared with the dashed curve in Figure 39. This comparison shows that decreasing the aspect ratio, W/H, from 0.4 to 0.34: (1) slightly increases the enhancement of the heat transfer in the conduction regime, and (2) yields approximately the same enhancement of the heat transfer in the boundary-layer regime and the same reduction of heat transfer in the transition regime.

As was pointed out in Chapter 2, wall roughness elements were added to enclosures in this study in a manner such that the volume of fluid in an enclosure with roughness elements was identical to the volume of fluid in the corresponding smooth-walled enclosure. If the rough-walled enclosures were not designed in this manner and the elements were merely mounted on the hot wall of the smooth-walled enclosure, the amount of fluid in the enclosure would be reduced. In this case it would be impossible to determine whether it was an alteration of the flow in the enclosure by the elements, or the decrease of the amount of fluid in the enclosure due to the addition of the roughness elements, or both of these effects, that caused any change in the rate of heat transfer across the enclosure. As will be shown here, this effect, which has been ignored by other investigators, can be quite important. Cases 53-56 were executed to investigate this effect. All of the dimensionless parameters for these flows are identical to those for the flows examined in cases 25, 31 37 and 43; that is, $Pr = 4.52$, $W/H = 0.4$, $A = 0.06$, $\delta = 0.25$ and $\delta_0 = 0.125$. The enclosures for cases 53-56, however, were designed by mounting the roughness elements on the hot wall of the corresponding smooth-walled enclosure such that the volume of fluid in these enclosures is reduced from that in cases 25, 31, 37 and 43 by 15%. This is illustrated for cases 53 and 56 in Figures 40 and 41, respectively, in which the arrows denote the location of the hot wall in the corresponding smooth-walled enclosure. The ratio of Nusselt numbers,

Case No. 53

$Gr = 4.07 \times 10^3$ $Pr = 4.52$ $W/H = 0.4$ $\delta = 0.25$ $A = 0.06$ $\delta_0 = 0.125$ $\overline{(Nu)}_R = 3.453$ $\overline{(Nu)}_R/\overline{(Nu)}_S = 1.146$

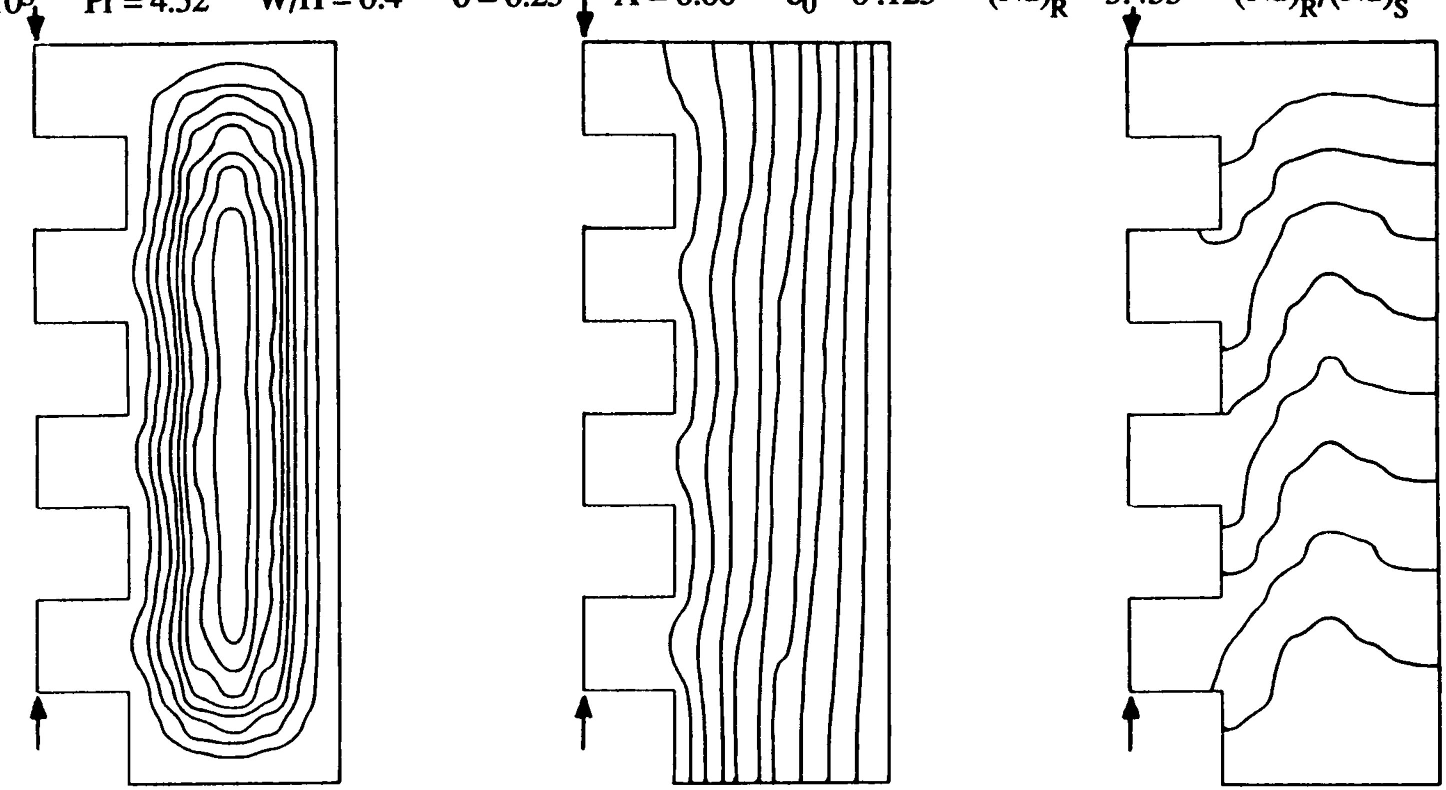

(a) Streamlines (b) Isotherms (c) Heat lines

[Arrows Denote the Location of the Hot Wall in the Corresponding Smooth-Walled Enclosure]

Figure 40. Computed Streamlines, Isotherms, and Heat Lines in a Rough-Walled Enclosure that Contains 15% Less Fluid than the Corresponding Smooth-Walled Enclosure (Case No. 53)

Case No. 56

$Gr = 4.07 \times 10^6$ $Pr = 4.52$ $W/H = 0.4$ $\delta = 0.25$ $A = 0.06$ $\delta_0 = 0.125$ $(\overline{Nu})_R = 23.13$ $(\overline{Nu})_R/(\overline{Nu})_S = 1.069$

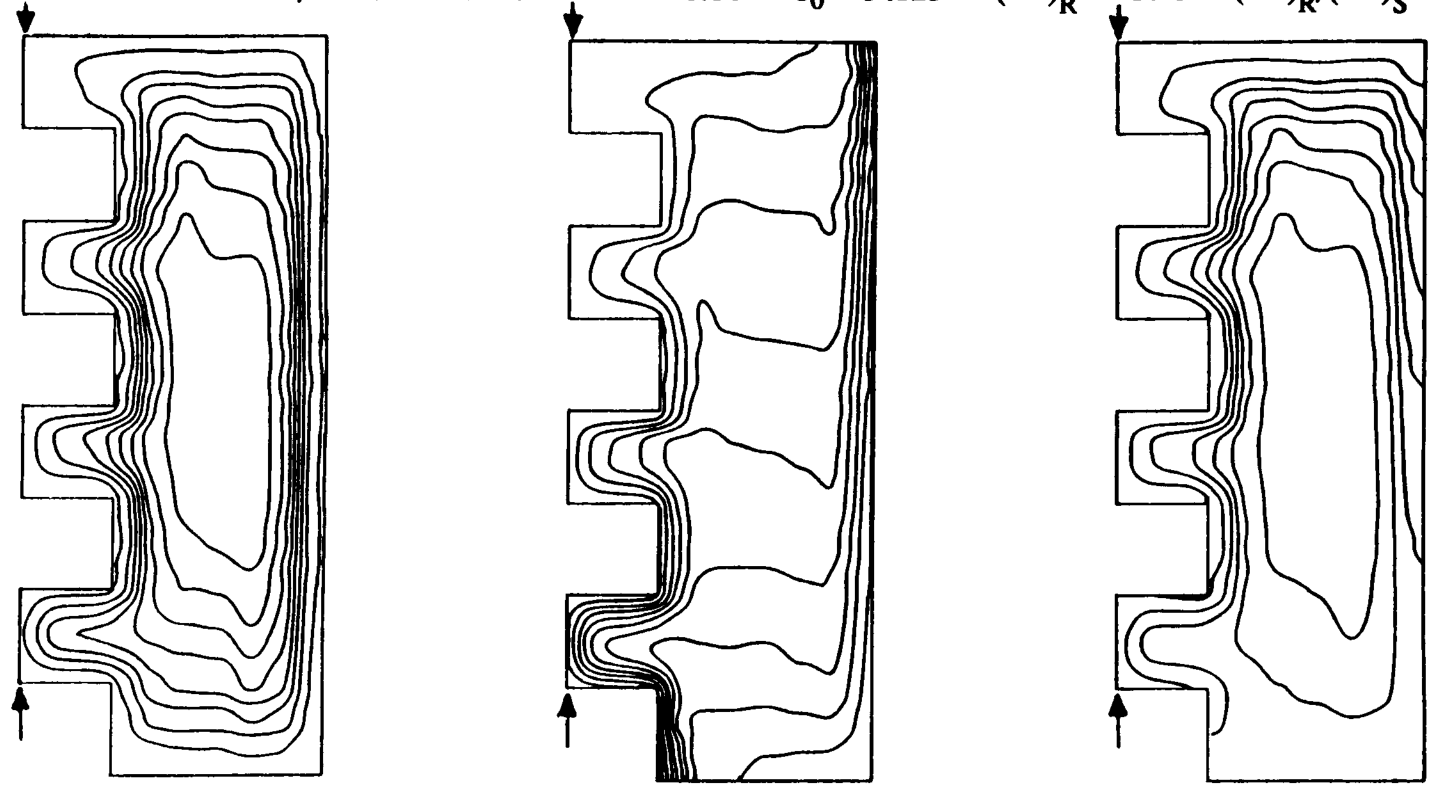

(a) Streamlines (b) Isotherms (c) Heat lines

[Arrows Denote the Location of the Hot Wall in the Corresponding Smooth-Walled Enclosure]

Figure 41. Computed Streamlines, Isotherms, and Heat Lines in a Rough-Walled Enclosure that Contains 15% Less Fluid than the Corresponding Smooth-Walled Enclosure (Case No. 56)

$\overline{(Nu)}_R/\overline{(Nu)}_S$, as a function of Grashof number for cases 25, 31, 37 and 43 is given by the solid curve in Figure 42. The dashed curve in Figure 42 is the analogous result for cases 53-56 in which the volume of fluid in the enclosure is reduced by 15%. Comparison of these two curves shows that adding roughness elements such that the volume of fluid is reduced causes: (1) a substantial increase in the heat transfer enhancement in the conduction regime, (2) only minor changes in the decrease in the heat transfer due to adding the elements in the transition regime, and (3) slight reductions of the heat transfer enhancement in the boundary-layer regime.

All of the cases in the parametric study for rectangular roughness elements that are discussed above are for flows in enclosures with 4 elements ($\delta = 0.25$). The effects of changing the period of the roughness element array, δ, from 0.25 to 0.5; that is, of reducing the number of elements from 4 to 2, will now be discussed. Eleven cases (26, 27, 29, 32, 33, 35, 38, 39, 41, 44 and 46) were executed to investigate these effects. The results of these cases are presented in Table 11 and in Figures 43-47.

Curve A in Figure 43 was constructed using the results of cases 29, 35, 41 and 46. The flows in these cases take place in water ($Pr = 4.52$) in enclosures for which $W/H = 0.4$, $\delta = 0.5$ (2 elements), $A = 0.12$ and $\delta_0 = 0$. Curve A will be compared with curve C (the dashed curve); which is for the flows in cases 28, 34, 40 and 45 that also take place in water and in an enclosure geometry that is identical to the flows of curve A, except that the period of the roughness element array, δ, is 0.25 (4 elements) instead of 0.5 (2 elements). Curve A shows that increasing δ from 0.25 to 0.5: (1) reduces the enhancement of the heat transfer [reduces $\overline{(Nu)}_R/\overline{(Nu)}_S$] in the conduction regime, (2) narrows the range of Grashof numbers in the transition regime in which the elements decrease the heat transfer

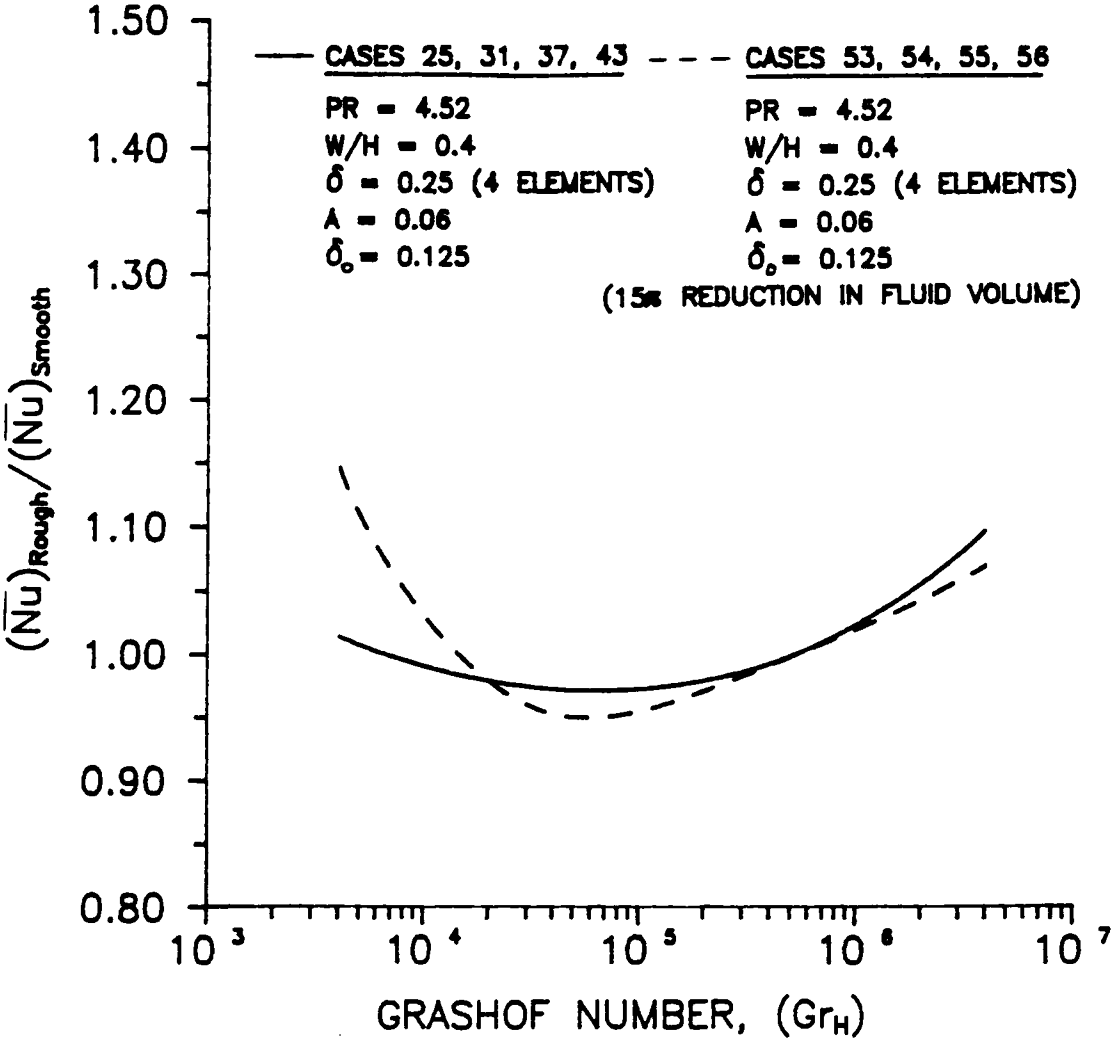

Figure 42. The Effect of Adding Wall Roughness Elements in a Manner Such that the Volume of Fluid in the Enclosure is Reduced

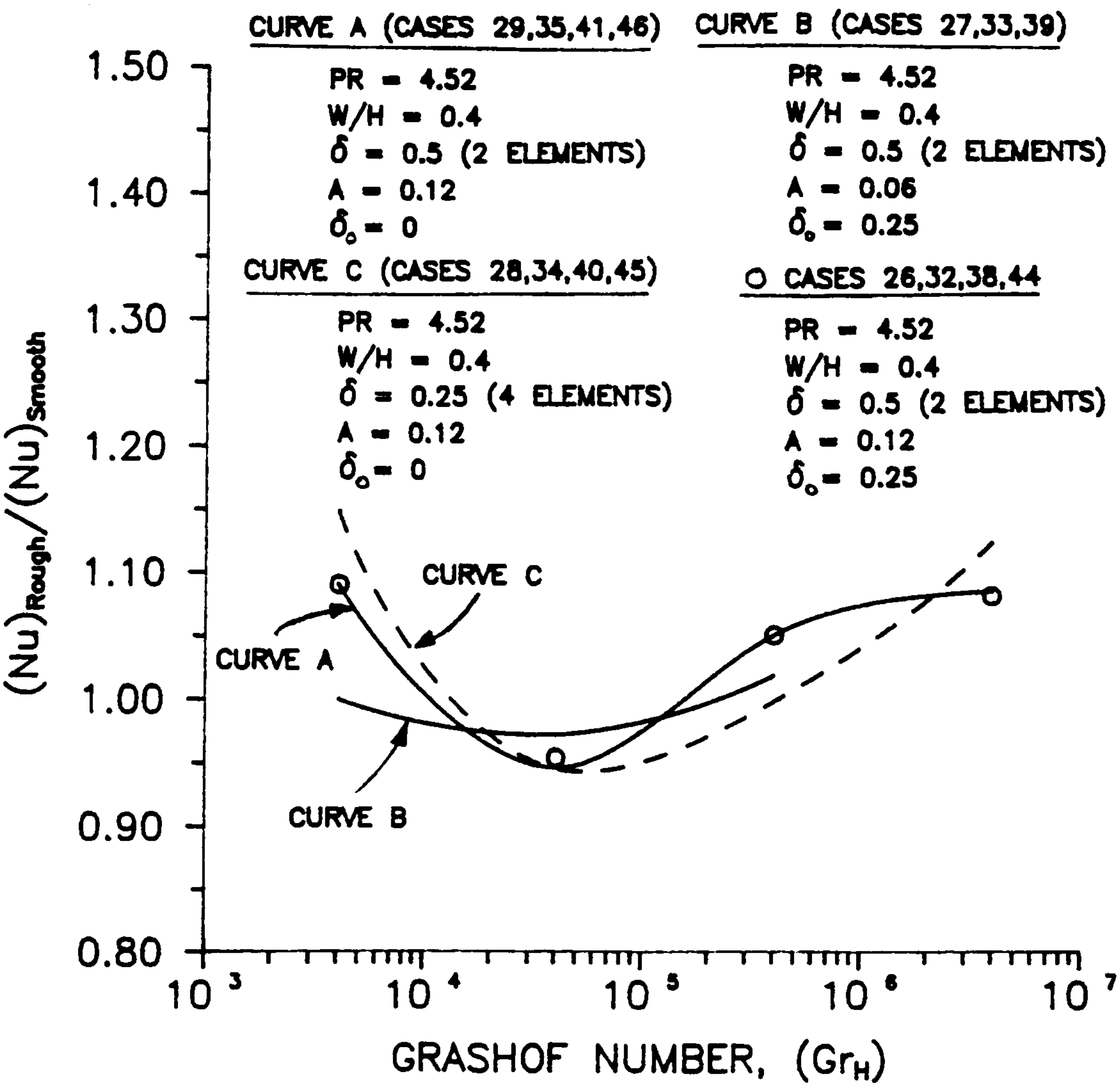

Figure 43. The Effects of Grashof Number, Period and Phase Shift of the Roughness Element Array, and Element Amplitude on the Ratio of Nusselt Numbers for an Enclosure With Two Rectangular Roughness Elements

Case No. 29

$Gr = 4.07 \times 10^3$ $Pr = 4.52$ $W/H = 0.4$ $\delta = 0.5$ $A = 0.12$ $\delta_0 = 0$ $\overline{(Nu)}_R = 3.285$ $\overline{(Nu)}_R/\overline{(Nu)}_S = 1.09$

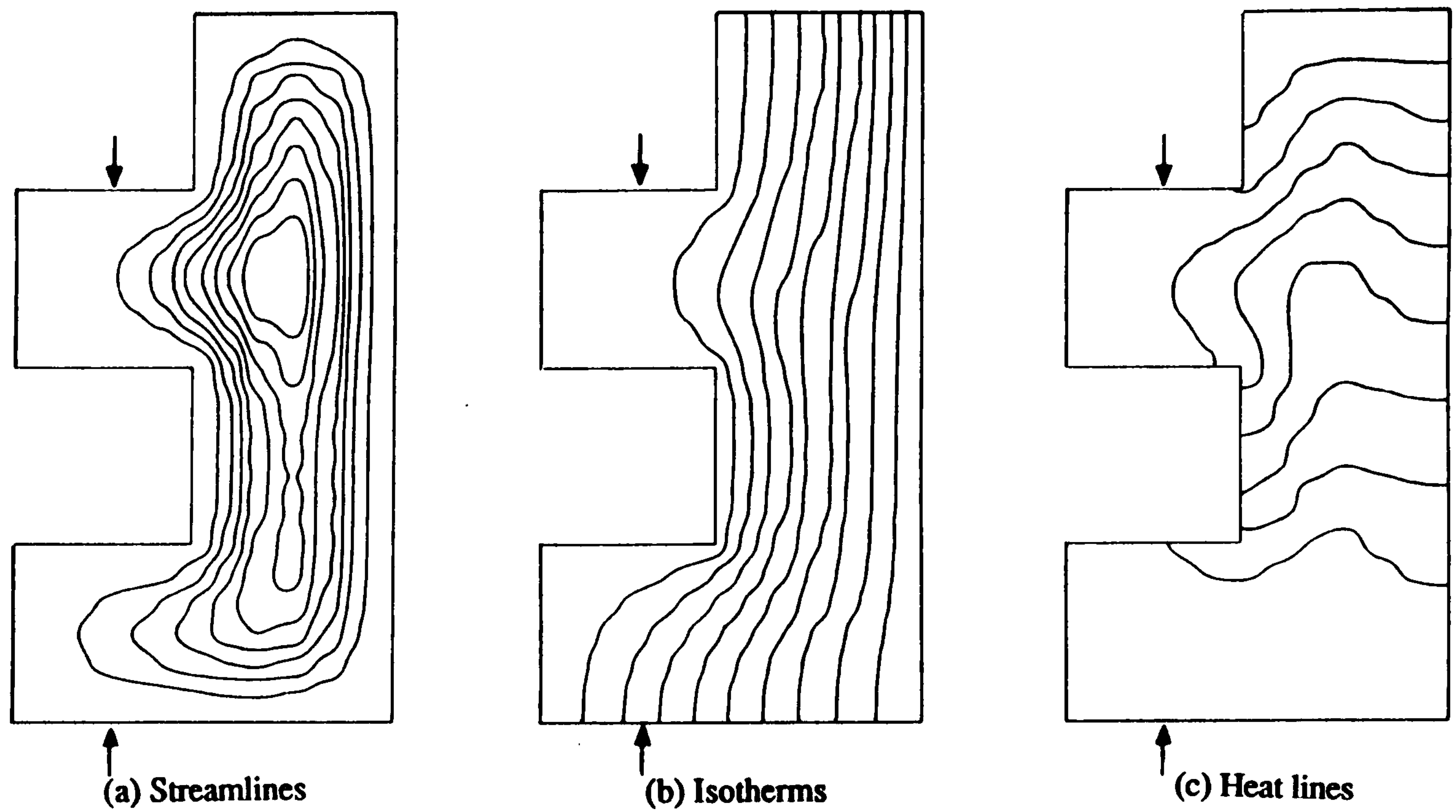

[Arrows Denote the Location of the Hot Wall in the Corresponding Smooth-Walled Enclosure]

Figure 44. Computed Streamlines, Isotherms, and Heat Lines in an Enclosure With an Aspect Ratio of $W/H = 0.4$ that Contains Two Rectangular Wall Roughness Elements ($\delta = 0.5$) [Case No. 29]

Case No. 46

$Gr = 4.07 \times 10^6$ $Pr = 4.52$ $W/H = 0.4$ $\delta = 0.5$ $A = 0.12$ $\delta_0 = 0$ $\overline{(Nu)}_R = 23.479$ $\overline{(Nu)}_R / \overline{(Nu)}_S = 1.085$

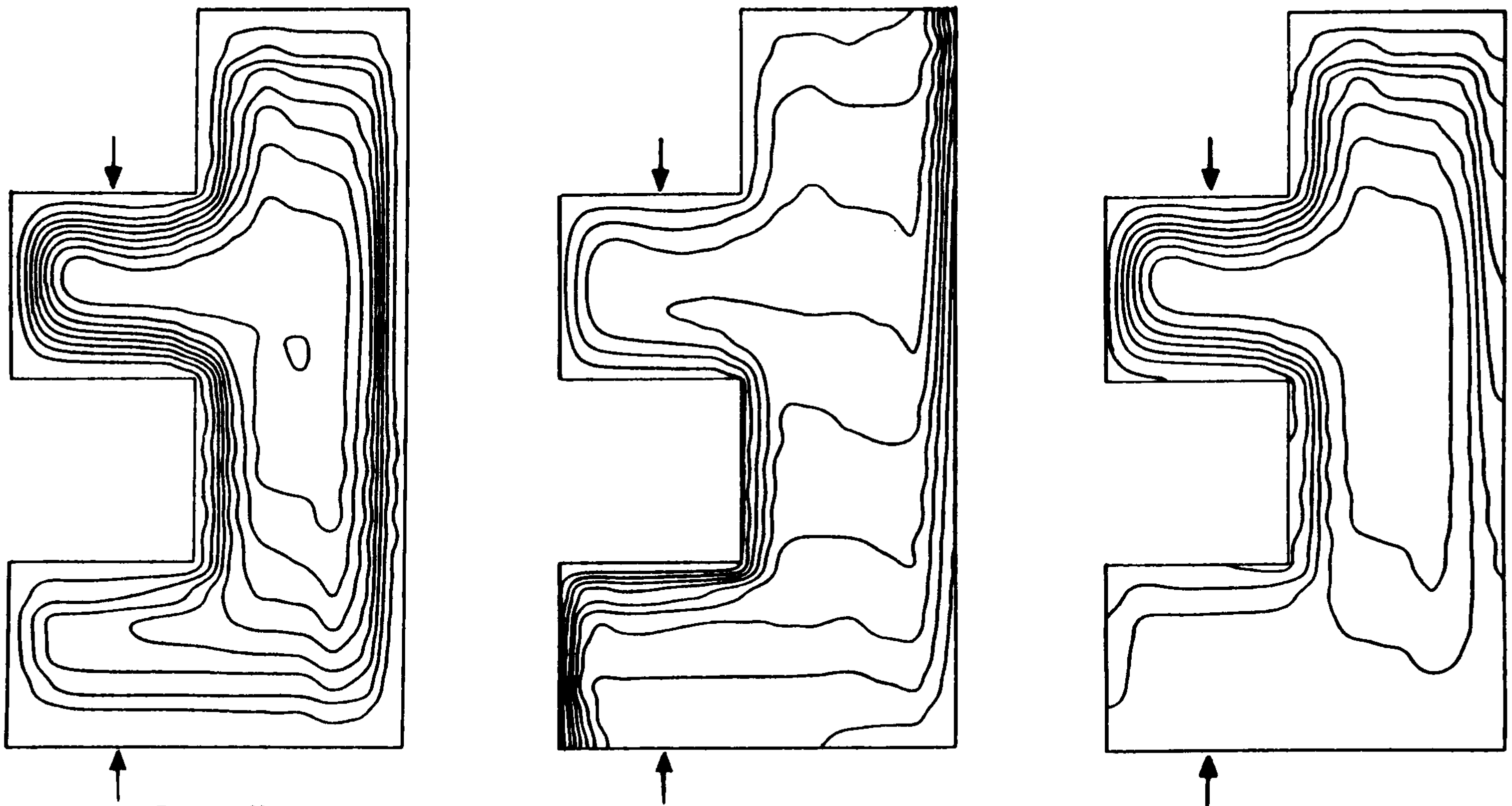

(a) Streamlines (b) Isotherms (c) Heat lines

[Arrows Denote the Location of the Hot Wall in the Corresponding Smooth-Walled Enclosure]

Figure 45. Computed Streamlines, Isotherms, and Heat Lines in an Enclosure With an Aspect Ratio of W/H = 0.4 that Contains Two Rectangular Wall Roughness Elements ($\delta = 0.5$) [Case No. 46]

Case No. 26

$Gr = 4.07 \times 10^3$ $Pr = 4.52$ $W/H = 0.4$ $\delta = 0.5$ $A = 0.12$ $\delta_0 = 0.25$ $\overline{(Nu)}_R = 3.284$ $\overline{(Nu)}_R/\overline{(Nu)}_S = 1.09$

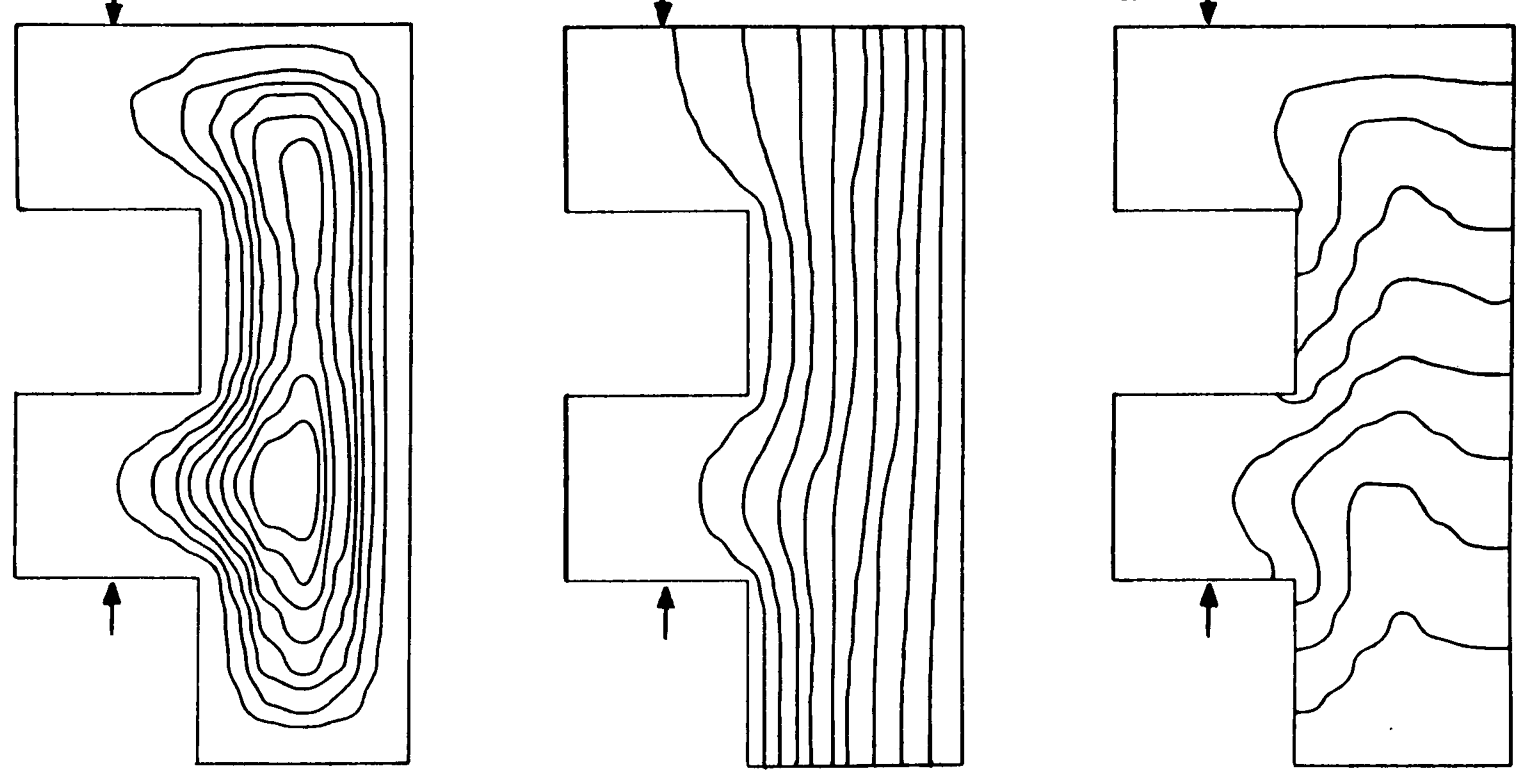

(a) Streamlines   (b) Isotherms   (c) Heat lines

[Arrows Denote the Location of the Hot Wall in the Corresponding Smooth-Walled Enclosure]

Figure 46. Computed Streamlines, Isotherms, and Heat Lines in an Enclosure With an Aspect Ratio of W/H = 0.4 that Contains Two Rectangular Wall Roughness Elements ($\delta = 0.5$) [Case No. 26]

Case No. 44

$Gr = 4.07 \times 10^6$ $Pr = 4.52$ $W/H = 0.4$ $\delta = 0.5$ $A = 0.12$ $\delta_0 = 0.25$ $(\overline{Nu})_R = 23.385$ $(\overline{Nu})_R/(\overline{Nu})_S = 1.081$

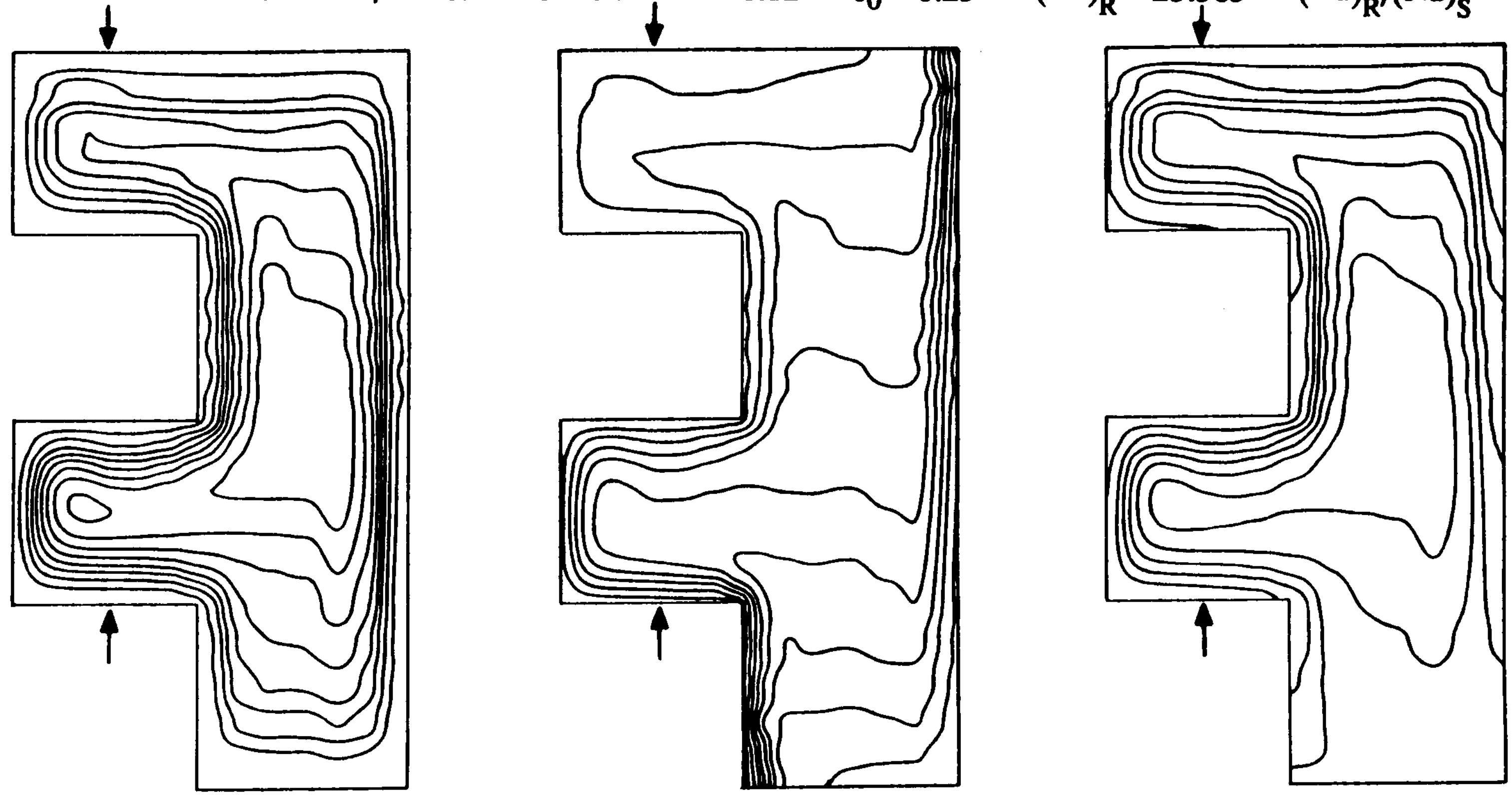

(a) Streamlines (b) Isotherms (c) Heat lines

[Arrows Denote the Location of the Hot Wall in the Corresponding Smooth-Walled Enclosure]

Figure 47. Computed Streamlines, Isotherms, and Heat Lines in an Enclosure With an Aspect Ratio of W/H = 0.4 that Contains Two Rectangular Wall Roughness Elements ($\delta = 0.5$) [Case No. 44]

and shifts this range toward lower Grashof numbers, (3) increases the enhancement of the heat transfer [increases $(\overline{Nu})_R/(\overline{Nu})_S$] in the boundary layer regime for Grashof numbers below approximately 2×10^6, but decreases the enhancement for Grashof numbers above approximately 2×10^6. An unusual feature of curve A is that it exhibits a leveling off with increasing Grashof number in the boundary layer regime. The streamlines, isotherms and heat lines for the flows at Grashof numbers of 4.07×10^3 (case 29) and 4.07×10^6 (case 46) are presented in Figures 44 and 45. These figures clearly show that these flows occur in the conduction and boundary layer regimes, respectively.

The ratios of Nusselt numbers, $(\overline{Nu})_R/(\overline{Nu})_S$, for the flows in cases 26, 32, 38 and 44 are plotted in Figure 43. These results, which are denoted by the circular plotting symbols, were calculated for the same values of all of the dimensionless parameters as those for the flows of curve A, except that the phase shift of the roughness element array, δ_0, was increased from 0 to 0.25. As may be seen in Figure 43, this change in δ_0 had virtually no effect on the ratio of Nusselt numbers, $(\overline{Nu})_R/(\overline{Nu})_S$, as a function of Grashof number (as given by curve A). (Recall that similar behavior was observed in Figure 31 for flows in enclosures with 4 roughness elements.) The streamlines, isotherms and heat lines for the flows of cases 26, ($Gr_H = 4.07 \times 10^3$) and 44 ($Gr_H = 4.07 \times 10^6$) are presented in Figures 46 and 47, respectively.

Finally, curve B in Figure 43 shows the effect of reducing the dimensionless amplitude of the elements, A from 0.12 to 0.06. This effect is seen to be same as it was for enclosures with $\delta = 0.25$ (4 elements); that is, the heat transfer enhancement, as portrayed by the ratio of Nusselt numbers, $(\overline{Nu})_R/(\overline{Nu})_S$, is reduced by this change in both the conduction and boundary-layer flow regimes.

CHAPTER 6

CONCLUSIONS AND RECOMMENDATIONS

6.1 Conclusions

Based on the results presented in the previous chapter, the following conclusions may be drawn:

(1) the NACHOS code has been experimentally verified for natural convection flows in rectangular enclosures containing large roughness elements,

(2) wall roughness elements can cause a substantial increase, or reduction, in the rate of heat transfer across an enclosure depending on the values of the dimensionless variables,

(3) the largest heat transfer enhancement found in this study was with sinusoidal roughness elements $[(\overline{Nu})_R/(\overline{Nu})_S = 1.355]$,

(4) if the roughness elements are added in a manner such that the volume of fluid in an enclosure is reduced, the heat transfer enhancement in the conduction regime is substantially increased, but only slight changes in the ratio of Nusselt numbers occur in the transition and boundary-layer flow regimes, and

(5) the following parametric trends were observed for enclosures with rectangular roughness elements:

   (a) when Pr, W/H, A, δ, δ_0 are fixed and Gr_H is varied, three distinct flow regimes (the conduction, transition and boundary-layer regimes) occur in an enclosure,

   (b) if only the Prandtl number is varied, there appears to be a strong Prandtl number effect on the ratio of Nusselt numbers, with higher Nusselt number ratios occuring at higher Parndtl numbers,

(c) if Gr_H, Pr, A, δ and δ_0 are fixed and the aspect ratio W/H is reduced, slight increases of the ratio of Nusselt numbers occur in the conduction regime, but in the transition and boundary-layer regimes this ratio remains essentially unchanged,

(d) if Gr_H, Pr, W/H, A and δ_0 are fixed and the period, δ, is increased; the ratio of Nusselt numbers is reduced in the conduction regime, increased up to a certain value of Gr_H in the boundary-layer regime, and is then again reduced above that value of Gr_H,

(e) if Gr_H, Pr, W/H, A and δ are fixed and the phase shift, δ_0, is varied; no significant change in the ratio of Nusselt numbers is observed, and,

(f) if Gr_H, Pr, W/H, δ and δ_0 are fixed and the amplitude of the elements, A, is reduced; the ratio of Nusselt numbers is reduced in both the conduction and boundary-layer flow regimes.

6.2 Recommendations for Further Research

The following recommendations are made for future work on the present topic:

(1) calculations should be performed for different roughness element geometries, and,

(2) another experiment should be performed using higher temperature difference across the enclosure to varify that the horizontal walls of the enclosure are essentially adiabatic surfaces.

REFERENCES

REFERENCES

Al-Arabi, M., and El-Refaee, M. M., 1978, "Heat Transfer by Natural Convection from Corrugated Plates to Air," *Int. J. Heat & Mass Trans.*, Vol. 21, pp. 357-359

Anderson, D. A., Tannehill, J. C., and Pletcher, R. H., 1984, *Computational Fluid Mechanics and Heat Transfer*, McGraw-Hill, New York

Anderson, R., and Bohn, M., 1986, "Heat Transfer Enhancement in Natural Convection Enclosure Flow," *J. of Heat Trans.*, Vol., 108, pp. 330-336

Arnold, J. N., 1978, "Heat Transfer by Natural Convection in Enclosed Rectangular Cavities," *Engineering Heat and Thermodynamics*, Ph. D. Dissertation, University of California, Los Angeles, California

Baker, H. D., Ryder, E. A., and Baker, N. H., 1975, *Temperature Measurement in Engineering*, Vol. 1, Omega Engineering, Inc., Stamford, Connecticut

Baker, A. J., 1983, *Finite Element Computational Fluid Mechanics*, Hemisphere Publishing Corporation, Washington

Beach, T., 1985a, *NACHOS - A Manual for University of Tennessee Users*, Technical Rpt. No. MAE-NCL-12, University of Tennessee, Knoxville, Tennessee

Beach, T., 1985b, *A Numerical Investigation of the Transient Natural Convection from Two Vertically Aligned Horizontal Cylinders*, M.S. Thesis, University of Tennessee, Knoxville, Tennessee

Bejan, A., 1984, *Convection Heat Transfer*, John Wiley, New York

Bilski, S. M., Lloyd, J. R., and Yang, K. T., 1986, "An Experimental Investigation of the Laminar Natural Convection Velocity Field in Square and Partitioned Enclosure," *Heat Transfer 1986: Proceedings of the Eighth International Heat Transfer Conference, Sanfrancisco, California* pp. 1513-1518

Catton, I., 1978, "Natural Convection in Enclosures," *International Heat Transfer Conference*

Chinnappa, J. C. V., 1970, "Free Convection in Air Between a 60^0 V-Corrugated Plate and a Flat Plate," *Int. J. Heat & Mass Trans.*, Vol. 13, pp. 117-123

Chow, L. C., and Tien, C. L., 1978, "An Examination of Four Differencing Schemes for Some Elliptic-Type Convection Equations," *Numerical Heat Transfer*, Vol. 1, pp. 87-100

deBoer, P. C. T., 1984, "Thermally Driven Motion of Strongly Heated Fluids," *Int. J. Heat & Mass Trans.*, Vol. 27, No. 12, pp. 2239-2251

Denny, V. E., and Clever, R. M., 1974, "Comparison of Galerkin and Finite Difference Methods for Solving Highly Nonlinear Thermally Driven Flows," *J. Comp. Physics*, Vol. 16, pp. 271-284

Eckert, E. R. G., and Jackson, T. W., 1951, *Analysis of Turbulent Free Convection Boundary Layer on Flat Plate*, NACA Report No. 1015

Eckert, E. R. G., and Goldstein, R. J., 1976, *Measurements in Heat Transfer*, Hemisphere Publishing Corporation, Washington

ElSherbiny, S. M., Hollands, K. G. T., and Raithby, G. D., 1982, "Effect of Thermal Boundary Conditions on Natural Convection in Vertical and Inclined Air Layers," *J. of Heat Trans.*, Vol. 104, pp. 515-520

ElSherbiny, S. M., Hollands, K. G. T., and Raithby, G. D., 1978, "Free Convection Across Inclined Air Layers with One Surface V-Corrugated," *J. of Heat Trans.*, Vol. 100, pp. 410-415

Fujii, T., Fujii, M., and Takeuchi, M., 1973, "Influence of Various Surface Roughness on the Natural Convection," *Int. J. Heat & Mass Trans.*, Vol. 16, pp. 629-640

Gartling, D. K., 1977a, *NACHOS - A Finite Element Computer Program for Incompressible Flow Problems, Part I - Theoritical Background*, SAND77-1333, Sandia Laboratories, Albuquerque, New Mexico

Gartling, D. K., 1977b, *NACHOS - A Finite Element Computer Program for Incompressible Flow Problems, Part II - User's Manual*, SAND77-1334, Sandia Laboratories, Albuquerque, New Mexico

Gebhart, B., Jaluria, Y., Mahajan, R. L., and Sammakia, B., 1988, *Buoyancy-Induced Flows and Transport*, Hemisphere Publishing Corporation, New York

Gerald, C. F., 1980, *Applied Numerical Analysis*, Addison-Wesley Publishing Company

Hauf, W., and Grigull, U., 1970 "Optical Methods in Heat Transfer," *Advances in Heat Transfer,* J. P. Harnet, T. F. Irvine, eds., Vol. 6, pp. 133-366

Heidari, M. Y., and Parsons, J. R., 1980, *The UTK Dept. of Mechanical and Aerospace Engineering Wollaston Prism Interferometer,* Rpt. No. MAE-NCL-2, University of Tennessee, Knoxville, Tennessee

Heya, N., Takeuchi, M., and, Fujii, T., 1982, "Influence of Surface Roughness on Free-Convection Heat Transfer from a Horizontal Cylinder," *Chemical Engg. Journal,* Vol. 23, pp. 185-192

Holman, J. P., 1984, *Experimental Methods for Engineers,* McGraw-Hill, New York

Hoogendorn, C. J., 1986, "Natural Convection in Enclosures," *Proceedings of the Eigth International Heat Transfer Conference*, San Francisco, Vol.1, Hemisphere Publishing Corporation, Washington, D. C., pp. 111-120

Huebner, K. H., 1975, *The Finite Element Method for Engineers,* John Wiley & Sons, New York

Incropera, F. P., and DeWitt, D. P., 1985, *Fundamentals of Heat and Mass Transfer,* John Wiley & Sons, New York

Irby, R. G., and Parsons, J. R., 1981, *Examination of Natural Convection From Selected Downward-Facing Heated Surfaces with the Wollaston Prism Interferometer,* Technical Rpt. No. MAE-NCL-3, University of Tennessee, Knoxville, Tennessee

Izumi, R., Yamashita, H., and Oyakawa, K., 1983, "Fluid Flow and Heat Transfer in Corrugated Wall Channels," *Bull. of JSME,* Vol. 26, No. 217, pp. 1146-1153

Jaluria, Y., 1980, *Natural Convection Heat and Mass Transfer,* Pergamon Press

Jaluria, Y., and Torrance, K. E., 1986, *Computational Heat Transfer*, Hemisphere, New York

Jessee, J. W., 1985, *The Developement of a Natural Convection Heat Transfer Research Facilitiy,* M. S. Thesis, University of Tennessee, Knoxville, Tennessee

Jofre, R. J., and Barron, F., 1967, "Free Convection Heat Transfer to a Rough Plate," *ASME paper no. 67-WA/HT-38*

Kaviany, M., 1984, "Effect of Protuberance on Thermal Convection in a Square Cavity," *J. of Heat Trans.*, Vol. 106, pp. 830-834

Kays, W. M., and Crawford, M. E., 1980, *Convective Heat and Mass Transfer*, McGraw-Hill, New York

Kimura, S., and Bejan, A., 1983, "The "Heatline" Visualization of Convective Heat Transfer," *J. of Heat Trans.*, Vol. 105, pp. 916-919

Kline, S. J., and McClintock, F. A., 1953, "Describing Uncertainties in Single-Sample Experiments," *Mechanical Engineering*, Vol. 25, pp. 3-8

Krane, R. J., and Jessee, J., 1983, "Some Detailed Field Measurements for a Natural Convection Flow in a Vertical Square Enclosure," *Proceedings of the ASME/JSME Thermal Engineering Joint Conference*, Honolulu, March 20-24, Vol. 1, pp. 323-329

Kreith, F., 1976, *Principles of Heat Transfer*, Intex Educational Publishers, New York

Merzkirch, W., 1974, *FlowVisualization*, Academic Press, New York

Minkowycz, W. J., Sparrow, E. M., ScHneider, G. E., and Pletcher, R. H., 1988, *Handbook of Numerical Heat Transfer*, Wiley, New York

O'Brein, J. E., and Sparrow, E. M., 1982, "Corrugated-Duct Heat Transfer, Pressure Drop, and Flow Visualization," *J. of Heat Trans.*, Vol. 104, pp. 410-416

Oran, E. S., and Boris, J. P., 1987, *Numerical Simulation of Reactive Flow*, Elsevier, New York

Ostrach, S., 1972, "Natural Convection in Enclosures," *Adv. In H. T.*, Vol. 8, pp. 161-227

Ostrach, S., 1982, "Natural Convection Heat Transfer in Cavities and Cells," *Heat Transfer 1982: Proceedings of the Seventh International Heat Transfer Conference, Munich, Germany*, Vol. 6, pp. 365-379

Patankar, S. V., 1980, *Numerical Heat Transfer and Fluid Flow*, McGraw-Hill, New York

Pepper, D. W., and Cooper, R. E., 1980, "Numerical Solution of Recirculating Flow by a Simple Finite Element Recursion Relation," *Computer and Fluids*, Vol. 8, pp. 213-223

Pollard, R. B., and Carlson, W. O., 1969, "An Experimental Investigation of the Effect of Baffles on Transient Natural Convection of a Confined Fluid," *Prog. In H. M. Trans.*, Vol. 2 pp. 23-40

Prasada Rao, D. R. V., Krishna, D. V., and Debnath, L., 1983, "Free Convection in Hydromagnatic Flows in Vertical Wavy Channel," *Int. J. Engg. Sci.*, Vol. 21, No. 9, pp. 1025-1039

Prasolov, R. S., 1961, "The Effects of Surface Roughness of Horizontal Cylinders on Heat Transfer to Air," *Inzh.-fiz. Zh.*, Vol. 4, pp. 3-7

Probert, S. D., and Ward, J., 1974, "Improvements in the Thermal Resistance of Vertical, Air-Filled, Enclosed Cavities," *Heat Transfer 1974: Proceedings of the International Heat Transfer Conference, Tokyo, Japan*, pp. 124-128

Ramakrishna, K., Seetharamu, K. N., and Sarma, P. K., 1978, "Turbulent Heat Transfer by Free Convection from a Rough Surface," *J. of Heat Trans.*, Vol. 100, pp. 727-729

Rao, C. N., 1982, "Natural Convection Heat Transfer of Heat Generating Fluids in Vertical Channels with Wavy Walls," *Rev. Roum. Phys.*, Vol. 27, No. 9, pp. 783-799

Roache, P. J., 1976, *Computational Fluid Dynamics*, Revised Version, Hermosa, Albuquerque, New Mexico

Said, S. A. M., 1986, *An Analytical and Experimental Investigation of Natural Convection Heat Transfer in Vertical Channels with a Single Obstruction*, Ph. D. Dissertation, University of Tennessee, Knoxville, Tennessee

Sastry, C. V. N., Murthy, V. N., and Sarma, P. K., 1976, "Effect of Discrete Wall Roughness on Free Convective Heat Transfer from a Vertical Tube," *Heat Transfer and Turbulent Buoyant Convection*, Vol. 2, Hemisphere, Washington D. C. pp. 651-661

Senas, V., Fletcher, L., and Aung, W., 1972, "Heat Transfer Measurements with a Wollaston Prism Schlieren Interferometer," *ASME paper no. 72-HT-9*, Presented at the AIChE-ASME Heat Transfer Conference, Denver, Colorado

Sernas, V., 1977, "The Wollaston Prism Schlieren Interferometer," von Karman Institute for Fluid Dynamics Lecture Series 96, *Advanced Measurements Techniques in Fluid Mechanics*

Shakerin, S., and Loehrke, R., 1987, "A Numerical Study of Natural Convection over Discrete Roughness Elements on a Vertical Heated Wall of an Enclosure," *Proc. of the ASME. JSME Thermal Engineering Joint Conf.*, Vol. II pp. 261-267

Shakerin, S., Bohn, M., and Loehrke, R. I., 1988, "Natural Convection in an Enclosure with Discrete Roughness Elements on a Vertical Heated Wall," *Int. J. Heat and Mass Trans.*, Vot. 31, pp. 1423-1430

Sparrow, E. M., and Chukaev, A., 1980, "Forced-Convection Heat Transfer in a Duct Having Spanwise-Periodic Rectangular Protuberances," *Numerical Heat Transfer*, Vol. 3, pp. 149-167

Torrance, K. E., and Rockett, J. A., 1969, "Numerical Study of Natural Convection in an Enclosure with Localized Heating From Below-Creeping Flow to the Onset of Laminar Instability," *Journal of Fluid Mechanics*, Vol. 36, pp. 33-

Vajravelu, K., and Sastry, K. S., 1978, "Free Convection Heat Transfer in a Viscous Incompressible Fluid Confined Between a Long Vertical Wavy Wall and a Parallel Flat Wall," *J. Fluid Mech.*, Vol. 86, part 2, pp. 365-383

Vajravelu, K., and Sastry, K. S., 1980, "Natural Convection Heat Transfer in Vertical Wavy Channels," *Int. J. Heat and Mass Trans.*, Vol. 23, pp. 408-411

Van Doormaal, J. P., Raithby, G. D., and Strong, A. B., 1981, "Prediction of Natural Convection in Nonrectangular Enclosures Using Orthogonal Curvilinear Coordinates," *Numerical Heat Transfer*, Vol. 4, pp. 21-38

Yao, L. S., 1983, "Natural Convection Along a Vertical Wavy Surface," *J. of Heat Trans.*, Vol. 105, pp. 465-468

Zienkiewicz, O. C., 1977, *The Finite Element Method*, McGraw-Hill, New York

APPENDICES

APPENDIX A

A BRIEF DISCUSSION OF THE NACHOS FINITE ELEMENT CODE

A.1 The Formulation of the Finite Element Equations

The finite element algorithm for energy conservation in a convective flow expressed in terms of the method of weighted residuals (MWR) deals directly with the governing differential equation $B(q) = 0$ and the boundary condition $b(q) = 0$. First, an approximate solution, say, q^h, is assumed to exist. Then, upon direct substitution in the governing equation and the boundary condition, $B(q^h)$ and $b(q^h)$ are statements of the error in the solution approximation. More detailed explanations are given by Baker (1983) and Gartling (1977,a).

The derivation of the finite element equations begins with the division of the continuum region of interest into a number of simply-shaped regions called "finite elements". Each element includes a set of nodal points at which the finite element approximation for each dependent variable, $q_e(x_i)$ is evaluated.

Hence, the semidiscrete approximation, $q^h(x_i)$ is defined as

$$q^h(x_i) \equiv \sum_{e=1}^{M} q_e(x_i)$$

where, $q_e(x_i)$ is defined in terms of the cardinal basis as

$$q_e(x_i) \equiv \{N_s(x_i)\}^T \{Q(t)\}_e \ .$$

The elements of $\{Q(t)\}_e$ are the nodal values of $q_e(x_i)$. N_s is the cardinal basis and s is the degree of the basis.

The basic concept of the finite element algorithm as defined within the framework of the method of weighted residuals, requires the approximation errors in $B(q^h)$ and $b(q^h)$ to be orthogonal to the cardinal basis, $\{N_s\}$. Combining these linearly independent constraints by using an arbitrary constant multiplier, λ, the finite element solution algorithm for the governing equations and associated boundary conditions can be shown to be given by:

$$\int_{R^2} \{N_s\}\, B(q^h)\, d\tau - \lambda \int_{\partial R} \{N_s\}\, b(q^h)\, d\sigma \equiv [0] \quad . \qquad \text{(A.1)}$$

Independent of the degree, s, of the basis $\{N_s\}$ equation (A.1) represents a system of ordinary differential (and algebraic) equations written on the unknown $q^h(x_i)$ of the form

$$Y(\{Q(t)\}) = [E]\,\{Q(t)\}' + [W + Z]\,\{Q(t)\} + \{d\} = \{0\} \qquad \text{(A.2)}$$

where the square matrices E, W, and Z represent thermal capacity, convection, and diffusion terms respectively. The column matrix d contains all the nonhomogeneous terms. The prime (') represents the ordinary derivative with respect to time (t). For steady-state solution, equation (A.2) reduces to the following form

$$\{H(Q)\} = [W + Z]\,\{Q\} + \{d\} = \{0\} \quad . \qquad \text{(A.3)}$$

The differential equations describing the laminar, two-dimensional, natural convection flows in the enclosures can be written in tensor notation as follows

Conservation of mass $$\frac{\partial u_i}{\partial x_i} = 0 \qquad \text{(A.4a)}$$

Conservation of momentum $$\rho \frac{Du_i}{Dt} = \frac{\partial \tau_{ij}}{\partial \alpha_j} + \rho g_i \qquad \text{(A.4b)}$$

Conservation of energy $$\rho c \frac{DT}{Dt} = -\frac{\partial q_i}{\partial x_i} \qquad \text{(A.4c)}$$

where the stress tensor is

$$\tau_{ij} = P\delta_{ij} + \mu\left(\frac{\partial u_i}{\partial x_j} + \frac{\partial u_j}{\partial x_i}\right) \qquad \text{(A.5a)}$$

and the heat flux vector is given by

$$q_i = -k\frac{\partial T}{\partial x_i}\ . \qquad \text{(A.5b)}$$

The equation of state may be written as

$$\rho = \rho_0\left[1 - \beta(T - T_\infty)\right]\ . \qquad \text{(A.6)}$$

In the above equations, u_i is the velocity component in the x_i coordinate direction, t is the time, P is the pressure, T is the temperature, ρ is the density, τ_{ij} is the stress tensor, q_i is the heat flux vector, μ is the viscosity, C_p is the specific heat, k is the thermal conductivity and β is the coefficient of volume expansion. D/Dt is the so-called substantial derivative and δ_{ij} represents the Kronecker delta.

Carrying out the general algorithm outlined above, the dependent variables (u_i, P, T) can be expressed in the following forms within each element:

$$u_i(x_i,t) = \{N_s(x_i)\}^T \{u(t)\}_i \tag{A.7a}$$

$$P(x_i,t) = \{N_s(x_i)\}^T \{P(t)\} \tag{A.7b}$$

$$T(x_i,t) = \{N_s(x_i)\}^T \{T(t)\} \tag{A.7c}$$

In equations (A.7) the u_i, P, and T are vectors of unknown nodal point variables and N_s are vectors of interpolation or basis functions. s is the degree of the basis. s is equal to one for a linear basis and two for a quadratic basis. The velocity components and the temperature are approximated by quadratic basis functions and the pressure by a linear basis function within each element. All dependent variables are required to be continuous from element to element. This continuity requirement is met through the appropriate summation of equations for nodes which are common to adjacent elements. The superscript "T" denotes a vector transpose and the subscript "i" denotes the coordinate directions, x and y.

Substituting the approximate forms given by equations (A.7) for u_i, P, and T into the field equations (equations A.4) yields the set of residuals, R_i, or error equations, as shown below.

Conservation of mass:

$$f_1(N_2, u_i) = R_1 \tag{A.8a}$$

Conservation of momentum:

$$f_2(N_2, N_1, N_2, u_i, P, T) = R_2 \tag{A.8b}$$

Conservation of energy:

$$f_3(N_2, N_2, T, u_i,) = R_3 \ . \tag{A.8c}$$

As discussed earlier, to use the MWR to reduce the residuals R_i, to zero over each element the residuals have to be made orthogonal to the basis; that is, we require that

$$< f_1, N_1 > = < R_1, N_1 > = 0 \tag{A.9a}$$

$$< f_2, N_2 > = < R_2, N_2 > = 0 \tag{A.9b}$$

and,

$$< f_3, N_2 > = < R_3, N_2 > = 0 \tag{A.9c}$$

where $< , >$ denotes the inner product defined by

$$< a, b > = \int_v a\, b \ dv \tag{A.10}$$

where v is the volume of the element.

Carrying out the above integrals yields the set of coupled matrix equations shown below:

Momentum and continuity:

$$[M]\,V' + [C(u)]\,V + [K(T)]\,V = F(T) \qquad \text{(A.11a)}$$

where $$V^T = (u_1{}^T, u_2{}^T, P^T)$$

and,

$$u^T = (u_1{}^T, u_2{}^T)$$

Energy:

$$[N]\,T' + [D(u)]\,T + [L(T)]\,T = G(T)\,. \qquad \text{(A.11b)}$$

where the prime (') terms represent the ordinary derivative with respect to time (t). In the above equations M and N matrices represent the mass and capacitance terms respectively. The C and D matrices represents the convection of momentum and energy, respectively; while the K and L matrices represent the diffusion of momentum and energy. The F and G vectors provide the forcing functions for the system.

For the steady-state flows of interest in this work the matrix equations can, therefore, be reduced to the following forms:

$$[C(u)]\,V + [K(T)]\,V = F(T) \qquad \text{(A.12a)}$$

$$[D(u)]\,T + [L(T)]\,T = G(T)\;. \qquad \text{(A.12b)}$$

The matrix equations (A.12) represent the discrete analogs of the conservation equations for an individual finite element.

Once the matrix equations have been assembled, the task of solving this large set of strongly coupled, nonlinear equations still remains. The solution procedure will be discussed later.

A.2 Element Construction

The element library in NACHOS consists of six-node isoparametric triangles and eight-node isoparametric quadrilaterals. In the present study the quadrilateral elements were employed for all the three different types of enclosures. The quadratic basis, or interpolation, functions for the velocity components (u_i) and the temperature (T) for the quadrilateral element are given by the vectors,

$$N_2 = 1/2 \begin{Bmatrix} 1/2\,(1-e)(1-f)(-e-f-1) \\ 1/2\,(1+e)(1-f)(e-f-1) \\ 1/2\,(1+e)(1+f)(e+f-1) \\ 1/2\,(1-e)(1+f)(-e+f-1) \\ (1-e^2)(1-f) \\ (1+e)(1-f^2) \\ (1-e^2)(1+f) \\ (1-e)(1-f^2) \end{Bmatrix}, \qquad \text{(A.13a)}$$

while the linear basis, or interpolation, functions for the pressure for this element are given by the vector:

$$N_1 = 1/4 \begin{Bmatrix} (1-e)(1-f) \\ (1+e)(1-f) \\ (1+e)(1+f) \\ (1-e)(1+f) \end{Bmatrix} \quad \text{(A.13b)}$$

where, e and f are the normalized or natural coordinates for the elements.

A.3 Outline of the Solution Procedure:

For the steady-state solutions NACHOS employes an algorithm that alternately solves equations (A.12) while continually updating the variable coefficient matrices to reflect the most recently computed values for the dependent variables. This algorithm consists of the following alternating procedure: the energy equation is advanced first using

$$[D(u^n)]\, T^{n+1} + [L(T^n)]\, T^{n+1} = G(T^n)\ . \quad \text{(A.15a)}$$

Next, the momentum equation is advanced using

$$[C(u^n)]\, V^{n+1} + [K(T^{n+1})]\, V^{n+1} = F(T^{n+1})\ . \quad \text{(A.15b)}$$

The solution algorithm keeps alternating between the energy and momentum equations, using updated values of temperature and velocity, as follows:

$$[D(u^{n+1})]\, T^{n+2} + [L(T^{n+1})]\, T^{n+2} = G(T^{n+1})$$

$$\cdot \quad \cdot \quad \cdot \quad \text{(A.16)}$$

$$\cdot \quad \cdot \quad \cdot$$

etc.

where the superscript n indicates the iteration number. The basic iteration scheme in equation (A.16) can often be accelerated by suitable choice of an interpolation procedure for the dependent variables used to evaluate the coefficient matrices. For example, the [K] or [L] matrices can be evaluated at $T^{*(n+1)}$ using

$$T^{*(n+1)} = \alpha T^{(n+1)} + (1-\alpha) T^{n} \quad . \qquad (0 < \alpha < 1)$$

NACHOS uses the above interpolation procedure for the temperature field with $\alpha = 1/2$. No interpolation is used for the velocity field.

APPENDIX B

FORMULATION AND SOLUTION OF THE FINITE DIFFERENCE EQUATIONS FOR THE HEAT FUNCTION AND THE STREAM FUNCTION

B.1 Introduction

As discussed in Chapter 3, the Poisson equations (2.34 and 2.40) that govern the distributions of the heat function and the stream function for flows in the smooth-walled enclosures and the enclosures with rectangular roughness elements were solved by using the finite difference techniques outlined in this appendix.

B.2 The Finite Difference Equation for the Heat Function

The governing equation (2.40) for the nondimensional heat function, $\mathcal{H}$, is rewritten here as follows:

$$\frac{\partial^2 \mathcal{H}}{\partial^2 x} + \frac{\partial^2 \mathcal{H}}{\partial^2 y} = \Pr \left[\frac{\partial (uT)}{\partial y} - \frac{\partial (vT)}{\partial x} \right] \quad . \tag{B.1}$$

The solution of this equation is to be obtained on the general, nonuniform rectangular grid shown in Figure B1. Expanding $\mathcal{H}$ in a Taylor series in the x-direction and truncating to three terms gives

$$\mathcal{H}_{i+1,j} = \mathcal{H}_{i,j} + (x_{i+1,j} - x_{i,j}) \left[\frac{\partial \mathcal{H}}{\partial x} \right]_{i,j} + \frac{(x_{i+1,j} - x_{i,j})^2}{2} \left[\frac{\partial^2 \mathcal{H}}{\partial x^2} \right]_{i,j} \tag{B.2}$$

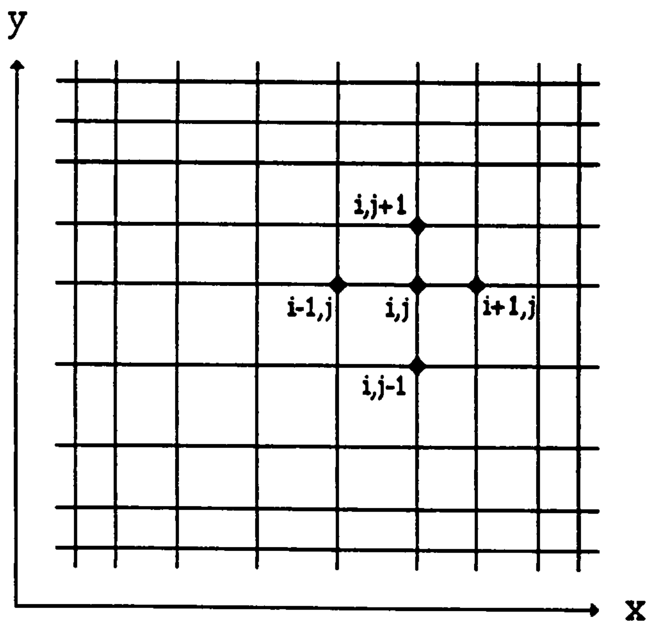

Figure B1. Nonuniform Grid for the Finite Difference Solutions of the Heat Function, $\mathcal{H}$, and the Stream Function, ψ

and,

$$\mathcal{H}_{i-1,j} = \mathcal{H}_{i,j} + (x_{i-1,j} - x_{i,j}) \left[\frac{\partial \mathcal{H}}{\partial x}\right]_{i,j} + \frac{(x_{i-1,j} - x_{i,j})^2}{2} \left[\frac{\partial^2 \mathcal{H}}{\partial x^2}\right]_{i,j} . \tag{B.3}$$

Multiplying equation (B.2) by $(x_{i-1,j} - x_{i,j})$ and equation (B.3) by $(x_{i+1,j} - x_{i,j})$ and subtracting the resulting equations gives

$$\left[\frac{\partial^2 \mathcal{H}}{\partial x^2}\right]_{i,j} = \left\{(A)\,\mathcal{H}_{i+1,j} - (B)\,\mathcal{H}_{i-1,j} - (A - B)\,\mathcal{H}_{i,j}\right\} \left\{\frac{2.0}{A\ B^2 - A^2\ B}\right\} \tag{B.4}$$

where:

$$A \equiv (x_{i-1,j} - x_{i,j}) \tag{B.5a}$$

$$B \equiv (x_{i+1,j} - x_{i,j}) . \tag{B.5b}$$

Proceeding in a similar fashion, it is readily shown that

$$\left[\frac{\partial^2 \mathcal{H}}{\partial y^2}\right]_{i,j} = \left\{(C)\,\mathcal{H}_{i,j+1} - (D)\,\mathcal{H}_{i,j-1} - (C - D)\,\mathcal{H}_{i,j}\right\} \left\{\frac{2.0}{C\ D^2 - C^2\ D}\right\} \tag{B.6}$$

where:

$$C \equiv (y_{i,j-1} - y_{i,j}) \tag{B.7a}$$

$$D \equiv (y_{i,j+1} - y_{i,j}) . \tag{B.7b}$$

Next, finite difference approximations must be found for the derivatives $\frac{\partial(uT)}{\partial y}$ and $\frac{\partial(vT)}{\partial x}$ that appear on the right-hand side of equation (B.1). Expanding the function (uT) in a Taylor series in the y-direction and truncating to three terms gives

$$(uT)_{i,j+1} = (uT)_{i,j} + (y_{i,j+1} - y_{i,j})\left[\frac{\partial(uT)}{\partial y}\right]_{i,j} + \frac{(y_{i,j+1} - y_{i,j})^2}{2}\left[\frac{\partial^2(uT)}{\partial y^2}\right]_{i,j} \quad \text{(B.8)}$$

and,

$$(uT)_{i,j-1} = (uT)_{i,j} + (y_{i,j-1} - y_{i,j})\left[\frac{\partial(uT)}{\partial y}\right]_{i,j} + \frac{(y_{i,j-1} - y_{i,j})^2}{2}\left[\frac{\partial^2(uT)}{\partial y^2}\right]_{i,j} . \quad \text{(B.9)}$$

Multiplying equation (B.8) by $(y_{i,j-1} - y_{i,j})^2$ and equation (B.9) by $(y_{i,j+1} - y_{i,j})^2$ and subtracting the resulting equations gives

$$\left[\frac{\partial(uT)}{\partial y}\right]_{i,j} = \frac{C}{D(C-D)}(uT)_{i,j+1} - \frac{D}{C(C-D)}(uT)_{i,j-1} - \frac{C+D}{C\,D}(uT)_{i,j} \quad \text{(B.10)}$$

where C and D are defined by equations (B.7).

Proceeding in a similar fashion, it is readily shown that

$$\left[\frac{\partial(vT)}{\partial x}\right]_{i,j} = \frac{A}{B(A-B)}(vT)_{i+1,j} - \frac{B}{A(A-B)}(vT)_{i-1,j} - \frac{A+B}{A\,B}(vT)_{i,j} \quad \text{(B.11)}$$

where A and B are defined by equations (B.5).

Substituting equations (B.4), (B.6), (B.10), and (B.11) into equation (B.1) gives the following finite difference approximation for the heat function:

$$\mathcal{H}_{i,j} = \left\{E + \frac{Pr}{2}(F + G)\right\}\left\{\frac{A\,B\,C\,D}{A\,B + C\,D}\right\} \quad \text{(B.12)}$$

where

$$E \equiv -\frac{1}{B(B-A)}\mathcal{H}_{i+1,j} + \frac{1}{A(B-A)}\mathcal{H}_{i-1,j} - \frac{1}{D(D-C)}\mathcal{H}_{i,j+1} + \frac{1}{C(D-C)}\mathcal{H}_{i,j-1}\,, \tag{B.13a}$$

$$F \equiv \frac{C}{D(C-D)}(uT)_{i,j+1} - \frac{D}{C(C-D)}(uT)_{i,j-1} - \frac{C+D}{C\,D}(uT)_{i,j}\,, \tag{B.13b}$$

and,

$$G \equiv -\frac{A}{B(A-B)}(vT)_{i+1,j} + \frac{B}{A(A-B)}(vT)_{i-1,j} + \frac{A+B}{A\,B}(vT)_{i,j}\,. \tag{B.13c}$$

Equation (B.12) is the finite difference form of the governing differential equation for the heat function, (B.1), and can be applied at any interior nodes of the grid. The extremely complex form of this equation is due to the fact that it was formulated for a general, nonuniform rectangular grid. For the special case of a uniform rectangular grid, it is easily shown that equation (B.12) reduces to the familiar central difference form.

B.3 The Finite Difference Forms of the Boundary Conditions for the Heat Function Equation

As before, the boundary conditions on the nondimensional heat function, $\mathcal{H}$, are given by equations (2.41), which are rewritten here as follows

$$\mathcal{H} = (x,0) = 0 \quad \text{for} \quad (x_L|_{y=0} \leq x \leq W/H) \tag{B.14a}$$

$$\mathcal{H}(x_L,y) = \int_0^s Nu(y)\,ds = \int_0^s -\left(\frac{\partial T}{\partial n}\right) ds \qquad \text{for } (0 \le y \le 1) \tag{B.14b}$$

$$\mathcal{H}(x,1) = \int_0^{s_{Max}} -\left(\frac{\partial T}{\partial n}\right) ds = (\text{constant}) = \overline{Nu} \quad \text{for } \left(x_L\Big|_{y=1} \le x \le W/H\right) \tag{B.14c}$$

and,

$$\mathcal{H}(1,y) = \overline{Nu} + \int_1^y -\left[\frac{\partial T(W/H,y)}{\partial x}\right) dy \qquad \text{for } (0 \le y \le 1)\ . \tag{B.14d}$$

For both smooth-walled enclosures and enclosures containing rectangular roughness elements, equation (B.14a) requires that

$$\mathcal{H}_{i,j} = 0 \tag{B.15}$$

for every nodal point on the bottom horizontal wall, while equation (B.14c) requires that

$$\mathcal{H}_{i,j} = \overline{Nu} \tag{B.16}$$

for every nodal point on the top horizontal wall. The boundary condition on the right-hand vertical wall of both of these types of enclosures is given by equation (B.14d). The finite-difference form of equation (B.14d) is given by

$$\mathcal{H}_{i,j} = \overline{Nu} + \sum \left[\tfrac{1}{2}\right] \left[\left(\frac{\partial T}{\partial x}\right)_{i,j} + \left(\frac{\partial T}{\partial x}\right)_{i,j-1}\right] \left[y_{i,j} - y_{i,j-1}\right] \tag{B.17a}$$

where the summation is performed over all of the grid points between the top of the right-hand vertical wall at x = W/H, y = 1 down to the nodal point at $(x_{i,j}, y_{i,j})$ and:

$$\left(\frac{\partial T}{\partial x}\right)_{i,j} = \left\{ (A2)^2 T_{i-1,j} - (A1)^2 T_{i-2,j} - [(A2)^2 - (A1)^2] T_{i,j} \right\} \left\{ \frac{1}{(A2)^2 (A1) - (A1)^2 (A2)} \right\} \qquad \text{(B.17b)}$$

$$\left(\frac{\partial T}{\partial x}\right)_{i,j-1} = \left\{ (B2)^2 T_{i-1,j-1} - (B1)^2 T_{i-2,j-1} - [(B2)^2 - (B1)^2] T_{i,j-1} \right\} \left\{ \frac{1}{(B2)^2 (B1) - (B1)^2 (B2)} \right\} \qquad \text{(B.17c)}$$

$$A1 \equiv (x_{i-1,j} - x_{i,j}) \qquad \text{(B.17d)}$$

$$A2 \equiv (x_{i-2,j} - x_{i,j}) \qquad \text{(B.17e)}$$

$$B1 \equiv (x_{i-1,j-1} - x_{i,j-1}) \qquad \text{(B.17f)}$$

and,

$$B2 \equiv (x_{i-2,j-1} - x_{i,j-1}) \ . \qquad \text{(B.17g)}$$

The use of the simple trapezoidal rule to numerically evaluate the integral in equation (B.14d) resulted in the summation that appears in equation (B.17a). A three-point finite difference scheme was used to obtain the desired accuracy in the temperature derivatives at the wall given by equations (B.17b) and (B.17c). Preliminary calculations showed the use of the three-point scheme is necessary, since if a two-point scheme was employed the contour plots of the heat function, $\mathcal{H}$, did not show the heat lines to be locally perpendicular to the vertical walls as they must be.

The boundary condition on $\mathcal{H}$ on the left-hand vertical wall is given by equation (B.14b). For a smooth-walled enclosure, this equation reduces to the simple form given by

$$\mathcal{H}(0,y) = \int_0^1 -\frac{\partial T}{\partial x} dy \qquad \text{for } (0 \leq y \leq 1) \ . \tag{B.18}$$

Using the same techniques as discussed above for the right-hand vertical wall, the finite-difference form of equation (B.18) is easily shown to be

$$\mathcal{H}_{i,j} = -\sum \left[\tfrac{1}{2}\right] \left[\left(\frac{\partial T}{\partial x}\right)_{i,j} + \left(\frac{\partial T}{\partial x}\right)_{i,j-1}\right] \left[y_{i,j} - y_{i,j-1}\right] \tag{B.19a}$$

where the summation is performed over all of the nodal points from the bottom of the wall at $x = 0$, $y = 0$ up to the nodal point at $(x_{i,j}, y_{i,j})$ and:

$$\left(\frac{\partial T}{\partial x}\right)_{i,j} = \left\{ (C2)^2 T_{i+1,j} - (C1)^2 T_{i+2,j} - [(C2)^2 - (C1)^2] T_{i,j} \right\} \left\{ \frac{1}{(C2)^2(C1) - (C1)^2(C2)} \right\} \tag{B.19b}$$

$$\left(\frac{\partial T}{\partial x}\right)_{i,j-1} = \left\{ (D2)^2 T_{i+1,j-1} - (D1)^2 T_{i+2,j-1} - [(D2)^2 - (D1)^2] T_{i,j-1} \right\} \left\{ \frac{1}{(D2)^2(D1) - (D1)^2(D2)} \right\} \tag{B.19c}$$

$$C1 \equiv (x_{i+1,j} - x_{i,j}) \tag{B.19d}$$

$$C2 \equiv (x_{i+2,j} - x_{i,j}) \tag{B.19e}$$

$$D1 \equiv (x_{i+1,j-1} - x_{i,j-1}) \tag{B.19f}$$

and,

$$D2 \equiv (x_{i+2,j-1} - x_{i,j-1}) \ . \tag{B.19g}$$

Determination of the appropriate finite-difference form of equation (B.14b) for the left-hand vertical wall in an enclosure with rectangular roughness elements will complete the set of required boundary conditions on $\mathcal{H}$. The same techniques employed for the right-hand vertical wall will be used to develop the required boundary conditions for the left-hand vertical wall. These boundary conditions will be written here in terms of <u>local coordinates</u> for a <u>single period</u> of the rectangular roughness element array. The shape of a single element in the array is given by equations discussed in Chapter 2, which are rewritten here as follows:

$$(-A \le x_L \le 0) \quad \text{for} \quad \bar{y} = 0 \tag{B.20a}$$

$$x_L = -A \quad \text{for} \quad (0 < \bar{y} < \delta/2) \tag{B.20b}$$

$$(-A \le x_L \le A) \quad \text{for} \quad \bar{y} = \delta/2 \tag{B.20c}$$

$$x_L = A \quad \text{for} \quad (\delta/2 < \bar{y} < \delta) \tag{B.20d}$$

and,

$$(0 \leq x_L \leq A) \quad \text{for} \quad \bar{y} = \delta \, . \tag{B.20e}$$

For $(-A \leq x_L \leq 0)$ and $\bar{y} = 0$, equation (B.14b) may be written as

$$\mathcal{H}(x_L, 0) = \int_0^{x_L} -\left(\frac{\partial T}{\partial \bar{y}}\right) d\bar{x} \tag{B.21a}$$

which yields

$$\mathcal{H}(-A, 0) = \int_0^{-A} -\left(\frac{\partial T}{\partial \bar{y}}\right) d\bar{x} \equiv \mathcal{H}_1 \, . \tag{B.21b}$$

For $x_L = -A$, $(0 < \bar{y} < \delta/2)$ equation (B.14b) reduces to

$$\mathcal{H}(-A, \bar{y}) = \mathcal{H}_1 + \int_0^{\bar{y}} -\left(\frac{\partial T}{\partial \bar{x}}\right) d\bar{y} \tag{B.22a}$$

which yields

$$\mathcal{H}(-A, \delta/2) = \mathcal{H}_1 + \int_0^{\delta/2} -\left(\frac{\partial T}{\partial \bar{x}}\right) d\bar{y} \equiv \mathcal{H}_2 \, . \tag{B.22b}$$

For $(-A \leq x_L \leq A)$ and $\bar{y} = \delta/2$, equation (B.14b) reduces to

$$\mathcal{H}(x_L, \delta/2) = \mathcal{H}_2 + \int_{-A}^{x_L} -\left(\frac{\partial T}{\partial \bar{y}}\right) d\bar{x} \tag{B.23a}$$

which yields

$$\mathcal{H}(A, \delta/2) = \mathcal{H}_2 + \int_{-A}^{A} -\left(\frac{\partial T}{\partial \bar{y}}\right) d\bar{x} \equiv \mathcal{H}_3 . \tag{B.23b}$$

For $x_L = A$ and $(\delta/2 < \bar{y} < \delta)$ equation (B.14b) gives

$$\mathcal{H}(A, \bar{y}) = \mathcal{H}_3 + \int_{\delta/2}^{\bar{y}} -\left(\frac{\partial T}{\partial \bar{x}}\right) d\bar{y} \tag{B.24a}$$

which yields

$$\mathcal{H}(A, \delta) = \mathcal{H}_3 + \int_{\delta/2}^{\delta} -\left(\frac{\partial T}{\partial \bar{x}}\right) d\bar{y} \equiv \mathcal{H}_4 . \tag{B.24b}$$

Finally, for $(0 \leq x_L \leq A)$ and $\bar{y} = \delta$ equation (B.14b) reduces to

$$\mathcal{H}(x_L, \delta) = \mathcal{H}_4 + \int_{A}^{x_L} -\left(\frac{\partial T}{\partial \bar{y}}\right) d\bar{x} \tag{B.25a}$$

which yields

$$\mathcal{H}(0, \delta) = \mathcal{H}_4 + \int_{A}^{0} -\left(\frac{\partial T}{\partial \bar{y}}\right) d\bar{x} \equiv \mathcal{H}_{Period} . \tag{B.25b}$$

The above integrations are carried out for all N_{PER} elements on the wall until $\mathcal{H}$ at the top of the wall is equal to the Nusselt number, $\overline{Nu}$.

The finite difference forms of equations B.21, B.22, B.23, B.24, and B.25 were developed using a three-point difference scheme to obtain the desired accuracy of the normal derivative of the temperature at the wall and the trapezoidal rule to numerically evaluate the integrals. Thus, these equations are quite similar to equations B.17a and B.19a and for the sake of brevity, need not be given here.

B.4 The Finite Difference Forms of the Governing Equation and Boundary Conditions for the Stream Function, ψ

The governing equation (2.34) for the nondimensional stream function, ψ, is rewritten as follows:

$$\frac{\partial^2\psi}{\partial x^2} + \frac{\partial^2\psi}{\partial y^2} = \frac{\partial u}{\partial y} - \frac{\partial v}{\partial x} \; . \tag{B.26}$$

The boundary conditions for this equation require that

$$\psi = 0 \tag{B.27}$$

on all solid boundaries.

Using the same procedures described in sections B.2 and B.3, the finite difference form of the governing equation for the stream function at any interior node of the grid may be written as,

$$\psi_{i,j} = \left\{ M + \frac{1}{2}(N + O) \right\} \left\{ \frac{A\ B\ C\ D}{A\ B + C\ D} \right\} \tag{B.28}$$

where:

$$M = -\frac{1}{B(B-A)}\psi_{i+1,j} + \frac{1}{A(B-A)}\psi_{i-1,j} - \frac{1}{D(D-C)}\psi_{i,j+1} + \frac{1}{C(D-C)}\psi_{i,j-1} \; , \tag{B.29a}$$

$$N = \frac{C}{D(C-D)}(u)_{i,j+1} - \frac{D}{C(C-D)}(u)_{i,j-1} - \frac{C+D}{C\ D}(u)_{i,j} \ , \tag{B.29b}$$

and,

$$O = -\frac{A}{B(A-B)}(v)_{i+1,j} + \frac{B}{A(A-B)}(v)_{i-1,j} + \frac{A+B}{A\ B}(v)_{i,j} \ . \tag{B.29c}$$

The functions A, B, C, and D are defined by equations (B.5) and (B.7).

The boundary conditions for stream function on all the walls of the enclosure are given by requiring that

$$\psi_{i,j} = 0 \tag{B.30}$$

on all solid surfaces.

B.5 A Brief Description of the Finite Difference Code Used to Solve For the Stream Function and the Heat Function

A special-purpose computer code was written to solve the Poisson equations (2.34 and 2.40) that govern the distributions of the heat function and the stream function. This code employs the finite difference forms of these equations and their boundary conditions that were developed in section B.4 of this Appendix. These finite difference equations were written in general form to allow the same nonuniform grid used by NACHOS to solve the field equations for the natural convection flow in enclosure to be employed in the determination of the distributions of the heat function and the stream function.

The program begins by reading in the x and y values of the grid points and the values of u, v and T at each grid point from the solution output file generated by NACHOS. These values of u, v and T are required to evaluate the right-hand members of equations (2.34) and (2.40). The program then initiates the iteration procedure by setting the values of the stream function and the heat function at all of the interior grid points equal to zero; however, if "better" starting values are available, they can be substituted at this point. The over-relaxation technique is used in the iteration process. Thus, the speed of convergence of the solution is strongly dependent on the value of the over-relaxation factor, ω. The optimum value of ω is always between 1.0 and 2.0 and depends on the number of grid points employed. In the present program, the optimum value of ω was calculated for each case by using the following relationship reported by Gerald (1980)

$$\omega_{opt} = \frac{4}{2 + [4 - (\cos \pi/p + \cos \pi/q)^{2}]^{0.5}} \qquad \text{(B.31)}$$

where:

p = number of mesh divisions in x-direction

and,

q = number of mesh divisions in y-direction .

Typical values of ω_{opt} obtained using Gerald's relationship are in the range from 1.62 to 1.74.

After the solution has been completed, the code generates the appropriate output files, which are used to supply the input data to the SURFACE II contouring program. SURFACE II then plots the heat function and the stream function distributions.

APPENDIX C

DATA REDUCTION TECHNIQUES FOR THE MACH-ZEHNDER INTERFEROMETER

The MZI can be used to obtain both qualitative and quantitative description of the temperature distribution in a flow-field. This instrument compares the light beam that traverses the test section with a reference light beam. The comparison is done by superimposing the test beam and the reference beam on a screen, which produces interference fringes. When the instrument is operating in the "infinite fringe mode", the fringes show the distribution of isotherms in the flow-field. If the instrument is set to operate in the "wedge fringe mode", however, the displacements of the fringes from their positions corresponding to a uniform temperature field in the test section can be used to calculate the temperature distribution in the flow-field. The temperature at any point in the flow-field is proportional to the fringe number, S, whose value is dependent on the relative deflection of the fringe. The proportionality constant is a function of the reference temperature, known characteristics of the instrument, and some quantities that can be measured.

The Aerolab 6 inch MZI located in the Natural Convection Laboratory at the University of Tennessee, Knoxville was used in the present investigation. Detailed discussions of this instrument, the techniques for its setup and alignment, and the data reduction procedures (used in this work) are given by Jessee (1985).

In the "wedge fringe mode", the fringes must be adjusted in such a way that the <u>undisturbed</u> fringes in a uniform temperature field are parallel to the direction in which the temperature gradient is to be measured. In the present experiment, it was decided to measure the temperature gradient across several horizontal planes of the enclosure. Thus, the MZI was adjusted such that the undisturbed wedge fringes were parallel to the top and bottom horizontal walls of the enclosure; that is, the fringes made an angle of 90 degrees with the smooth (cold) vertical wall of the enclosure. In the data reduction technique for the MZI, a reference temperature must always be known.

The fringe number S, is assigned in such a manner that its value is equal to zero at the reference temperature. For the present enclosure experiment, the reference temperature can be either the hot wall temperature or the cold wall temperature. As mentioned by Jessee (1985), the selection of the reference temperature in an enclosure is very important to insure the accuracy of the temperatures calculated from the interferogram fringes. Jessee (1985) suggested that at any horizontal plane in the enclosure, the selection of the hot wall or the cold wall temperature as the reference temperature should be made on the basis of the following two criteria: (1) the fringe on the interferogram at the reference point should be sharp, and (2) the fringe on the interferogram at the reference point should be relatively less deflected than the fringe at the corresponding point on the opposite wall of the enclosure; that is, at a point of relatively lower temperature gradient.

The selection of reference temperature also decides which equations are to be used for reducing the data for temperature distribution in the enclosure test section. There are two basic possibilities: (a) if cold wall temperature is the the reference temperature, then the temperatures at different locations across the enclosure along a particular horizontal plane are always higher than the reference temperature; or, (b) if the hot wall temperature is the reference temperature, then the temperatures at different locations across the enclosure along a particular horizontal plane are always lower than the reference temperature.

Usually, an interferogram is not of the same size as the actual test section. Therefore, all the distances that are measured on an interferogram must be divided by a magnification factor, M, which is defined as,

$$M \equiv \left[\frac{\text{distance measured on the interferogram (negative)}}{\text{corresponding distance in the actual test section}} \right]. \qquad \text{(C.1)}$$

As shown in Figure C1, the reference beam was blocked and a ruler was placed in the test section, and a picture was taken. The magnification factor was calculated by measuring the distances between the divisions marked on the ruler as it appears in the picture and dividing by the actual distances on the ruler.

The method for calculating uncorrected fringe number S, as reported by Jessee (1985), will now be discussed. The value of S is equal to zero at the reference temperature and increases in moving along the horizontal plane towards the opposite wall of the enclosure. The technique for calculating this can be illustrated by using Figure C2. The fringe number, S, increases by one as the reference line (shown as dashed line in Figure C2) crosses each wedge fringe. For the temperatures which are referenced to the cold wall temperature, the fringe number increases in going from right to left [Figure C2(a)]. For the temperatures which are referenced to the hot wall temperature, the fringe number increases in giong from left to right [Figure C2(b)]. Thus, fringe number at C is equal to fringe number at A plus one. The fringe number at any intermediate point (say at B) between two wedge fringes is given by the equation,

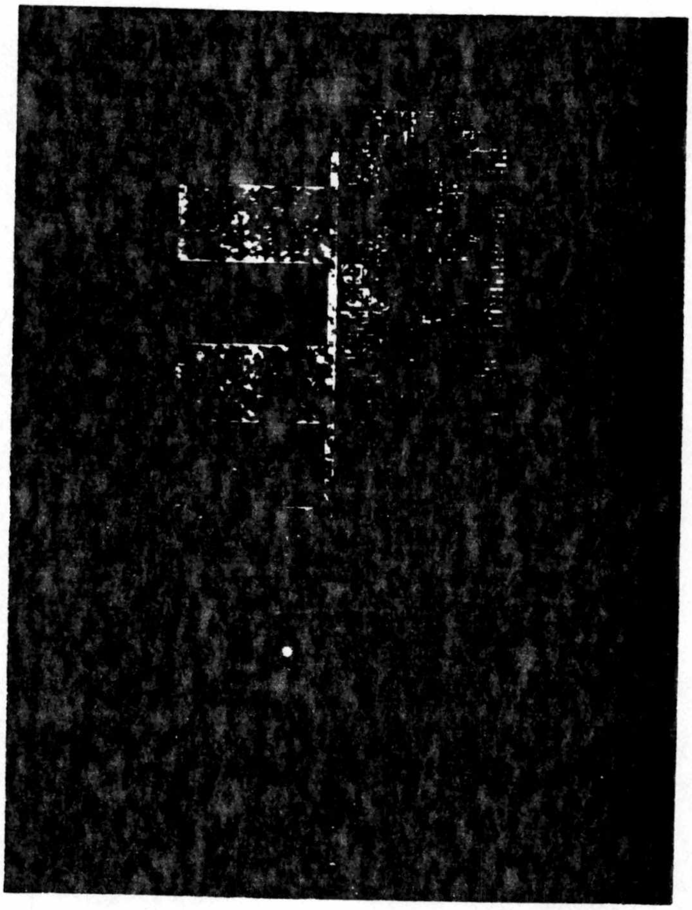

Figure C1. Setup of the Test Section for Determining the Magnification Factor

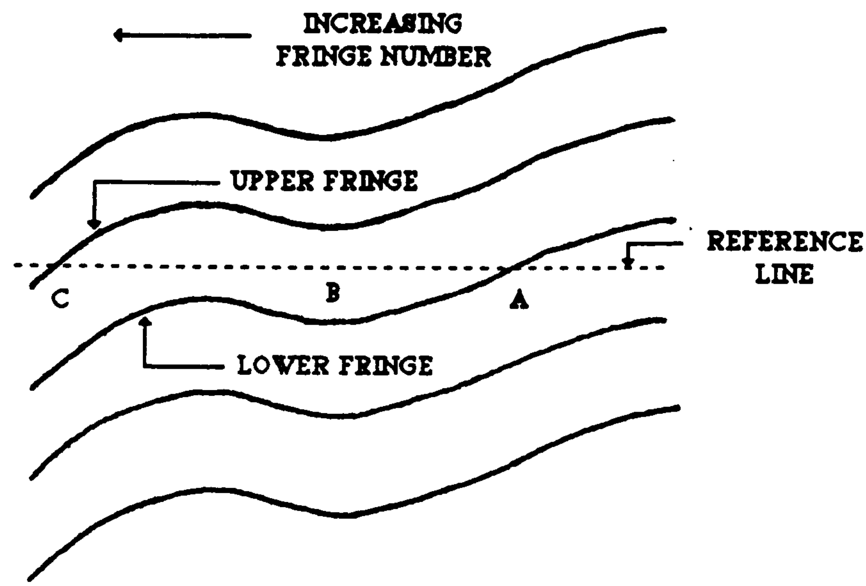

(a) For Temperatures Referenced to Cold Wall

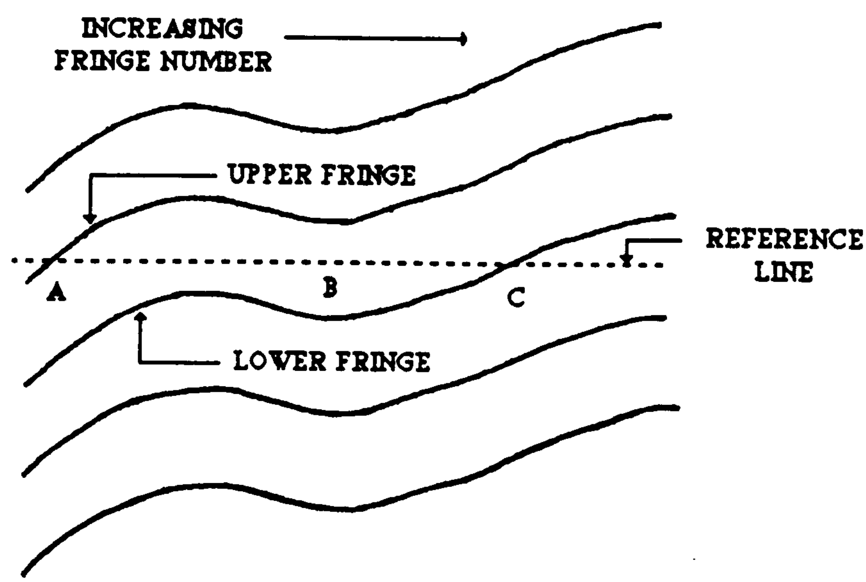

(b) For Temperatures Referenced to Hot Wall

Figure C2. Designation of Points for Calculating Fringe Number and Fractional Shift

$$S_{at\ B} = S_{at\ A} + \text{Fractional Shift.} \tag{C.2}$$

For the tempeartures which are referenced to the cold wall temperature,

$$\text{Fractional Shift} = \frac{y_{Reference} - y_{Lower}}{y_{Upper} - y_{Lower}} \tag{C.3}$$

and, for the temperatures which are referenced to the hot wall temperature,

$$\text{Fractional Shift} = \frac{y_{Upper} - y_{Reference}}{y_{Upper} - y_{Lower}}. \tag{C.4}$$

In equations (C.3) and (C.4), $y_{Reference}$, y_{Upper}, and y_{Lower} are the values of the y coordinates at location B, of the reference line, upper fringe, and lower fringe respectively.

As reported by Hauf and Grigull (1970), the refraction error ΔS_1 is given by

$$\Delta S_1 = \frac{n \lambda Z}{12 \bar{b}^2}. \tag{C.5}$$

In the above equation, n, which is the index of refraction for air, λ, which is the wavelength of the He-Ne laser used in the MZI, and Z, which is the length of the test section along the light beam path are all known quantities. $\bar{b}$ is the mean value of the fringe spacing. As reported by Jessee (1985), the fringe spacing, b, is calculated as the difference between two consecutive values of the x coordinate for the fringe locations. The mean value of the fringe spacing, $\bar{b}$, is the arithmatic mean of the adjacent values of b. These calculations are shown in Tables F1, F3,

and F5. Next, the corrected fringe number, S_{ideal}, is calculated by using the following two equations for the two different catagories discussed earlier.
For the temperatures which are referenced to the cold wall

$$S_{ideal} = S + \Delta S_1 - (\Delta S_1)_w \,, \tag{C.6}$$

and for the temperatures which are referenced to the hot wall

$$S_{ideal} = S - \Delta S_1 + (\Delta S_1)_w \tag{C.7}$$

where $(\Delta S_1)_w$ is the value of ΔS_1 at the wall.

Finally, the temperatures are calculated using the following two equations.
For the temperatures referenced to the cold wall

$$T = \frac{T_w}{1 - a\, S_{ideal}} \,, \tag{C.8}$$

and for the temperatures referenced to the hot wall

$$T = \frac{T_w}{1 + a\, S_{ideal}} \,. \tag{C.9}$$

In the equations (C.8) and (C.9), T_w is the wall temperature, which is also the reference temperature. The constant, a , as repoted by Hauf and Grigull (1970), is given by:

$$a = \frac{2\,\lambda\, R\, T_w}{3\, Z\, \bar{r}\, P_{at}} \,. \tag{C.10}$$

In the above equation, λ, which is the wavelength of the He-Ne laser source, Z, which is the length of the of the test section along the light beam path, R, which is the ideal gas constant for air, $\bar{r}$, which is the specific refractivity of air are all known quantities. The values of the absolute temperature of the wall, T_w, and the atmospheric pressure, P_{at}, are determined by seperate measurements.

The values of all the variables required to calculate the temperature, T, using equations (C.8) and (C.9) are now known.

APPENDIX D

DATA REDUCTION TECHNIQUES FOR THE WOLLASTON PRISM INTERFEROMETER

The WPI actually produces a fringe shift that is directly proportional to the density gradient in the test fluid (Sernas, 1977). Fortunately, the constant of proportionality between the measured fringe shift and the density gradient is a function only of known characteristics of the instrument and quantities that can be measured. Furthermore, if the test fluid is an ideal gas (such as the air used in the present experiments) and the atmospheric pressure is known, the ideal gas law may be used to express the density gradient in terms of the temperature gradient in the test fluid. According to the Fourier conduction law, multiplying this temperature gradient by the thermal conductivity of the fluid yields the local heat flux in the direction of the temperature gradient. Thus, no calibration of the WPI is required and the local wall heat flux, $\dot{q}_W$, may be calculated directly from the measured values of the fringe shift, ΔS, and the fringe spacing, S, using the following relationship given by Sernas (1977):

$$\dot{q}_W = \left[\frac{\lambda\ R\ T_w{}^2\ k_w}{K_{GD}\ Z_{eff}\ h\ P_{at}\ \mathrm{Sin}\ \theta}\right]\left[\frac{\Delta S}{S}\right]. \tag{D.1}$$

λ, which is the wavelength of the He-Ne laser used in the WPI, R, which is the ideal gas contant for air, and K_{GD}, which is the Gladstone-Dale constant for air, are all known constants. The values of the absolute temperature of the wall, T_w, and the atmospheric pressure, P_{at}, are determined by independent measurements. The thermal conductivity of the air, k_w, is evaluated at the wall temperature, T_w, by interpolating tabulated experimental data for this property for air. The methods for determining the values of the effective length of the optical path in the test section, Z_{eff}, the double image distance, h, and the local angle between the wall and the direction normal to the undisturbed (straight) reference fringes, θ, the fringe spacing, S, and the fringe displacement, ΔS, are described below.

First, f, the focal length of the mirror that focuses the beam of light that exits the test section and v, the distance from the camera to the spherical mirror, must be measured. Then, the quantity u, which is defined by the relationship

$$\frac{1}{u} = \frac{1}{f} - \frac{1}{v} \tag{D.2}$$

must be calculated. Next, the wedge angle of the Wollaston prism, β, must be either measured or taken from the manufacturer's specifications and w, the distance from the focal point of the focusing mirror to the centerline of the Wollaston prism, must be measured. Then, the double image distance, h, may be calculated as follows:

$$h = \frac{\beta \pi}{180} \left(f - \frac{uw}{f} + w \right) . \tag{D.3}$$

In general, an interferogram is not the same size as the actual test section. Thus, all distances that are measured from an interferogram must be divided by a magnification factor, M, which is defined as:

$$M \equiv \left[\frac{\text{distance measured on the interferogram (negative)}}{\text{corresponding distance in the actual test section}} \right] . \tag{D.4}$$

For this purpose, a picture of the test section was taken by removing the Wollaston prism from the optical setup. The magnification factor for the WPI was found by measuring the height of the roughness element in this picture and dividing the value by the actual measured height of the roughness element.

The appearance of a typical undisturbed (reference) fringe pattern obtained in the enclosure with the WPI is shown in Figure D1. As may be seen in this figure, the Wollaston prism and the polarizers are adjusted such that the reference fringes make an angle of 30 to 60 degrees with respect to the heated and cooled walls. This insures that the requirement for a fringe to terminate at a wall in order for a fringe shift to be measured at that wall is satisfied. The coordinates of the four arbitrarily selected points, which are numbered 1 through 4 in Figure D1, must be measured in order to perform the required calculations (as shown below). The origin for measuring these coordinates on the interferogram is specified at an arbitrary location (0,0).

The so-called "fringe angle", α, which is shown in Figure D1, is the angle between the undisturbed fringes and the horizontal. α is calculated using the following expression

$$\alpha = \tan^{-1}\left[\frac{x_2 - x_1}{y_2 - y_1}\right] . \tag{D.5}$$

The angle θ is defined as the angle between the wall and the direction normal to the undisturbed (straight) reference fringes. The expressions for computing θ in terms of the fringe angle, α, at various locations on the smooth (cold) and rough (hot)

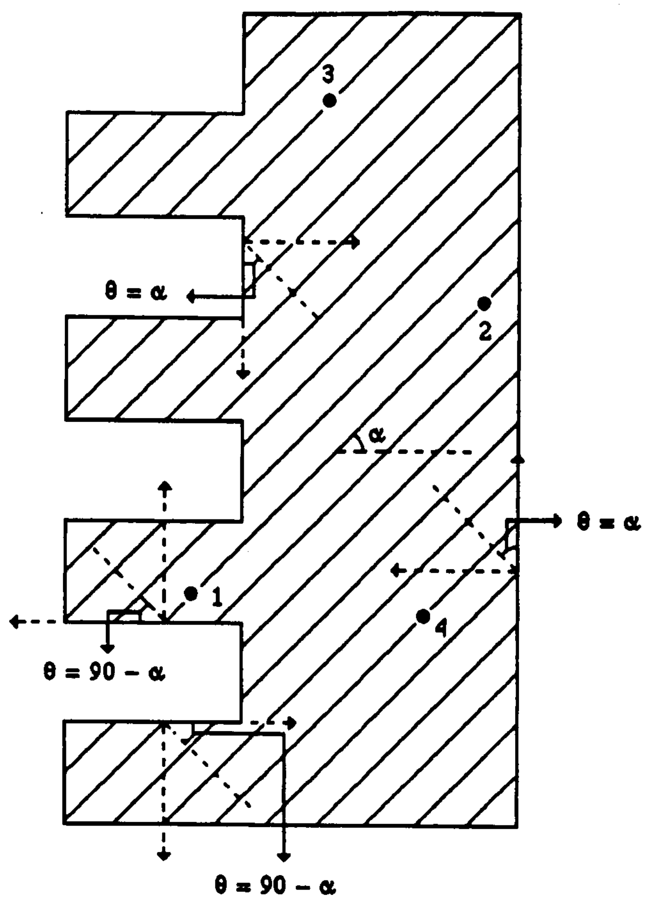

Figure D1. Definition of the Angle θ, and Designation of Points on the Undisturbed (Reference) Fringes that Will be Used in the Data Reduction Procedure vertical walls of the enclosure are shown in Figure D1. For all points on the cold wall,

$$\theta = \alpha, \tag{D.6}$$

as it is for all points located on vertically-oriented segments of the hot wall. For all points located on horizontally-oriented segments of the hot wall, θ is given by

$$\theta = 90 - \alpha\ . \tag{D.7}$$

After measuring the coordinates of points 1 through 8 (as shown in Figures D1 and D2), the following expressions given by Irby and Parsons (1981) may be used to compute the fringe spacing, S, and the fringe displacement, (ΔS), as

$$S = \left[\frac{1}{N}\right]\left[\frac{(y_1 - y_2)x_4 + (x_2 - x_1)y_4 + (x_1 - x_2)y_3 + (y_2 - y_1)x_3}{\sqrt{(y_1 - y_2)^2 + (x_2 - x_1)^2}}\right] \tag{D.8}$$

and,

$$(\Delta S) = \left[\frac{(y_1 - y_2)x_6 + (x_2 - x_1)y_6 + (x_1 - x_2)y_5 + (y_2 - y_1)x_5}{\sqrt{(y_1 - y_2)^2 + (x_2 - x_1)^2}}\right] \tag{D.9}$$

where N is the number of fringes between points 3 and 4.

Next, the boundary layer thickness, δ, is calculated as

$$\delta = \frac{\delta_{int}}{M} = \frac{\sqrt{(x_8 - x_7)^2 + (y_8 - y_7)^2}}{M} \tag{D.10}$$

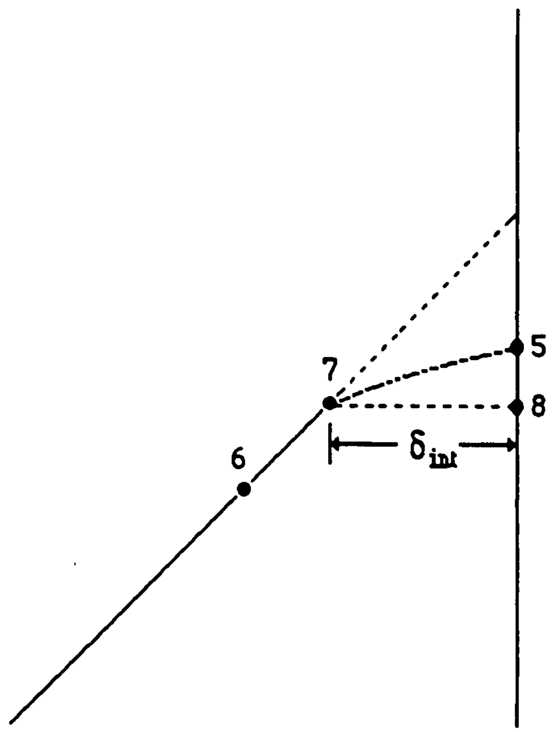

Figure D2. Definition of Points Used to Calculate the Fringe Displacement, ΔS, at the Wall where δ_{int} is shown in Figure D2. The determination of δ allows the end effect correction to the optical path length, $(\Delta Z)_{end}$, to be calculated using the following expression given by Sernas (1977):

$$(\Delta Z)_{end} = (2)\left[\frac{\delta/h}{2 - h/\delta}\right]\left[\left(\frac{\delta}{3}\right)\left(1-\sqrt{1 - \frac{h^2}{\delta^2}}\right) + \left(\frac{h^2}{\delta}\right)\ln\left(\frac{\delta}{h}\right)\left(1+\sqrt{1 - \frac{h^2}{\delta^2}}\right) - \left(\frac{2}{3}\right)\left(\frac{h^2}{\delta}\right)\sqrt{1 - \frac{h^2}{\delta^2}}\right] . \quad \text{(D.11)}$$

Then, the effective optical path length in the enclosure is given by

$$Z_{eff} = Z + (\Delta Z)_{end} . \quad \text{(D.12)}$$

The values of all the variables needed to compute the local wall heat flux, $\dot{q}_w$, using equation D1 are now known.

APPENDIX E

ASSEMBLY AND ALIGNMENT OF THE TEST ENCLOSURE

The same procedure was used to align the enclosure in the optical paths of both the WPI and the MZI. The procedures for the alignment of the WPI are described in detail by Irby and Parsons (1981) and the corresponding procedures for the MZI are given by Jessee (1985). Thus, this Appendix is limited to a discussion of the assembly and alignment of the test enclosure itself.

The assembly of the enclosure begins with the vertical isothermal walls. After mounting the thermocouples in the vertical walls as described in Chapter 4, the copper cover plates were tightly screwed to the backs of these walls. A rubber gasket coated with silicon sealant was inserted between each wall and its cover plate to prevent leaks. As mentioned previously, the thermocouple wires exit the vertical walls by way of holes drilled through the back cover plates. Thus, the next step in the assembly procedure was to seal these holes with epoxy to prevent leaks.

The cold (smooth) vertical wall was then bolted to one of the vertical aluminum walls of the outer enclosure and the hot (rough) vertical wall was attached to the outer vertical aluminum wall of the outer enclosure by the alignment screws, which are shown in Figure 4. The horizontal spacing between the hot and cold vertical walls was then set with the alignment screws such that the aspect ratio of the enclosure, (W/H), was 0.4. A wooden spacer was inserted between the walls during this step to insure that the walls remained parallel to each other.

Next, the partially assembled test enclosure was mounted on a traversing mechanism (Jessee, 1985) and moved into the optical path of either the WPI or the MZI. The traversing mechanism was then adjusted until the test section was centrally illuminated by the He-Ne laser light source of the interferometer. A custom-made bubble level was then placed on the isothermal walls and the test enclosure was leveled by adjusting the leveling screws on the base of the traversing mechanism. The insulated horizontal walls were then installed such that the insulating thin-film surfaces formed the top and bottom surfaces of the enclosure. The top and bottom aluminum horizontal walls of the outer enclosure each have four alignment screws as shown in Figure 4. These screws were tightened until the thin-film surfaces were in firm contact with the top and bottom edges of the vertical isothermal walls.

When using either interferometer, it is always necessary to align the enclosure such that its walls are parallel to the beam of light that traverses the test section. It was decided to perform this alignment using purely optical techniques. For this purpose, two metal pins of the same length and diameter were taped to the opposite ends of one of the rectangular roughness elements on the hot wall. The pins were attached so that they were vertically oriented, located at the same distance from the cold wall and their exposed lenghts in the test beam were identical. Next, if the enclosure was located in the WPI the prism was removed, or if it was located in the MZI the reference beam was blocked. The He-Ne laser light source was then turned on and the images of the enclosure and the pins viewed with a magnifying glass on the screen used to record the interferograms. The leveling screws on the traversing mechanism were then adjusted until the two ends of the pins were at the same level on the screen. The traversing mechanism platform was then rotated about a vertical axis until the two images of the pins were superimposed and became a single sharp image. These adjustments insured that the actual test section (and not the outer aluminum enclosure) was level and parallel to the test beam. The orientation of the enclosure with respect to the traversing mechanism was then fixed by attaching a locking bracket made especially for these experiments and the pins were removed from the hot wall. Then, either the prism was replaced in the WPI or the reference beam of the MZI was unblocked.

To complete the assembly of the enclosure, it was necessary to install and align the glass end windows. It is important that these windows be installed such that they are parallel to each other and perpendicular to the test beam. This was accomplished by employing the so-called "reflection-off-the-glass" technique, which will now be described. First, one of the plexiglas end pieces in which the glass window was already installed was mounted on the end of the enclosure which was the furtherest away from the laser light source. Then a small mirror was taped to the outside surface of this window such that its silvered surface faced into the enclosure and there was no gap between the mirror and the glass. A paper screen, which was pierced by a small hole, was then placed between the laser and the enclosure and the laser was turned on. The ray of light that passed through the hole in the screen then traversed the test section, struck the mirror, and was reflected back onto the screen. The window alignment screws, which are shown in Figure 5, were then adjusted such that the reflected beam passed back through the hole in the screen. This can only occur when the glass window is perpendicular to the laser beam. The other plexiglas end piece and glass window were then installed. The mirror was then removed from the first window that was aligned and taped to the outer surface of the other window with its silvered surface facing away from the test enclosure. The second glass window was then aligned in the same manner as the first window and the mirror and screen were removed from the experiment.

Finally, the water hoses from the constant temperature baths and circulators were connected to the water inlet and outlet tubes on the backs of the vertical isothermal walls and the thermocouple wires were connected to the HP data acquisition system. These steps completed the assembly and alignment of the test enclosure.

APPENDIX F

PRESENTATION AND REDUCTION OF THE DATA TAKEN WITH THE MACH-ZEHNDER INTERFEROMETER

The MZI data was reduced using the procedures outlined in Appendix C. The values of the fixed constants required to reduce this data are given by:

$\lambda \equiv$ wavelength of the He-Ne laser = 2.076 x 10^{-6} (ft)

R $\equiv$ ideal gas constant for air = 53.35 (ft-lb_f/lb_m- ^0R)

$\bar{r} \equiv$ specific refractivity for air = 24.117 x 10^{-4} ft^3/lb_m

n $\equiv$ index of refraction for air = 1.0002719

The Mach-Zehnder interferograms for the undisturbed and disturbed fringes are given in Figures F1 and F2, respectively. The values of the measured variables were found to be:

$P_{at} \equiv$ atmospheric pressure = 2049.08 (lb_f/ft^2)

$(T_w)_{hot\ wall} \equiv$ temperature of the rough vertical wall = 551.23 (^0R) (= 306.24 ^0K)

$(T_w)_{cold\ wall} \equiv$ temperature of the smooth vertical wall = 518.06 (^0R) (= 287.81 ^0K)

Z $\equiv$ length of the test section (length of the optical path) = 0.80833 (ft)

M $\equiv$ magnification factor = 0.94736

After making the measurements listed above, the constant a, given by equation C.10 was calculated for the hot wall and the cold wall. The values of this constant were found to be

$(a)_{hot\ wall} = 0.010189$ (at $T_w = 551.23\ ^0R$)

$(a)_{cold\ wall} = 0.009576$ (at $T_w = 518.06\ ^0R$).

(Enclosure at a Uniform Temperature of 24.0 ^{0}C)

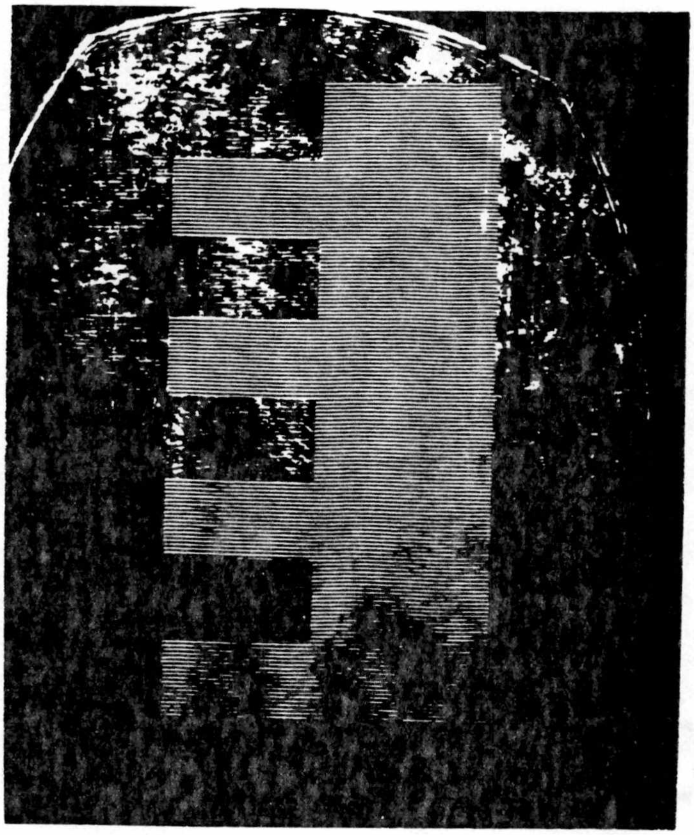

Figure F1. Mach-Zehnder Interferogram (Undisturbed Wedge Fringes)

$Gr = 1.69 \times 10^6$
$Pr = 0.72$
$W/H = 0.4$
$A = 0.12$
$\delta = 0.25$
$\delta_0 = 0$

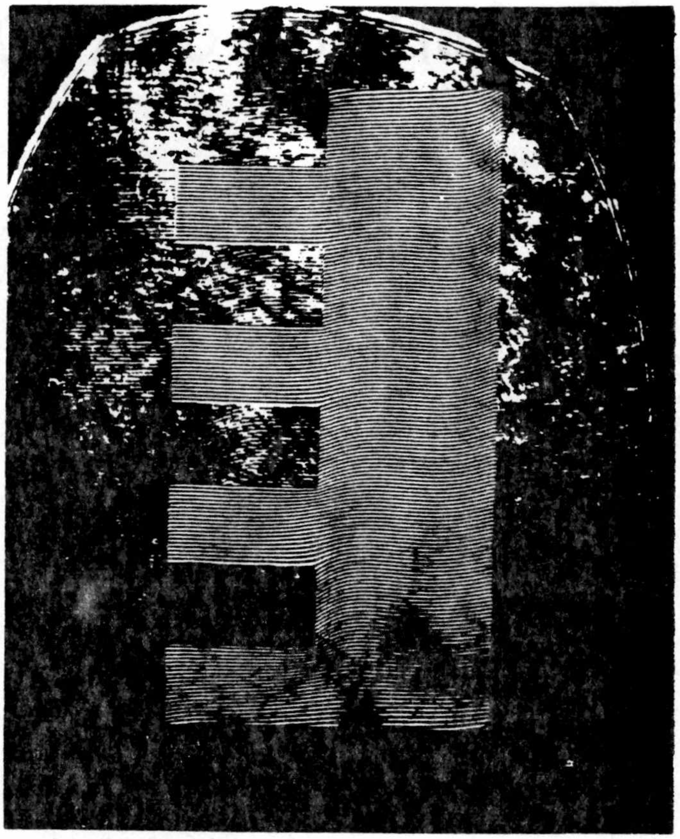

Figure F2. Mach-Zehnder Interferogram (Deflected Wedge Fringes)

The remaining calculations had to be performed at each location where the temperature was evaluated. The fractional shift and the mean value of the fringe spacing, $\bar{b}$, are calculated by using the techniques described in Appendix C. The values of the fractional shift and the mean fringe spacing are listed in Tables F1, F3 and F5 for the locations along the bottom horizontal wall, along a horizontal plane across the enclosure located at y/H = 0.56, and along the top horizontal wall, respectively. It can be noted here that when the reference line (dashed line as shown in Figure C2) crosses a wedge fringe, there is no fractional shift. The fringe number, S, at that location is a whole number. Therefore, the corresponding entries in Tables F1, F3, and F5 at these locations are left blank. The refractive error, ΔS_1, was calculated by using equation C.5. As discussed in Appendix C, for the temperatures which are referenced to the cold wall, equations C.6 and C.8 were used to calculate the corrected fringe number, S_{ideal}, and the temperature, T, respectively. Similarly, for the temperatures which are referenced to the hot wall, equations C.7 and C.9 were used for calculating the corrected fringe number, S_{ideal}, and the temperature, T, respectively. The results of these calculations are listed in Table F2 for the temperatures along the bottom horizontal wall, in Table F4 for the temperatures along a horizontal plane across the enclosure located at y/H = 0.56, and in Table F6 for the temperatures along the top horizontal wall.

An uncertainty analysis for the MZI is given in Appendix H.

Table F1. MZI Interferogram Data for the Calculation of Fringe Spacing and Fractional Shift on the Bottom Horizontal Wall

Location No.	x-Cordn. Measured Along the Enclosure Width (in)	$\Delta x = b$ (in)	$\bar{b}$ (in)	y_{Upper} (in)	$y_{Reference}$ (in)	y_{Lower} (in)	Fractional Shift
1	0.01671		--	0.72480	0.71600	0.70480	0.56
		0.08234					
2	0.09905		0.08339	--	0.71600	--	--
		0.08444					
3	0.18349		0.09500	0.72420	0.71600	0.70420	0.59
		0.10556					
4	0.28905		0.10556	0.72950	0.71600	0.71040	0.29319
		0.10555					
5	0.39460		0.09712	--	0.71600	--	--
		0.08867					
6	0.48327		0.09712	0.72060	0.71600	0.70170	0.75661
		0.10556					
7	0.58883		0.10556	0.72760	0.71600	0.70730	0.42857
		0.10555					
8	0.69438		0.10028	--	0.71600	--	--
		0.09501					
9	0.78939		0.10028	0.72570	0.71600	0.70380	0.55708
		0.10555					
10	0.89494		0.09395	--	0.71600	--	--
		0.08234					
11	0.97728		0.09395	0.72090	0.71600	0.69790	0.78696
		0.10555					
12	1.08283		0.10556	0.72460	0.71600	0.70200	0.61947
		0.10556					
13	1.18839		0.10556	0.72850	0.71600	0.70550	0.45652
		0.10556					
14	1.29395		0.10556	0.73010	0.71600	0.70700	0.38961
		0.10555					
15	1.39950		0.10556	0.73140	0.71600	0.70780	0.34746
		0.10556					
16	1.50506		0.10556	0.73330	0.71600	0.70960	0.27004
		0.10556					
17	1.61061		0.14382	--	0.71600	--	--
		0.18209					
18	1.79270		--	--	0.71600	--	--

Table F2. MZI Data for the Temperature Distribution on the Bottom Horizontal Wall

Location No.	Distance Measured from the Left-Hand Vertical Wall of the Enclosure (ft)	S	ΔS_1	S_{ideal}	$T(^0F)$
1	0.00139	5.56	0.0	5.56	87.52
2	0.00825	5.00	0.0029	5.0029	84.46
3	0.01529	4.59	0.0	4.59	82.21
4	0.02409	4.29319	0.0	4.29319	80.60
5	0.03288	4.00	0.00214	4.00214	79.04
6	0.04027	3.75661	0.0	3.75661	77.72
7	0.04907	3.42857	0.0	3.42857	75.98
8	0.05787	3.00	0.00200	3.00200	73.72
9	0.06578	2.55708	0.0	2.55708	71.39
10	0.07458	2.00	0.00228	2.00228	68.52
11	0.08144	1.78696	0.0	1.78696	67.41
12	0.09024	1.61947	0.0	1.61947	66.55
13	0.09903	1.45652	0.0	1.45652	65.72
14	0.10783	1.38961	0.0	1.38961	65.38
15	0.11663	1.34746	0.0	1.34746	65.16
16	0.12542	1.27004	0.0	1.27004	64.77
17	0.13422	1.00	0.00097	1.00097	63.40
18	0.14939	0.00	0.0	0.0	58.39

Table F3. MZI Interferogram Data for the Calculation of Fringe Spacing and Fractional Shift on a Horizontal Plane at $y^*/H = 0.56$

Location No.	x-Cordn. Measured Along the Enclosure Width (in)	$\Delta x = b$ (in)	$\bar{b}$ (in)	y_{Upper} (in)	$y_{Reference}$ (in)	y_{Lower} (in)	Fractional Shift
1	0.0	0.10450	--	--	1.56500	--	--
2	0.10450	0.10556	0.10503	--	1.56500	--	--
3	0.21006	0.10555	0.10556	--	1.56500	--	--
4	0.31561	0.10556	0.10555	--	1.56500	--	--
5	0.42117	0.14725	0.12641	--	1.56500	--	--
6	0.56842	0.18779	0.16752	--	1.56500	--	--
7	0.75621	0.09352	0.14066	1.57250	1.56500	1.55340	0.39270
8	0.84973	0.13063	0.11208	--	1.56500	--	--
9	0.98036	0.10476	0.11770	--	1.56500	--	--
10	1.08512	0.10609	0.10543	1.57655	1.56500	1.55715	0.59536
11	1.19121	0.11136	0.10873	1.57900	1.56500	1.55970	0.72539
12	1.30257	0.12244	0.11690	1.57750	1.56500	1.55760	0.62814
13	1.42501	0.11295	0.11770	1.57270	1.56500	1.55205	0.37288
14	1.53796	0.08608	0.09952	1.57350	1.56500	1.55440	0.44503
15	1.62404	0.07827	0.08218	--	1.56500	--	--
16	1.70231	0.06091	0.06959	--	1.56500	--	--
17	1.76322	0.02343	0.04217	--	1.56500	--	--
18	1.78665		--	1.57390	1.56500	1.55360	0.43842

Table F4. MZI Data for the Temperature Distribution on a Horizontal Plane at $y^*/H = 0.56$

Location No.	Distance Measured from the Left-Hand Vertical Wall of the Enclosure (ft)	S	ΔS_1	S_{ideal}	$T(^0F)$
1	0.0	0.0	0.0	0.0	91.56
2	0.00871	0.0	0.0	0.0	91.56
3	0.01751	0.0	0.0	0.0	91.56
4	0.02630	0.0	0.0	0.0	91.56
5	0.03510	0.0	0.0	0.0	91.56
6	0.04737	0.0	0.00072	0.0	91.56
7	0.06302	0.3927	0.0	0.39342	89.36
8	0.07081	1.0	0.00160	0.99912	86.01
9	0.08170	2.0	0.00145	1.99927	80.56
10	0.09043	2.59536	0.0	2.59608	77.35
11	0.09927	2.72539	0.0	2.72611	76.66
12	0.10855	2.62814	0.0	2.62886	77.18
13	0.11875	2.37288	0.0	2.37360	78.54
14	0.12816	2.44503	0.0	2.44575	78.16
15	0.13534	3.0	0.00298	2.99774	75.22
16	0.14186	4.0	0.00416	3.99656	69.99
17	0.14694	5.0	0.01133	4.98939	64.89
18	0.14889	5.43842	0.0	5.43914	62.62

Table F5. MZI Interferogram Data for the Calculation of Fringe Spacing and Fractional Shift on the Top Horizontal Wall

Location No.	x-Cordn. Measured Along the Enclosure Width (in)	$\Delta x = b$ (in)	$\bar{b}$ (in)	y_{Upper} (in)	$y_{Reference}$ (in)	y_{Lower} (in)	Fractional Shift
1	0.0		--	--	1.62800	--	--
		0.10556					
2	0.10556		0.11100	1.64120	1.62800	1.62000	0.62264
		0.11643					
3	0.22199		0.11100	--	1.62800	--	--
		0.10556					
4	0.32754		0.10556	1.63170	1.62800	1.61000	0.17051
		0.10556					
5	0.43310		0.10556	1.63620	1.62800	1.61420	0.37273
		0.10556					
6	0.53865		0.10556	1.64130	1.62800	1.61950	0.61001
		0.10556					
7	0.64421		0.09807	1.64600	1.62800	1.62430	0.82949
		0.09057					
8	0.73478		0.11353	--	1.62800	--	--
		0.13648					
9	0.87126		0.08070	--	1.62800	--	--
		0.02491					
10	0.89617		0.03304	--	1.62800	--	--
		0.04117					
11	0.93734		0.03764	--	1.62800	--	--
		0.03410					
12	0.97144		--	--	1.62800	--	--

Table F6. MZI Data for the Temperature Distribution on the Top Horizontal Wall

Location No.	Distance Measured from the Left-Hand Vertical Wall of the Enclosure (ft)	S	ΔS_1	S_{ideal}	$T(^0F)$
1	0.0	0.0	0.0017	0.0	91.56
2	0.00880	0.62264	0.0	0.62434	88.08
3	0.01850	1.0	0.00163	1.00007	86.00
4	0.02730	1.17051	0.0	1.17221	85.06
5	0.03609	1.37273	0.0	1.37443	83.95
6	0.04489	1.61001	0.0	1.61171	82.65
7	0.05368	1.82949	0.0	1.83119	81.46
8	0.06123	2.0	0.00156	2.00014	80.55
9	0.07261	3.0	0.00309	2.99861	75.22
10	0.07468	4.0	0.01845	3.98325	70.06
11	0.07811	5.0	0.01422	4.98748	64.90
12	0.08095	6.0	0.00999	5.99171	59.84

APPENDIX G

PRESENTATION AND REDUCTION OF THE DATA TAKEN WITH THE WOLLASTON PRISM INTERFEROMETER

The WPI data was reduced using the procedures outlined in Appendix D. The values of the fixed constants required to reduce this data are given by:

$\lambda \equiv$ wavelength of the He-Ne laser = 2.076×10^{-6} (ft)

R ≡ ideal gas constant for air = 53.35 ($ft\text{-}lb_f/lb_m\text{-}{}^0R$)

$(K_{GD})_{hot\ wall} \equiv$ Gladstone-Dale constant for air for the rough vertical wall

= 3.658×10^{-3} (ft^3/lb_m)

and,

$(K_{GD})_{cold\ wall} \equiv$ Gladstone-Dale constant for air for the smooth vertical wall

= 3.536×10^{-3} (ft^3/lb_m).

The Wollaston Prism interferograms for the undisturbed and disturbed fringes are given in Figures G1 and G2, respectively. The values of the measured variables were found to be:

$P_{at} \equiv$ atmospheric pressure = 2116.8 (lb_f/ft^2)

$(T_w)_{hot\ wall} \equiv$ temperature of the rough vertical wall = 544.76 (${}^0R$)

$(T_w)_{cold\ wall} \equiv$ temperature of the smooth vertical wall = 510.14 (${}^0R$)

f ≡ focal length of the spherical mirror that focuses the beam of light that exits the test section = 4.93 (ft)

v ≡ distance from the camera to the sperical mirror = 7.63 (ft)

(Enclosure at Uniform Temperature of 19.8 ^0C)

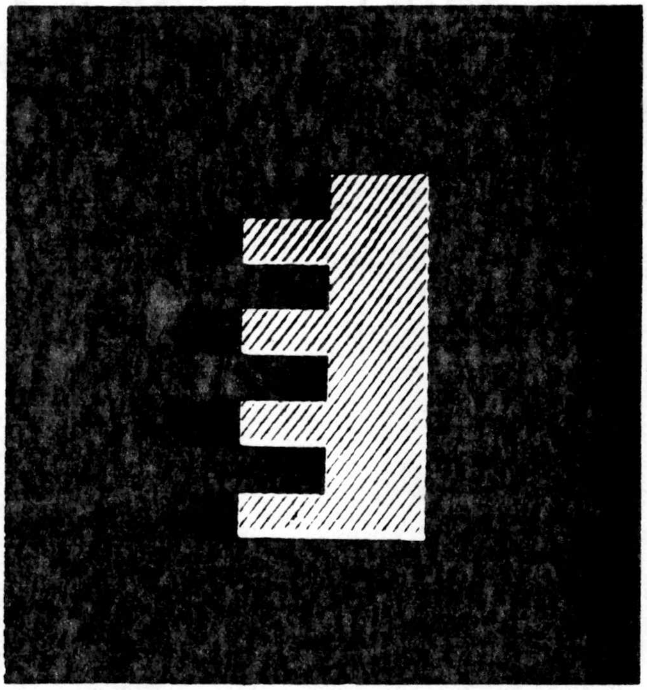

Figure G1. Wollaston Prism Interferogram (Undisturbed Fringes)

$Gr = 1.90 \times 10^6$
$Pr = 0.72$
$W/H = 0.4$
$A = 0.12$
$\delta = 0.25$
$\delta_0 = 0$

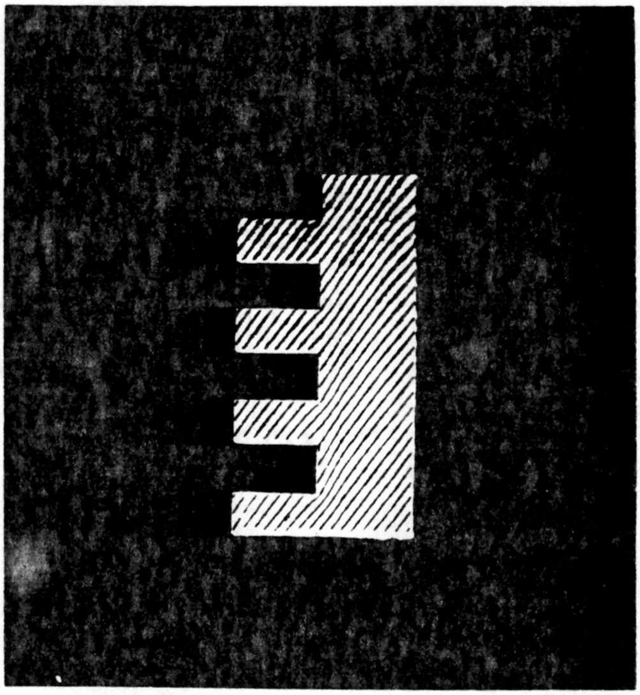

Figure G2. Wollaston Prism Interferogram (Deflected Fringes)

$w \equiv$ distance from the focal point of the focusing mirror to the centerline of the Wollaston Prism = 1.56 (ft)

$Z \equiv$ length of the test section (length of the optical path) = 0.80833 (ft)

$\beta \equiv$ wedge angle of the Wollaston Prism = 0.0527 (deg)

$M \equiv$ magnification factor = 0.53204

$(x_i,y_i) \equiv$ coordinates of reference points 1 through 4 [given in inches as measured on the interferogram (no magnification)]

$$(x_1,y_1) = (1.06650, 0.62470)$$

$$(x_2,y_2) = (1.52905, 1.25100)$$

$$(x_3,y_3) = (1.22605, 1.46470)$$

$$(x_4,y_4) = (1.48665, 0.49160)$$

and,

$N \equiv$ number of fringes between reference points 3 and 4 = 17.

In addition to the above measurements, the x- and y-coordinates of the reference points 5, 6, 7, and 8 (defined in Figure D2) were measured from the interferograms for each location at which the wall heat flux was calculated. These values are listed in Tables G1 and G2.

In order to measure the above coordinates, the interferogram was placed on the stage of the Nikon microscope in such a way that the y-axis of the microscope was parallel to the cold vertical wall. By positioning the interferogram in this manner, the measurements of the coordinates y_7 and y_8 were not required to calculate the boundary layer thickness δ, using equation D.10. This applies to all points on the cold vertical wall and on the vertically-oriented segments of the hot wall because the values of y_7 and y_8 are identical at each of these locations. Similarly, the measurements of the coordinates x_7 and x_8 were not required to

Table G1. Measured Coordinates of Reference Points 5, 6, 7, and 8 for All Locations on the Cold Wall

Location No.	Distance Measured Along the Wall from the Bottom of the Enclosure (in)	x_5 (in)	y_5 (in)	x_6 (in)	y_6 (in)	x_7 (in)	y_7 (in)	x_8 (in)	y_8 (in)
1	0.138	--	--	--	--	--	--	--	--
2	0.284	--	--	--	--	--	--	--	--
3	0.427	--	--	--	--	--	--	--	--
4	0.558	1.6108	0.3320	1.5071	0.2044	1.5605	--	1.6103	--
5	0.702	1.6102	0.4087	1.4578	0.2168	1.5444	--	1.6105	--
6	0.838	1.6083	0.4808	1.4330	0.2597	1.5226	--	1.6114	--
7	0.982	1.6112	0.5574	1.3905	0.2811	1.5036	--	1.6120	--
8	1.122	1.6112	0.6320	1.4323	0.4137	1.5298	--	1.6105	--
9	1.265	1.6112	0.7082	1.4178	0.4721	1.5238	--	1.6118	--
10	1.407	1.6101	0.7835	1.3922	0.5178	1.5091	--	1.6130	--
11	1.552	1.6101	0.8608	1.4181	0.6303	1.5190	--	1.6128	--
12	1.692	1.6079	0.9350	1.4057	0.6901	1.4951	--	1.6090	--
13	1.835	1.6079	1.0113	1.4075	0.7712	1.5065	--	1.6089	--
14	1.975	1.6088	1.0857	1.3994	0.8364	1.5087	--	1.6092	--
15	2.113	1.6064	1.1593	1.3665	0.8698	1.5166	--	1.6093	--
16	2.261	1.6092	1.2381	1.3979	0.9920	1.5210	--	1.6067	--
17	2.399	1.6075	1.3114	1.4058	1.0800	1.5106	--	1.6082	--
18	2.542	1.6075	1.3874	1.3736	1.1148	1.5031	--	1.6078	--
19	2.671	1.6052	1.4563	1.3756	1.1960	1.5110	--	1.6071	--
20	2.813	1.6037	1.5315	1.4242	1.3405	1.5145	--	1.6049	--
21	2.958	1.6050	1.6086	1.3709	1.3468	1.5105	--	1.6042	--
22	3.095	1.6022	1.6814	1.3915	1.4536	1.5131	--	1.6038	--
23	3.239	1.6003	1.7583	1.4094	1.5566	1.5221	--	1.6036	--
24	3.410	1.6014	1.8493	1.3570	1.5617	1.5188	--	1.6059	--

Table G2. Measured Coordinates of Reference Points 5, 6, 7, and 8 for All Locations on the Hot Wall

Location No.	Distance Measured Along the Wall from the Bottom of the Enclosure (in)	x_5 (in)	y_5 (in)	x_6 (in)	y_6 (in)	x_7 (in)	y_7 (in)	x_8 (in)	y_8 (in)
1	0.087	0.6713	0.0777	0.7675	0.2207	0.7212	--	0.6671	--
2	0.391	--	--	--	--	--	--	--	--
3	0.442	--	--	--	--	--	--	--	--
4	0.878	0.9070	0.2456	0.7878	0.0947	--	0.1797	--	0.2497
5	1.000	0.9723	0.2480	0.8384	0.0805	--	0.1613	--	0.2497
6	1.118	1.0343	0.2500	0.8897	0.0704	--	0.1462	--	0.2516
7	1.381	1.1166	0.3258	1.3478	0.6920	1.1959	--	1.1139	--
8	1.541	1.1165	0.4110	1.3993	0.8379	1.1959	--	1.1139	--
9	2.456	--	--	--	--	--	--	--	--
10	2.814	--	--	--	--	--	--	--	--
11	3.073	--	--	--	--	--	--	--	--
12	3.630	1.0331	0.7199	0.8935	0.5437	--	0.6835	--	0.7228
13	3.935	1.1148	0.8120	1.3560	1.1688	1.1974	--	1.1137	--
14	4.087	1.1159	0.8928	1.3587	1.2488	1.1953	--	1.1159	--
15	4.970	--	--	--	--	--	--	--	--
16	5.290	--	--	--	--	--	--	--	--
17	5.579	--	--	--	--	--	--	--	--
18	6.477	1.1182	1.2966	1.2874	1.5436	1.1800	--	1.1116	--
19	6.625	1.1171	1.3745	1.3614	1.7230	1.1578	--	1.1171	--
20	7.509	--	--	--	--	--	--	--	--
21	7.825	--	--	--	--	--	--	--	--
22	8.095	--	--	--	--	--	--	--	--
23	9.175	--	--	--	--	--	--	--	--

calculate δ at all points on the horizontally-oriented segments of the hot wall. As mentioned earlier, the local heat flux on the solid walls of the enclosure is proportional to the fringe shift ΔS. Thus, no measurements were taken at the points on the interferograms where no fringe shifts could be observed. The appropriate entries for these points in Tables G1 and G2 are, therefore, left blank.

After making the measurements listed above, the calculations described below were performed. The thermal conductivities of the air at the hot wall and the cold wall temperatures were found to be

$$(k_w)_{hot\ wall} = 0.01509\ (Btu/hr\text{-}ft\text{-}^0F) \qquad (at\ T_w = 544.76\ ^0R)$$

$$(k_w)_{cold\ wall} = 0.01437\ (Btu/hr\text{-}ft\text{-}^0F) \qquad (at\ T_w = 510.14\ ^0R)$$

respectively. The quantity, u, defined by equation D.2 was computed as 13.92 (ft) and the double image distance, h, was given by equation D.3 as 0.1917×10^{-2} (ft). The fringe angle, α, was computed using equation D.5 as 53.56 degrees. Equation D.6 then gave the angle θ as 53.56 degrees for all points on the cold wall and on the vertically-oriented segments of the hot wall. Equation D.7 gave a value of θ equal to 36.44 degrees for all points located on the horizontally-oriented segments of the hot wall. Finally, equation D.8 gave a value of the fringe spacing, S, as 3.862×10^{-3} (ft).

The remaining calculations had to be performed at <u>each location</u> on the vertical walls where the local wall heat flux was evaluated. These calculations entailed using equations D.9, D.10, D.11, D.12, and D.1 to compute the fringe displacement, ΔS, the boundary layer thickness, δ, the end effect correction to the optical path length, $(\Delta Z)_{end}$, the effective optical path length, Z_{eff}, and the local wall heat flux, $\dot{q}_w$, respectively. The results of these calculations are listed in Table G3 for the cold vertical wall and Table G4 for the hot vertical wall. <u>No fringe shifts could be detected on the horizontal walls of the enclosure.</u>

Table G3. Calculated Values for All Locations on the Cold Wall

Location No.	ΔS (ft)	δ (ft)	$(\Delta Z)_{end}$ (ft)	Z_{eff} (ft)	$\dot{q}_w$ (Btu/ht-ft^2)
1	0.0	--	--	--	0.0
2	0.0	--	--	--	0.0
3	0.0	--	--	--	0.0
4	60.52×10^{-5}	78.00×10^{-4}	35.06×10^{-4}	0.81184	6.929
5	67.63×10^{-5}	10.36×10^{-3}	39.81×10^{-4}	0.81231	7.738
6	75.74×10^{-5}	13.91×10^{-3}	44.85×10^{-4}	0.81282	8.661
7	10.60×10^{-4}	16.99×10^{-3}	48.27×10^{-4}	0.81316	12.117
8	11.38×10^{-4}	12.65×10^{-3}	43.20×10^{-4}	0.81265	13.019
9	12.31×10^{-4}	13.78×10^{-3}	44.67×10^{-4}	0.81280	14.080
10	14.00×10^{-4}	16.27×10^{-3}	47.55×10^{-4}	0.81309	16.000
11	14.10×10^{-4}	14.69×10^{-3}	45.77×10^{-4}	0.81291	16.118
12	13.81×10^{-4}	17.84×10^{-3}	49.15×10^{-4}	0.81325	15.784
13	15.04×10^{-4}	16.03×10^{-3}	47.27×10^{-4}	0.81306	17.192
14	16.45×10^{-4}	15.74×10^{-3}	46.96×10^{-4}	0.81303	18.803
15	16.90×10^{-4}	14.52×10^{-3}	45.57×10^{-4}	0.81289	19.326
16	19.32×10^{-4}	13.45×10^{-3}	44.25×10^{-4}	0.81276	22.098
17	20.17×10^{-4}	15.29×10^{-3}	46.45×10^{-4}	0.81298	23.058
18	21.27×10^{-4}	16.40×10^{-3}	47.67×10^{-4}	0.81310	24.318
19	24.47×10^{-4}	15.05×10^{-3}	46.18×10^{-4}	0.81295	27.973
20	25.36×10^{-4}	14.02×10^{-3}	44.96×10^{-4}	0.81283	28.998
21	26.77×10^{-4}	14.68×10^{-3}	45.76×10^{-4}	0.81291	30.606
22	27.99×10^{-4}	14.21×10^{-3}	45.19×10^{-4}	0.81285	32.003
23	27.65×10^{-4}	12.76×10^{-3}	43.35×10^{-4}	0.81267	31.619
24	20.85×10^{-4}	13.64×10^{-3}	44.49×10^{-4}	0.81278	23.842

Table G4. Calculated Values for All Locations on the Hot Wall

Location No.	ΔS (ft)	δ (ft)	$(\Delta Z)_{end}$ (ft)	Z_{eff} (ft)	$\dot{q}_W$ (Btu/ht-ft^2)
1	66.04×10^{-5}	84.74×10^{-4}	36.43×10^{-4}	0.81198	8.750
2	0.0	--	--	--	0.0
3	0.0	--	--	--	0.0
4	48.72×10^{-5}	10.96×10^{-3}	40.76×10^{-4}	0.81241	8.737
5	64.98×10^{-5}	13.85×10^{-3}	44.75×10^{-4}	0.81281	11.647
6	76.63×10^{-5}	16.52×10^{-3}	47.79×10^{-4}	0.81311	13.731
7	26.99×10^{-4}	12.84×10^{-3}	43.46×10^{-4}	0.81268	35.733
8	22.58×10^{-4}	12.84×10^{-3}	43.46×10^{-4}	0.81268	29.889
9	0.0	--	--	--	0.0
10	0.0	--	--	--	0.0
11	0.0	--	--	--	0.0
12	60.54×10^{-5}	61.48×10^{-4}	31.15×10^{-4}	0.81145	10.869
13	15.63×10^{-4}	13.11×10^{-3}	43.81×10^{-4}	0.81271	20.693
14	14.20×10^{-4}	12.44×10^{-3}	42.95×10^{-4}	0.81263	18.795
15	0.0	--	--	--	0.0
16	0.0	--	--	--	0.0
17	0.0	--	--	--	0.0
18	93.64×10^{-5}	10.71×10^{-3}	40.38×10^{-4}	0.81237	12.402
19	94.36×10^{-5}	63.75×10^{-4}	31.74×10^{-4}	0.81151	12.510
20	0.0	--	--	--	0.0
21	0.0	--	--	--	0.0
22	0.0	--	--	--	0.0
23	0.0	--	--	--	0.0

An uncertainty analysis for the WPI is given in Appendix H.

APPENDIX H
UNCERTAINTY ANALYSIS

It is important to perform some kind of analysis on all experimental data. The uncertainties of the WPI and the MZI data will be calculated in this Appendix. The calculations will be done by using the technique presented by Kline and McClintock (1953). In this technique, the uncertainty of the experimental data is calculated by a careful estimation of the uncertainties of the various experimental measurements.

H.1 Uncertainty Analysis of WPI Data

An uncertainty analysis of the local heat flux values obtained by WPI was performed. To calculate the local heat flux, equation (D.1) was used. This equation is rewritten as,

$$\dot{q}_w = \left[\frac{\lambda \; R \; T_w^{\;2} \; k_w}{K_{GD} \; h \; P \; \mathrm{Sin}\theta \; S}\right] \left[\frac{\Delta S}{Z_{eff}}\right]. \qquad \text{(H.1-1)}$$

Assume that uncertainty in $\dot{q}_w$ is due to uncertainty in the quantities h, ΔS, S, T_w, P, θ, Z_{eff}. Uncertainty due to the quantities k_w, λ, K_{GD}, and R are neglected. The equation for the double image distance is,

$$h = \beta \left(f - \frac{uw}{f} + w\right)$$

then,

$$\frac{\partial h}{\partial \beta} = \left(f - \frac{uw}{f} + w\right) \; ; \quad \frac{\partial h}{\partial f} = \beta \left(1 + \frac{uw}{f^2}\right)$$

$$\frac{\partial h}{\partial u} = -\frac{\beta w}{f}\ ; \quad \frac{\partial h}{\partial w} = \beta\,(1 - \frac{u}{f}).$$

Assume the uncertainty of the following parameters:

$$\omega_\beta = 5\%,\ \omega_f = 1.0 \text{ inch},\ \ \omega_w = 0.15 \text{ inch},\ \omega_v = 0.25 \text{ inch},$$

and the values of the following parameters are:

$$f = 59.11 \text{ inches},\ \ v = 91.50 \text{ inches},\ w = 18.69 \text{ inches}$$

also,

$$\frac{1}{u} = \frac{1}{f} - \frac{1}{v}$$

$$\text{or,}\ \ u = \frac{1}{(\frac{1}{f} - \frac{1}{v})} = \frac{vf}{v - f} = \frac{91.50 \text{ x } 59.11}{91.50 - 59.11} = 166.98 \text{ inches}$$

$$\frac{\partial u}{\partial f} = \frac{v}{v - f} + (\frac{1}{v - f})^2 vf$$

$$\frac{\partial u}{\partial v} = \frac{f}{v - f} - (\frac{1}{v - f})^2 vf$$

$$\omega_u = \sqrt{(\omega_f \frac{\partial u}{\partial f})^2 + (\omega_v \frac{\partial u}{\partial v})^2}$$

$$\text{or,}\ \ \omega_u = \Big[\Big\{1.0(\frac{91.50}{91.50 - 59.11} + \frac{91.50\text{x}59.11}{(91.50 - 59.11)^2})\Big\}^2 + \Big\{0.25(\frac{59.11}{91.50 - 59.11} - \frac{91.50\text{x}59.11}{(91.50 - 59.11)^2})\Big\}^2\Big]^{0.5}$$

or, $\omega_u = 8.02$ inches $= 4.81\%$ = uncertainty in (u).

Simillarly the uncertainty in double image distance can be obtained as,

$$\omega_h = \sqrt{(\omega_\beta \frac{\partial h}{\partial \beta})^2 + (\omega_f \frac{\partial h}{\partial f})^2 + (\omega_u \frac{\partial h}{\partial u})^2 + (\omega_v \frac{\partial h}{\partial w})^2}$$

or,

$$\omega_h = \Big[\{ \frac{0.0026\,\pi}{180} (59.11 - \frac{166.98\text{x}18.69}{59.11} + 18.69) \}^2$$

$$+ \{ 1.0 \frac{0.0527\,\pi}{180} (1.0 + \frac{166.98\text{x}18.69}{(59.11)^2}) \}^2$$

$$+ \{ 8.02 \frac{0.0527\,\pi}{180} (- \frac{18.69}{59.11}) \}^2$$

$$+ \{ 0.25 \frac{0.0527\,\pi}{180} (1.0 - \frac{166.98}{59.11}) \}^2 \Big]^{0.5}$$

or, $\omega_h = 0.00315$ inch $= 13.70\%$ = uncertainty in double image distance.

Assume the following uncertainties:

$\omega_{\Delta S} = 1.5\%$ $\omega_S = 1.5\%$ $\omega_T = 1.0\ ^0R$

$\omega_\theta = 1\%$ $\omega_P = 0.705\ lb_f/ft^2$ $\omega_{Zeff} = 1\%$.

From equation (H.1-1), the following expressions can be written:

$$\frac{\partial \dot{q}_w}{\partial Z_{eff}} = \left[\frac{\lambda\ R\ T_w^{\ 2}\ k_w}{K_{GD}\ h\ P\ \mathrm{Sin}\theta\ S}\right]\left[-\frac{\Delta S}{Z_{eff}^{\ 2}}\right] = \frac{-C(\Delta S)}{Z_{eff}^{\ 2}}$$

$$\frac{\partial \dot{q}_w}{\partial h} = \left[\frac{-\lambda\ R\ T_w^{\ 2}\ k_w}{K_{GD}\ h^2\ P\ \mathrm{Sin}\theta\ S}\right]\left[\frac{\Delta S}{Z_{eff}}\right] = \frac{-C(\Delta S)}{h\ Z_{eff}}$$

$$\frac{\partial \dot{q}_w}{\partial \Delta S} = \left[\frac{\lambda\ R\ T_w^{\ 2}\ k_w}{K_{GD}\ h\ P\ \mathrm{Sin}\theta\ S}\right]\left[\frac{1}{Z_{eff}}\right] = \frac{C}{Z_{eff}}$$

$$\frac{\partial \dot{q}_w}{\partial S} = \left[\frac{-\lambda\ R\ T_w^{\ 2}\ k_w}{K_{GD}\ h\ P\ \mathrm{Sin}\theta\ S^2}\right]\left[\frac{\Delta S}{Z_{eff}}\right] = \frac{-C(\Delta S)}{S\ Z_{eff}}$$

$$\frac{\partial \dot{q}_w}{\partial T_w} = \left[\frac{\lambda\ R\ 2T_w\ k_w}{K_{GD}\ h\ P\ \mathrm{Sin}\theta\ S}\right]\left[\frac{\Delta S}{Z_{eff}}\right] = \frac{2C(\Delta S)}{T_w\ Z_{eff}}$$

$$\frac{\partial \dot{q}_w}{\partial P} = \left[\frac{-\lambda\ R\ T_w^{\ 2}\ k_w}{K_{GD}\ h\ P^2\ \mathrm{Sin}\theta\ S}\right]\left[\frac{\Delta S}{Z_{eff}}\right] = \frac{-C(\Delta S)}{P\ Z_{eff}}$$

$$\frac{\partial \dot{q}_w}{\partial \theta} = \left[\frac{-\lambda\ R\ T_w^{\ 2}\ k_w\ \mathrm{Cos}\theta}{K_{GD}\ h\ P\ \mathrm{Sin}^2\theta\ S}\right]\left[\frac{\Delta S}{Z_{eff}}\right] = \frac{-C(\Delta S)}{\mathrm{Tan}\theta\ Z_{eff}}$$

where,

$$C = \left[\frac{\lambda\ R\ T_w^{\ 2}\ k_w}{K_{GD}\ h\ P\ \mathrm{Sin}\theta\ S}\right].$$

Using the technique described by Kline and McClintock (1953), the uncertainty in local heat flux can be calculated from the following expression:

$$\omega_{\dot{q}_w} = \Big[(\omega_{Z_{eff}}\frac{\partial \dot{q}_W}{\partial Z_{eff}})^2 + (\omega_h\frac{\partial \dot{q}_W}{\partial h})^2 + (\omega_{\Delta S}\frac{\partial \dot{q}_W}{\partial \Delta S})^2 + (\omega_S\frac{\partial \dot{q}_W}{\partial S})^2 + (\omega_{T_w}\frac{\partial \dot{q}_W}{\partial T_w})^2$$
$$+ (\omega_P\frac{\partial \dot{q}_W}{\partial P})^2 + (\omega_\theta\frac{\partial \dot{q}_W}{\partial \theta})^2\Big]^{0.5}$$

.

For the cold wall $T_w = 50.14\ ^0F = 510.14\ ^0R$, which gives $C = 774.56$.

Therefore,

$$\omega_{\dot{q}_w} = \Big[(-\frac{0.01\ Z_{eff}\ C\ \Delta S}{Z_{eff}^2})^2 + (-\frac{0.137\ h\ C\ \Delta S}{h\ Z_{eff}})^2 + (\frac{0.015\ \Delta S\ C}{Z_{eff}})^2$$
$$+ (-\frac{0.015\ S\ C\ \Delta S}{S\ Z_{eff}})^2 + (\frac{(1.0)(2)C\ \Delta S}{T_w\ Z_{eff}})^2$$
$$+ (-\frac{0.00033\ P\ C\ \Delta S}{P\ Z_{eff}})^2 + (-\frac{0.01\ \theta\ C\ \Delta S}{\mathrm{Tan}\theta\ Z_{eff}})^2\Big]^{0.5}$$

or, $$\omega_{\dot{q}_w} = \frac{C(\Delta S)}{Z_{eff}}\Big[(-0.01)^2 + (-0.137)^2 + (0.015)^2 + (-0.015)^2 + (0.00392)^2 + (-0.00033)^2 + (-0.0069)^2\Big]^{0.5}$$

or, $\omega_{\dot{q}_w} = 107.83\ \frac{\Delta S}{Z_{eff}}$ = uncertainty in heat flux along the cold wall.

At $\Delta S = 9.0891 \times 10^{-3}$ inch and $Z_{eff} = 0.81282$ ft, the local heat flux is

$$\dot{q}_W = 8.6613\frac{\mathrm{Btu}}{\mathrm{hr\ ft}^2}.$$

$$\text{Therefore,} \quad \omega_{\dot{q}_w} = 1.2058 \, \frac{\text{Btu}}{\text{hr ft}^2}$$

$$\text{or,} \quad \omega_{\dot{q}_w} = \frac{1.2058}{8.6613} = 13.92\% \text{ uncertainty in local heat flux along cold wall.}$$

Similarly,

For the hot wall $T_w = 84.76\ ^0F = 544.76\ ^0R$, which gives $C = 896.59$.

Therefore,

$$\omega_{\dot{q}_w} = \Big[\Big(-\frac{0.01\, Z_{eff}\, C\, \Delta S}{Z_{eff}^2}\Big)^2 + \Big(-\frac{0.1370\, h\, C\, \Delta S}{h\, Z_{eff}}\Big)^2 + \Big(\frac{0.015\, \Delta S\, C}{Z_{eff}}\Big)^2$$

$$+ \Big(-\frac{0.015\, S\, C\, \Delta S}{S\, Z_{eff}}\Big)^2 + \Big(\frac{(1.0)(2) C\, \Delta S}{T_w\, Z_{eff}}\Big)^2$$

$$+ \Big(-\frac{0.00033\, P\, C\, \Delta S}{P\, Z_{eff}}\Big)^2 + \Big(-\frac{0.01\, \theta\, C\, \Delta S}{\text{Tan}\theta\, Z_{eff}}\Big)^2 \Big]^{0.5}$$

$$\text{or,} \quad \omega_{\dot{q}_w} = \frac{C(\Delta S)}{Z_{eff}} \Big[(-0.01)^2 + (-0.137)^2 + (0.015)^2 + (-0.015)^2 + (0.00367)^2 + (-0.00033)^2 + (-0.0069)^2 \Big]^{0.5}$$

$$\text{or,} \quad \omega_{\dot{q}_w} = 124.82 \, \frac{\Delta S}{Z_{eff}} = \text{ uncertainty in heat flux along the hot wall.}$$

At $\Delta S = 3.2388 \times 10^{-2}$ inch and $Z_{eff} = 0.81268$ ft, the local heat flux is

$$\dot{q}_w = 35.7325 \frac{Btu}{hr\ ft^2}.$$

$$\text{Therefore,}\quad \omega_{\dot{q}_w} = 4.9744 \frac{Btu}{hr\ ft^2}$$

or, $\omega_{\dot{q}_w} = \dfrac{4.9744}{35.7325} = 13.92\%$ uncertainty in local heat flux along hot wall.

The Nusselt number, Nu, is defined as

$$Nu = \frac{hH}{k} = \frac{\dot{q}_w H}{k(T_H^* - T_C^*)} \qquad \text{(H.1-2)}$$

Assume that uncertainty in Nu is due to uncertainties in the quantities $\dot{q}_w$, H, T_H^* and T_C^*. Uncertainty due to thermal conductivity, k, is neglected. From equation (H.1-2) the following expressions can be written:

$$\frac{\partial(Nu)}{\partial \dot{q}_w} = \frac{H}{k(T_H^* - T_C^*)}$$

$$\frac{\partial(Nu)}{\partial H} = \frac{\dot{q}_w}{k(T_H^* - T_C^*)}$$

$$\frac{\partial(Nu)}{\partial T_H^*} = -\frac{\dot{q}_w H}{k(T_H^* - T_C^*)^2}$$

$$\frac{\partial(Nu)}{\partial T_C^*} = \frac{\dot{q}_w H}{k(T_H^* - T_C^*)^2}$$

The uncertainty in Nusselt number is given by,

$$\omega_{Nu} = \sqrt{\left(\omega_{\dot{q}_w} \frac{\partial(Nu)}{\partial \dot{q}_w}\right) + \left(\omega_H \frac{\partial(Nu)}{\partial H}\right)^2 + \left(\omega_{T^*_H} \frac{\partial(Nu)}{\partial T_H^*}\right)^2 + \left(\omega_{T^*_C} \frac{\partial(Nu)}{\partial T_C^*}\right)^2} \quad \text{(H.1-3)}$$

Here, $H = 3.448/12 = 0.2833$ (ft), $k = 0.015$ Btu/hr-ft ^{0}F, $T_H^* = 84.76\ ^0$F, $T_C^* = 50.14\ ^0$F, $\dot{q}_w = 35.7325$ Btu/hr ft^2 and $\omega_{\dot{q}_w} = 4.9744$ Btu/hr ft^2.

Assume the following uncertainties:

$$\omega_{T^*_H} = \omega_{T^*_C} = 0.1\ ^0\text{F} \qquad\qquad \omega_H = 1\%.$$

Substituting the above values in equation (H.1-3), the uncertainty in the Nusselt number is obtained as:

$$\omega_{Nu} = 2.76.$$

H.2 Uncertainty Analysis of MZI Data

It is discussed in Appendix C that two equations namely equations (C.8) and (C.9) were used to calculate the temperature distribution of the test section. In this section, the uncertainties associated in using these two equations will be discussed using the technique described by Kline and McClintock (1953).

H.2.1 Uncertainty in Using Equation (C.8)

Equation (C.8) can be rewritten as

$$T^* = \frac{T^*_w}{1 - \dfrac{C_1 T^*_w}{P\ Z} S} \qquad \text{(H.2-1)}$$

where, $$C_1 = \frac{2\lambda R}{3\bar{r}} = \frac{(2)(2.076 \times 10^{-6})(53.35)}{(3)(24.1171 \times 10^{-4})} = 0.03062.$$

Assume that the uncertainty in temperature, T^*, is due the uncertainties in the parameters T^*_w, P, Z, and S. Uncertainty due to C_1 is neglected. According to the technique described by Kline and McClintock (1953), the uncertainty in temperature is given by the following expression:

$$\omega_{T^*} = \sqrt{\left(\omega_{T^*_w} \frac{\partial T^*}{\partial T^*_w}\right)^2 + \left(\omega_P \frac{\partial T^*}{\partial P}\right)^2 + \left(\omega_Z \frac{\partial T^*}{\partial Z}\right)^2 + \left(\omega_S \frac{\partial T^*}{\partial S}\right)^2} \qquad \text{(H.2-2)}$$

From equation (H.2-1) the following expressions can be written:

$$\frac{\partial T^*}{\partial T^*_w} = \frac{D_1 + \left(\frac{C_1 S}{P Z}\right) T^*_w}{D_1^2}$$

$$\frac{\partial T^*}{\partial P} = -\frac{\left(\frac{C_1 S}{P^2 Z}\right) T^{*2}_w}{D_1^2}$$

$$\frac{\partial T^*}{\partial Z} = -\frac{\left(\frac{C_1 S}{P Z^2}\right) T^{*2}_w}{D_1^2}$$

$$\frac{\partial T^*}{\partial S} = \frac{\left(\frac{C_1}{P Z}\right) T^{*2}_w}{D_1^2}$$

where, $$D_1 = 1 - (\frac{C_1\,T^*_w}{P\;Z})\,S.$$

The following table is obtained by substituting nominal values of $T^*_w = 518.06\ ^0R$, $P = 2049.08\ lb_f/ft^2$, $Z = 0.80833$ ft, and $S = 0$, & 5.56 (the minimum & approximate maximum value of S).

	S = 0	S = 5.56
$\partial T^*/\partial T^*_w$	1.0	1.116
$\partial T^*/\partial P$	0.0	− 0.015
$\partial T^*/\partial Z$	0.0	− 38.074
$\partial T^*/\partial S$	4.962	5.535

Thus form equation (H.2-2), at S = 0,

$$\omega_{T^*} = \sqrt{(\omega_{T^*_w})^2 + (4.962\omega_S)^2}$$

and at S = 5.56,

$$\omega_{T^*} = \sqrt{(1.116\omega_{T^*_w})^2 + (-\,0.015\omega_P)^2 + (-\,38.074\omega_Z)^2 + (5.535\omega_S)^2}\ .$$

Assume the following values of the uncertainties:

$\omega_{T^*_w} = 1.0\ ^0R$ $\quad$ $\omega_P = 0.705\ lb_f/ft^2$ $\quad$ $\omega_Z = 0.008$ ft $\quad$ $\omega_S = 0.1$.

Substituting these values the uncertainty in temperature is obtained as follows:

at $S = 0$ $\qquad \omega_{T^*} = 1.12\ ^0R$, and

at $S = 5.56$ $\quad \omega_{T^*} = 1.28\ ^0R$.

The dimensionless temperature, T, is defined as

$$T = \frac{T^* - T^*_C}{T^*_H - T^*_C} = \frac{T^* - T^*_C}{\Delta T^*} \tag{H.2-3}$$

where, $T^*_C = 518.06\ ^0R$ and $\Delta T^* = 33.17\ ^0R$.

The uncertainty in dimensionless temperature is given by

$$\omega_T = \sqrt{\left(\omega_{T^*} \frac{\partial T}{\partial T^*}\right)^2 + \left(\omega_{T^*_C} \frac{\partial T}{\partial T^*_C}\right)^2 + \left(\omega_{\Delta T^*} \frac{\partial T}{\partial \Delta T^*}\right)^2} \ . \tag{H.2-4}$$

From equation (H.2-3) the following expressions can be written:

$$\frac{\partial T}{\partial T^*} = \frac{1}{\Delta T^*}$$

$$\frac{\partial T}{\partial T^*_C} = -\ \frac{1}{\Delta T^*}$$

$$\frac{\partial T}{\partial (\Delta T^*)} = -\frac{T^* - T^*_C}{(\Delta T^*)^2} .$$

At S = 0, $T^* = 518.06\ {}^0R$ and at S = 5.56, $T^* = 547.19\ {}^0R$. Assume that the uncertainties in T^*_C and ΔT^* are:

$$\omega_{T^*_C} = \omega_{\Delta T^*} = 1.0\ {}^0R.$$

Substituting the above values in equation (H.2-4), the uncertainty in nondemensional temperature is obtained as follows:

at S = 0 $\quad \omega_T = 0.05$, and

at S = 5.56 $\quad \omega_T = 0.06$.

H.2.2 Uncertainty in Using Equation (C.9)

Equation (C.9) can rewritten as

$$T^* = \frac{T^*_w}{1 + \frac{C_2\, T^*_w}{P\ Z}\ S} \tag{H.2-5}$$

where,
$$C_2 = \frac{2\lambda\ R}{3\bar{r}} = \frac{(2)(2.076 \times 10^{-6})(53.35)}{(3)(24.1171 \times 10^{-4})} = 0.03062.$$

Assume that the uncertainty in temperature, T^*, is due the uncertainties in the parameters T^*_w, P, Z, and S. Uncertainty due to C_2 is neglected. Same as in section H.2.1, equation (H.2-2) can be used to calculate the uncertainty in temperature.

From equation (H.2-5) the following expressions can be written:

$$\frac{\partial T^*}{\partial T^*_w} = \frac{D_2 - (\frac{C_2\,S}{P\,Z})\,T^*_w}{D_2^2}$$

$$\frac{\partial T^*}{\partial P} = \frac{(\frac{C_2\,S}{P^2\,Z})\,T^{*\,2}_w}{D_2^2}$$

$$\frac{\partial T^*}{\partial Z} = \frac{(\frac{C_2\,S}{P\,Z^2})\,T^{*\,2}_w}{D_2^2}$$

$$\frac{\partial T^*}{\partial S} = -\frac{(\frac{C_2}{P\,Z})\,T^{*\,2}_w}{D_2^2}$$

where, $$D_2 = 1 + (\frac{C_2\,T^*_w}{P\,Z})\,S.$$

The following table is obtained by substituting nominal values of $T^*_w = 551.23\ ^0R$, $P = 2049.08\ lb_f/ft^2$, $Z = 0.80833$ ft, and $S = 0$, & 6 (the minimum & approximate maximum value of S).

	$S=0$	$S=6$
$\partial T^*/\partial T^*_w$	1.0	0.888
$\partial T^*/\partial P$	0.0	0.015
$\partial T^*/\partial Z$	0.0	37.029
$\partial T^*/\partial S$	5.617	− 4.989

Thus from equation (H.2-2), at S = 0,

$$\omega_{T*} = \sqrt{(\omega_{T*_w})^2 + (5.617\omega_S)^2}$$

and at S = 6,

$$\omega_{T*} = \sqrt{(0.888\omega_{T*_w})^2 + (0.015\omega_P)^2 + (37.029\omega_Z)^2 + (-4.989\omega_S)^2} \ .$$

Assume the following values of the uncertainties:

$\omega_{T*_w} = 1.0\ ^0R$ $\omega_P = 0.705\ lb_f/ft^2$ $\omega_Z = 0.008$ ft $\omega_S = 0.1$.

Substituting these values the uncertainty in temperature is obtained as follows:

at $S = 0$ $\omega_{T*} = 1.15\ ^0R$, and

at $S = 6$ $\omega_{T*} = 1.06\ ^0R$.

Same as in section H.2.1, equation (H.2-4) can be used to calculate the uncertainty in the nondimensional temperature, T. Here, at $S = 0$, $T^* = 551.23\ ^0R$ and at $S = 6$, $T^* = 519.51\ ^0R$. Assume that the uncertainties in T^*_C and ΔT^* are:

$$\omega_{T^*_C} = \omega_{\Delta T^*} = 1.0\ ^0R.$$

Substituting the above values in equation (H.2-4), the uncertainty in nondemensional temperature is obtained as follows:

at $S = 0$ $\qquad \omega_T = 0.05$, and

at $S = 6$ $\qquad \omega_T = 0.04$.

VITA

Md. Ruhul Amin was born in Dhaka, Bangladesh in 1954. He received the Bachelor of Science degree in Mechanical Engineering in April 1977 from Bangladesh University of Engineering and Technology, Dhaka. He worked as a Mechanical Engineer for more than four years in Bangladesh and in Libya.

In January 1982, the author entered the Graduate School of The University of Tennessee at Chattanooga and received the Master of Science degree in Mechanical Engineering in December 1983. He joined the Graduate School of The University of Tennessee, Knoxville in January 1984. He received the degree of Doctor of Philosophy with a major in Mechanical Engineering in August 1989. While in the graduate school, he taught undergraduate courses.

The author is a member of the American Society of Engineering Education and associate member of the American Society of Mechanical Engineers. Currently, he is working as an Assistant Professor in the Department of Mechanical Engineering at Montana State University, Bozeman. The author is married to Shadmani and has a daughter, Ruhani.